Aerodynamics of Wings in Tandem at Low Reynolds Numbers

by

Syed Hassan Raza Shah

A dissertation submitted to the Graduate Faculty of
Auburn University
in partial fulfillment of the
requirements for the Degree of
Doctor of Philosophy

Auburn, Alabama
December 09, 2023

Keywords: Unsteady Aerodynamics, Tandem Wings, Low Reynolds Number Flows

Approved by

Anwar Ahmed, Chair, Professor of Aerospace Engineering
Roy Hartfield, Walt and Virginia Woltosz Professor of Aerospace Engineering
Ehsan Taheri, Assistant Professor of Aerospace Engineering
Jay Khodadadi, Alumni Professor of Mechanical Engineering

Abstract

The aerodynamic interactions between two wings of NACA0012 section arranged in tandem configuration were experimentally investigated at low Reynolds number of 20,000 and 100,000 in the wind tunnel and water tunnel. The force/moment measurements, wake surveys, and flow visualization results at pre and post-stall angles of attack ranging from -90 to +90 degrees were compared with the data of the isolated wing to determine the aerodynamic interactions. At Re_c = 20,000, a highly nonlinear lift response was observed without discrete stall and four distinct lift behavior regions. Flow visualization revealed laminar instability waves, vortex shedding, and complex interactions between surface vortices and trailing edge vortices in the wake. At Re_c = 100,000, conventional lift behavior was exhibited with a linear lift curve at pre-stall angles of attack, abrupt leading-edge stall, and static stall hysteresis. Surface flow visualization showed signatures of laminar separation bubble and progression with changing angle of attack. For the tandem configuration, three test cases consisted of: 1) changing the angle of attack of upstream wing while holding the downstream wing at fixed angles of attack; 2) holding the upstream wing at fixed angles while sweeping the downstream wing; and 3) simultaneously varying the angles of attack of both wings. Results highlighted complex aerodynamic couplings between the wings in tandem configurations in the form of upstream wing wake induced downwash on the downstream wing, modifying local velocity and turbulence intensity, altering the pressure distribution and wake trajectory depending on the relative geometric angle, stagger, and gap. The interactions manifest themselves as boundary layer transition, separation, and vortex shedding for each wing. The combined L/D ratio improved in the post-stall region and a novel "secondary stall" phenomenon was observed in the form of a sudden decrease in lift and drag of the upstream wing. Secondary stall showed dependence on wing spacing and angle of attack but was independent of Reynolds number and aspect ratio. Flow visualization indicated that the downstream wing suppressed vortex shedding from the upstream wing at a critical distance by preventing shear layer interaction that reduced lift and drag simultaneously. Spectral analysis of signals from hotwire and force sensor confirmed the aeroelastic coupling between the wake turbulence and wings for relative positions of the wings.

Acknowledgments

I would like to express my profound appreciation and heartfelt gratitude to all those who have provided support during my doctoral journey.

I would like to express my deepest gratitude to my advisor, Professor Dr Ahmed, for his invaluable guidance, support, and patience throughout my PhD studies. Professor Ahmed has been an inspiring mentor who has profoundly shaped my intellectual development. His immense knowledge, enthusiasm for research, and commitment to academic excellence have motivated me to become a better scholar and person. I am indebted to Professor Ahmed for the countless hours he has spent discussing my work, reading my drafts, and providing me with insightful feedback. Despite his busy schedule, he has always made time to meet with me whenever I needed advice or had questions about my research. I could not have completed this dissertation without his dedication and unwavering belief in my abilities, even when I doubted myself.

I am grateful to my dissertation committee members for their devoted time and for serving on my committee. Furthermore, I extend my appreciation to Andy Weldone, Cyrus, and Nicolas, for their assistance in setting up the experiment. Their ability to meet my requirements promptly and effectively was truly remarkable. I would also like to thank the Chair of the Aerospace Engineering department, Dr Thurow, for providing me with the requisite resources and support to conduct my research and shape my thinking process.

I sincerely thank my family for their constant love, encouragement, and support throughout my academic journey. My parents have been pillars of strength, providing wisdom and motivation without which I could not have succeeded. I am grateful to my wife, Sakina, and children, Daniya, Muslim, and Haniya. Their unwavering companionship has inspired me through difficult and triumphant times alike. I am also grateful for the care and companionship of my siblings.

I also wish to thank my friends for their steadfast support, motivation, and understanding throughout the highs and lows of my PhD journey. Their benevolence and faith in me have been integral, and I could not have succeeded without them. In particular, I would like to recognize Saad Javaid, Banjo, Shahid, Luqman, Mehfooz, Saleem, Mujtaba, Shehzeb, and Shahan for making my time so rewarding. Additionally, I sincerely appreciate the countless individuals whose work has enriched and motivated my research, particularly Dr Funda Kurtulus.

In conclusion, I am grateful to everyone who has played a role in my PhD journey. Thank you all for your support, encouragement, and inspiration.

Dedication

To all those who left us during this long journey, your absence is keenly felt and you will be forever missed.

Table of Contents

List of Figures

List of Tables

Nomenclature

A	axial force
AR	aspect ratio
c	chord length
C_D	coefficient of drag = D/0.5$\rho_\infty U_\infty^2 S$
C_L	coefficient of lift = L/0.5$\rho_\infty U_\infty^2 S$
C_M	coefficient of pitching moment = M/0.5$\rho_\infty U_\infty^2 S\, c$
C_{Du}	uncorrected drag
C_{Lmax}	maximum lift coefficient
D	drag
deg	degrees
G	gap, normal distance between the wings
L/D	lift-to-drag ratio
L	lift
M	pitching moment
$M_{c/2}$	pitching moment about mid-chord

$M_{c/4}$	pitching moment about quarter chord
N	normal force
P_∞	freestream static pressure
P_o	total pressure
P_{static}	static pressure
q_∞	freestream dynamic pressure, $\rho_\infty U_\infty^2/2$
Re	Reynolds Number = $\rho Ul/\mu$
Re_c	chord based Reynolds number = $\rho Uc/\mu$
Re_{cr}	critical Reynolds number
S	surface area of the wing
s	stagger, streamwise distance between the wings
sAR	semi-aspect ratio
TI	turbulence intensity, TI = rms(u′) / U x 100%
u'	perturbation velocity
U_∞	freestream velocity

Greek symbols

α	angle of attack
α_{eff}	effective angle of attack
ϵ	downwash angle
ϵ_o	downwash angle at $\alpha = 0$
μ	dynamic viscosity
ρ_∞	freestream density

Chapter 1

Introduction

"The most amazing lesson in aerodynamics I ever had was the day I climbed a thermal in a glider at the same time as an eagle. I witnessed close-up, effortlessness, and lightness combined with strength, precision, and determination."— Norman Foster

The enduring fascination with flight has consistently driven the exploration of new possibilities and the pushing of boundaries, especially in terms of the size, speed, and mission capabilities of flying vehicles. As an essential parameter in aerodynamics, the Reynolds number classifies different flow regimes and the aerodynamic behavior of wings and aircraft. Low Reynolds number flows (< 500,000) are characterized by increased viscous effects and are typically associated with small size, low atmospheric density, and reduced air speeds. The aerodynamic behavior of wings at low Reynolds numbers is inherently unsteady and is influenced by various factors, such as wing thickness, camber distribution, aspect ratio, state of the boundary layer, slipstream effects, and unsteady flight conditions such as when encountering gusts and/or freestream turbulence. In many civil and military engineering applications, there is a requirement for generating high lift, which pushes the boundaries of the angle of attack and can result in extreme incidence angles leading to significant flow separation over the wing surfaces. Uncontrolled flow separation can adversely affect aerodynamic performance and potentially cause catastrophic failure. At low Reynolds numbers, the change in the angle of attack and upstream flight conditions also results in non-linear variation in aerodynamic forces and moments. These intricate nonlinear aerodynamic characteristics and flow separation before the natural transition from laminar to turbulent boundary layer have limited commercially viable and mission-capable design solutions.

Since the 1980s, the interest in sailplanes, high-altitude low-speed aircraft, UAVs (Unmanned Aerial Vehicles), RPVs (Remotely Piloted Vehicles), and ultra-light human-powered flights, vertical axis turbines, bio-inspired flying vehicles mimicking insect flights and perching birds, etc. has ignited a pursuit of low Reynolds number aerodynamics, which remains a thriving area of exploration to this day with more recent applications such as MAVs (Micro Air Vehicles), NAVs (Nano Air Vehicles), and extraterrestrial flights like at Mars. Advancements in diagnostic technology, high-resolution force balances, pressure measurements, quantitative flow visualization techniques, and progress in computational capabilities have provided valuable insights and a better understanding of the behavior and characteristics of low Reynolds number aerodynamics, establishing it as an active research area that calls for further in-depth understanding.

Most studies aimed to improve aerodynamic efficiency, get the required amount of lift in a small volume, and delay the stall angle. An effective approach to delay stall and minimize separation for enhanced aerodynamic performance and efficiency at higher angles of attack could be by employing tandem wing configurations. The aerodynamic advantages obtained through flying in close formation for flocks of birds [1] and formation flight [2] are well known. In tandem wing designs, both the front and rear wings have comparable spans and areas, with each actively contributing to lift generation. This contrasts with traditional wing-tail or canard-wing layouts where the empennage solely provides pitching moment control. The origins of the tandem wing configuration trace back to the 19th century, with notable early designs including D.S. Brown's design in 1873, Langley Aerodrome-1894, Blériot VI-1907, Fokker V8 German fighter tandem-winged quintupriplane-1917, Caproni Ca.60-1921, Peyret Tandem-1922, Mignet Pou-Du-Ciel-1930s, Miles Libellula tandem-wing aircraft concept - 1941, and others. However, the configuration did not gain widespread adoption at that time due to limitations in understanding the complex aerodynamic interactions between the two wings as well as structural challenges posed by the heavier aircraft designs of the era [3]. Tandem wing aircraft designs in the latter half of the 20th century, showed better performance in terms of maximum take-off weight, top speed, and endurance such as the Quickie in 1977, Viking Dragonfly in 1980, Scaled Composites propeller and jet models, and the Proteus etc. The interest in convertiplanes and small unmanned aerial vehicles (UAVs) in the 21st century, along with advancements in aerospace composites, led to a resurgence of tandem configurations. Notable modern tandem wing designs include the Bell and Boeing Quad TiltRotor (QTR), Dragonfly Tango UAV, tube-launched retractable/switchable wing UAVs, United 40 MALE UAV, Airbus A3 Vahana, Poik-2, Eraole aircraft, Langley Aerodrome No. 8 (LA-8), UAV Nuuva, and Atea VTOL.

The two-wing arrangement confers several aerodynamic benefits beyond delaying stall onset [4]. The distributed lift helps reduce induced drag compared to a single wing [5], it presents a compact solution for generating sufficient lift in space-constrained applications like urban air mobility and micro air vehicles (MAVs) [6–10]. Tandem wing configuration also enables the reduced span for better ground handling and structural rigidity for low wing-loading (weight-to-area ratio) designs such as solar-powered unmanned aerial vehicles, ultralight high-altitude aircraft, and high-altitude pseudo-satellites [11]. The potential for thinner wings and improved stall characteristics exists, as flow separation on the forward wing earlier than the rear wing can preclude a nose-up stall. The tandem wing has become a popular choice for vertical take-off and landing (VTOL) in modern urban transport applications and tube-launched MAV swarms. For VTOL designs, having two sets of rotors - one on the forward wing and one on the rear wing allows for better stability and control [11]. Twin-wing designs are also often found in nature for low Reynolds number flyers for example dragonflies, moths, butterflies, flying fish, microraptors, etc.

Tandem wings can provide compactness, reduced drag, and higher speed compared to conventional layouts, but challenges remain. The use of two pairs of wings leads to the reduced wing size hence the reduction of chord-based Reynolds number. The laminar boundary layer in the Re regime is susceptible to separating even at small angles of attack, producing unsteady wake structures and having high profile drag. The wake of a finite wing comprises downwash and tip vortices. The strength of the tip vortices, length scale, and shedding frequency of the coherent structure present in the wake change with the angle of attack and Reynolds number.

At extreme angles of attack, a wing behaves like a bluff body, and strouhal number of vortex shedding matches with the wake of a cylinder. Hence, a rear wing operating in the wake of the front wing is subject to local perturbed upstream conditions, streamwise and spanwise vorticity impingement, and experiences a reduced effective angle of attack due to the downwash and velocity deficit to produce lesser aerodynamic forces and buffeting. The interaction is maximum when the center of the wake impinges the leading edge of the trailing wing [12]. Negative interference may also increase drag, and alter the stability characteristics and handling qualities.

In a tandem configuration, the aerodynamic response of the rear wing depends on the front wing, and at the same time, the presence of the rear wing alters the wake of the front wing. consequently, the wings are aerodynamically coupled, requiring simultaneous investigation. The overall response of the wings depends upon the geometric angles of attack of both wings, spacing between the wings, and Reynolds number. Understanding the aerodynamic behavior of wings in tandem is crucial to producing mission-capable and functional designs. The objectives of the present work are to investigate the effect of wing-vortex interactions on the aerodynamic characteristics of streamwise oriented wings at low Reynolds numbers for an angle of attack range of -90 to 90 degrees using force/moment measurements and a variety of flow visualization in the wind and water tunnels.

1.1 Literature review

In this section, the low Reynolds number aerodynamics response of both finite and infinite wings subjected to disturbed upstream conditions, wake impingement from an upstream body, and tandem wings aerodynamics are reviewed and summarized encompassing both past and current research.

Low Reynolds number flows are characterized by the boundary layer behavior pertaining to separation, transition, and reattachment. The relationship between Reynolds number and the maximum lift-to-drag ratio as adapted by Winslow et al [13] from the data presented by McMaster and Henderson [14], and Muller [15] is shown in Figure 1.1. Lift-to-drag ratio (L/D) is a measure of aerodynamic efficiency and determines the performance of an aerial vehicle, including range, endurance, turn radius, ceiling, and other performance parameters [16]. It is observed that below Re < 10^5, the performance of conventional smooth airfoils deteriorates as compared to rough or even flat plate airfoils. It is desirable to improve lift to drag ratio and delay the stall angles to have stable, mission-capable, and efficient designs [15]. Wings are designed to meet certain performance requirements having design constraints, therefore, a general rule may not be applied when comparing different wings [17].

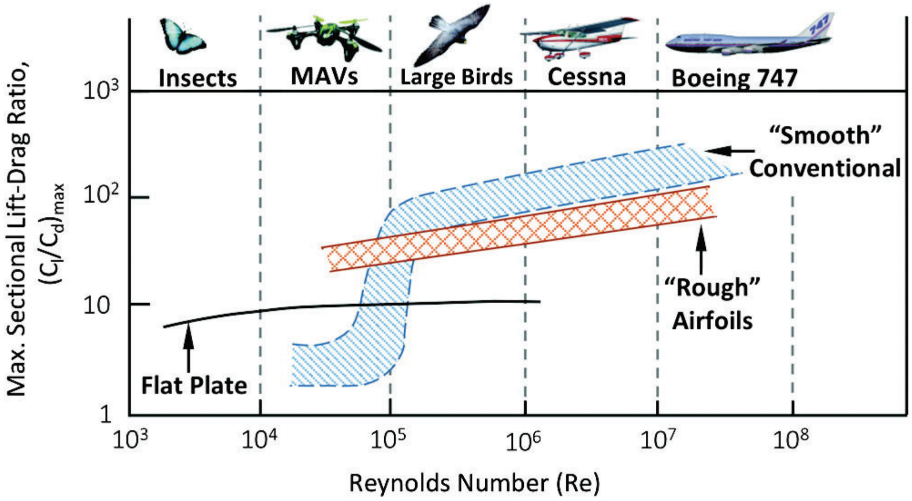

Figure 1.1: Effect of Reynolds number on maximum lift-to-drag ratio [13].

McMasters and Henderson [14] identified two possible design approaches to achieve high lift-to-drag ratios for low Reynolds number wings. The first approach is to have lower drag, which can be achieved by delaying the transition on both the upper and lower surfaces, resulting in overall lower skin friction drag, and by mitigating the adverse pressure gradient to avoid separation at the trailing edge. The second approach focuses on achieving higher lift, which depends on the pressure distribution and boundary layer transition location over the suction side only. To obtain higher values of maximum lift, the highest possible pressure loading should be near the leading edge of the wing section, followed by the transition at the recovery point to avoid laminar separation.

At low Reynolds numbers, a laminar boundary layer is unable to undergo a natural transition to a turbulent boundary layer before separation and is susceptible to separation when encountering an adverse pressure gradient [18]. There are two possible scenarios for the separated boundary layer concerning reattachment after separation (a) with the increase of angle of attack, the separation point moves towards the leading edge resulting in a pronounced shear layer but the shear layer is unable to reattach and (b) the separated shear layer is entrained by the freestream and it gains enough momentum through turbulent shear stresses and it reattaches as the turbulent boundary layer. The region bounded by the separation and reattachment points is known as a laminar separation bubble (LSB), which effectively represents a dead flow or slow-recirculating region [19]. The schematic of the separation bubble is shown in Figure 1.2(a). Laminar separation and formation of separation bubbles both have a detrimental effect on airfoil performance [20, 21].

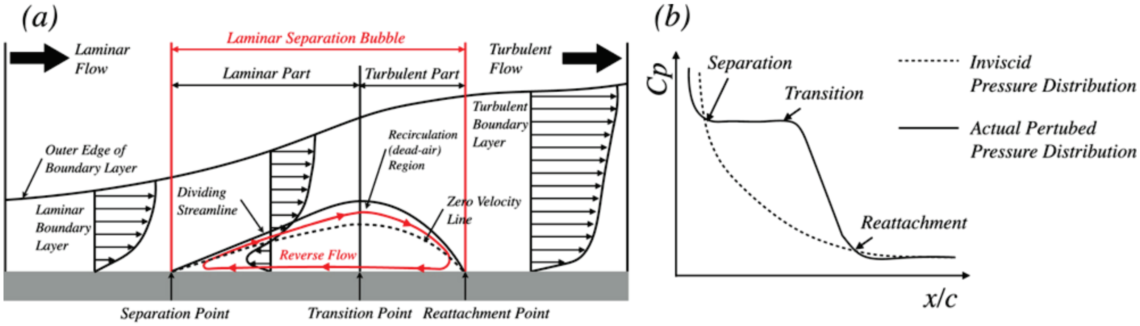

Figure 1.2: (a) Schematic diagram of the LSB adapted from Carmichael [20] and (b) shapes of pressure distribution adapted from Roberts (1980) [25] and modified by Lee et al. (2015) [26].

The necessary condition for the formation of a separation bubble is to have laminar separation, but this alone is not sufficient and it depends on Reynolds number, assuming other factors such as free-stream turbulence and pressure distribution are not considered [21]. If the Reynolds number is very high, a transition may occur before the theoretical laminar separation point, making the formation of the bubble impossible. Conversely, a low Reynolds number would lack sufficient momentum for reattachment. Typically, laminar separation is followed by the formation of laminar (or transitional) separation bubbles for $50{,}000 \leq \mathrm{Re} \leq 500{,}000$. The size and spatial location of the bubble changes with an increase in the angle of attack [22]. Ohtake et al [23] tested NACA0012 experimentally and reported a nonlinear lift curve slope in the range of 10^4 and 10^5 depending on separation and reattachment mechanism. Similar results were also reported by Winslow et al [13] using computations. For $10{,}000 < \mathrm{Re} < 50{,}000$, boundary layer separation occurs near the trailing edge even at very low angles of attack. With an increase in the angle of attack, the separation point reaches the leading edge, and a stall occurs accompanied by a decrease in the lift. The separated free shear layer after laminar separation in this range of Re typically does not undergo a transition to turbulent [15]. For Re < 10,000, classified as an ultra-low Reynolds number, the separated shear layer remains laminar for an extended duration without reattaching to the surface, and no stall phenomenon is observed [24]. Roberts [25] investigated laminar separation bubbles for thin airfoils and found that because of the slow recirculating region, the pressure distribution over the wing was altered in comparison to inviscid flow. As a consequence pressure plateau was observed over the length of the separation bubble which was followed by a sharp recovery due to the reattachment as shown in Figure 1.2(b). Lee [26] demonstrated through large eddy simulation that the LSB may not show the plateau pressure region depending on the Reynolds numbers, and the occurrence of the plateau region preceding the rapid pressure recovery region was observed exclusively for the steady-fluctuating laminar separation bubble and not for the steady LSB. The author distinguished two types of separation bubbles based on turbulent kinetic energy (TKE) distribution within the bubbles. A separation bubble was considered steady when TKE was negligibly small (2% of free stream velocity) at lower Reynolds numbers (Re_c = 5000 and 6100) through the entire LSB, whereas at higher Reynolds numbers (Re_c = 11000 and 20000), however, two distinct regions were observed within the LSB, the first region had almost zero TKE and fluctuations were observed downstream portion of the bubble, hence it was called steady-fluctuating laminar separation bubble.

O'Meara and Mueller [27] conducted an experimental investigation to document the structure and behavior of laminar separation bubbles at low Reynolds numbers. The separation bubble flow field over the airfoil was surveyed using hot-wire anemometers for 12 different conditions to isolate the effects of Reynolds number, angle of attack, and disturbance environment. Results showed that the laminar separation bubble formed on the $NACA66_3 - 018$ airfoil decreased in length and thickness as the chord Reynolds number increased. The increase in disturbance level caused the reduction in the length of the bubble and the suction peak grew in absolute magnitude. Hence, the authors concluded that the effects of the disturbance environment were similar to those produced by the increase in the chord Reynolds number, and an almost linear relationship was observed between the bubble thickness and the total bubble length. At α = 12 degrees, the length and thickness of the bubble increased because of a more severe adverse pressure gradient before "bursting". Gaster [28] classified separation bubbles as ’long’ or ’short’ based on the length-to-displacement thickness ratio, while Tani [21] proposed differentiating bubbles based on their impact on pressure distribution. A long bubble reduces the suction peak, creating an extended suction plateau that is both lowered and elongated with an increase in incidence angle. Conversely, the presence of a short bubble does not significantly affect the peak suction.

The separation and reattachment mechanism of the separated boundary layer with increasing angle of attack determines the stall behavior. Jones [29] was the first to identify different types of stalls at low Reynolds numbers. McCullough and Gault [30] classified three "pure" stall behaviors namely trailing-edge stall, leading-edge stall, and thin-airfoil stall. Additionally, a fourth type of stall exists which is a combination of two "pure" stalls. These stalls are represented in Figure 1.3.

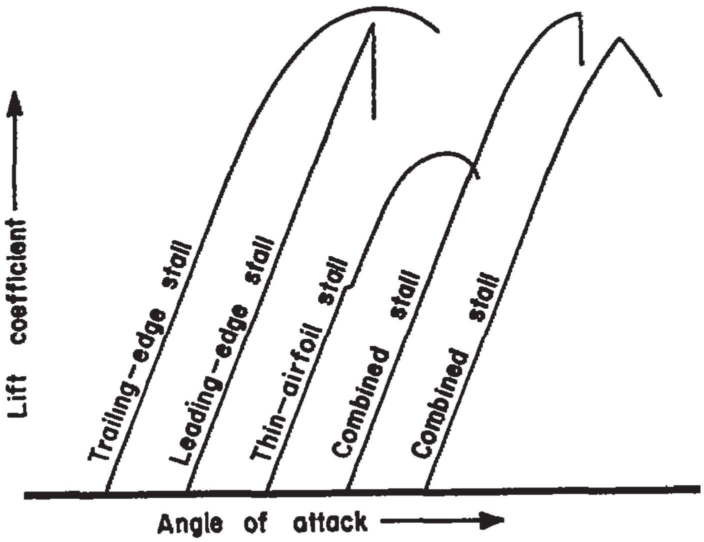

Figure 1.3: Classification of stall characteristics [30].

Trailing-edge stall is characterized by gradual and continuous force and moment variations, as well as a well-rounded lift-curve peak. Turbulent separation is initiated from the trailing edge and the separation point moves toward the leading edge with an increase in the angle of attack. In contrast to the trailing-edge stall, little or no change in the lift-curve slope is exhibited by the leading-edge stall before reaching the maximum lift. This indicates that the lift curve slope remains relatively constant until lift reaches its maximum value. However, once maximum lift is attained, a further increase in the angle of attack causes the lift to decrease abruptly. This type of stall occurs due to the abrupt separation caused by the "bursting" of the leading-edge separation bubble without subsequent reattachment. The thin airfoil stall is observed in airfoils with a rounded leading edge. A rounded lift-curve peak, similar to the trailing-edge stall, characterizes it. The name can be misleading because this type of stall can also occur on thick airfoils. However, this behavior is typically observed in thin flat plates. Flow separates near the leading edge and reattaches downstream, and as the angle of attack increases, the reattachment point moves towards the trailing edge. Combined stalls feature two types of stalls and one is preceded by the other. The lift-curve peak may have a semi-rounded shape or be relatively sharp, deviating from the well-rounded peak observed in the trailing-edge stall, when the leading-edge stall is preceded by the trailing-edge stall. Another type of combined stall occurs when the leading edge stall is followed by a thin-airfoil stall.

Schmitz [31] reported a critical Reynolds number for various airfoil shapes within the range of Re < 150,000, through wind tunnel testing. It was found that the transition from a laminar to a turbulent boundary layer and the reattachment of the separated shear layer at the critical Re, resulted in an increase in the lift and a decrease in the drag coefficients, leading to a high lift-to-drag ratio (L/D) after reattachment. Mueller and Batill [32] investigated an infinite wing comprising $NACA66_3 - 018$ section at chord-based Reynolds numbers ranging from 40,000 to 400,000 using direct force measurements, smoke, and surface flow visualization techniques. Force data were recorded at Re = 40,000, 130,000, and 400,000. The wing response for each of these three Reynolds numbers exhibited radical differences. With an increase in Reynolds number, the size of the separation bubble decreased. At the lowest Reynolds number tested (Re= 40,000), a sudden increase in the lift was caused by the formation of a leading-edge separation bubble on a smooth airfoil at α = 8 deg. The incident of turbulent separation has the potential to impact laminar separation, as it leads to a decrease in circulation, reducing local velocities across the airfoil and expanding the separation bubble. The decline in pressure gradient along the airfoil, corresponding to the reduction in circulation, tends to postpone turbulent separation. As a result, the interaction between laminar and turbulent boundary layer separation does not constitute a divergent process [30]. Mueller and Pohlen [33] investigated the influence of wind-tunnel freestream disturbances on low Reynolds numbers using Lissaman 7769 airfoil under different levels of freestream disturbances and acoustic levels. The results showed that an increase in the upstream turbulence level eliminated the stall hysteresis and boundary layer transition very close to the leading edge. The effect of upstream turbulence was similar to boundary layer tripping and a model with small fabrication defects over the surface. Wang et al [34] presented the relationship between critical Reynolds number and turbulence intensity by testing NACA0012 airfoil at three freestream turbulence levels (0.6%, 2.6%, and 6.0%) and two Reynolds numbers of 5,300 and 20,000. It was observed that the critical Reynolds number decreases exponentially with an increase in turbulence intensity and results were found to be in agreement with the values reported by Carmicheal [20] and Huang and Lin [35]. It was found that the increase in turbulence intensity increased C_{Lmax} but the effect was more pronounced for ultra-low Reynolds numbers (< 10,000) as compared to the low Reynolds numbers investigated. Effective Reynolds number may be calculated using turbulence factor (TF) and critical Reynolds number(Re_{cr}) by utilizing the relation $TF = Re_{eff}/Re_{cr}$. Kase et al [36] tested NACA0012 airfoil at Re = 36,000 in a blowdown type wind tunnel. The authors found that the increase in upstream turbulence levels from TI = 0.7% to 12.6% resulted in a decrease in the nonlinearity of aerodynamic characteristics and also eliminated the "dead band" at low angles of attack around zero degrees.

Paula et al [37] investigated the effect of wing thickness on symmetric airfoils in the range of 50,000 to 290,000. The results show that the thinner airfoil(NACA 0012) at Reynolds numbers (>100,000) resisted trailing edge separation and had a higher lift curve slope but the smaller leading edge radius caused earlier leading edge separation hence maximum lift coefficient was less than thicker airfoils. Conversely, thicker airfoil(NACA 0030) at Re < 100,000 had massive flow separation at the leading edge and therefore lesser maximum lift coefficient. The transitional Reynolds number also depend on airfoil thickness, Huang and Lin [35] found transitional Re to be greater than 70,000 for NACA 0012, whereas for thick airfoils like NACA0025, it was reported at Re=150,000 by Yarusevych et al [38].

The flow separation and formation of laminar separation bubbles are unsteady phenomena and the location of transition of the separated shear layer is not confined to a point location but a finite region [39]. Unsteady separation and reattachment occur at multiple points downstream which results in unsteady vortex shedding. Huang and Lin [35] investigated the unsteady characteristics of the flow over the surface and its effect on the shed vortices and shear-layer instabilities. They classified it into four modes laminar (mode I), subcritical (mode II), transitional (mode III), and supercritical (mode IV). For mode I, the velocity signals in the wake are smooth and periodic, for mode II, they become fluctuating, for mode III, become irregular and vortices lose coherency, for mode IV the signals become periodic again with turbulent fluctuations as shown in Figure 1.4.

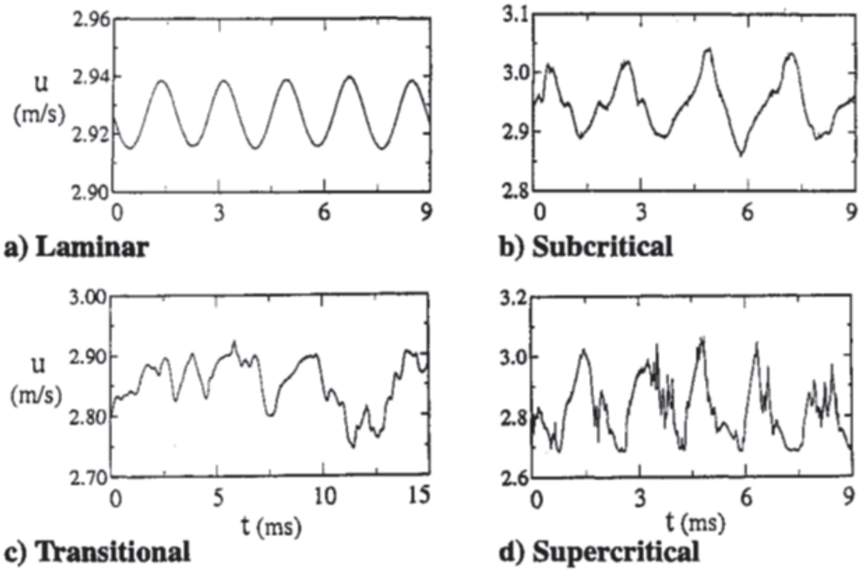

Figure 1.4: Typical hot-wire signals for vortex shedding in four characteristic modes, Re = 27,610: a) α = 1 deg,b) α = 4.5 deg, c) α = 8 deg, and d) α = 16 deg [35].

Lin and Pauley [40] conducted a numerical study to explore vortex shedding from a separated shear layer at different Reynolds numbers and angles of attack. The separated shear layer is naturally unstable due to the presence of Kelvin-Helmholtz instabilities. These instabilities grow after the transition phase, leading to the formation of vortices as the shear layer rolls up. In the laminar free shear layer, the vortices have their axis of vorticity perpendicular to the flow direction. Yarusevych et al [41] discussed the coherence and length scale of the wake vortices when the separated shear layer reattaches to form a laminar separation bubble. This coherence and length scale depends on the Reynolds number and, indirectly, on the angle of attack, as depicted in Figure 1.5. The research provided an overview of the coherent structure in the wake of an airfoil at low Reynolds numbers of $55,000 < Re < 210,000$. The analysis utilized smoke wire for flow visualization and hot wire anemometry to study the spectral content of flow structure over the wing and in the wake. At a particular angle of attack before stall, the increasing Reynolds number decreases vertical length scales in wake structures. The research also discussed experimental techniques to accurately capture the weaker and orthogonal velocity signals. The transitional effect, coherence, and length scales depend upon the formation of laminar separation bubbles, which depend upon the Reynolds number. Jung and Park [42] found that the vortex shedding frequency decreases with the increase in the angle of attack for a static airfoil. Kurtulus [43] computationally investigated the NACA0012 section wing at Reynolds number of 1000 for the angle of attack range of 0 to 90 degrees. The unsteadiness of aerodynamic forces was identified by plotting maximum and minimum amplitude along with the mean values. The mean and unsteady vortex patterns were computed for pre, post, and deep stall angles of attack. The results showed the growth and splitting of vortices at different angles of attack. The Strouhal number, which represents the non-dimensional shedding frequency in the wake, showed different values for the extreme angle of attack ranges.

The real-life applications involving wings rarely operate in a disturbance-free environment. Factors like formation flights, gusts, and encounters with the wake of upstream bodies make the presence of upstream disturbances and turbulence inevitable. The vortex interaction with the follower wing is closely related to the vortex strength and distortion upstream. These disturbances can affect the handling qualities by altering the lift-to-drag ratio and moment characteristics. Rockwell [44] gave an outstanding review centered on

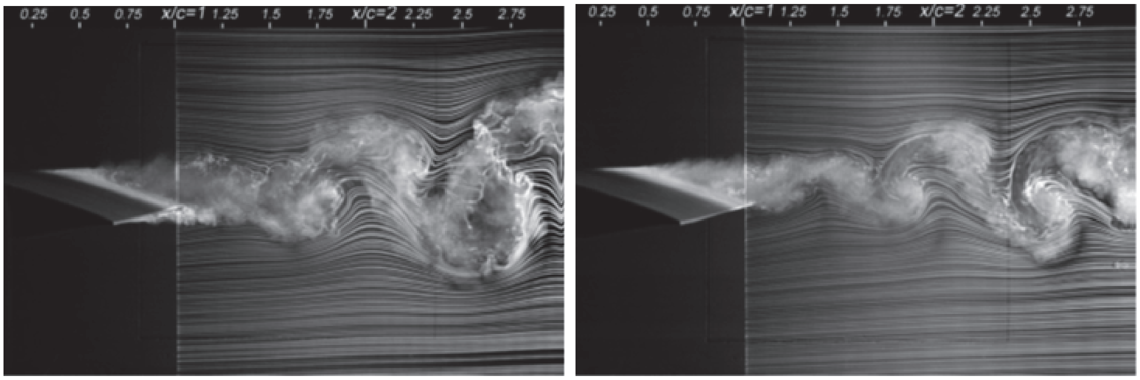

(a) Axial Force (b) Normal Force

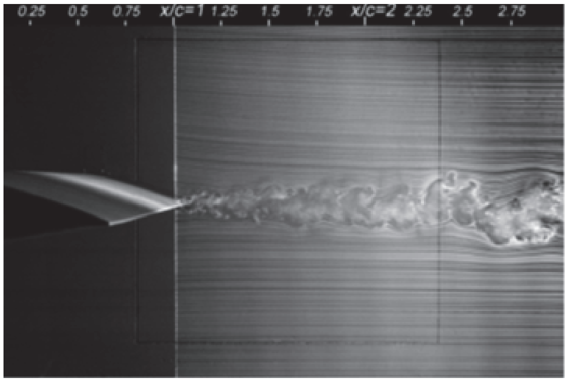

(c) Normal Force

Figure 1.5: Flow visualization at α = 5 deg (a) Re = 55 × 10^3 (b) Re = 100 × 10^3 (c) Re = 150 × 10^3 [41].

vortex-body interaction, with a particular focus on direct and nearly direct impingement. The vortex-body interactions were categorized based on the orientation of the incident vortex with the leading edge. This orientation was defined by the alignment of the vortex axis with the axis of the body, as illustrated in Figure 1.6.

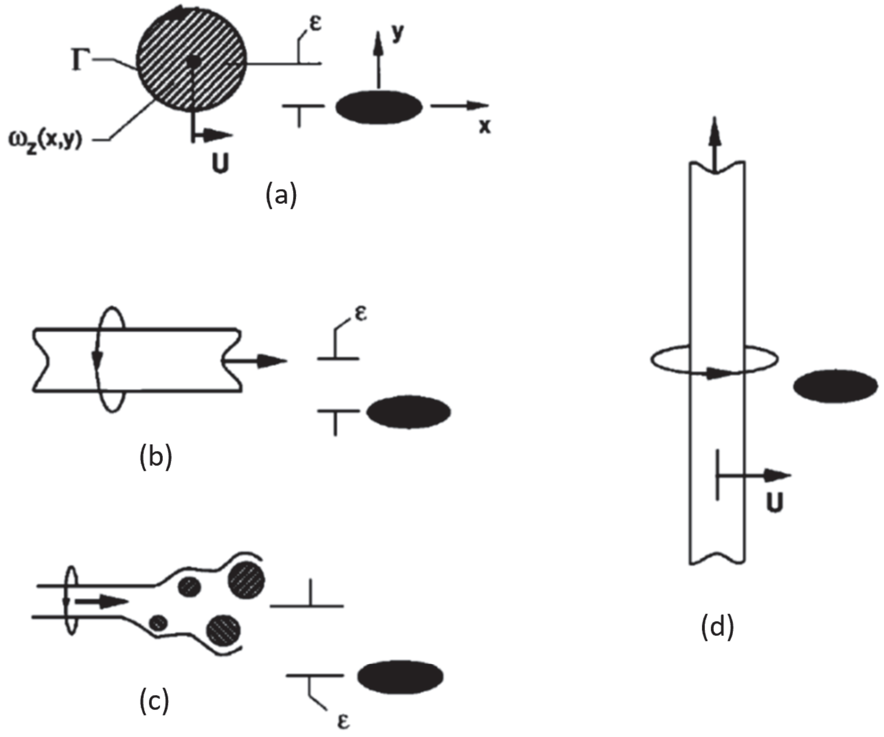

Figure 1.6: Representations of basic classes of vortex-body encounter: (a) parallel vortex; (b,c) streamwise (perpendicular) vortex without and with breakdown; and (d) normal vortex interactions [44].

Michelsen and Mueller [12] experimentally examined the performance of a Wortmann FX63-137 airfoil under wake interference from an upstream airfoil at a Reynolds number of 150,000. The findings revealed that the wake deficit caused by the upstream airfoil resulted in reduced lift and drag for the downstream airfoil when compared to operating as a single wing. However, there was a positive increase in pitching moments. The influence became more significant with higher angles of attack of the upstream airfoil, as the deficit grew, as well as vertical offset in the maximum velocity deficit location from the centerline. Walker and Robinson [45] studied the impact of orthogonal unsteady vortex interaction resulting from the pitching motion of an upstream wing on a stationary downstream wing. The experiment involved the use of NACA0015 section airfoils for both the upstream and downstream wings, with a chord length of six inches. The semi-span of the upstream wing was 1.8c, while that of the downstream wing was 2.5c. The wings were aligned in the streamwise direction. The downstream wing was subjected to the tip and dynamic stall vortex from the upstream wing. It was found that the trailing wing experienced transient aerodynamic loads. They concluded that the unsteady loads were primarily caused by the fluctuating upstream conditions rather than the direct impingement of vortex structures. Jones and Cetiner [46] conducted an overview of gust encounters on the unsteady response of the rigid wings. The effects of transverse gust, vortex gust, and streamwise gust were discussed. These three types of gust encounters are shown in Figure 1.7. The transient transverse and vortex gust encounters resulted in a sharp increase in lift, but it was followed by a sudden decrease with the vortex leaving the wing. The lift increase was attributed to the formation of a strong leading-edge vortex during the encounter. In the case of streamwise encounters, the oscillatory loads observed on the wings varied with the gust amplitude and frequency. These variations were attributed to changes in upstream conditions, while the effective angle of attack did not necessarily change. The gust ratio was defined as the maximum velocity in the flow disturbance normalized by the freestream velocity. In transverse or vortex gust encounters with large gust ratios, extensive flow separation occurred, thus the production of aerodynamic forces was dominated by inviscid effects. Contrarily, in a streamwise gust encounter at low incidence angles, a high gust ratio did not always lead to flow separation. Therefore, forcing in a streamwise gust encompassed both inviscid and viscous effects.

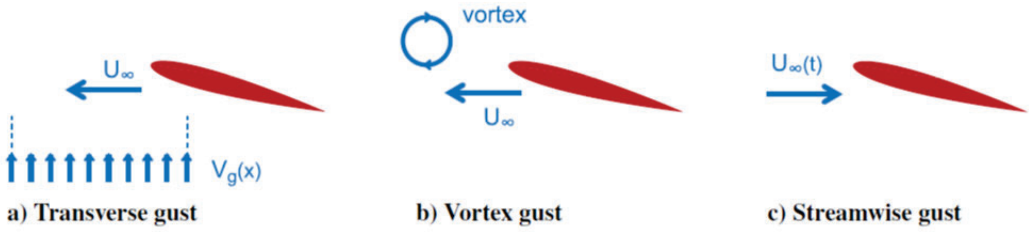

Figure 1.7: Schematic of three canonical gust encounters [46].

Yarusevysch et al [47] experimentally investigated a NACA0025 section two dimensional wing at Re = 57,000, 100,000, and 150,000 and three angles of attack 0,5 and 10 degrees in the presence of periodic disturbances through acoustic excitation using qualitative surface flow visualization and wake survey with hotwire anemometry. The results showed that the boundary layer separation can be suppressed by external acoustic excitation at a particular frequency and appropriate amplitudes that result in higher lift, lower drag, and thinner wake. Zhang at el [48] investigated a NACA0012 profile wing of AR = 4 at Re = 100,000 in the presence of upstream wake produced by different thickness elliptical leading edge bluff bodies having sharp and boat tail backs as shown in Figure 1.8. The researchers made several interesting observations. First, the presence of quasi-periodic large-scale coherent vortical structures significantly contributed to lift enhancement and stall delay. Particle Image Velocimetry and Proper Orthogonal Decomposition (POD) analysis revealed the formation of leading-edge vortices and subsequent reattachment akin to the dynamic stall observed in oscillating wings. Moreover, the study revealed the existence of an optimal offset distance from the wake centerline, where maximum lift enhancement occurred. At these specific locations, smaller amplitude flow oscillations led to the formation of a larger separation bubble in the post-stall regime, instead of direct impingement at the wake centerline. So the thickness of the wake generator played a role in determining the lift coefficients. An increase in wake generator thickness resulted in higher maximum lift coefficients, mainly due to the slower decay of shed vortices in the wake.

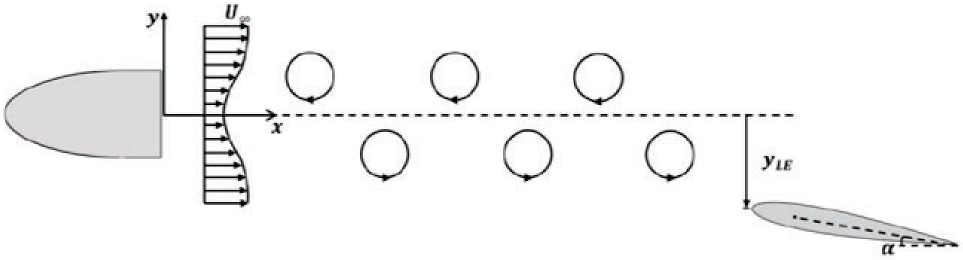

Figure 1.8: Schematic of a wing in the wake of a wake generator [48].

Lefebvre and Jones [49] investigated the performance of an airfoil in the wake of a cylinder, with a diameter equal to the chord length at Reynolds number range of 80,000 to 125,000. The researchers varied the gap between the cylinder and airfoil from 1 to 5 chord length. Two distinct cylinder wake behavior upstream of the wing were observed. For gaps less than 2c, the counter-rotating vortices in the wake induced negative drag on the airfoil but for gaps greater than 3c Von Karman vortex street was formed which resulted in an oscillating flow field.

Barnes et al [50] conducted a computational investigation focusing on the impingement of a streamwise-oriented vortex with a wing near its tip. The situation mimicked the impingement of wing tip vortices from an upstream wing onto a downstream wing in a formation flight. The wing was positioned at a positive angle of attack, and the vortex of constant strength was generated upstream at different vertical positions. The spanwise location of the impinging vortex was fixed. The path of the incident vortices didn't follow freestream directions, and helical instabilities were observed upstream of the region where direct impingement took place on the leading edge. The pressure gradient over the wing and the relative position of the incident vortex determined the favorable or adverse condition for the instabilities to grow as shown in Figure 1.9. Barnes et al [51] in an additional investigation explored the interaction of wingtip vortices of opposite directions in a plane at a Reynolds number of 30,000. The relative alignment of the wing tips was varied. The presence of the rear wing provided an upward/downward and inboard/outboard trajectory on the upper and lower surface that was found to depend on the impingement location relative to the wing tip. The inboard flow resulted in rapid decay because of the surface loads. An increase in the lift of the rear wing compared to the single wing was observed because of the induced upwash, which increased the effective angle of attack. A change in the rolling moment was also observed. The rear wing may experience unsteady loads and buffeting based on the relative lateral position. The increasing angle of attack of the front wing resulted in the strengthening of the incident vortex as shown in Figure 1.10.

Chen et al [52] conducted experiments on the interaction of tip vortices with downstream wings. They studied both counter-rotating and co-rotating vortices. It was observed that when there was no direct impingement or the wing tips were separated by more than twice the vortex core radius, the time-averaged structures of the tip vortices from the front wing remained relatively unchanged. However, there was a significant change in the tip vortex from the rear wing. McKenna et al [53] identified that the progression of the incident vortex was

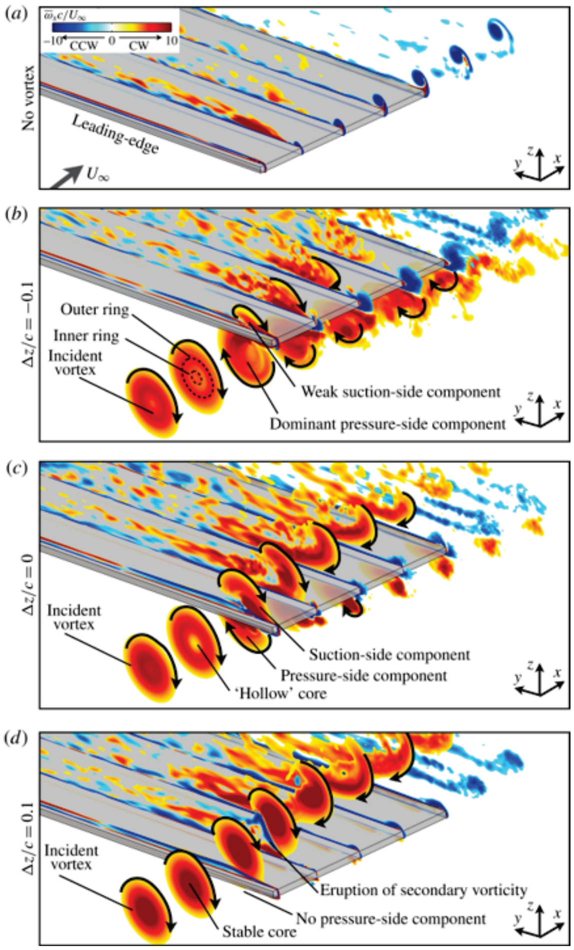

Figure 1.9: Slices of time-averaged streamwise vorticity at several chord-wise positions [50].

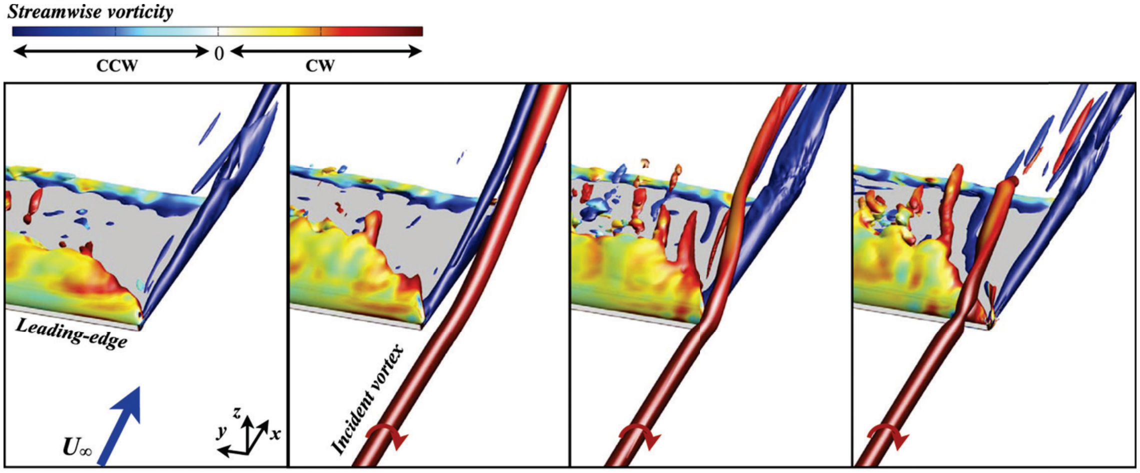

(a) Single wing (b) Δy = 0.00 (c) Δy = 0.15 (d) Δy = 0.30

Figure 1.10: Time-mean iso-surface of Q-criterion colored by streamwise vorticity (Q = 2) [51].

affected by the upstream influence of the rear wing, and this effect strongly relied on the spanwise location of the vortex impingement. Notably, this influence was not confined to the immediate local region just upstream of the leading edge of the rear wing but could extend up to one chord length upstream. Turhan et al [54] studied the response of a stationary wing in the wake of a periodically plunging upstream airfoil using direct lift measurements and particle image velocimetry at Re = 20,000. The results indicated that the maximum lift force occurred when the leading edge of the wing was positioned at or slightly above the wake centerline. The peak lift coefficients decreased with increase in deflection angle of the wake when the upstream airfoil was plunging at a nonzero mean angle of attack.

Scharpf and Muller [55] investigated the tandem wing configuration at a chord-based Reynolds number of 85,000 using Wortmann FX63-137 airfoils. The investigation involved direct force measurements, static pressure distributions, and smoke flow visualizations. The two airfoils were identical and were aligned in the streamwise direction with a 1.5c distance between the c/4 point on each airfoil. The results demonstrated that the tandem configuration increased the range of Reynolds numbers where separated flow hysteresis occurred. The coefficient of aerodynamic forces and moments for both upstream and downstream wings were obtained for the angle of attack range of -20 to 20 degrees while keeping the other wing fixed at 0, 5, and 10 degrees. the force measurements revealed that the presence of the front wing decreased the effective angle of attack of the rear wing. As a result, the rear wing produced less lift at all angles of attack and had a higher stall angle. Furthermore, the presence of the front wing affected the separation bubble, either suppressing it or altering its length depending on the angle of attack. When the rear wing was positioned at a positive incidence angle, it caused changes in the pressure distribution over the suction side of the front wing, resulting in reduced lift and drag. The most interesting observation was that the flow separation on the front wing resulted in the flow separation over the rear wing. In other words, flow attachment on the rear wing required attached flow on the front wing as shown in Figure 1.11.

Fanjoy and Dorney [56] studied tandem wing interaction at a Reynolds number of 6×10^6 experimentally and observed that the decrease in streamwise spacing resulted in greater

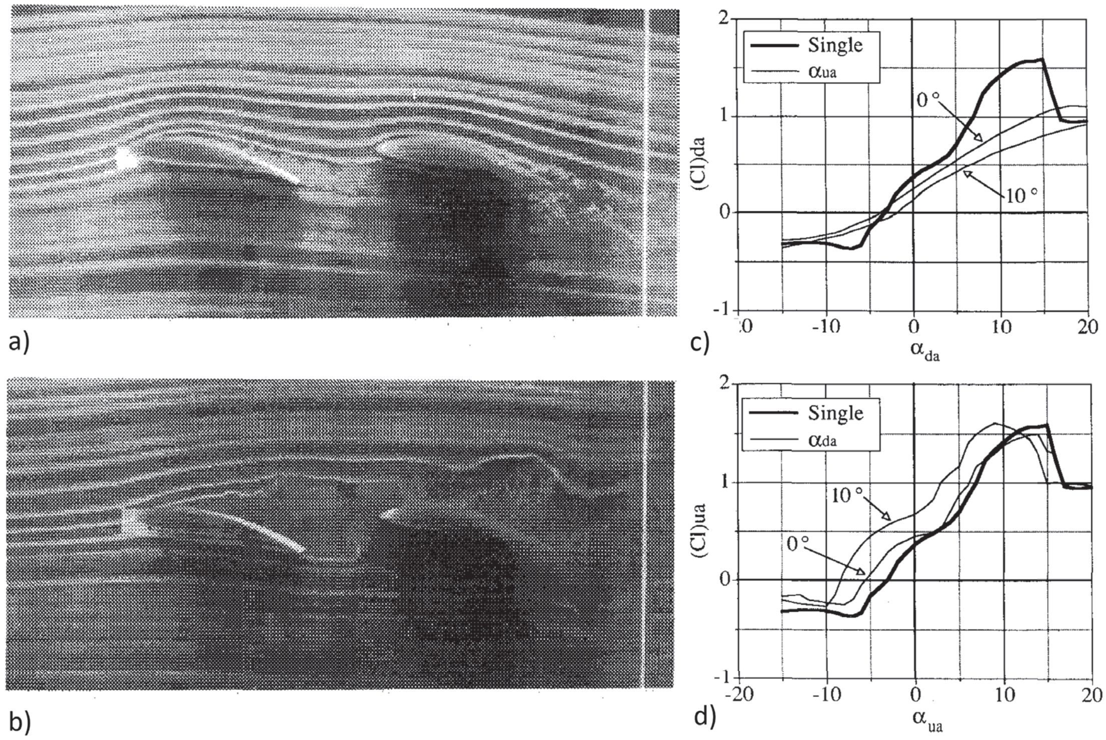

Figure 1.11: Tandem airfoils at Re = 8.5 x 10^4, illustrating the separation hysteresis phenomenon for both upstream and downstream airfoils at 10 deg: a) attached-flow condition; b) separated-flow condition (c) Lift coefficient of the downstream airfoil for upstream airfoil at 0 and 10 deg (d) Lift coefficient of the upstream airfoil for downstream airfoil at 0 and 10 deg for stagger = 1.5c, gap = 0 [55].

interaction. The rear airfoil was found to be operating at shallower angles of attack for all conditions with direct impingement of wake at small angles of attack. Another numerical study conducted by Fanjoy et al [57] at a Reynolds number of 6×10^6 on two NACA0012 section 2D wings in tandem demonstrated that, with moderate-to-large streamwise spacing, the rear wing performed similarly to the front airfoil at lower angles of attack. However, at higher angles of attack, the rear wing exhibited a lower lift-to-drag ratio compared to the front wing. Decreasing the stagger distance resulted in increased lift and reduced drag on the front wing, while causing reduced lift and increased drag on the rear wing. Jones et al [58] experimentally investigated biplanes and tandem wings at a Reynolds number 100,000 with different vertical and horizontal spacing by employing two flat plates of a semi-aspect ratio of 2. They observed the benefits of the wings in tandem at higher angles of attack and the post-stall region due to the direct wake interaction of the two wings. The maximum lift coefficient was sensitive to the stagger and gap between the wings. The results were in agreement with the tests carried out by Ahmed and Kohama [59] by utilizing SYM-1B profiled infinite wings at a Reynolds number of 2.8×10^5. Jones et al [60] also tested spanwise flexible front and rigid rear wings in tandem configuration. They found the presence of a rigid rear wing had a profound effect on flow-induced vibrations of the front flexible wing and also the flexibility changed the location of shear layer impingement on the trailing wing. Khan and Mueller [61] conducted an experimental study on the impact of canard tip vortex on an airfoil, using Wortmann FX 63-137 profiles at a Reynolds number of 150,000. The canard tip was aligned with the mid-span of the main wing, positioned 3c downstream and with varying vertical positions. The results revealed significant effects on the aerodynamics of the main wing due to the tip vortex and wake from the canard. This was attributed to the momentum deficit in the wake induced by the canard locally upstream of the wing and the resulting net downwash due to tip vortices. Consequently, the main wing experienced reduced aerodynamic loads, with a greater reduction in drag compared to lift, resulting in a higher L/D ratio for the canard-wing configuration than for the single wing. However, this effect diminished at higher angles of attack.

Faure et al [62] tested wing-tail arrangement experimentally using strain gauges and particle image velocimetry at a Reynolds number of 5.83×10^4 based on wing chord. The chord length of the tail was half of the wing. The two-dimensional studies utilized NACA 23012 airfoils while maintaining a 3c distance between the leading edges in the streamwise direction and 1c vertically. The force data showed no impact on the wing because of the tail however for the tail, the stall was not observed and the lift kept on increasing with a reduced lift curve slope. The study identified two possible effects on the tail i.e. wake influence and vortex forcing. The wing wake influenced the pressure and suction side of the wake and resulted in a change in the pressure difference between the upper and lower side of the tail as shown in Figure 1.12.

Chou et al [63] investigated the flow structures between two tandemly arranged airfoils at a Reynolds number of 100,000 by employing NACA0012 profile wings. The front and rear wings had the chord length of 15cm and 10 cm respectively. The study suggested that the maximum distance between the front and rear wing cannot exceed 4 times the chord length of

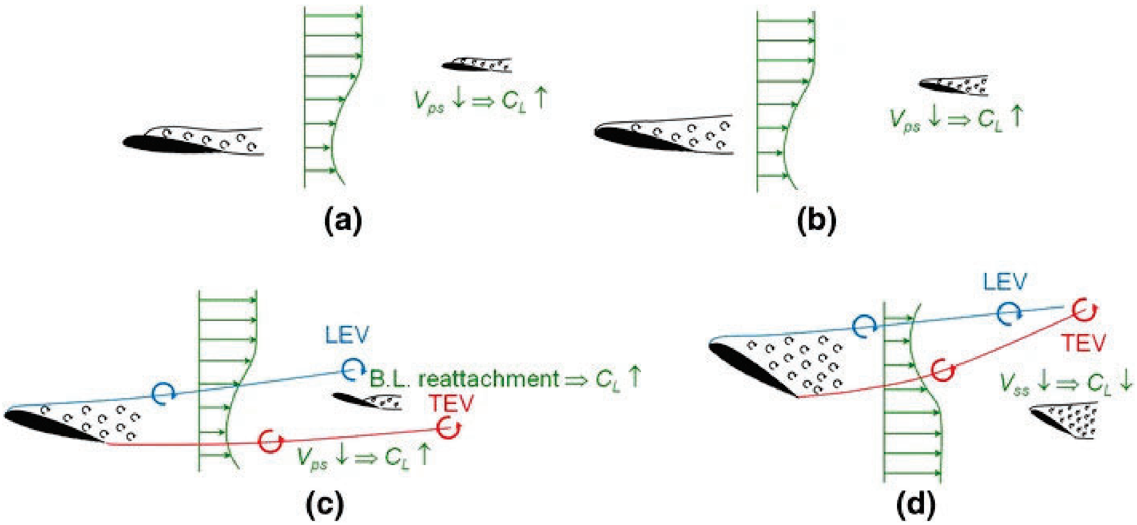

Figure 1.12: Sketches of the flow development around the tail corresponding to (a) α = 5 deg, (b) α = 10 deg, (c) α = 15 deg, and (d) α = 30 deg [62].

the front wing because of the range, and roll up of the vorticity sheet in the spreading wake as shown in Figure 1.13.

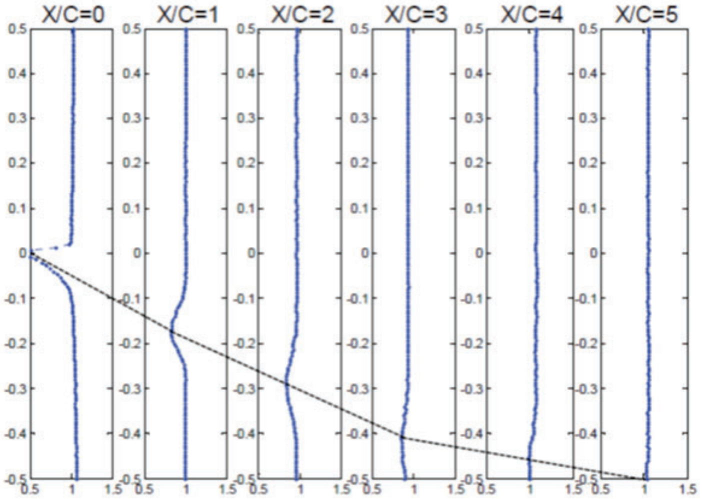

Figure 1.13: Streamwise mean velocity development along downstream at α =10 deg [63].

The computational results by Zhang et al [9] showed that the tandem wing configuration helped to increase lift to drag ratio more for the thicker airfoil as compared to thinner for closely coupled wings. Chen and Wang [64] employed Prandtl's lifting line theory to predict the section lift coefficients for wings in tandem at various angles of attack and spacing. The results obtained revealed that larger negative gaps and stagger led to improved lift characteristics. The study concluded that the advantages of the tandem wing configuration were more pronounced when the incidence angle and span of the front wing were reduced, or when the incidence angle and span of the rear wing were increased. Whereas Cai et al [65] utilized high-fidelity simulations and identified that at a higher Reynolds number of 13.9 x 10^6, the front wing aerodynamics was insensitive to variation in the gap and stagger.

While research on vortex interactions for tandem wings has focused primarily on flapping wings [66–69], gaining a better understanding of the unsteady behavior and interaction of static wings under steady external conditions at low Reynolds numbers would also expand our knowledge of the vortex shedding observed in flapping airfoils during this flight regime. The analytical models used to describe flapping motions often rely on quasi-steady approaches [70]. Rojratsirikul et al. [71] and Gordnier [72] have observed close coupling between unsteady vortex shedding for tandem wing configurations. Near stall and at post-stall angles of attack, large amplitude fluctuations in lift are observed at static angles of attack. The former is considered to result from periodic switching between stalled and unstalled states. The post-stall behavior of tandem wing configurations remains unexplored.

Low Reynolds number applications often attain post-stall angles of attack. For example, micro air vehicles (MAVs) fly at high angles of attack to overcome the poor efficiency associated with low Reynolds numbers. Therefore, gaining a comprehensive understanding of the aerodynamic physical characteristics of wings in tandem configuration subject to unsteady loads under steady conditions necessitates a detailed analysis across the full range of angles of attack.

1.1.1 Summary

At low Reynolds numbers, the aerodynamic response of a wing is highly dependent on the laminar-turbulent transition, laminar separation, and reattachment. This results in the formation of laminar separation bubbles that are sensitive to parameters such as angle of attack and upstream turbulence levels. Downstream of separation, unsteady reattachment induces the generation and shedding of coherent structures into the wake. In a tandem wing configuration, the downstream wing operates in the disturbed flow from the upstream wing.

Thus, the aerodynamic response is coupled with the relative positions and incidence angles of both wings. Furthermore, the wake interference from the rear wing can alter the aerodynamic response of the front wing under certain conditions. A comprehensive investigation of tandem wings across a range of angles of attack, Reynolds number, spacing, and vertical offsets is therefore crucial to understanding the aerodynamic interactions between the wings and the implications these couplings have on the combined force and moment characteristics.

1.2 Objectives of Research

The objective of this research is to investigate the aerodynamic response of static rigid wings under steady upstream flow conditions at low Reynolds numbers. It is also imperative for developing a complete theoretical framework to interpret the intricate unsteady aerodynamics of interaction. The complex aerodynamic interplay between trailing vortices and wake with the downstream wing, along with the implications on the upstream body, have yet to be fully understood. Experimental analysis conducted at low Reynolds numbers facilitates exploration encompassing both unsteady and viscous effects on the aerodynamic response of tandem wings.

This work emphasizes the aerodynamic response of finite aspect ratio rigid wings in tandem at low Reynolds numbers for the full spectrum of angles of attack ±90 degrees. Extensive wind tunnel testing will obtain force and moment data, complemented by hot-wire anemometry and various flow visualization techniques for physical insight. The specific goals are:

- Investigate the effect of the front wing on the aerodynamic performance of the rear wing at various angles of attack. Examine how the velocity deficit, downwash, and turbulence intensity generated by the front wing impact the lift, drag, and stall characteristics of the rear wing.

- Study the effect of the rear wing on the front wing performance. Determine how the rear wing alters the local flow conditions around the front wing, modifying its lift, drag, and stall behavior. Quantify these interactions at different front and rear wing angle of attack combinations.

- Analyze the simultaneous coupled effects between the front and rear wings across a range of angles of attack. Map the aerodynamic interactions and measure the magnitude of influence each wing has on the other. Identify beneficial and detrimental combinations for overall system performance.
- Examine the underlying flow physics of tandem wing interactions. Visualize wake structures, velocity profiles, and turbulence to identify mechanisms by which the wings influence each other. Relate flow features to force measurements on the wings.

Changes in the positioning and angle of attack influence the intensity and magnitude of the unsteady interactions between the wings. The substantial datasets produced will furnish perspective into the fundamental understanding of the flow physics of tandem wings under low Reynolds number conditions. The acquired knowledge can direct future research and design optimization involving tandem wings including MAVs, NAVs, bio-inspired flapping wings, and other small aerial vehicles, vertical axis turbines, etc.

Chapter 2

Experimental Facilities and Techniques

Experiments at low Reynolds numbers pose unique challenges due to the small magnitude of the aerodynamic forces produced. Several factors such as the model geometry and testing conditions influence not only the magnitude of the forces but may also alter the flow behavior. As a result, there are often slight variations in the results obtained in different wind tunnels. These factors include but are not limited to, the freestream turbulence level, angularity and uniformity of flow in the test section, the accuracy and resolution of the force balance, the signal-to-noise ratio in measurements, surface finish and size of the wing model relative to the test section dimensions, the mounting arrangement and clearance of the wing model from the end plate or wall (in the case of two-dimensional or reflection plane testing), corner effects and the formation of corner vortices, etc. Therefore, comprehensively delineating the experimental setup and protocols while addressing associated challenges and limitations is crucial. This chapter provides details of the experimental facilities, the wing models, the data acquisition, and the flow visualization techniques employed to obtain aerodynamic data for wings tested both in isolation and in tandem configurations.

2.1 Wind Tunnel facility

The force measurements and surface flow visualization experiments were conducted in the open-return type subsonic wind tunnel located at Auburn University. The wind tunnel has a contraction ratio of 6.25:1 and features a test section that is 8ft long and has a cross-sectional area of 2ft × 2ft. The test section of the wind tunnel is made up of clear acrylic which provides optical access for flow visualization. The wind tunnel is capable of a continuously variable flow with a maximum velocity of 140 ft/sec and has a peak turbulence intensity of 0.31%. The wind tunnel is equipped with a frequency controller to control the airspeed in the test section. The wind tunnel facility is shown in Figure 2.1.

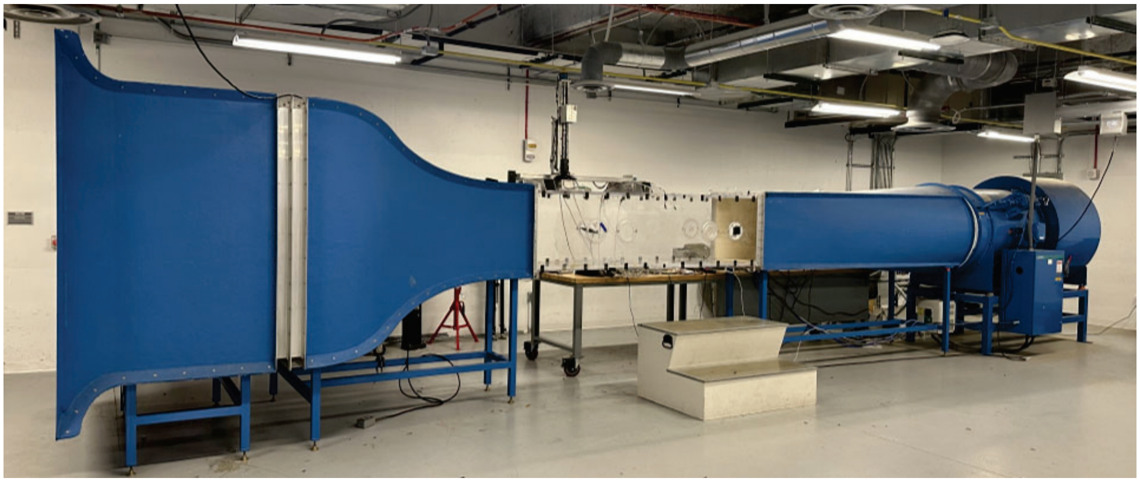

Figure 2.1: 2ft x 2 ft open return wind tunnel.

The speed in the test section was determined using a pitot-static tube connected to a manometer. Bernoulli's equation was utilized to derive the velocity relationship as shown in eq. 2.1. The freestream density(ρ_∞) was calculated per the equation of state shown in eq. 2.2.

$$U_\infty = \sqrt{\frac{2(P_o - P_{static})}{\rho_\infty}} \tag{2.1}$$

$$\rho_\infty = \frac{P_\infty}{RT} \tag{2.2}$$

Where, P_{static} is static pressure in the test section, P_o is total pressure, R is universal gas constant, T is ambient temperature and P_∞ is atmospheric pressure. P_∞ was measured with a Setra Digital Barometer. Before each run, the wind tunnel speed was corrected to account for variations in ambient pressure and temperature. During the test runs, the variations in temperature and pressure were observed to be minimal and were recorded periodically. The variation in density and velocity were accounted for each run by maintaining a constant dynamic pressure in the test section during test runs. For Reynolds number calculations, Sutherland's formula for viscosity was used to account for temperature changes. The variation in Reynolds number during the test runs were less than ± 500.

2.1.1 Flow Quality in the Test Section

The mean velocity and turbulence survey in the empty test section was conducted using hot wire anemometry. The methodology and intricacies of hot-wire anemometry will be elucidated in the subsequent section. The turbulence intensity (TI) was computed using the relation $TI = u'/\bar{U}$, where u' is the RMS(root mean square) of the velocity fluctuations and $\bar{U}$ is the mean velocity. The changes in the dynamic pressure across the cross-section of the test section remained within 0.50%. The dynamic pressure corresponding to different Re are presented in Table 1, and the variation of TI at different velocities is shown in Figure 2.2. A maximum turbulence intensity of 0.31% was recorded at U_∞ = 70 ft/sec and a minimum of 0.23% was at U_∞ = 80 ft/sec.

Table 2.1: Turbulence Intensity and dynamic pressure in the test section

Re	20,000	40,000	60,000	80,000	100,000
q_∞, lbf/ft^2	0.35	1.38	3.12	5.54	8.7

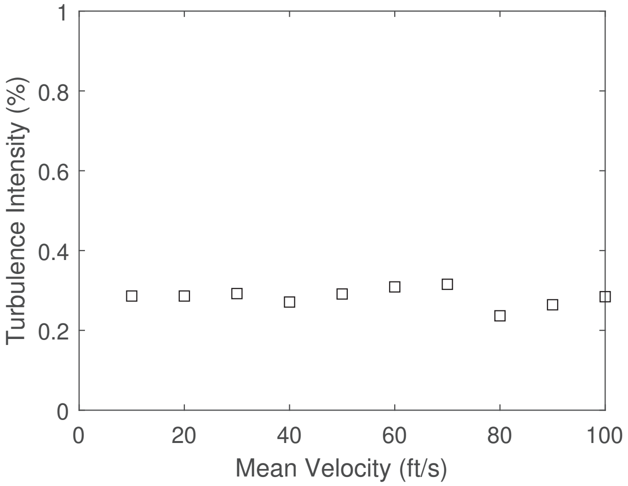

Figure 2.2: Centerline turbulence intensity in the test section at different velocities.

The flow angularity in the test section was determined by employing a 5-hole probe. This probe allowed for the measurement of flow angularity in two orthogonal planes by utilizing pressure ports situated on the circumference of its elliptical head. To ensure comprehensive measurements, the probe was mounted on a two-axis traversing system. The variation in flow angularity was found to be less than 0.20 degrees.

2.2 Wing Models

The test models comprised of NACA0012 wing sections. The details of the models used for force measurements and flow visualization in the wind and water tunnels are provided in the following subsections.

2.2.1 Wing Models for force/moment Measurements

The selection of the wing model size depends on various factors, most importantly blockage in the test section, minimum stable velocity obtainable to meet the low Reynolds number requirements, and resolution of the force sensor compared to the magnitude of aerodynamic forces produced. Keeping all of this in consideration, two identical NACA0012 section wings with a chord length of 2.3in were used. The wings had a rectangular planform area and length of 13.8in to achieve an aspect ratio of 6. The wings had no aerodynamic or geometric twist. The wings were made from aluminum utilizing CNC machining. Wing tips were rounded to mitigate separation at the sharp edge by revolving the airfoil profile around the chord line, as shown in Figure 2.3. The wing span corresponded to approximately 57% of the test section height. It is recommended that the wing span be no more than 70% of the test section height [73] to avoid an interference between wingtip vortices and test section walls.

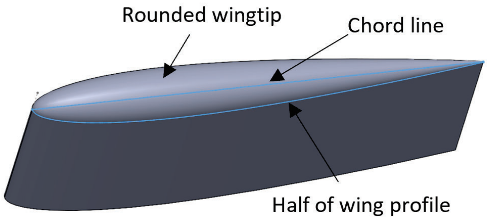

Figure 2.3: Rounded wingtip.

The wings were carefully sanded with silicon carbide of 240 and 1500 grit sandpapers and painted with Flat black paint to obtain a glare-free smooth surface finish. After sanding and painting, the surface was smooth to the touch, smoother than the original machined surface [74]. The wings had 1/4-20 threaded rods at the mid-chord for mounting to the force sensor and were installed in the wind tunnel in a cantilever arrangement. Therefore, the length of the wings represents the semi-span and semi-aspect ratio (sAR) as shown in Figure 2.4. In this work, aspect ratio (AR) is alternately used instead of sAR.

The solid blockage ratio is defined as the ratio of the projected area of the wing to the cross-sectional area of the test section. The maximum blockage ratio of AR = 6 wing at 90 degrees was less than 5.5%. A solid blockage ratio of less than 6% is preferred to avoid local flow acceleration and blockage effects [75]. Thus, the experimental setup was well under this threshold, and therefore, no blockage corrections were applied to the processed data. Wind tunnel boundary corrections are discussed in detail in subsequent section.

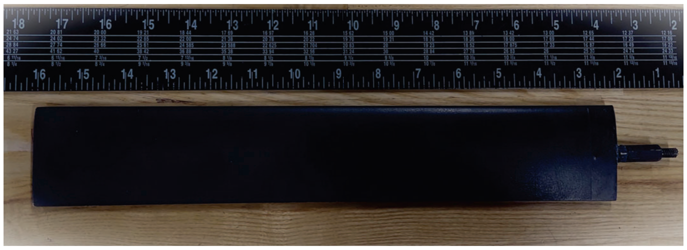

Figure 2.4: NACA0012 wing utilized in the present study.

2.2.2 Wing Models for Flow Visualization

A set of wings was manufactured using 3D printing technology at the Mechanical Polymer Additive Manufacturing Laboratory, ME3D, located at Auburn University. Stratasys F370 printers were employed, and the wings were printed using resin. The wings of 4in chord length were printed in multiple sections and assembled to achieve the desired aspect ratio of 4 as shown in Figure 2.5. Stainless steel rods were incorporated at different chordwise locations to provide structural reinforcement to minimize bending and shaking. Wing sections also underwent careful sanding to achieve a smooth and even surface. Mizoguchi and Itoh [76] reported that at low Reynolds numbers the qualitative behavior of wings for an aspect ratio of

3 and greater remains the same. Therefore, the wings with 4in chord were used for qualitative surface flow visualization and dye flow visualization in the water tunnel as the longer chord length allowed to achieve desired Reynolds numbers at lower velocities in the water tunnel and ease in reading flow features in the wind tunnel. The lift characteristics for both wings (AR = 6 and AR = 4) were compared and shown in Figure 2.6. The results show that they were in good agreement at pre-stall angles of attack and for post-stall angles of attack in qualitative agreement. Therefore, flow visualizations carried out by utilizing wings with AR = 4, truly represent the underlying flow physics.

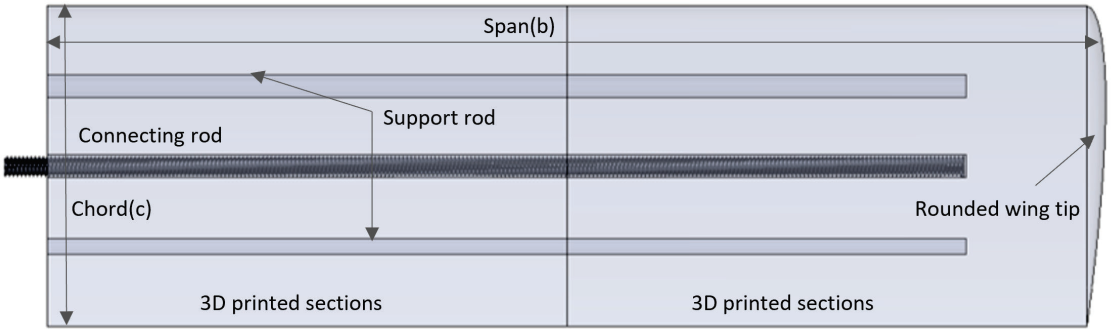

Figure 2.5: CAD model of 3D printed assembled wing,

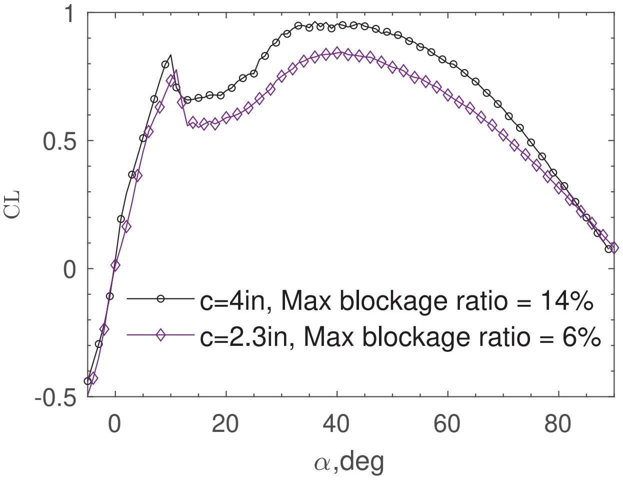

Figure 2.6: Effect of blockage ratio on lift coefficient at Re=100,000.

2.3 Force/Moment Measurements and Data Acquisition

An ATI (F/T) six-component Gamma force sensor was used to directly measure aerodynamic forces and moments. This sensor offered a high resolution, with a sensitivity of 1/320 pound-force (lbf) for forces and 1/160 pound-force-inch (lbf-in) for moments. A NEMA-23 stepper motor equipped with a 5:1 planetary reduction gearbox was utilized to change the angle of attack. This configuration enabled precise adjustments and a resolution of 0.008 degrees, ensuring fine control over the angle of attack. The normal (N) and axial (A) forces measured by the force sensor were transformed into lift (L) and drag (D) using simple transformation; as shown in eq 2.3 and eq. 2.4. The moment measured at the mid-chord was transferred to the quarter-chord using eq. 2.5.

$$L = Ncos\alpha - Asin\alpha \tag{2.3}$$

$$D = Nsin\alpha + Acos\alpha \tag{2.4}$$

$$M_{c/4} = M_{c/2} - \frac{1}{4}L \tag{2.5}$$

The force sensor was attached to the motor shaft, and the wings were mounted directly onto the force sensor at the mid-chord. Wings were installed vertically from the ceiling of the test section and a small gap of less than 0.1 inches was maintained between the wing and the ceiling to prevent contact. Marchman et al [77] observed that at low Reynolds numbers, the sealing gap did not affect the zero lift angle and lift curve slope of symmetric airfoils. The arrangement of the force sensor, stepper motor, and reducer gearbox is shown in Figure 2.7.

To investigate wings in tandem, two identical force measurement setups were used. The spacing between the wings was adjusted via longitudinal and transverse slots located on the upper wall of the test section, as illustrated in Figure 2.8 (a). For clarity, the front and rear wings will hereafter be referred to Wing-1 and Wing-2, respectively. Notably, the slots were routinely sealed following each adjustment of the relative spacing between the wings. The streamwise spacing or stagger(s) denotes the distance between the trailing edge of Wing-1 and the leading

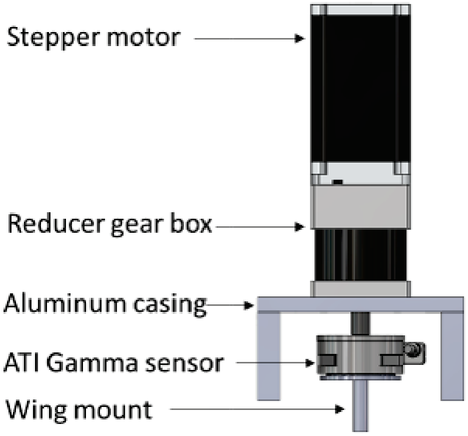

Figure 2.7: Force sensor and motor assembly.

edge of Wing-2, both set at zero incidence. The vertical gap(G) represents the perpendicular distance between the chord lines of Wing-1 and Wing-2 as shown in Figure 2.8(c).

A multifunction NI USB-6210 data acquisition board was utilized to acquire and record data from each force sensor and to control motors. A custom LabVIEW® application was used to synchronize the sensors and motors. This configuration enabled testing wings in isolation and in tandem configuration. The force and moment data were sampled at 1 kHz, and for each angle of attack, the force and moment signals were recorded for 10 seconds, resulting in 10,000 samples. This sampling duration and collected data were deemed sufficient to establish steady-state mean values. Additionally, a 4-second delay was introduced between incrementing the angle of attack and the start of acquisition. In some cases, to investigate the temporal response of the aerodynamic coefficients due to the aerodynamic interaction, data was collected over extended intervals. The zero angle of attack for each wing was determined experimentally by sweeping through a range of negative to positive angles of attack and identifying the angle at which the lift was zero. The details of the wiring diagram of the data acquisition board, stepper motor, hardware configuration and LabVIEW application can be found in Appendix A.

2.4 Wind Tunnel Boundary Corrections for Three-Dimensional Flows

The presence of a wing model in the test section particularly at high angles of attack and the growth of the wall boundary layer may result in increased values of aerodynamic forces

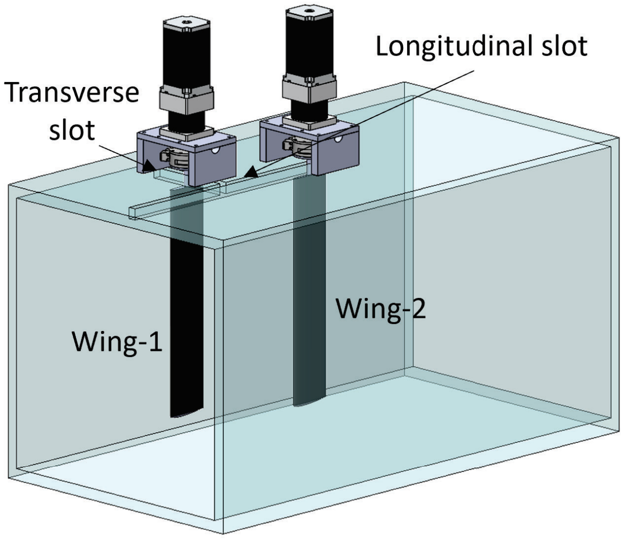

(a) Isometric view.

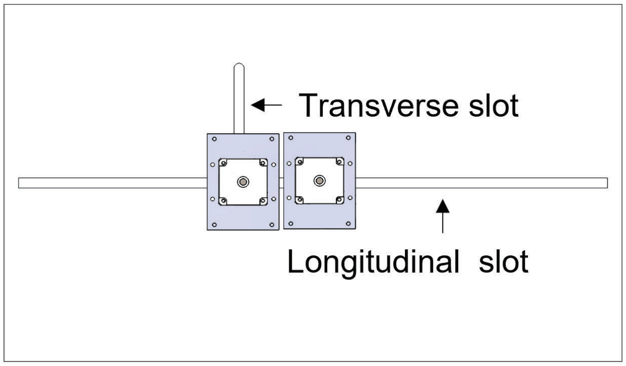

(b) Top view.

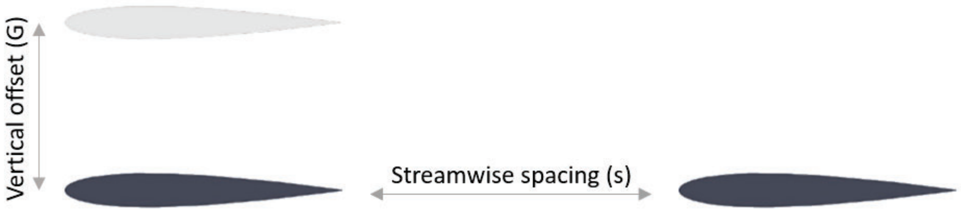

(c) Spacing between the wings.

Figure 2.8: Arrangement of wings in tandem configuration.

measured. It is necessary to calculate the interference incurred by the test section walls which are discussed below. The methodology proposed by Barlow et al [73] was followed.

2.4.1 Horizontal Buoyancy

The decrease in the static pressure along the test section because of boundary layer growth results in additional drag force on the model as it is "drawn" downstream. The variations of static pressure in the test section were evaluated by traversing a pitot-static tube along the centerline. The variation in static pressures was recorded using a Validyne DP45-16 differential pressure transducer. The pressure gradient along the test section was computed and variations relative to the inlet static pressure were quantified at every 4 inches starting from the beginning of the test section, as shown in Figure 2.9. The results showed that the static pressure remained essentially constant throughout the entire test section.

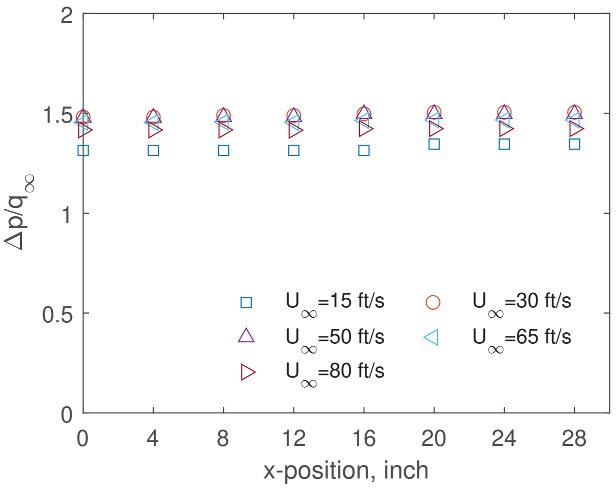

Figure 2.9: Center-line pressure in the test section at different velocities.

2.4.2 Solid Blockage

Solid blockage refers to the reduction of the area through which air flows adjacent to the model because of the test section walls, consequently, flow accelerates according to the continuity and Bernoulli equation which results in higher values of the aerodynamic forces depending upon the size of the model as compared to the cross-sectional area of the test section. Thom's short-form formulation [78] using eq 2.6 was used to calculate the solid blockage.

$$\frac{\Delta V_{sb}}{V_u} = \epsilon_{sb} = \frac{K(Volume)}{(A)^{3/2}} \tag{2.6}$$

where, ΔV_{sb} is the change in velocity due to solid blockage, V_u is the uncorrected velocity, K = 0.90 for a three-dimensional wing, Volume of the wing calculated as 0.7 × model thickness × model chord × model span, and A is the area of the test section

The effect of blockage correction was found to be less than 0.04%.

2.4.3 Wake Blockage

The velocity in the wake of the body is less than the freestream and to conserve the momentum using a control volume approach, the velocity outside the wake must increase as a consequence pressure drops downatream. Hence a drag correction is required for the purpose. The change in drag as per Maskell's Method [73] is given by;

$$\Delta C_{Dw} = \frac{K_1 \tau_1 (Volume)}{(A)^{3/2}} C_{Du} \tag{2.7}$$

where, ΔC_{Dw} is the change in drag due to wake blockage, C_{Du} is the uncorrected drag, K_1 = 1.01 for a three-dimensional wing, τ_1 = 0.575 as per wing and test section dimensions.

The effect of wake blockage was found to be less than 0.03%.

2.4.4 Streamline Curvature

The constrained wind tunnel testing environment leads to compression of the streamlines around the airfoil model. This alters the effective camber profile as seen by the oncoming airflow, enhancing lift, pitching moment, and angle of attack. The τ_2 correction factor quantifies the magnified upwash at any downstream point P relative to the quarter-chord. Given the small quarter-chord distance and sizable test section dimensions, the τ_2 value was negligible. Thus, applying streamline curvature corrections was unwarranted.

Due to the small scale of the wings compared to the wind tunnel test section, in addition to using high-precision, low-range ATI gamma sensors, boundary corrections were not necessary and the results presented in this study are uncorrected.

2.5 Uncertainty Analysis and Repeatability of Measurements

The uncertainty in the experimental measurements can be attributed to random and systematic errors, which are also referred to as precision and bias. The bias in the aerodynamic coefficients is attributed to the resolution of the sensor, and the precision limits were set by mean and standard deviations of the output. The normal and axial components of the forces directly obtained from the force sensors had a normal distribution as shown in Figure 2.10.

The bias in the force values was estimated by setting the forces to zero and computing lift, drag, and moment data at each angle of attack for no flow condition, as shown in Figure 2.11. The bias was found to be less than an order of 10^{-2}. Figure 2.12 represents the precision limit obtained by calculating the mean and standard deviation of aerodynamic forces at a Reynolds number of 100,000 with a 95% confidence interval [76]. In the pre-stall angle of attack range, the uncertainty remained less than 3% and 2% for C_L and C_D, respectively, and the maximum uncertainty in C_L and C_D was approximately 7% and 5%, respectively, at post-stall angles of attack.

The aerodynamics at low Reynolds numbers is fundamentally unsteady, so the force-time history was used to obtain time-mean average values of the aerodynamic coefficients. Therefore, the aerodynamic forces acquired through the data acquisition setup must be repeatable. The data was obtained twice for each test case to verify and ensure repeatability.

2.6 Verification of Experimental Setup

Figure 2.13 shows the lift versus angle of attack of Wing-1 (AR=6) in isolation at a Reynolds number of 100,000. The experimental results were compared with the data presented by Lind et al [79] for a two-dimensional NACA0012 wing at a Reynolds number of

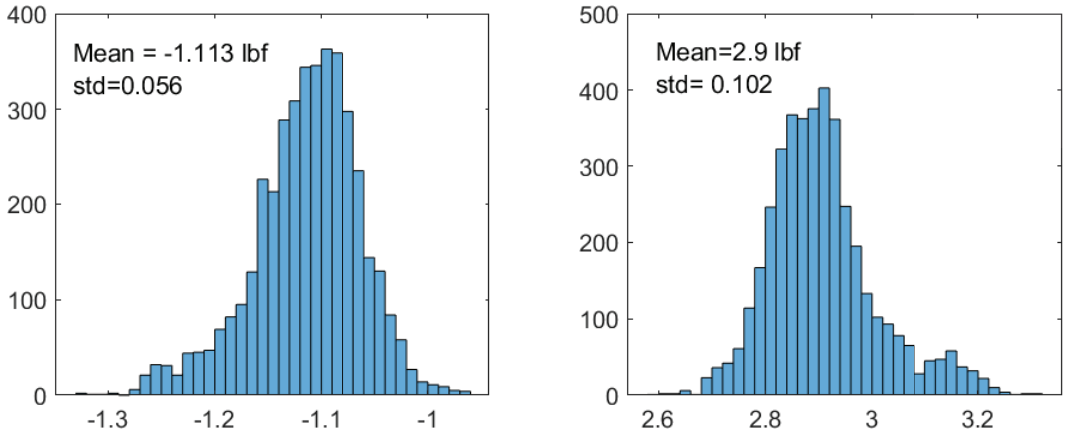

(a) Axial Force

(b) Normal Force

Figure 2.10: Distribution of axial and normal forces of isolated wing obtained by the force sensor at a Reynolds number of 100,000 and α = 7 degrees.

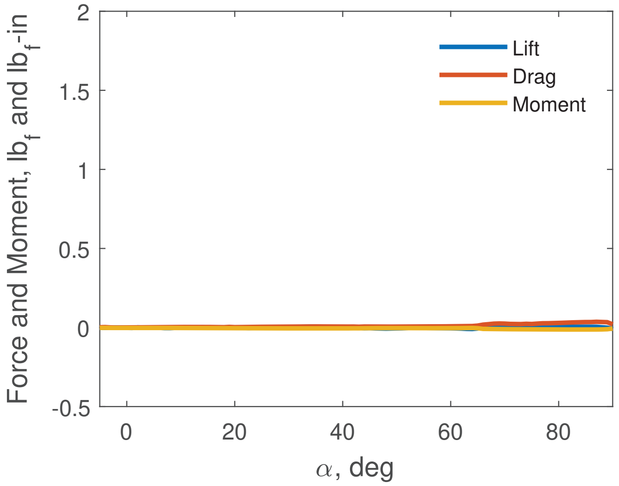

Figure 2.11: Aerodynamic forces and moments for no-flow condition.

110,000, and Lee and Han [80] for NACA0012 wing of aspect ratio 6 at a Reynolds number of 100,000. The present data matches well in the pre-stall angle of attack range, whereas the agreement of coefficient of lift in the post-stall and higher angles of attack is only qualitative and this discrepancy of data was attributed to the higher maximum blockage ratio and jig effects associated with their experimental setups which may result in exaggerated secondary peaks [81].

The present dataset also conforms to the trends observed by various researchers [13,23,82, 83] at similar Reynolds numbers, for both two-dimensional and three-dimensional NACA0012

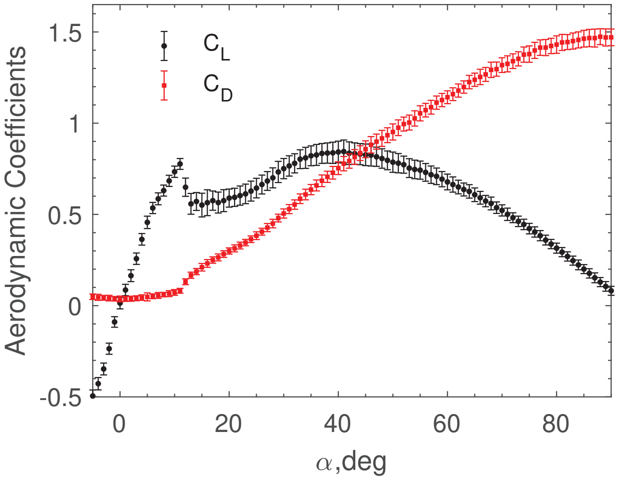

Figure 2.12: Uncertainty bands for C_L and C_D at Re=100,000.

wings. Therefore, the isolated wing data serves as the reference baseline in the present study. Any deviations in the results for tandem wing configuration will be attributed to aerodynamic interactions.

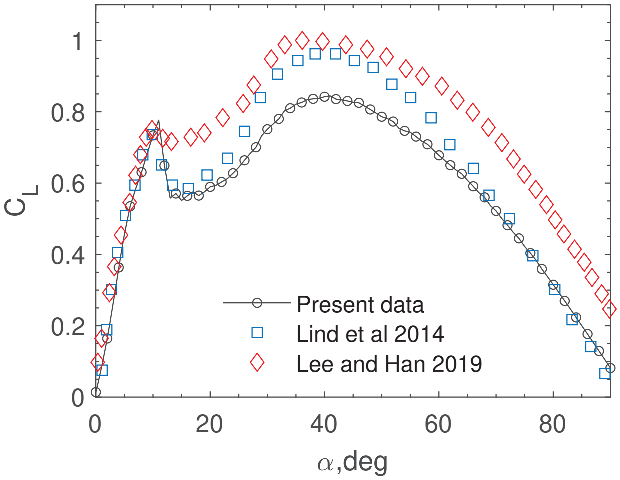

Figure 2.13: C_L vs α of Wing-1 in isolation having an aspect ratio of 6 at Re = 100,000.

To test tandem wings, it was important to have identical results for the wings in isolation. Figure 2.14 shows the lift and drag coefficients for isolated Wings-1 and Wing-2 at Re = 100,000. The identical results confirmed any deviation from baseline data in tandem arrangements will be due to aerodynamic interaction rather than experimental variability.

At Re = 20,000, the drag force magnitude, particularly at small angles of attack, and the dynamic pressure were very small, comparable to the noise, resolution, and uncertainty of the experimental setup. Hence, drag data is not reported at this Reynolds number. Instead, the analysis of tandem wing aerodynamic interaction utilizes only lift force, which is an order of magnitude greater than drag. Figure 2.15 presents a comparison of the lift coefficients for Wing-1 and Wing-2 in isolation at Re = 20,000. The results are identical except for $\alpha > 40$ degrees for Wing-1. The flow at this Reynolds number is very sensitive and any imperfections in the wing surfaces from machining could cause this discrepancy. Therefore, it was decided to compare aerodynamic interaction results to the respective isolated wings.

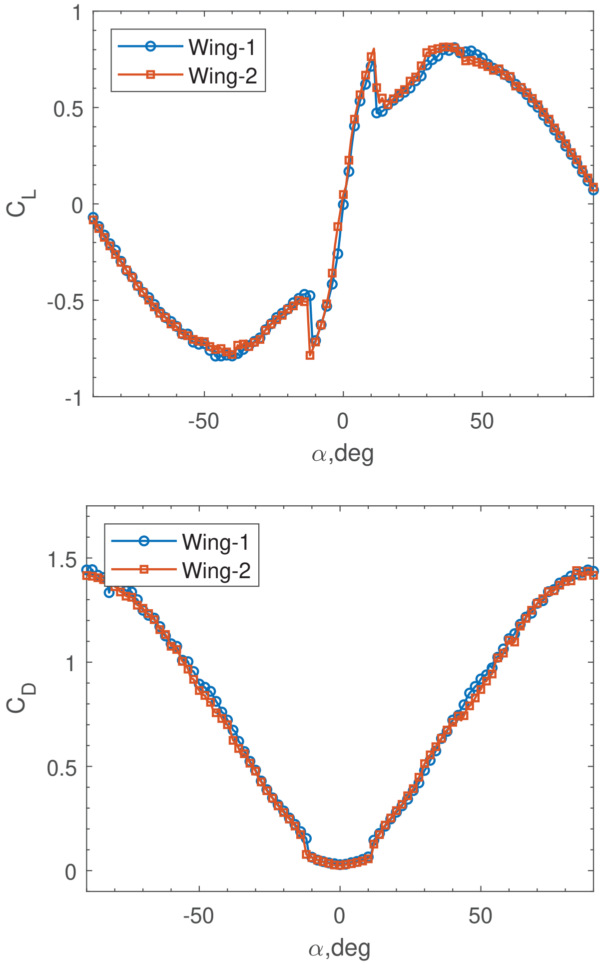

Figure 2.14: C_L and C_D vs α for Wing-1 and Wing-2 in isolation at Re= 100,000.

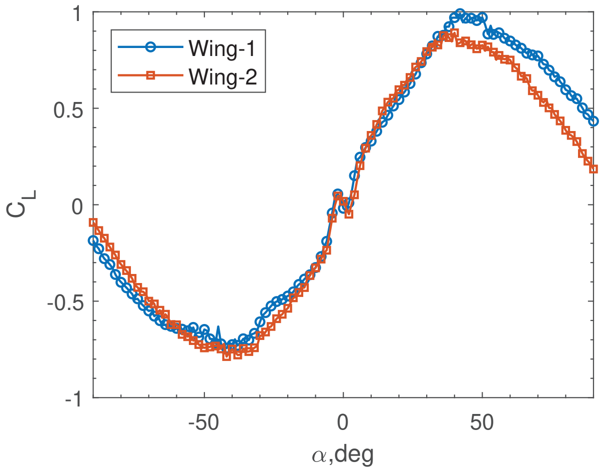

Figure 2.15: C_L vs α for Wing-1 and Wing-2 in isolation at Re= 20,000.

2.7 Hot Wire Anemometery

The measurement of the wake downstream of wings and flow quality in the empty tunnel were conducted using a Dantec Dynamics 55P11 single-wire probe with a diameter of 5µm and a length of 1.25mm. The wire probe was connected to a Dantec Dynamics 54T30 Constant Temperature Anemometer (CTA) module. The total resistance of the hot wire system was calculated by adding the cold resistance of the hot wire, cable resistance, and probe holder resistance. These resistance values were used to set the position of dip switches located in the CTA module according to the manufacturer's instructions. An overheat ratio of 0.8 was maintained for the wire. The overheat adjustment setting modifies the operational temperature at which the hot-wire anemometer sensor is maintained and it is defined as the ratio of the difference between the resistances at operating and ambient temperature to resistance at ambient temperature. The output from the CTA module was connected to the NI USB-6251 BNC DAQ board, which was connected in parallel with an oscilloscope. The raw voltage signals were converted to appropriate velocities using calibration data, enabling the computation of wake spectra, perturbation velocity, and identification of unsteady flow features. The calibration curve of the hotwire data is shown in Figure 2.16. The calibration of the hot wire signal was performed independently using a pressure chamber connected to a pressure reservoir, with the hot wire placed at the exit of the jet. The chamber was equipped with a precision valve and a manometer to regulate the pressure at the desired level. The velocity at the exit of the chamber was subsequently calculated based on these pressure settings. The signal was obtained at 10kHz and 50,000 samples were recorded for each data point.

A single hotwire cannot determine the flow direction, meaning it cannot identify the reverse flow. However, it is effective in determining separated shear layers and calculating turbulence levels.

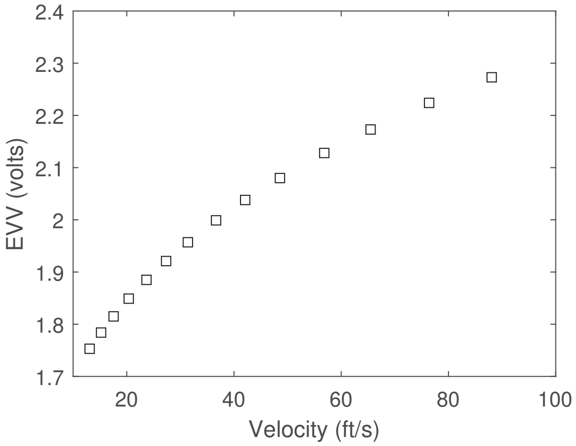

Figure 2.16: Hotwire Calibration curve.

2.8 Flow Visualization

To gain deeper insights into flow physics and complex aerodynamic interactions, a variety of visualization techniques were employed. These techniques play a crucial role in understanding the underlying phenomena and capturing the nuances of fluid dynamics for different configurations and flow conditions.

2.8.1 Surface Flow Visualization

The surface flow visualization was conducted at Re=100,000 and selected angles of attack by utilizing a mixture of kerosene, oleic acid, and titanium dioxide, in the right proportions. The mixture was applied evenly on the wing surface in the spanwise direction. The wind tunnel was set to run at lower speeds and the excess mixture was removed carefully before running the wind tunnel for 30 minutes at the desired speed allowing for the evaporation of the oil. As a result, residual particles settled on the wings, enabling the acquisition of vital information about flow separation, formation of the laminar separation bubble, transition, reattachment, and wing-tip vortices. Photographs were taken immediately to avoid any movement of residual oil due to gravity. Sketch of different flow features was superimposed on the flow visualization photographs to describe different flow features as shown in Figure 3.15.

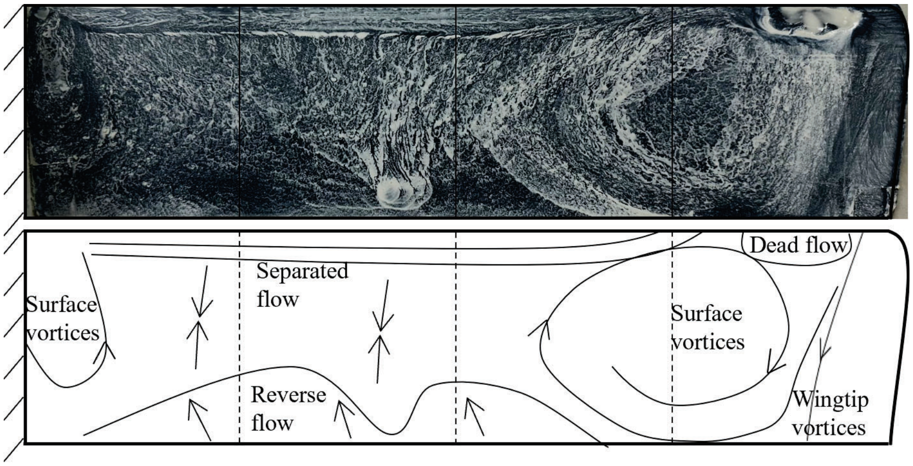

Figure 2.17: Surface flow visualization at α = 12 degrees and Re=100,000 for the isolated wing.

2.8.2 Dye Flow Visualization

Two-dimensional flow visualization to study the surface and wake structures was carried out using planar laser-induced fluorescence (PLIF) in a closed-loop water tunnel installed in the Vortex Dynamics Lab of Auburn University, shown in Figure 2.19. The tunnel has a transparent 18in x 18in test section and is capable of velocities up to 3.8ft/sec. The maximum freestream turbulence intensity is less than 1% at the peak velocity. Wings with an aspect ratio of 4 were mounted horizontally in a cantilever position, and the tunnel was operated in a free surface mode. Fluorescence dye was injected near the leading edge of the wings using a gravity-assisted system. PLIF was accomplished using a 5W argon-ion laser passing through an OZ Optics laser light sheet generator. Videos recorded at 60 frames/sec were analyzed to study the flow features. The schematic of the flow visualization setup is shown in Figure 2.19. Flow in the center plane was considered quasi-symmetric for wings with aspect ratios greater than 3 at

Figure 2.18: Water Tunnel Facility, Vortex Dynamics Lab.

low Reynolds numbers of the order of 10^4. Figure 2.20 shows a sample visualization at Re = 20,000, enabling the study of the mechanism of aerodynamic interaction.

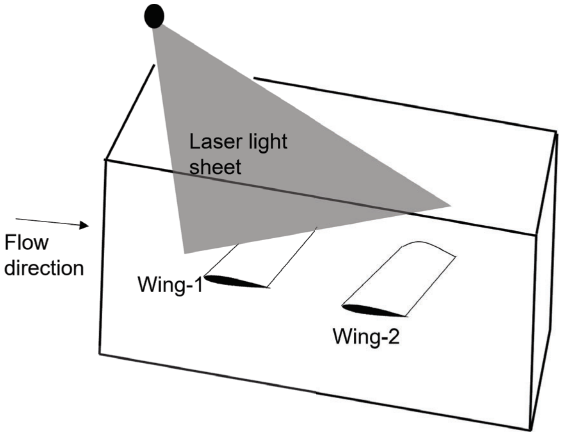

Figure 2.19: Schematic of the flow visualization set up in the water tunnel.

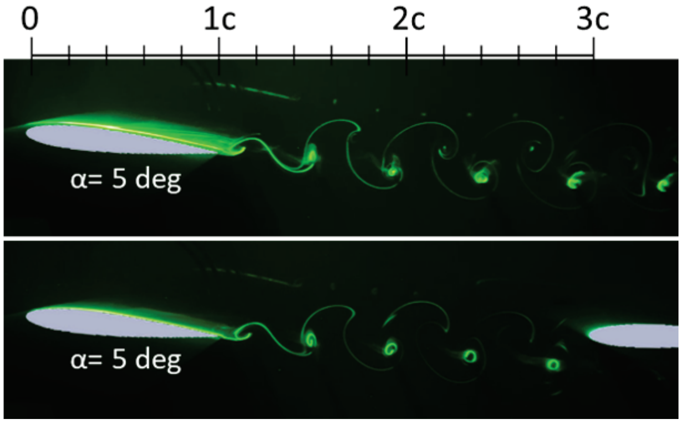

Figure 2.20: Dye flow visualization at α = 5 degrees in isolation and tandem configuration.

2.9 Wind Tunnel Testing Procedure and Test Matrix

Wind tunnel testing of isolated and wings in tandem was conducted at Re_c of 20,000 and 100,000. The test section was sealed with heavy-duty duct tape after adjusting the spacing between the wings before every test run and the wings were positioned at α = 0 degrees. The tunnel flow was stabilized by running for a few minutes before setting the angle of attack. Force and moment data for both wings were simultaneously recorded using an automated LabVIEW application. The raw data was processed and analyzed in MATLAB ® as shown in Figure 2.21. This experimental procedure enabled a parametric investigation of the aerodynamic interaction between the wings for angle of attack, spacing, gap, and Reynolds number. Three specific test cases were investigated for the tandem wing arrangements, and a set of experiments for each case are summarized in Table 2.2.

Table 2.2: Test Matrix

Reynolds number	20,000 and 100,000
Stagger (s)	0.5c to 4c
Gap(G)	0 - 1c
Case 1	α_1 sweep from -90 to 90 deg α_2 = 0, 5, 10, 20, 40 deg
Case 2	α_1 = 0, 4, 8, 11, 20, 40 deg α_2 sweep from -90 to 90 deg
Case 3	α_1 and α_2 sweep from -90 to 90 deg

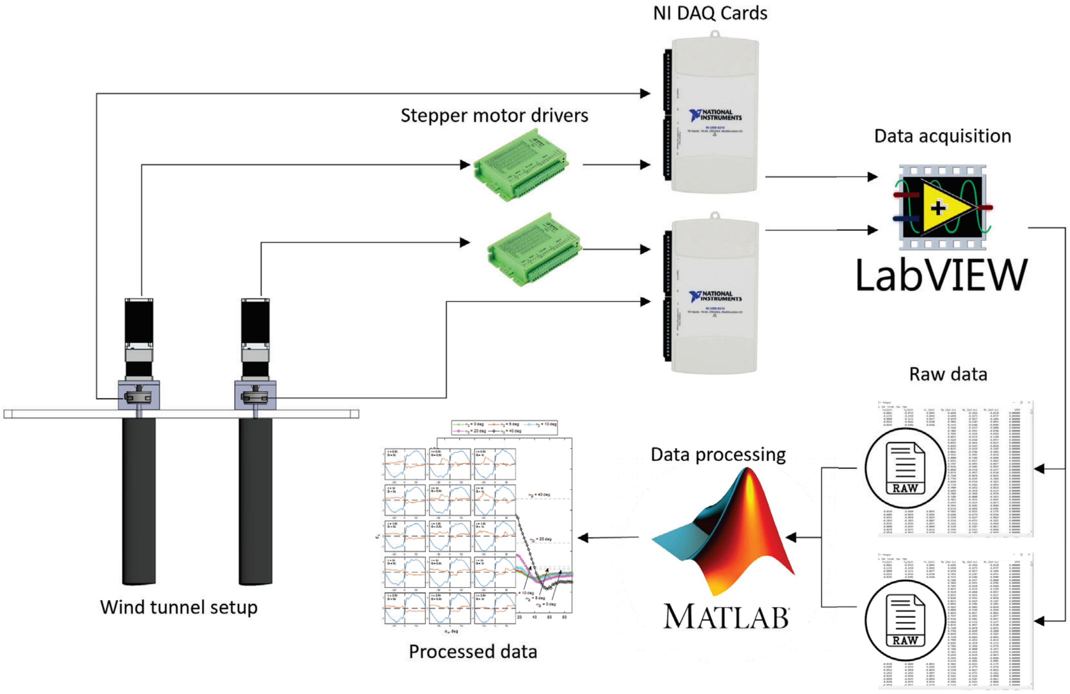

Figure 2.21: Block diagram of data acquisition setup.

Chapter 3

Aerodynamics of an Isolated Wing at Low Reynolds Numbers

This chapter includes the aerodynamics of an isolated NACA0012 wing, providing a baseline for investigating aerodynamic interactions. The aerofoil was evaluated independently across various angles of attack and Reynolds numbers to comprehensively determine its lift, drag, and moment coefficients. Boundary layer separation, transition, reattachment traits, and coherent wake structures were analyzed via surface and dye flow visualizations. The isolated wing served as a canonical configuration, enabling baseline data for identifying interactive effects in subsequent tandem arrangements. The steady-state aerodynamic characterization established a reference framework for analyzing time-averaged and transient interactions between wings in tandem.

3.1 Aerodynamic Response at Low Reynolds numbers

Figure 3.1 shows the mean lift coefficients as a function of angle of attack for a range of Reynolds numbers between 20,000 to 100,000. For clarity, data point markers are exhibited at 2-degree intervals despite acquisition at each angle from -90 to 90 degrees. Qualitative behavior at higher angles of attack was unchanged for the Reynolds number, although C_{Lmax} decreased at lower Re. An approximately 9% reduction in C_{Lmax} was discerned when decreasing the Reynolds number from 100,000 to 40,000, however, post-stall lift proved independent of Re_c. A conspicuous variation in the lift curve manifested at small angles of attack, within the range α = -3 to 3 degrees, for Re = 20,000 and 40,000. At Re = 20,000, a classical stall was absent, with lift increasing nearly linearly for $4 \leq \alpha \leq 40$ degrees.

Separation and reattachment mechanics alongside laminar separation bubble formation principally dictated stall characteristics and aerodynamic response [13]. Hence, Re = 20,000 and 100,000 constitute very low and low Reynolds number regimes. Consequently, the aerodynamic interaction of tandem wings was explored at these conditions, with a detailed examination of aerodynamic response at Re_c = 20,000 and 100,000 provided in the following sections.

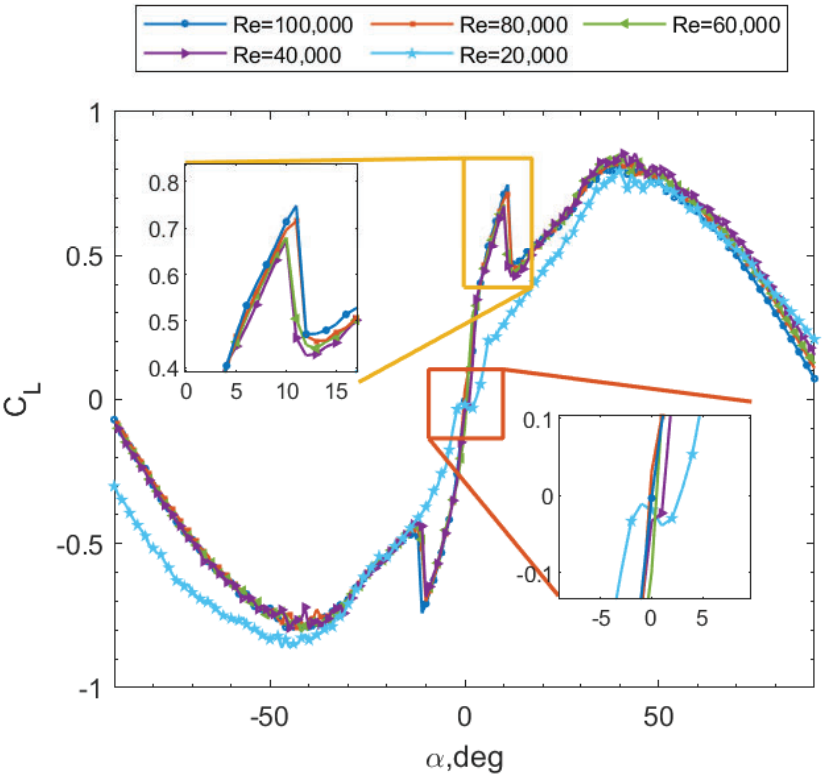

Figure 3.1: C_L vs α at different Reynolds numbers.

3.2 Reynolds Number = 20,000

Figure 3.2 presents lift coefficients for increasing and decreasing angles of attack. The results show the presence of an anticlockwise hysteresis loop. The lift curve made a convex shape for decreasing angles of attack with a sustained higher lift for $\alpha \leq 30$ degrees. The counterclockwise loop indicated an absence of the formation of a separation bubble.

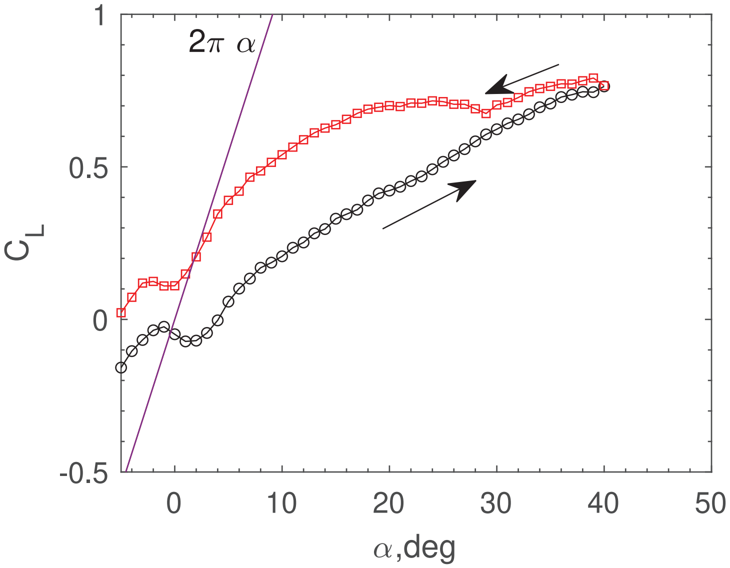

Figure 3.2: C$_L$ vs α for statically increasing and decreasing angles of attack at Re = 20,000.

Figure 3.3 shows aerodynamic coefficients, L/D ratio, and lift curve slope for -5 $\leq \alpha \leq$ 90. The most interesting phenomenon observed at this Re_c was the absence of a classical stall. The change in lift and drag was continuous. The slope of the lift curve remained below 2π for all α except 5 to 8 degrees where values approached 9. The slope of lift curve was half of the thin airfoil theory and the moment coefficient was near zero. The lift curve was divided into four distinct regions as shown in Figure 3.3a. The lift curve was highly non-linear and a reduction in lift with the increase in angle of attack for Region I. Similar non-linear behavior in the lift curve was also observed by Ohtake et al [23] at a Reynolds number range of 10,000 to 60,000 and by Mueller et al. [33] for Re = 130,000. Pranesh et al [84] reported a negative lift at small angles of attack at Re ≤ 40,000 for NACA0012 airfoil and found that the negative lift behavior diminished with the increase in freestream turbulence. This is also referred to as the "Dead band" because the increase in the angle of attack from zero degrees doesn't result in lift production [85]. This region has been identified as Region I in Figure 3.3a. Laminar separation was observed near the trailing edge even at $\alpha \approx 0$ degrees as shown in Figure 3.4. Due to the wing being symmetric, similar separation occurred on the other side of the wing and the trailing edge remained in the separated state at all angles of attack. For small positive α, the separated flow on the lower surface reversed at the trailing edge and entered the separation region on the upper surface as presented in Figure 3.5. The separated region, along with uneven boundary layer growth on both sides, resulted in an effective negative camber. The curling of separated flow from the lower to upper surface also violated the Kutta condition. To preserve the Kutta condition, net negative circulation was generated, producing a negative lift [86]. Ohtake et al [23] identified the angle of attack limits for the non-linearity and high and low lift gradient for Reynolds number of 10,000 to 100,000. It is important to reemphasize that the flow at a low Reynolds number is sensitive to experimental conditions including freestream turbulence, wing model accuracy, surface roughness, structural vibrations, load measurement setup, and their combination. Hence, there are always slight variations when tests are conducted at different facilities. As the angle of attack was increased beyond Region I, the separation points moved toward the leading edge on the suction side and towards the trailing edge on the pressure side, and recovery from the negative lift occurred to produce a positive lift as shown in Figure 3.6 (Flow Visualization results). For Regions II and III, the increase in α resulted in an increase in lift but the lift curve slope was much smaller for Region III. Lift decreased monotonically in region IV without attaining zero value at $\alpha = 90$ degrees.

3.2.1 Flow Visualization

The flow visualization results presented in Figure 3.6 clearly show that the separated shear layer remained laminar for an extended distance downstream before transition, and a laminar separation bubble was not observed, leading to the absence of a stall. The separated shear layer rolled up, and the Kelvin-Helmholtz (K-H) instabilities resulted in the formation of K-H vortices. Shedding frequency and boundary layer thickness increased with increasing angle of attack. Most of the past studies remain focused on the over-the-surface or near-wake flow structures [24, 35, 43]. Huang et al [87] identified five regimes for the evolution of surface flow based on the angle of attack and that included attached flow, trailing edge vortex, separation vortex, leading-edge vortex, and bluff body effects. The present work includes the visualization of wake structures 3c downstream of the trailing edge. At $\alpha = 0$ degrees, the laminar flow remained attached over the entire wing surface except near the trailing edge.

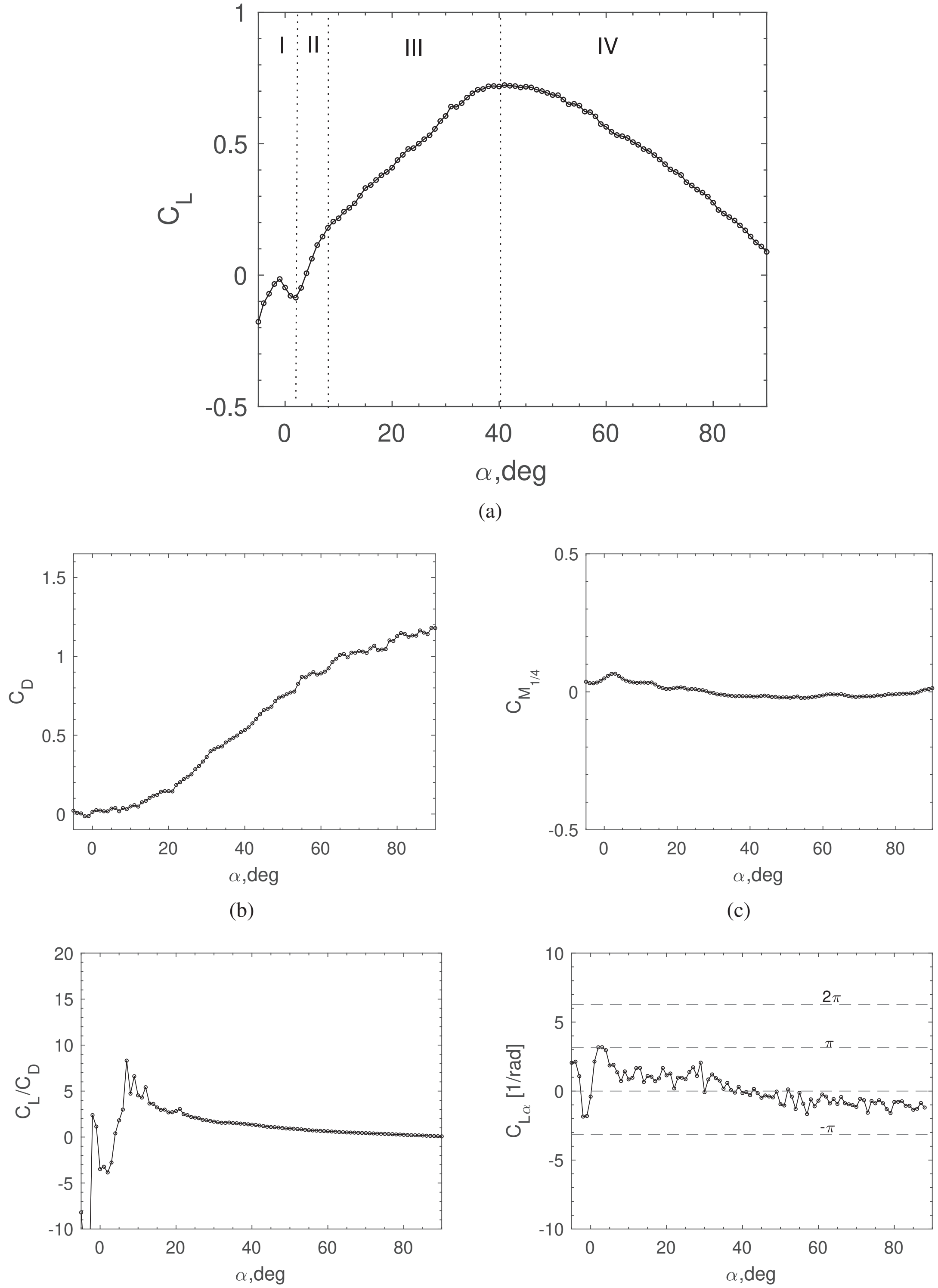

(a)

(b)

(c)

(d)

(e)

Figure 3.3: Mean aerodynamic coefficients of isolated Wing at Re = 20,000.

Flow left the trailing edge in a sinusoidal wavy pattern that continued up to 1c downstream before amplifying into a von Karman vortex street. These structures maintained coherence up to 3c downstream and had a wavelength around 0.5c. At α = 5 degrees, the separation point moved toward the leading edge at x/c $\approx$ 0.6, and the phase difference between upper and lower surfaces developed into alternately shedding von Karman vortices. As the trailing edge separation point traveled upstream, a trailing edge vortex started to form, though the flow remained attached at the leading edge. Higher angles of attack caused earlier and more unstable von Karman-type vortices. For α = 10 degrees, the shear layers from upper and lower surfaces were amplified immediately resulting in the formation of unstable alternate vortices. For α = 15 and 25 degrees, near-wall vortices were formed within the separated shear layer due to the increase in vorticity through the merging with the reverse flow. These surface vortices then proceeded to roll downstream and subsequently grew in size due to entrainment. At the trailing edge, the near wall vortex interacted with the counter-rotating trailing edge vortex from the lower side of the wing. As the counterclockwise rotating trailing-edge vortex grew in size, it merged with one of the secondary vortices near the leading edge before eventually convecting downstream. Consequently, the process of alternate shedding between a surface vortex and a trailing-edge vortex in the wake was established. For α = 35 degrees, instability waves from the leading and trailing edges could not directly interact due to the wider gap [35] but the Karman vortices formed further downstream. For very large angles of attack (not shown) bluff body effects are dominant.

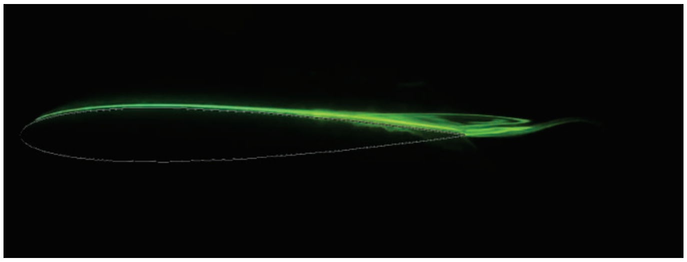

Figure 3.4: Dye flow visualization at α = 0 deg, Re_c = 20,000.

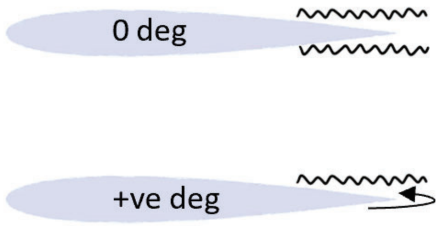

Figure 3.5: Sketch representing curling of flow at trailing edge to result in nonlinearity at small angles of attack, Re_c = 20,000.

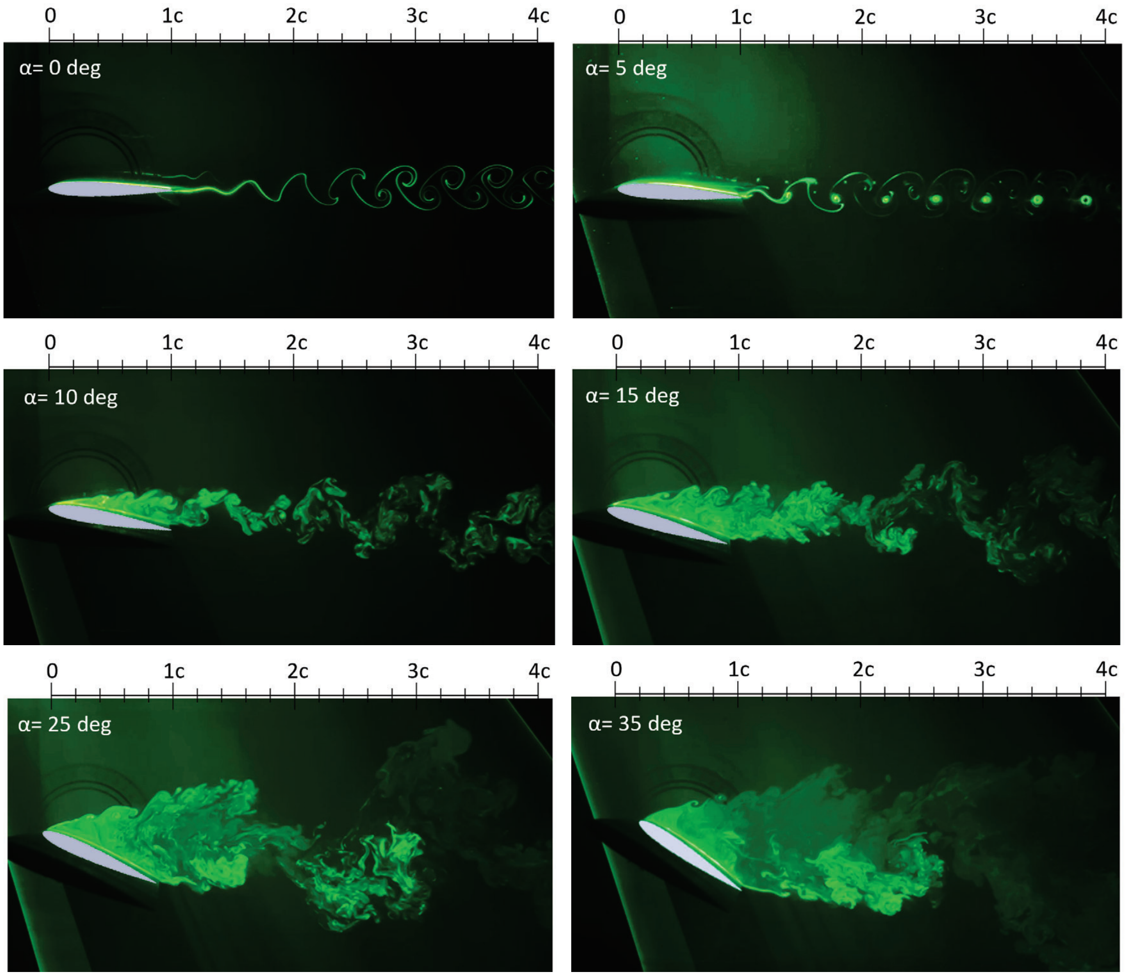

Figure 3.6: PLIF Dye Flow Visualisation of Isolated Wing, Re_c = 20,000.

3.2.2 Wake Velocity Survey

Velocity surveys were conducted in the wake of the isolated lead wing at various downstream locations. The wake surveys were carried out at the mid-span, where tip and corner vortices did not affect the assumed two-dimensional flow. Figures 3.7 to 3.12 show the wake survey data obtained by traversing a pitot-static tube 1.5c above and below the centerline of the wing in 0.1in increments. Data was acquired for α_1 = 0, 4, 8, 11, 20 degrees. The wake is defined as the region downstream of a wing where the flow velocity is reduced due to the presence of the upstream body. The shear layers originating from the upper and lower surfaces increase turbulence levels inside the wake. This turbulence entrains the surrounding fluid, causing the flow to accelerate. Overall, the wake is characterized by a slower moving fluid of high turbulence intensity compared to the freestream flow. The evolution of the wake velocity profile and turbulence level depends on parameters such as the wing geometry, angle of attack, Reynolds number, and distance downstream. Therefore, the wake doesn't have rigid definable boundaries, and often wake half width is used to characterize it. The size and location of the maximum velocity deficit are important in determining the aerodynamic interaction for wings in tandem.

Dynamic pressure data was obtained at 2kHz for 2sec at each step, averaged and later converted into velocity. The data was smoothed using a Savitzky-Golay filter [88]. The filtered data have minimal effects on the wake width and center [89]. For all angles of attack, the location of maximum velocity deficit remained very close to the centerline or slightly above at higher angles, indicating flow separation and reduced downwash effects at this Reynolds number. Compared to Re = 100,000 (Figure 3.16), the velocity deficit was notably greater at small angles of attack for Re = 20,000. This implies increased drag at low angles due to greater pressure drag resulting from earlier flow separation onset at the lower Reynolds number of 20,000. The earlier transition to turbulent flow around an airfoil at higher Reynolds numbers delays flow separation, keeping the boundary layer attached for a greater range of angles of attack. This allows the wing to generate lift more efficiently with less pressure drag at low angles around 0° to 8°. However, at the low Reynolds number of 20,000 studied here, the laminar boundary layer is more prone to separation even at mild angles. The resulting formation of a separated wake region leads to increased pressure drag. Quantitatively, the maximum wake velocity deficits at 0° angle of attack reached approximately $0.5U_\infty$ at Re = 20,000, whereas deficits only reached around $0.1U_\infty$ at Re = 100,000.

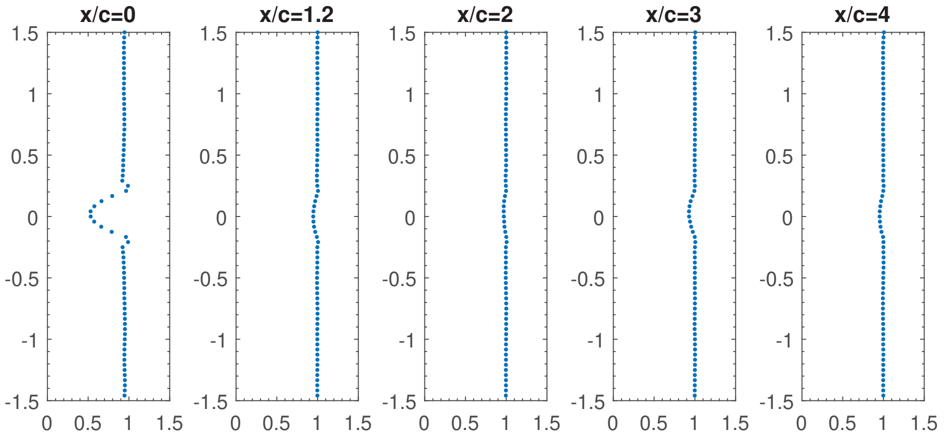

Figure 3.7: Velocity survey at $\alpha = 0$, Re = 20,000

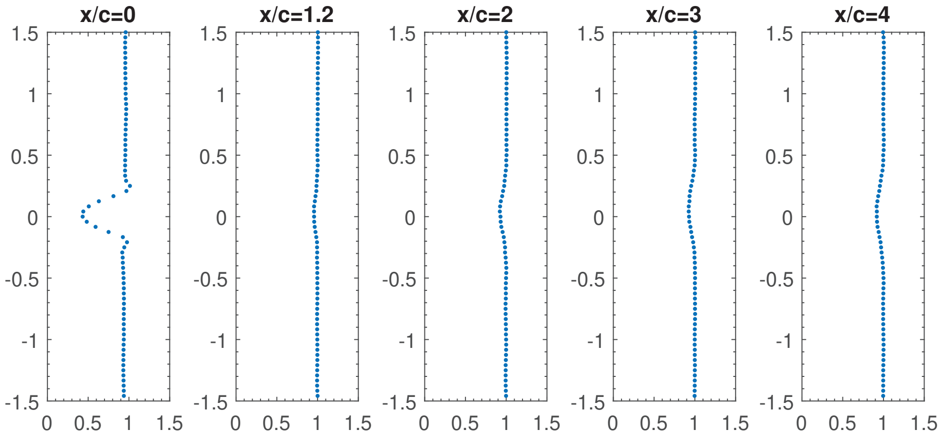

Figure 3.8: Velocity survey at $\alpha = 4$ deg, Re = 20,000

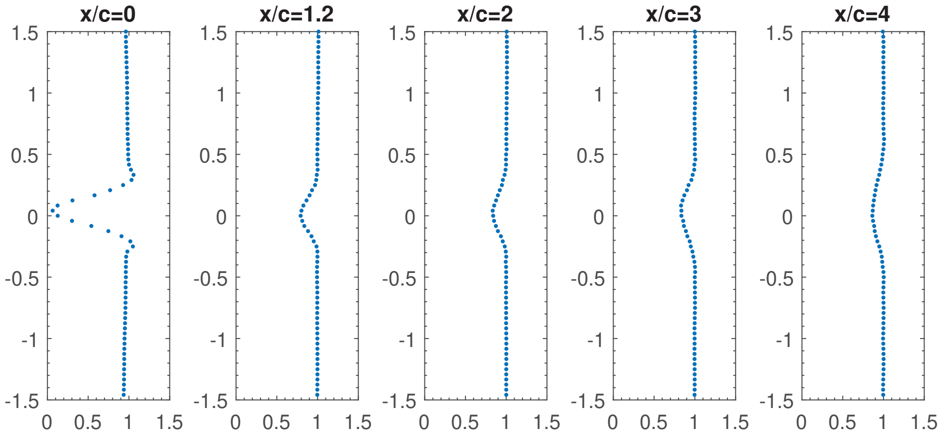

Figure 3.9: Velocity survey at $\alpha = 8$ deg, Re = 20,000

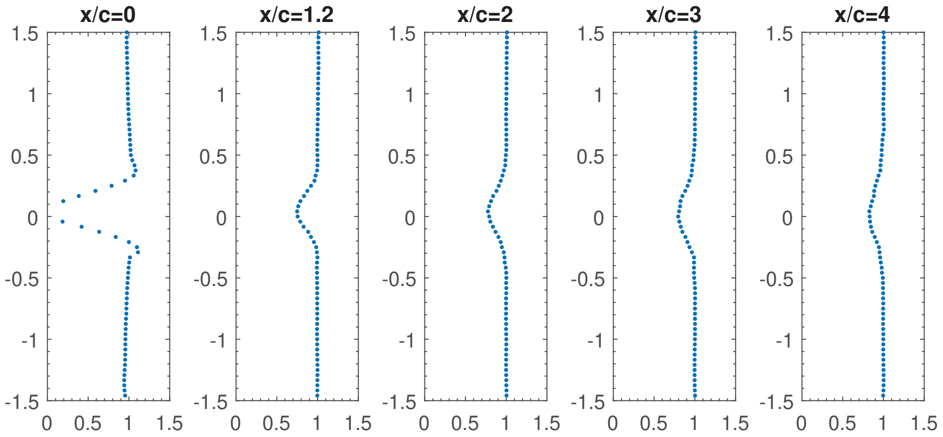

Figure 3.10: Velocity survey at α = 11 deg, Re = 20,000

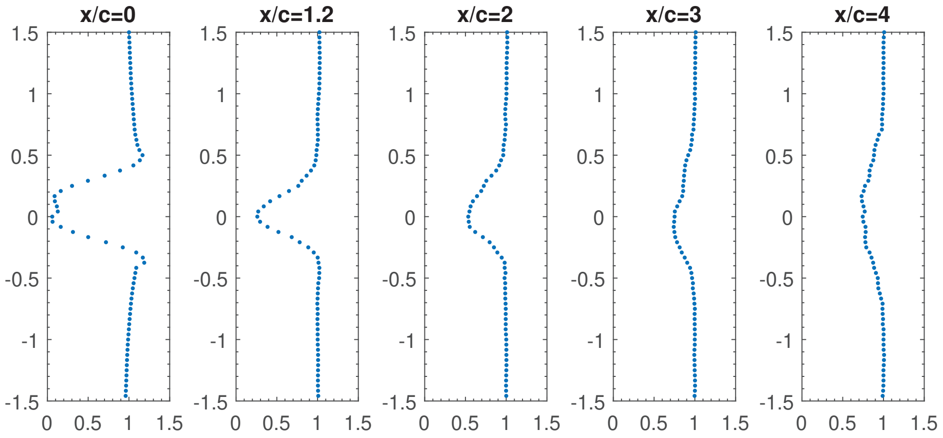

Figure 3.11: Velocity survey at α = 20 deg, Re = 20,000

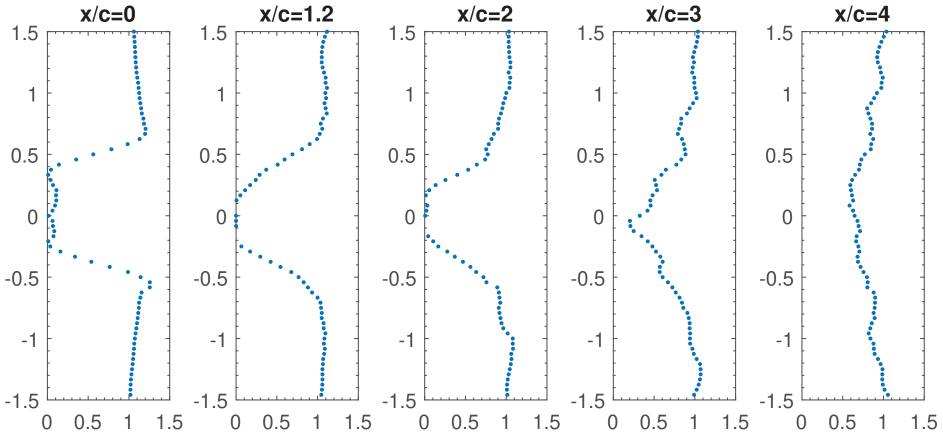

Figure 3.12: Velocity survey at α = 40 deg and Re = 20,000

3.3 Reynolds Number = 100,000

Mean lift coefficients at Re = 100,000 for the angle of attack ranging from -5 to 15 degrees are shown in Figure 3.13. The angle of attack was increased and decreased statically in 1 degree increments and results were also compared with the thin airfoil theory.

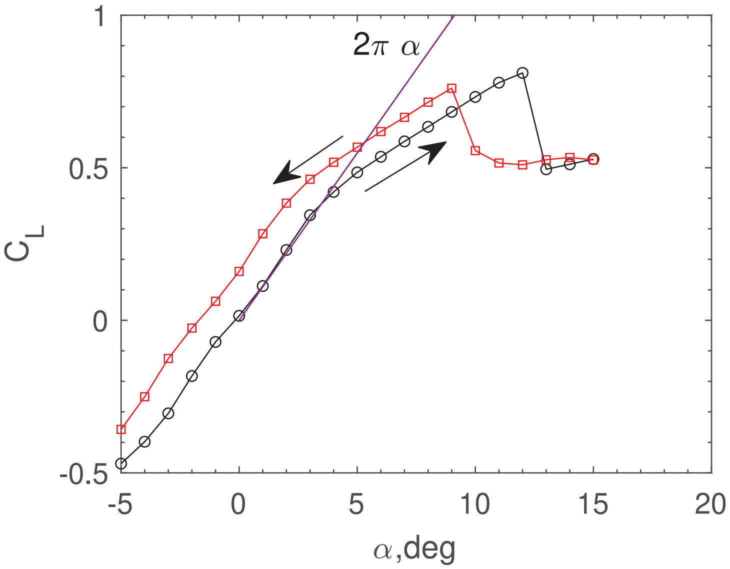

Figure 3.13: C_L vs α for statically increasing and decreasing angles of attack at Re = 100,000.

The results demonstrate that the lift curve was linear in parts. For increasing angles of attack, the coefficient of lift followed the thin airfoil theory values ($2\pi\alpha$) up to α = 4 degrees, beyond which the slope of the curve decreased but remained constant until reaching the stall angle. At the stall, the lift decreased suddenly without any warning. The stall was abrupt and intense, characterized by a sharp peak, indicating a leading-edge stall caused by the sudden bursting of the separation bubble without subsequent reattachment. This stall behavior is commonly seen in moderately thick wings with thicknesses ranging from 9% to 15% [90]. A static hysteresis was observed when decreasing the angle of attack. Flow reattached at α = 9 degrees and with a further decrease in angle of attack, the lift followed the increasing angle of attack behavior but with slightly higher values. This increase in the lift for decreasing angle of attack is related to the unsteady phenomenon of laminar separation bubble and reattachment, and the variation in thickness and length of the bubble may incur changes in lift. The change in lift for increasing and decreasing angles of attack has also been reported in the literature for dynamic analysis [91, 92]. The hysteresis loop was clockwise, which is related to the formation of a short separation bubble at the leading edge and leading edge stall angle. This bubble fails to reattach until a smaller angle of attack is reached with decreasing angles of attack [93] which was later confirmed through surface flow visualization.

Figure 3.14 presents the mean aerodynamic coefficients versus the full range of angle of attack from -5 to 90 degrees. The increase in the angle of attack resulted in changes in the slope of lift curve and hence represents distinct underlying phenomena. The lift data shows that with the increase in the angle of attack beyond the stall angle, the lift initially decreased and then started to increase until it reached a maximum value, remaining almost constant within the α range of approximately 30 to 45 degrees. The lift decreased linearly with a constant slope as the angle of attack was further increased, but it did not reach zero at α = 90 degrees. This small amount of lift can be attributed to several factors, including wing deflection at high angles of attack due to the cantilever arrangement, suction at the rounded leading edge, and the polar method of recording force and moment data, where the angle of attack was varied for a specific speed [94]. Similar observations were made using the lift curve slope versus angle of attack plot (refer Figure 3.14e, which exhibited an almost constant slope before the stall, except at around zero degrees. The slope remained lower than the 2π value suggested by the potential flow theory. The drag bucket followed the conventional trend. The drag curve made a plateau before reaching the maximum value at 90 degrees, and the maximum value of the drag coefficient remained close to 1.5 which is consistent with the results reported by Lind et al [95]. A maximum L/D of approximately 15 was observed in the α range of 5 to 8 degrees, and it sharply decreased at the stall, reaching zero linearly due to simultaneous decreases in lift and increases in drag at higher and extreme angles of attack. The lift curve was divided into four distinct regions named from I to IV on the basis of the lift gradient and the aerodynamic interaction of wings in tandem was investigated for each region.

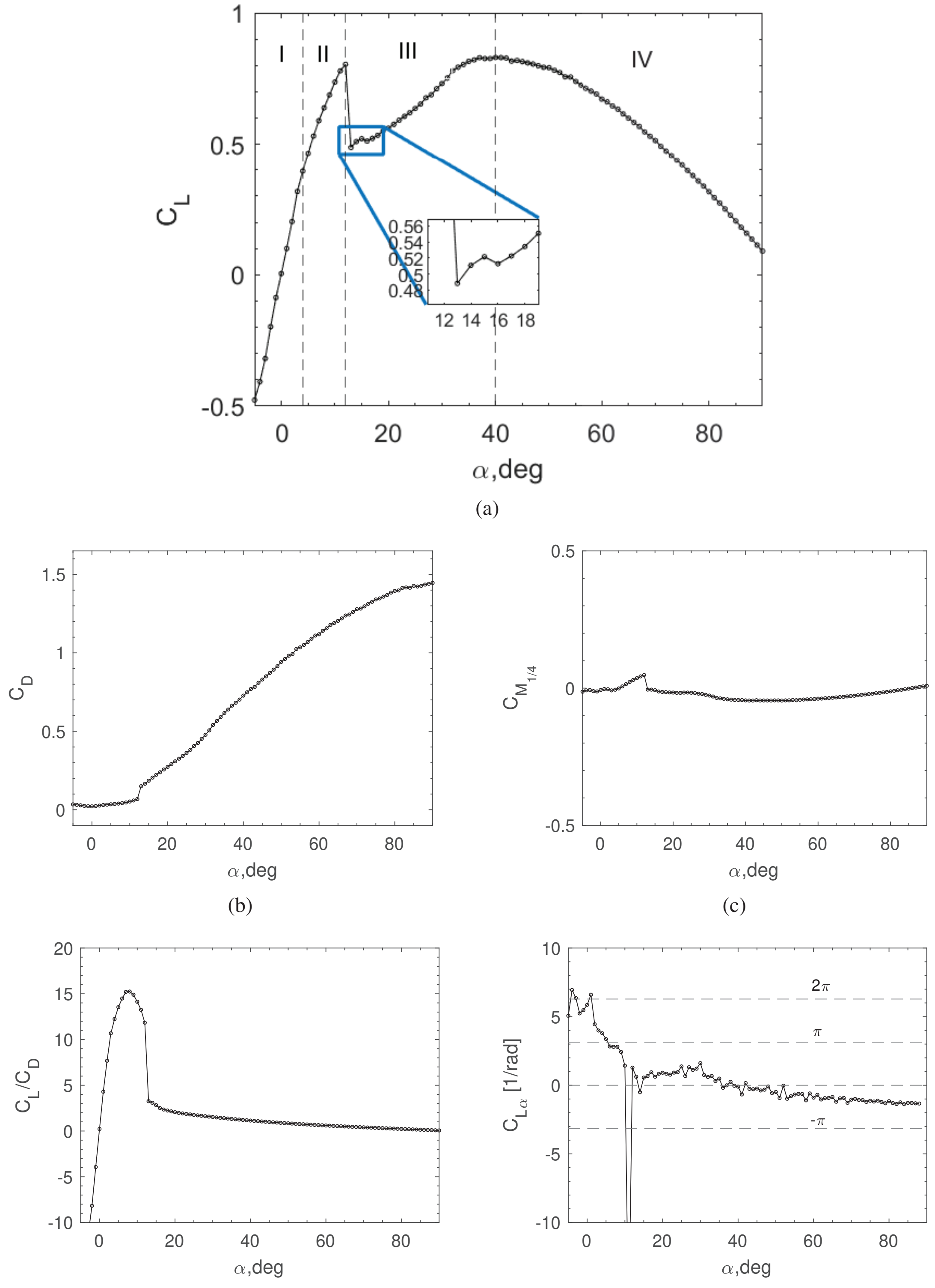

(a)

(b)

(c)

(d)

(e)

Figure 3.14: Mean aerodynamic coefficients of isolated Wing at Re = 100,000.

3.3.1 Surface Flow Visualization

Surface flow visualization of the suction side of the wing was carried out for α range of 0 to 14 degrees. The representative sketches are shown in Figure 3.15 and the original photographs taken are included in Appendix B. The results show that at α = 0 degrees, a large separation region formed on the upper surface of the wing from about 0.4c till the trailing. The separation bubble was two-dimensional except at the wing root and tip. A similar separation region also formed on the lower surface of the wing (not shown) since the wing was symmetrical. The separation bubble shrank in size at α = 2 degrees with a reattachment line observed at around 0.8c. At α = 4 degrees, the separation bubble further shrunk and moved toward the leading edge. The separation bubble existed between 0.25c to 0.6c approximately. α = 0 to 4 deg represent Region-I as shown in Figure 3.14. For Region-II (α = 6, 8 nd 10 degrees), a short separation bubble existed at the leading edge at 0.05c and the flow remained fully attached till the trailing edge after reattachment. Hence the two-slope behavior in the pre-stall α range is attributed to laminar boundary layer separation occurring before the natural transition to a turbulent boundary layer and the formation of long and short separation bubbles. At small angles of attack near zero, separation bubbles form on both the upper and lower surfaces. With the increase in angle of attack, the separation point on the pressure side moves towards the trailing edge and completely vanishes at further high angles of attack to produce fully attached flow. It is hypothesized that the higher lift slope in Region-I is due to the presence of separation bubbles on both surfaces which increases the effective camber and thickness distribution. Reverse flow at the trailing edge was also observed before the stall at α = 10 degrees but the flow was attached over more than 50% of the wing surface. For α = 12 to 14 degrees, a stable two-cell separation was observed. The separated shear layer at the leading edge was bounded by a normal vortex core that trailed downstream. The normal vortices were formed by the interaction of leading-edge vortices, wing-tip vortices, and reverse flow. This behavior can be observed in the force data (marked in Figure 3.14), where lift became constant. The two-cell separation behavior had a similar effect on drag but the magnitude was much smaller. Similar observations were reported by Yon and Katz [96] for NACA0015 of aspect ratio 6 wing tested at Re = 620,000.

3.3.2 Wake Velocity Survey

Figures 3.16 to 3.21 show the wake survey data at α_1 = 0, 4, 8, 11, 20 degrees for isolated Wing-1 at Re_c = 100,000. It is interesting to note that at pre-stall positive angles of attack, the location of the maximum velocity deficit shifted downwards due to greater downwash, and the velocity deficit decreased with an increase in downstream distance. However, after stall at higher angles of attack, it moved upwards, indicating a fully separated flow and reduced downwash. At α_1 = 40 degrees, the velocity deficit attained zero values, which signifies fully separated and reversed flow. More importantly, away from the wing at around y/c = ± 0.7, it attained a velocity equal to $1.2U_\infty$. It should be reiterated that the wings were rotated about the mid-chord point. Therefore, the offset in the maximum deficit location was not due to changes in the distance of the leading and trailing edges from the centerline. The increase in the angle of attack resulted in a wider spread of the wake deficit. This indicates that in a tandem configuration, the lead wing would influence the follower wing even at greater gap distances.

Double maxima were observed at x/c = 0 for α = 20 and 40 degrees, and these maxima were asymmetric, as shown in Figure 3.10. The upper maximum was slightly smaller than the bottom one. The asymmetry is attributed to the development of boundary layers differently on upper and lower surfaces because of the different pressure gradients. The development of wake downstream of a wing is a complex phenomenon governed by an asymmetry in double maxima, an increase in turbulence intensity, and boundary layer behavior leading to the evolution of the wake downstream particularly at higher angles of attack.

3.4 Unsteady Response

The behavior of a wing at a low Reynolds number is inherently unsteady even at steady upstream conditions. Unsteady aerodynamic modes refer to the oscillatory motion or instability that can occur in flows. Depending on the Reynolds number and angles of attack,

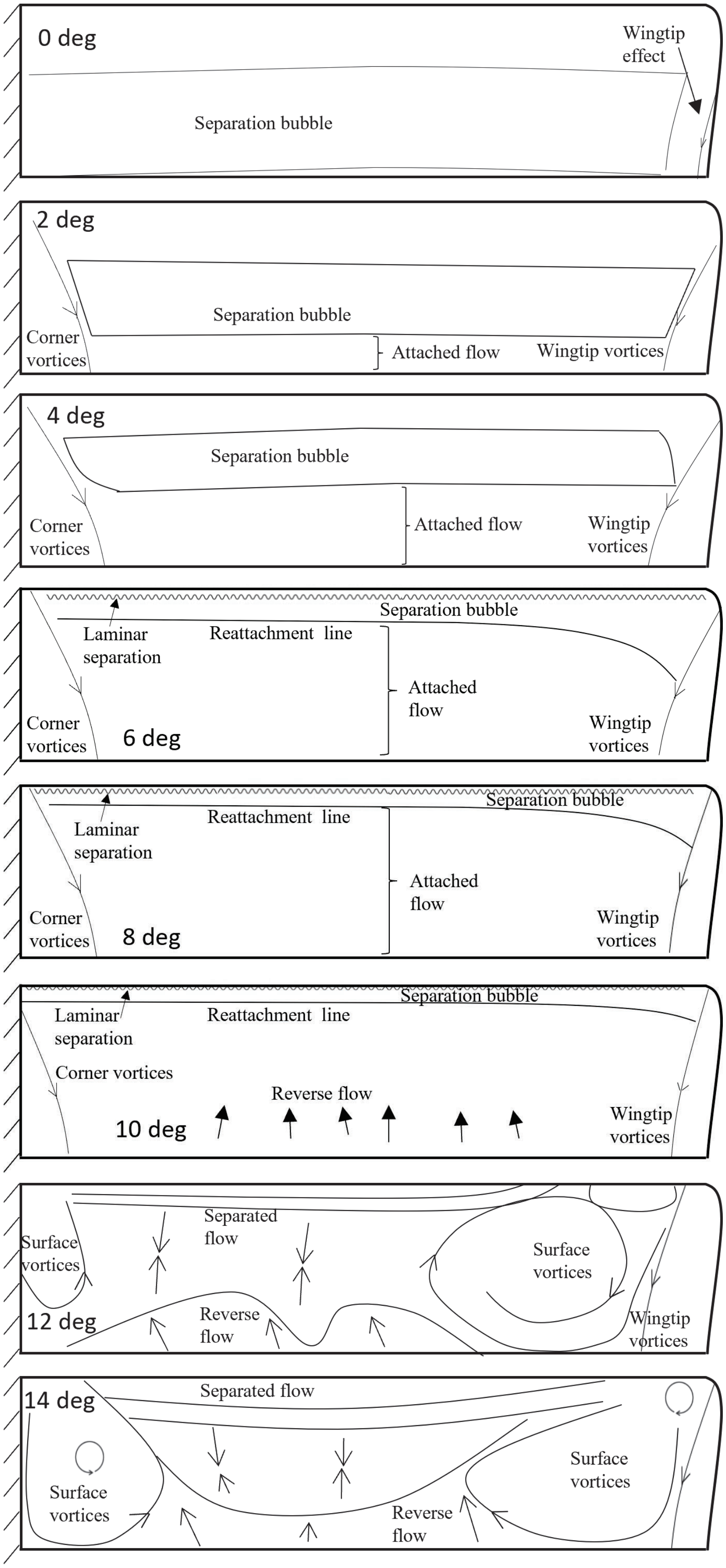

Figure 3.15: Surface flow visualization of isolated Wing at different α and Re = 100,000.

the flow separates and reattaches in an unsteady, periodic fashion, leading to vibrations or flutter. Poincaré maps are a technique used to analyze these unsteady motions by looking at periodic orbits. A Poincaré section is defined, which intersects the periodic trajectories transversely. The trajectories are projected onto the section, and the intersection points are plotted to create the map. The Poincaré map provides a visualization of the system dynamics and periodicity. Fixed points indicate stable periodic orbits. Other behaviors like quasi-periodicity or chaos can also be identified from the map structure. The wings used in the present study were attached to the force in the cantilever hence the vibrate with the flow. The time history of the aerodynamic forces contains the effect of unsteady aerodynamic loads and aeroelastic behavior. Thus this analysis is beyond the scope of this research and the plots are included in Appendix C for reference only and are not discussed further and were not plotted for wings in tandem.

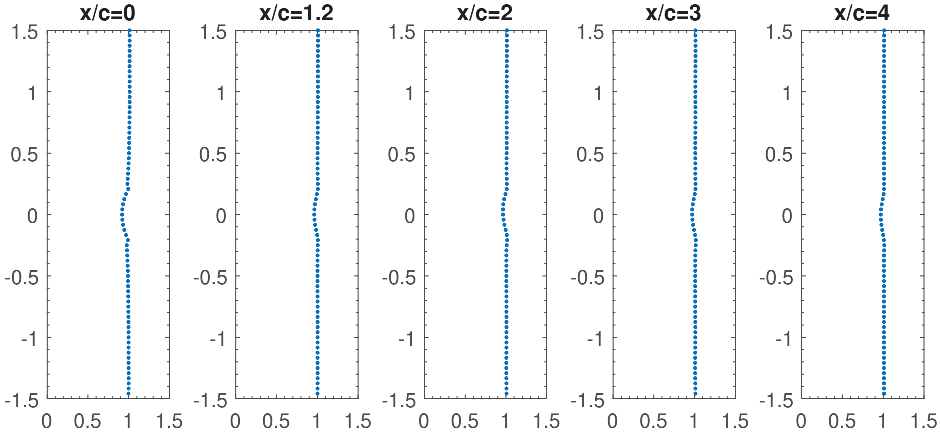

Figure 3.16: Velocity survey at α = 0, Re = 100,000

3.5 Chapter Summary

Experiments were conducted at low Reynolds numbers to serve as a reference baseline for studying the aerodynamic interaction of wings in tandem configuration.

At Re = 20,000, NACA0012 wing of finite aspect ratio exhibited highly nonlinear lift behavior without a discrete stall. Four distinct regions were based on lift curve and angle of attack: negative lift coefficients at low angles of attack attributable to flow separation and

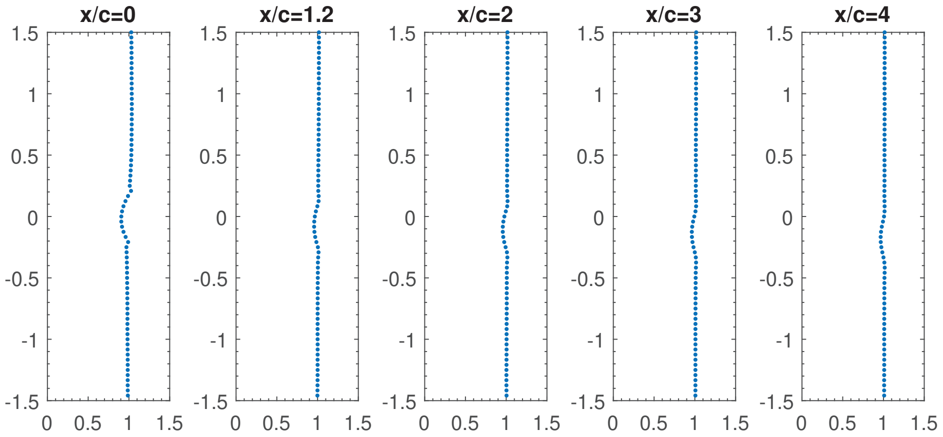

Figure 3.17: Velocity survey at α = 4 deg, Re = 100,000

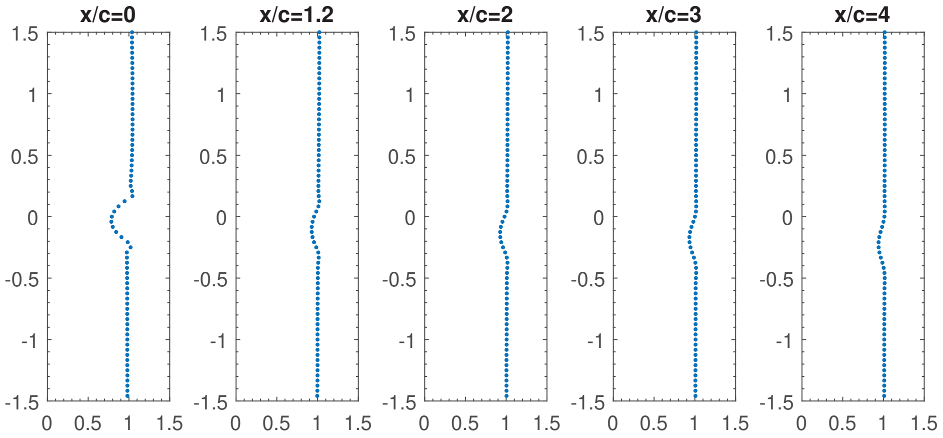

Figure 3.18: Velocity survey at α = 8 deg, Re = 100,000

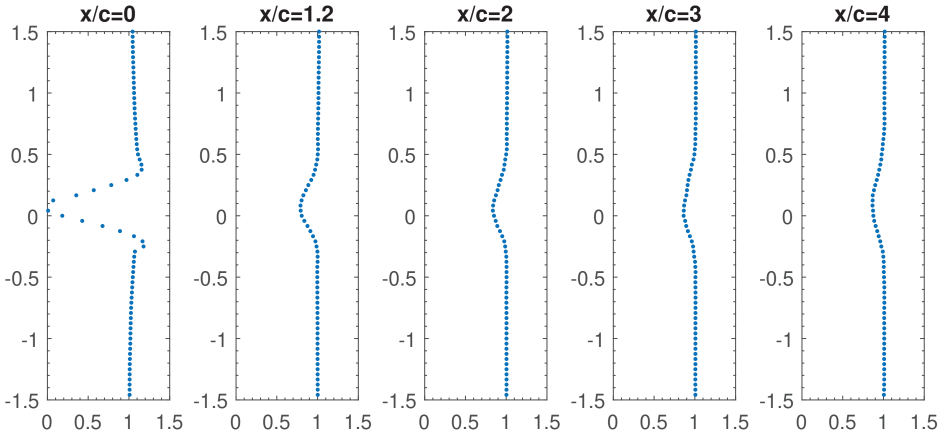

Figure 3.19: Velocity survey at α = 11 deg, Re = 100,000

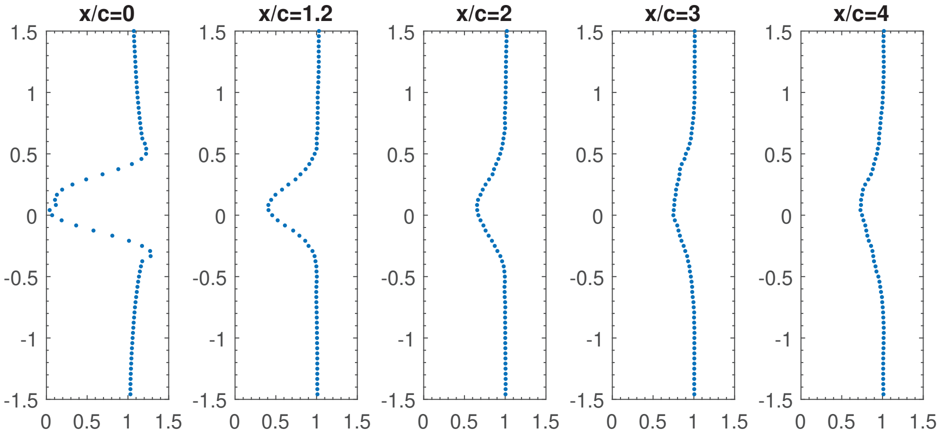

Figure 3.20: Velocity survey at α = 20 deg, Re = 100,000

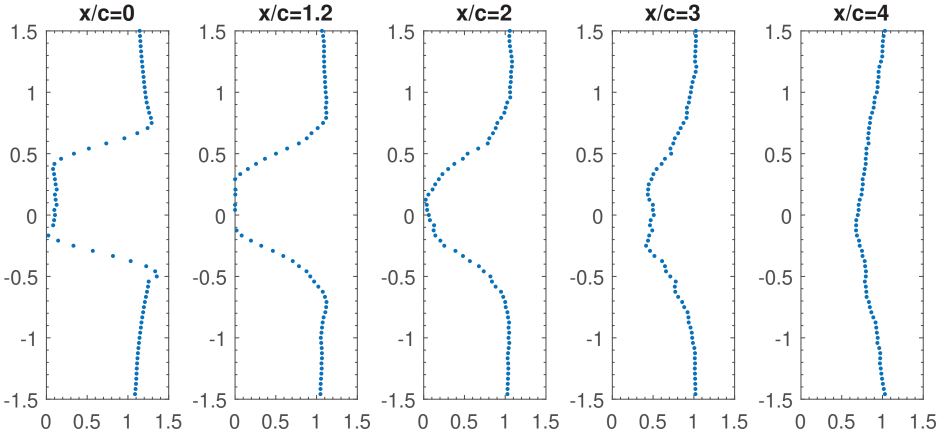

Figure 3.21: Velocity survey at α = 40 deg, Re = 100,000

reversal at the trailing edge (Region I); increasing lift with angle of attack as the separation points moved upstream towards the leading edge (Region II); reduced lift slope with large separated flow regions (Region III); and decreasing lift at high angles as massively separated flow enveloped much of the airfoil (Region IV). The wake flows were dominated by laminar instability waves, vortex shedding, and interactions between surface vortices and counter-rotating trailing edge vortices. At Re = 100,000, the lift curve assumed a more conventional shape with linear increase, abrupt leading edge stall, and hysteresis. Surface flow visualization revealed changing separation bubble size and location with angle of attack. In Region I, substantial separation bubbles on both the pressure and suction surfaces augmented the effective camber and thickness, inducing a higher lift slope. Regions II and III exhibited progressive upstream displacement of the separation point until pervasive separated flow ensued in Region IV. The Reynolds number effects on boundary layer transition and separation profoundly altered airfoil performance and wake structure.

Chapter 4

Aerodynamics of Wings in Tandem at Low Reynolds numbers

This chapter included the aerodynamics of finite aspect ratio wings in tandem for three test cases involving different combinations of angles of attack, as outlined in Table 2.2. Wing-2 was positioned directly downstream of Wing-1 at a stagger of s = 1.2c, and a gap of G = 0. The subscripts '1' and '2' are utilized to denote parameters corresponding to Wing-1 and Wing-2, respectively. Additionally, the subscript 'i' is employed in the figures and discussions to signify values associated with an isolated wing for comparison purposes. Aerodynamic coefficients for both Wing-1 and Wing-2 were determined utilizing freestream velocity as a reference, and the angle of attack was also calculated relative to the freestream despite Wing-2 being positioned in the wake and encountering modified local upstream conditions. The results for Re =20,000 and 100,000 are presented separately.

Direct force/moment measurements, flow visualizations, and wake surveys were carried out to explain the underlying physics of tandem wing interference phenomena. The analysis of these three test cases provides insight into the complex aerodynamic couplings that manifest between wings positioned in close tandem arrangement under different operating conditions.

4.1 Case-1: α_1 sweep ± 90 degrees, and α_2 fixed at 0, 5, 10, 20, and 40 degrees

The angle of attack of Wing-1 was varied from 0 to ± 90 degrees while Wing-2 remained at fixed positive angles of attack. This configuration mimics having Wing-2 at negative α_2 when Wing-1 sweeps from 0 to -90 degrees, owing to the symmetrical airfoil and zero gap.

4.1.1 Re = 100,000

Figures 4.1 and 4.2 present the lift and drag response of Wing-1 with Wing-2 in tandem at Re = 100,000. Interestingly, Wing-1 results were largely symmetric for both the positive and negative ranges of α_1, the symmetry of the results implies the upstream wing (Wing-1) primarily drives the interaction through its wake characteristics. The influence of Wing-2 on the lift and slope of the lift curve of Wing-1 was minimal for pre-stall α_1. However, some differences in the lift response of Wing-1 were observed compared to the isolated case as follows:

- Higher α_2 resulted in a greater reduction of C_{L1max}, more prominently for negative α_1. As such at α_2 = 40 degrees, C_{L1max} reduced by approximately 20% compared to the isolated wing.
- A slight change in α_{1stall} also occurred for positive range of α_1 for different fixed angles of attack of Wing-2.
- A sharp drop in lift at the stall was exacerbated for higher α_2.
- A secondary stall occurred around α_1 = 21 degrees. Secondary stall characteristics and dependency are discussed further in detail in Chapter 5.
- In the tandem configuration, the lift generated by Wing-1 remained lower than that of the isolated wing after the onset of the secondary stall. Furthermore, the magnitude of the secondary lift peak exhibited by Wing-1 was considerably diminished in the tandem arrangement compared to the isolated wing case.
- For α_1 > 60 degrees, lift values collapsed to match the isolated wing irrespective of the angle of attack of Wing-2, suggesting that Wing-2 did not affect Wing-1 at the angle of attack where bluff body effects dominated.

The presence of Wing-2 resulted in a decrease in the drag of Wing-1 at both pre-stall and post-stall angles of attack compared to the isolated wing. Irrespective of the angle of attack

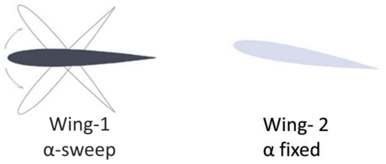

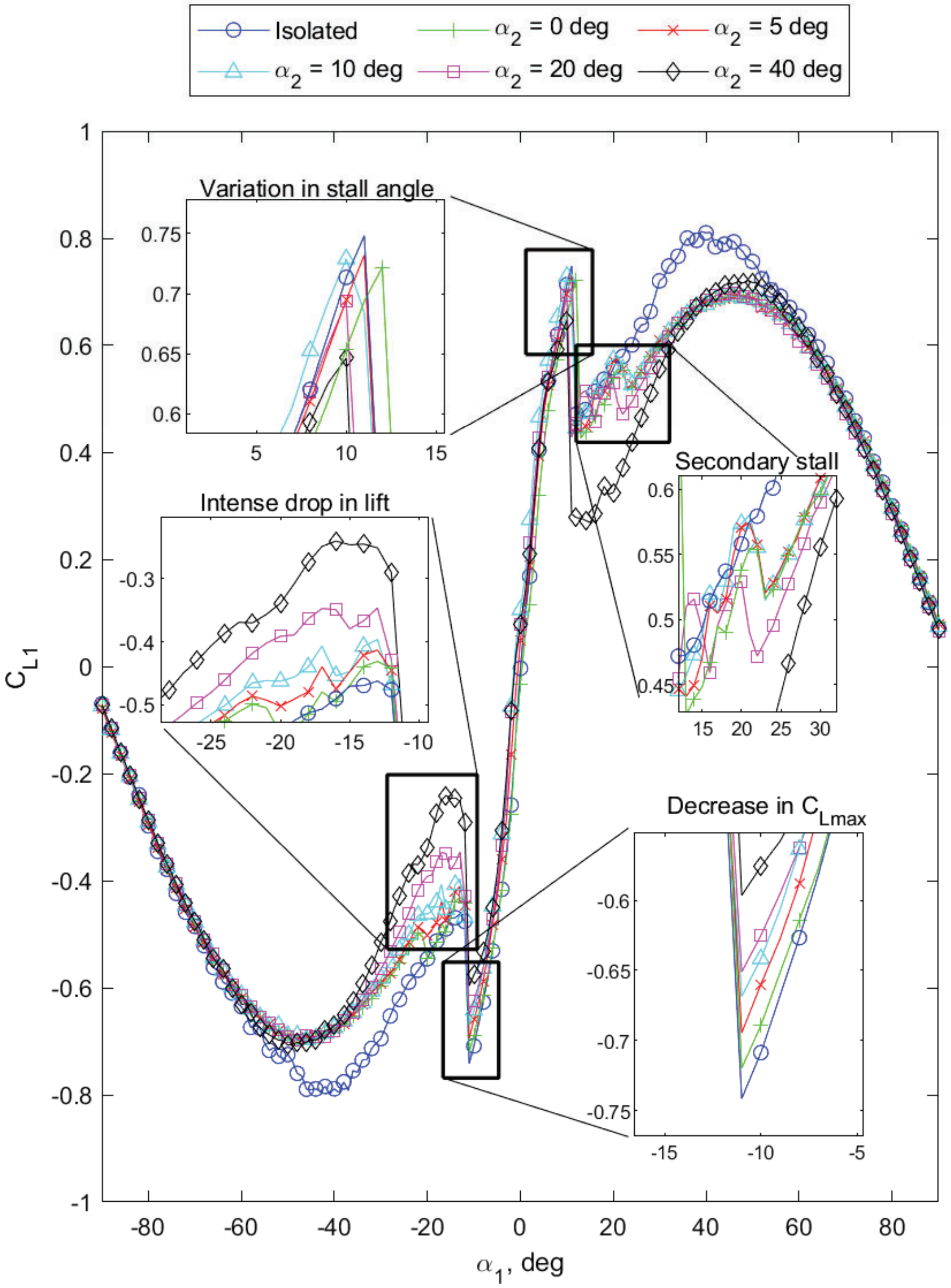

Figure 4.1: C_{L1} vs α_1, Re = 100,000.

of Wing-2, the drag of Wing-1 was lower in the tandem configuration than the isolated wing for the full range of angle of attack. The minimum drag on Wing-1 occurred when Wing-2 was fixed at an angle of 40 degrees. This reduction in drag of Wing-1 is hypothesized to stem from decreased pressure differential upstream and downstream of Wing-1 in the presence of Wing-2. Furthermore, the sharp rise in drag at the stall was mitigated on Wing-1, becoming less pronounced as the angle of attack of Wing-2 was increased. Interestingly the decrease in lift at stall for Wing-1 was most intense when α_2 = 40 degrees, whereas the increase in drag was minimal. The data also exhibited a secondary stall evident in the drag measurements, characterized by a sudden concurrent decrease in both lift and drag. This differs from the primary stall where lift decreases but drag increases. Beyond the secondary stall, the drag values of Wing-1 aligned for different angles of attack of Wing-2 but remained below that of the isolated wing. This implies that in the post-stall region after the secondary stall, the drag response of Wing-1 is not affected by the angle of attack of Wing-2, and the lower value of drag in this range of angle of attack, as compared to the isolated wing, is not due to the blockage produced by Wing-2 but through wake alterations and pressure differentials.

The time-averaged lift and drag coefficients of Wing-2 held at fixed angles of attack in the wake of Wing-1 are shown in Figure 4.3 and 4.4. The dashed lines in the figures represent the mean lift and drag of Wing-2 at the given angle of attack in isolation. The results show that the lift and drag of Wing-2 at a fixed angle of attack varied with the change in α_1 because of the wake characteristics of Wing-1 that change with α_1 and it altered local upstream conditions and effective angle of attack of Wing-2.

The lift response of Wing-2 was examined at various fixed angles of attack as it operated in the wake of the upstream Wing-1. The key observations across the range of α_1 studied are discussed below:

α_2 = 0 degrees: Wing-2 fixed at zero angle of attack produced lift at non-zero α_1. Wing-2 had no lift at α_1 = 0 degrees, positive lift for negative α_1, and negative lift for positive α_1. Increasing α_1 beyond the Wing-1 stall angle caused both wings to stall together, indicating that attached flow on Wing-2 requires attached flow on Wing-1. The stall was sharp and sudden like a leading edge stall for both the wings. C_{L2} remained nearly constant after the primary

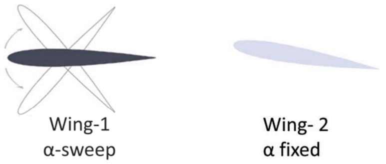

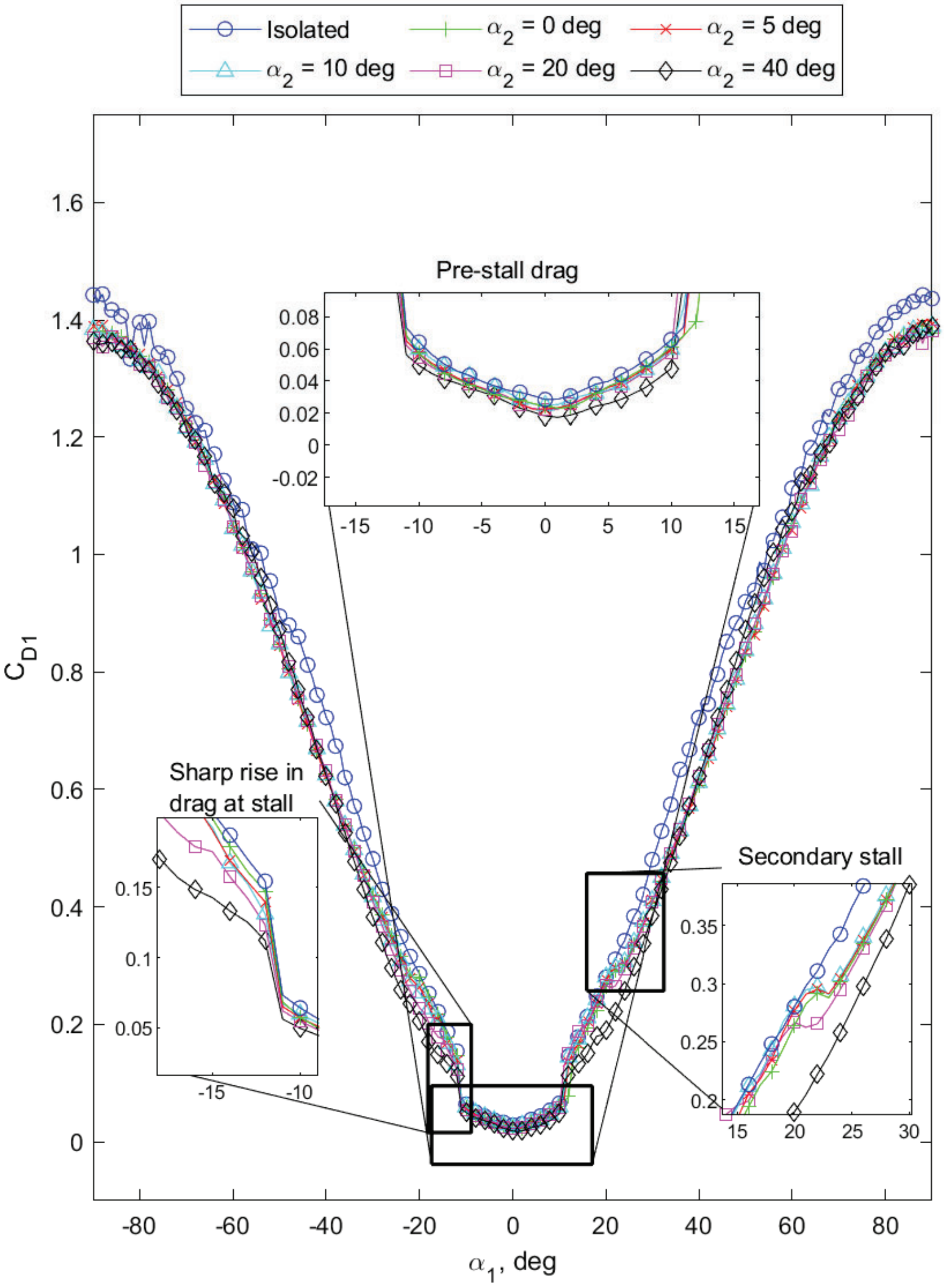

Figure 4.2: C_{D1} vs α_1, Re = 100,000.

stall until α_1 = 21 degrees before a second drop, corresponding to the secondary stall. Beyond the secondary stall, Wing-2 lift curve conformed to Wing-1 behavior but with a much lower magnitude, nearly zero for $|\alpha_1| > 70$ degrees.

The lift produced by Wing-2 for $|\alpha_1| > 0$ is likely due to the downwash produced by Wing-1. The downwash from Wing-1 has opposite directions for α_1 sweep of 0 to 90 degrees and 0 to -90 degrees. Therefore, Wing-2 experienced a downwash for positive α_1 and an upwash for negative α_1. The effect of downwash particularly at the pre-stall angles of attack of Wing-1 can be observed by the location of maximum velocity deficit location downstream of Wing-1 as shown in Figure 3.16. As per the momentum theory, the downwash angle (ϵ) can be calculated by using the following relation.

$$\epsilon = \epsilon_0 + \frac{\partial \epsilon}{\partial \alpha}\alpha \tag{4.1}$$

For a symmetric wing at the zero-lift angle of attack, ϵ_0 is zero. Thus, assuming an elliptical lift distribution, the relationship for downwash and effective angle of attack on Wing-2 can be simplified as follows:

$$\epsilon \approx \frac{2C_{L1}}{\pi AR} \tag{4.2}$$

$$\alpha_{2eff} = -\epsilon + \alpha_2 \tag{4.3}$$

Using equation 4.3, the downwash angle at α_1 = 11 degrees was estimated to be approximately -5 degrees. However, the lift coefficient C_{L2} was considerably lower than that of the isolated wing. It is understood that the downwash alone does not influence Wing-2 and the lift coefficient is due to the combination of multiple factors including velocity deficit in the wake of Wing-1, as freestream velocity was used to calculate aerodynamic coefficients. By applying the velocity correction calculated through the wake profile data as shown in Figure 3.19, the lift coefficient increased but it was still less than the isolated wing at that angle of attack. Thus, the aerodynamic response of Wing-2 appears to be governed by both the downwash angle and wake velocity deficit from the upstream wing, but the response could not be directly calculated from them alone. The increase in turbulence level locally upstream of

Wing-2 also plays a crucial role in determining the Wing-2 response. Moreover, the wake trajectory of Wing-1 is also expected to play a role in determining the aerodynamic response of Wing-2. The increase in turbulence level is expected to reduce the lift curve slope hence the lift reduction but delay the stall [97]. Scharpf and Mueller [55] observed using smoke visualization, the wake passes underneath the rear wing for pre-stall angles of attack of the front wing, contributing to the lift reduction. Therefore decrease in lift of Wing-2 at pre-stall angles of Wing-1 was also governed by the trajectory of the wake passing over or under Wing-2 depending upon the relative position of both the wings.

$\alpha_2 = 5$ degrees: Wing-2 produced 37% less lift when Wing-1 was at $\alpha_1 = 0$ degrees likely due to the downwash, velocity deficit from Wing-1 reducing local velocity upstream of Wing-2 and the wake trajectory. For negative α_1, C_{L2} sharply increased until both wings stalled suddenly with a noticeable secondary stall. For positive α_1, C_{L2} decreased until 40 degrees, reaching zero around $\alpha_1 = 30$ degrees, without discrete stall. Wing-2 lift slope changes conformed to Wing-1 behavior.

$\alpha_2 = 10$ degrees: C_{L2} was below the isolated wing lift at $\alpha_1 = 0$ degrees. For positive α_1, C_{L2} gradually decreased, reaching zero at $alpha_1 \approx 35 degrees. For negative \alpha_1$, lift increased until Wing-1 stall then sharply decreased.

$\alpha_2 = 20$ and 40 degrees: The most interesting behavior was at $\alpha_2 = 20$ degrees. In the pre-stall range of α_1, C_{L2} was slightly higher than the isolated wing lift and it increased sharply once wing-1 stalled for both negative and positive ranges of α_1. A further increase in α_1 caused C_{L2} to drop and reached zero at $\alpha_1 = 35$ degrees. For $\alpha_2 = 40$ degrees, C_{L2} remained close to the isolated wing lift before Wing-1 stall. For the positive α_1 range, the stall was sharp with a discrete secondary stall.

Figure 4.4 presents the drag response of Wing-2 held at various positive angles of attack in the tandem configuration. The drag behavior was not symmetric for positive and negative ranges of α_1, indicating that the drag interaction arises through blockage effects and pressure distribution between the wings. At higher angles of attack of Wing-1, the drag of Wing-2 was substantially reduced, even producing thrust. This thrust generation highlights the potential aerodynamic benefits of tandem wings through favorable interference effects, especially at

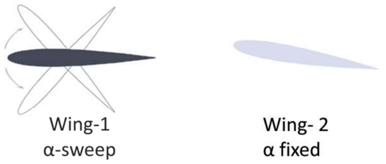

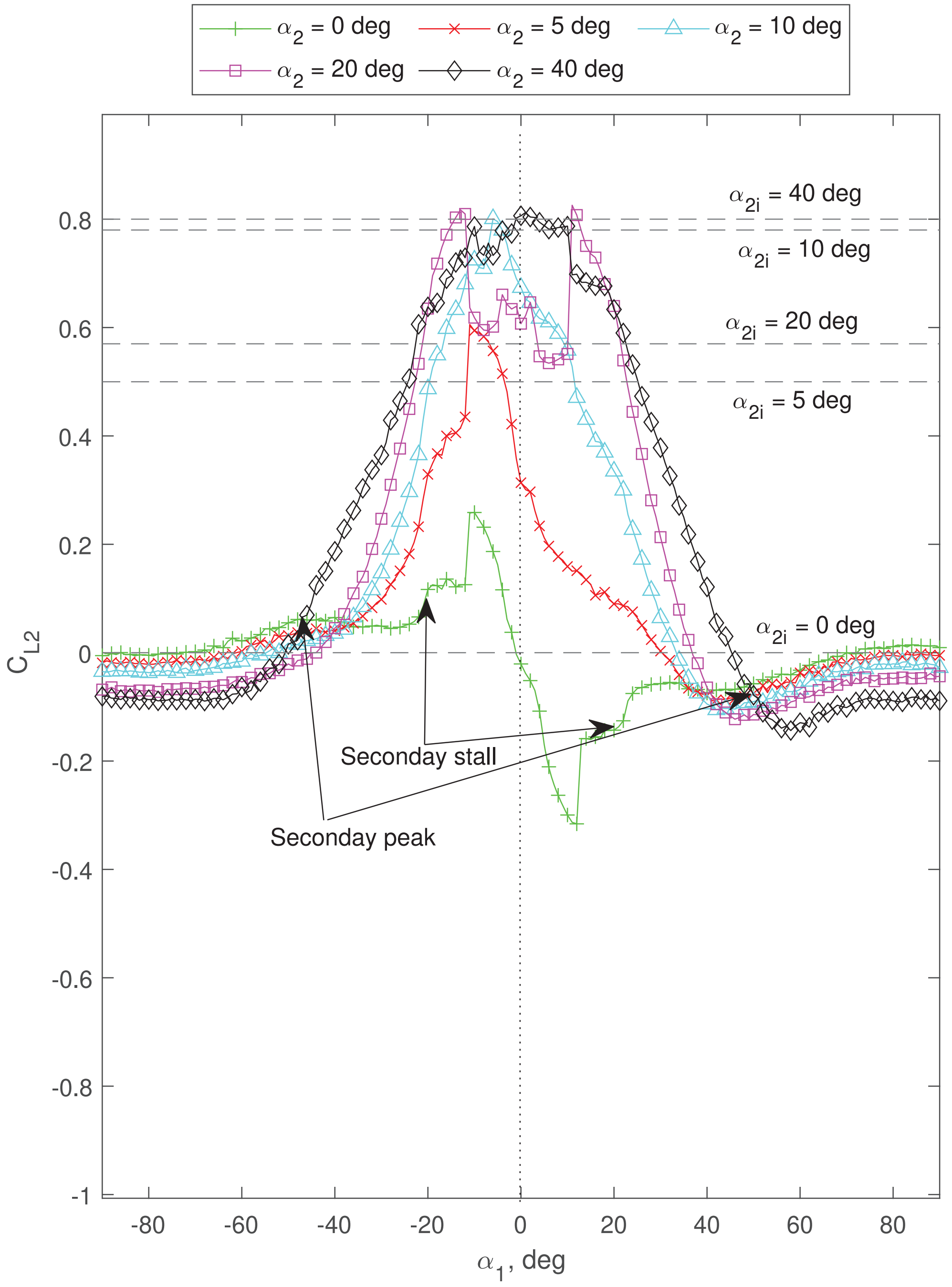

Figure 4.3: C_{L2} vs α_1 for Wing-2 held at different angles of attack, Re = 100,000.

higher angles of attack incidences. For α_2 = 20 degrees, the onset of stall of Wing-1 resulted in an increase in lift and a decrease in drag of Wing-2. This can be explained by the fact that the flow separation of Wing-1 resulted in a decreased pressure upstream of Wing-2, which caused the drag reduction. On the other hand, the wake of Wing-1 moved upward (Figure 3.21) due to the reduction in downwash, hence the pressure on the suction side of Wing-2 decreased, and as a consequence, its lift increased.

One of the most salient observations was for α_2 = 40 degrees. The lift and drag curves were nearly identical, with the magnitude of drag slightly less than lift. Before the stall of Wing-1, lift and drag of Wing-2 remained constant, with values equal to the isolated baseline wing. However, after Wing-1 stall, lift and drag of Wing-2 decreased simultaneously, reaching negative values around $\alpha_1 = 44$ degrees. For angles of attack > 40 degrees, the Wing-1 wake was fully separated and dominated by reverse flow. This caused the Wing-2 to experience massively altered oncoming flow conditions, leading to the synchronized reduction and eventual reversal of lift and drag forces.

Surface flow visualization for wings in tandem with α_1 = 6 degrees and α_2 = 0 degrees is presented in Figure 4.5. The figure shows that the size and the location of the laminar separation bubble on Wing-1 were unchanged compared to the isolated wing case (Figure 3.15). However, the separation bubble on Wing-2 at α_2 = 0 degrees angle of attack exhibited contraction in size relative to the isolated configuration. Additionally, the tip vortices originating from Wing-1 and impinging on Wing-2 were discernible on the surface of Wing-2. At pre-stall angles of attack, the effect of impinging tip vortices was confined to a very small region. The contraction of LSB can be attributed to the increased turbulence intensity in the wake of Wing-1 and locally upstream of Wing-2, which likely altered the transition and hence laminar separation and reattachment behavior.

The velocity deficit and turbulence depend on α_1 and C_{L1}, setting the onset flow for Wing-2. Hence, Wing-2 lift response was dictated by Wing-1 through downwash, velocity deficit, and wake characteristics. At higher angles of attack of Wing-1, when downwash diminished, the response of Wing-2 is dependent upon the velocity deficit, and base pressure downstream of Wing-1. Figure 4.6 shows the wake survey results carried out by using a single probe hotwire

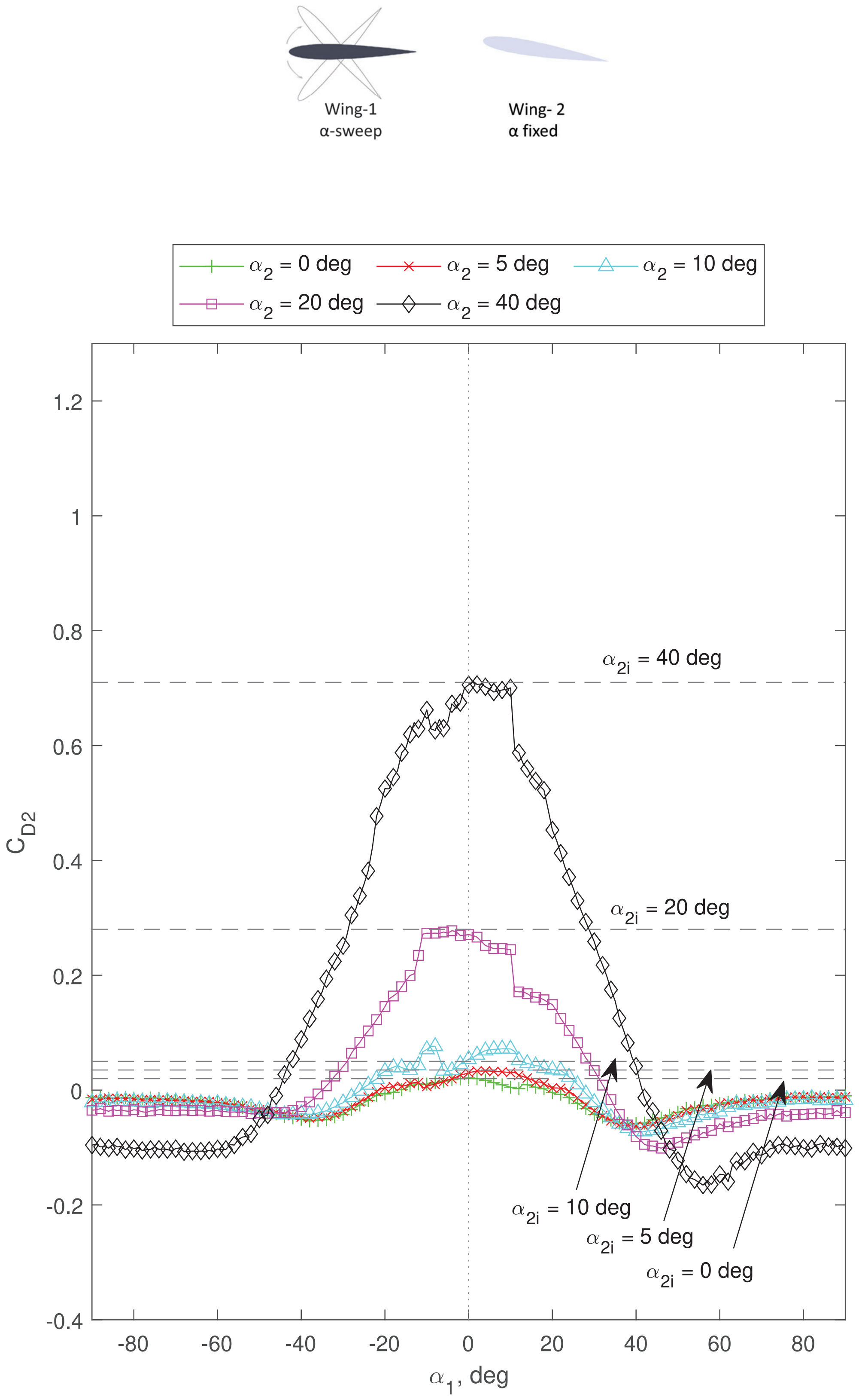

Figure 4.4: C_{D2} vs α_1 for Wing-2 held at different incidence angles, $Re_c = 100,000$.

to measure the turbulence intensity and velocity fluctuation in the streamwise directions. The survey was carried mid-point between the wings. Results clearly show that the turbulence intensity increased in the wake of Wing-1 as compared to the freestream velocity and TI was less for the isolated wing case for all α_1 investigated except at $\alpha_1 = 20$ degrees.

Therefore, while a simple downwash model provides an initial approximation of the induced incidence on Wing-2, the complex interactions arising from the wake velocity profile, turbulence intensity, and trajectory of wake from the upstream wing play a significant role. A comprehensive understanding of these interconnected factors is required to accurately predict the performance of tandem wings across a range of configurations and angles of attack. The downwash angle alone does not fully capture the intricacies of the aerodynamic interactions between the tandem wings.

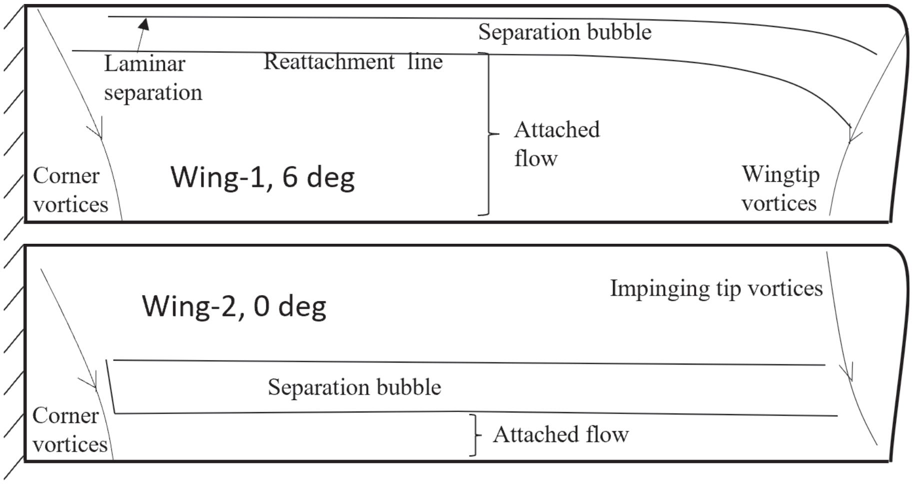

Figure 4.5: Surface flow visualization in tandem configuration α_1 = 6 deg and α_2 = 0 deg, Re = 100,000.

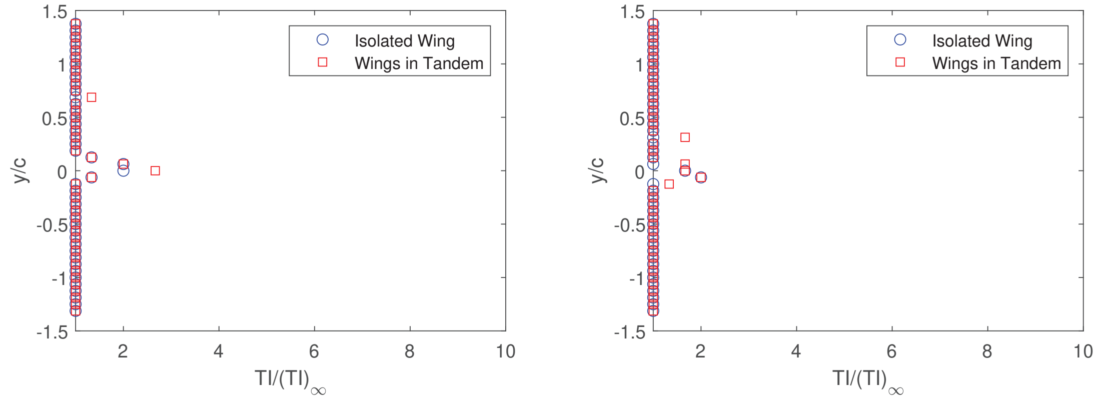

(a) α_1 = 0 deg (b) α_1 = 4 deg

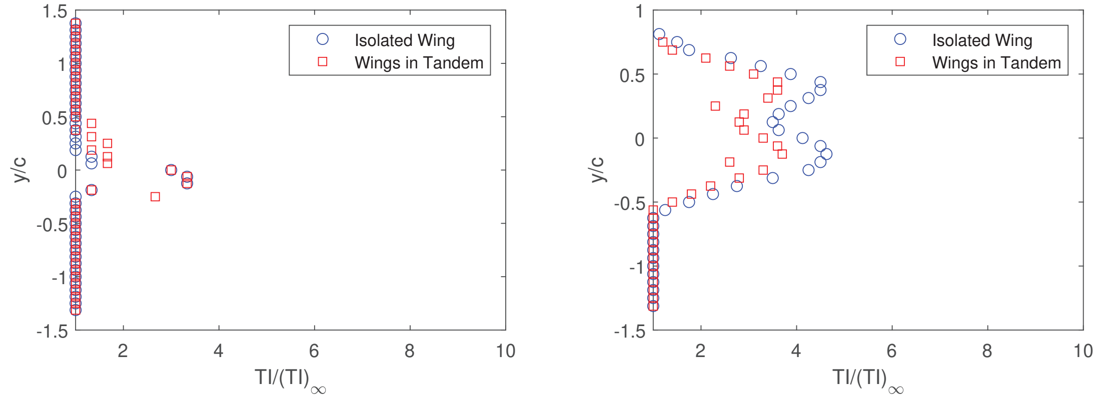

(c) α_1 = 10 deg (d) α_1 = 20 deg

Figure 4.6: Turbulence intensity in the wake of Wing-1 in isolation and tandem configuration, Re = 100,000.

4.1.2 Re = 20,000

Figure 4.7 and 4.8 show the lift response of Wing-1 and Wing-2 respectively for α_1 sweep of ±90 degrees when Wing-2 was held at different angles of attack. The lift response of Wing-1 in tandem configuration qualitatively resembled its response at Re_c= 100,000. The results show that the presence of Wing-2 reduced the secondary peak of Wing-1, and a sharp decrease in the slope of the lift curve was also evident between 5 degrees < α_1 < 22 degrees. This steep decrease was more pronounced and occurred at lower α_1 for higher α_2 values. The decrease in slope is likely due to the deflection of wake towards the leading edge of Wing-2 and that was more pronounced at higher α_2 (refer Figure 6.6).

The wake survey data (refer Figures 3.12 to 3.7) show that the location of maximum velocity deficit didn't move downward in the downstream direction which suggests that the effect of Wing-1 on Wing-2 was primarily because of the velocity deficit and increase in turbulence intensity. Compared to the isolated wing, Wing-2 produced more lift when held at 5 and 10 degrees for Wing-1 at zero degrees. The lift decreased with increasing α_1 of Wing-1. The increase in the lift was due to the impingement of vortices originating from Wing-1 on the leading edge of Wing-2 as shown in flow visualization results (refer Figure 4.10). These impinging vortices rolled over the surface of wing-2 and made a situation analogous to the formation of leading-edge vortices (LEV). The formation of LEV results in accelerating the flow over the surface of the wing to reduce pressure and increase lift [98]. Conversely, lift was considerably lower for Wing-2 at 20 and 40 degrees when α_1 = 0 degrees. Wake survey data demonstrated that the wake deficit region was small and proximate to the centerline. Consequently, at higher angles of attack of Wing-2, the velocity deficit was close to the lower side resulting in a reduction in pressure and hence the lift. From flow visualization as shown in Figure 4.10, it is observed that the upstream presence of Wing-1 at small angles of attack delayed separation by energizing the boundary layer over Wing-2. At higher angles of attack, Wing-1 creates a wider wake and thus a higher velocity deficit. Therefore, for increasing α_1, the lift of Wing-2 decreased.

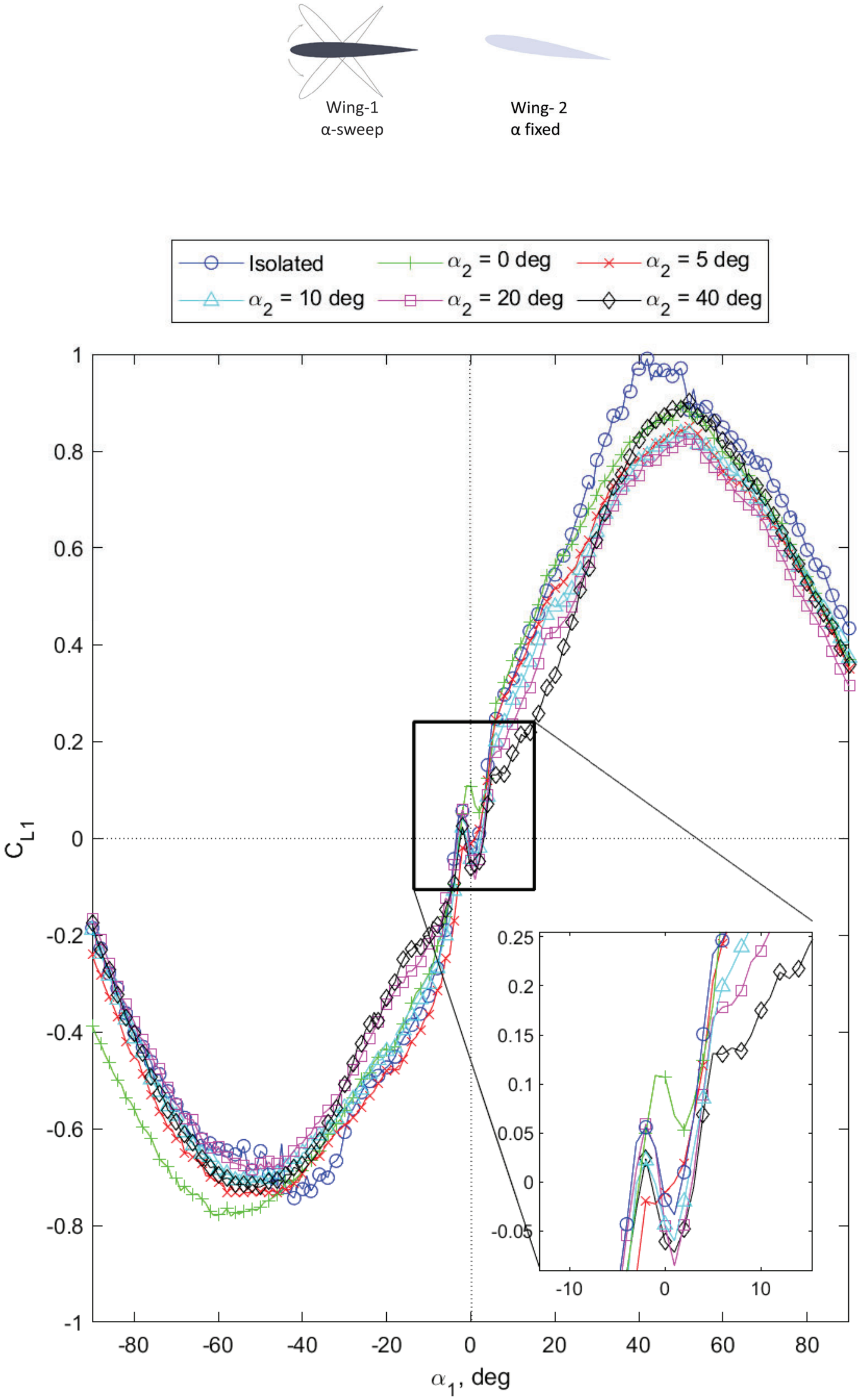

Figure 4.7: C_{L1} vs α_1, Re = 20,000.

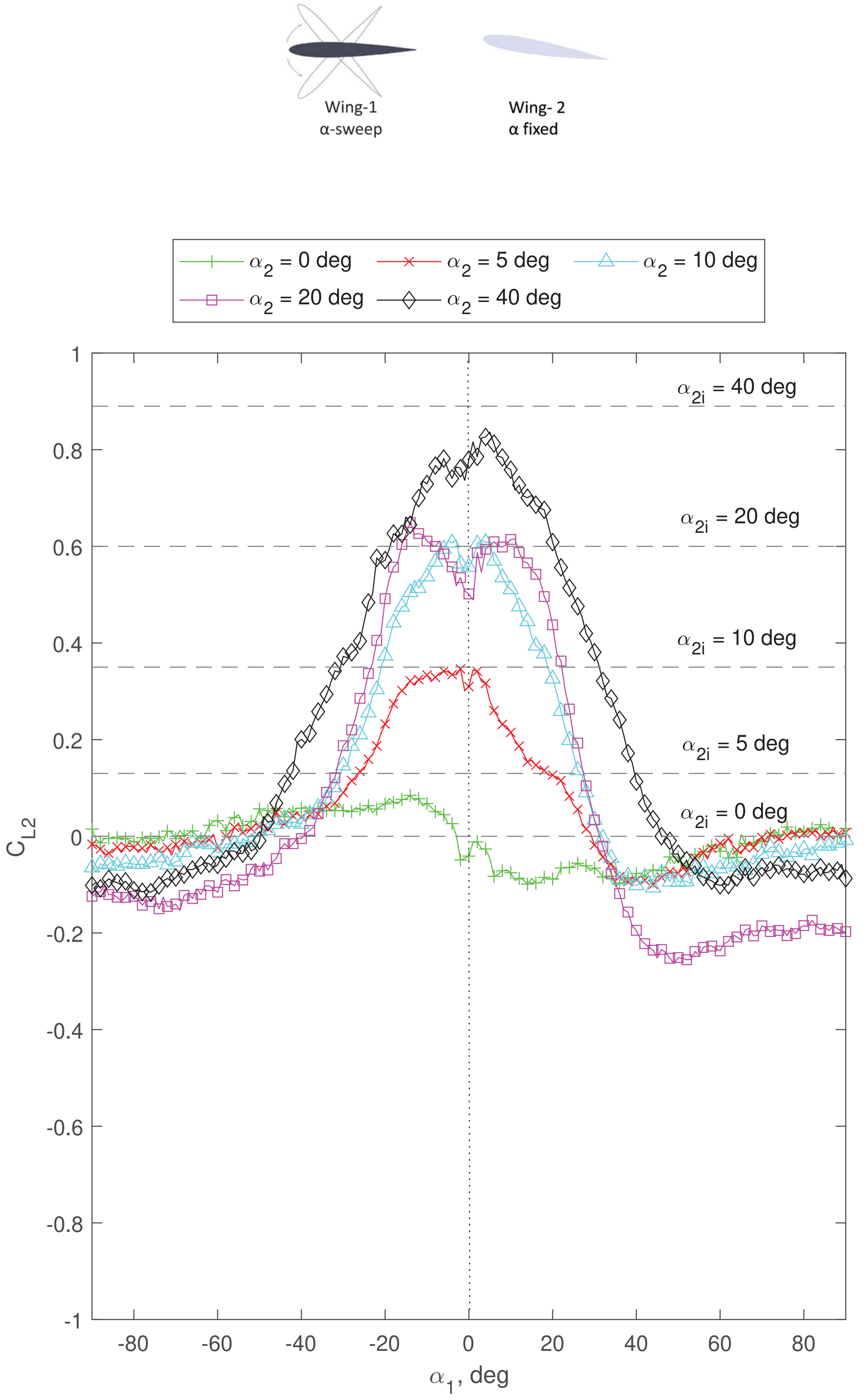

Figure 4.8: C_{L2} vs α_1 for Wing-2 held at different angles of attack, Re = 20,000.

Flow visualization results for wings in tandem at different angles of attack of Wing-1 and Wing-2 fixed at $\alpha_2 = 0$ is shown in Figure 4.9 and 4.10. The results show that at low angles of attack of Wing-2 the vortex street impinging on the leading edge of Wing-2 underwent bifurcation (Figure 4.9). The two counter-rotating vortices traversed over both surfaces of Wing-2. The circulation orientation of the impinging vortices was congruent with that of the bound vortex. In proximity to the trailing edge of Wing-2, a circulation region was discernible, with the distinct wakes of both wings also observable. Further downstream at approximately 1c, the wakes coalesced. For $\alpha_1 \geq 10$ degrees the vortical street became unstable. In the tandem configuration, the presence of Wing-2 suppressed the formation of alternate rotating vortices originating from the leading edge and trailing edge of Wing-1.

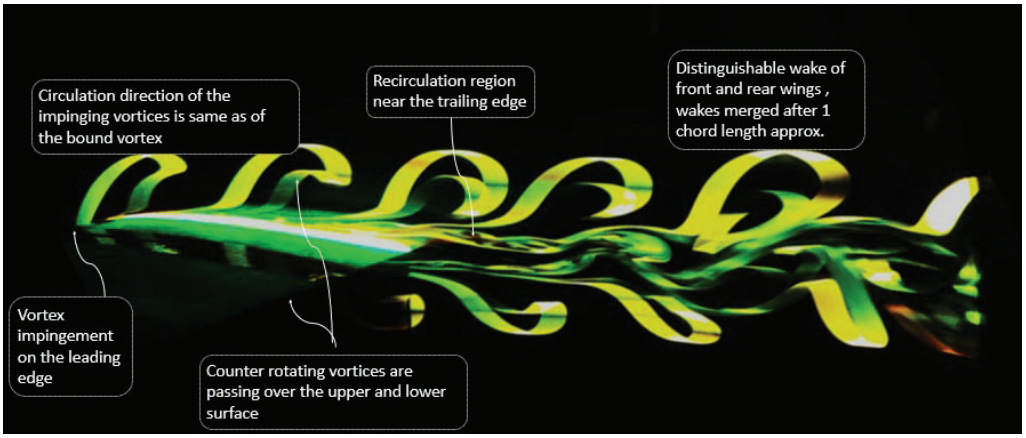

Figure 4.9: Dye flow visualization of Wing-2 in tandem configuration at $\alpha_2 = 0$, Re = 20,000.

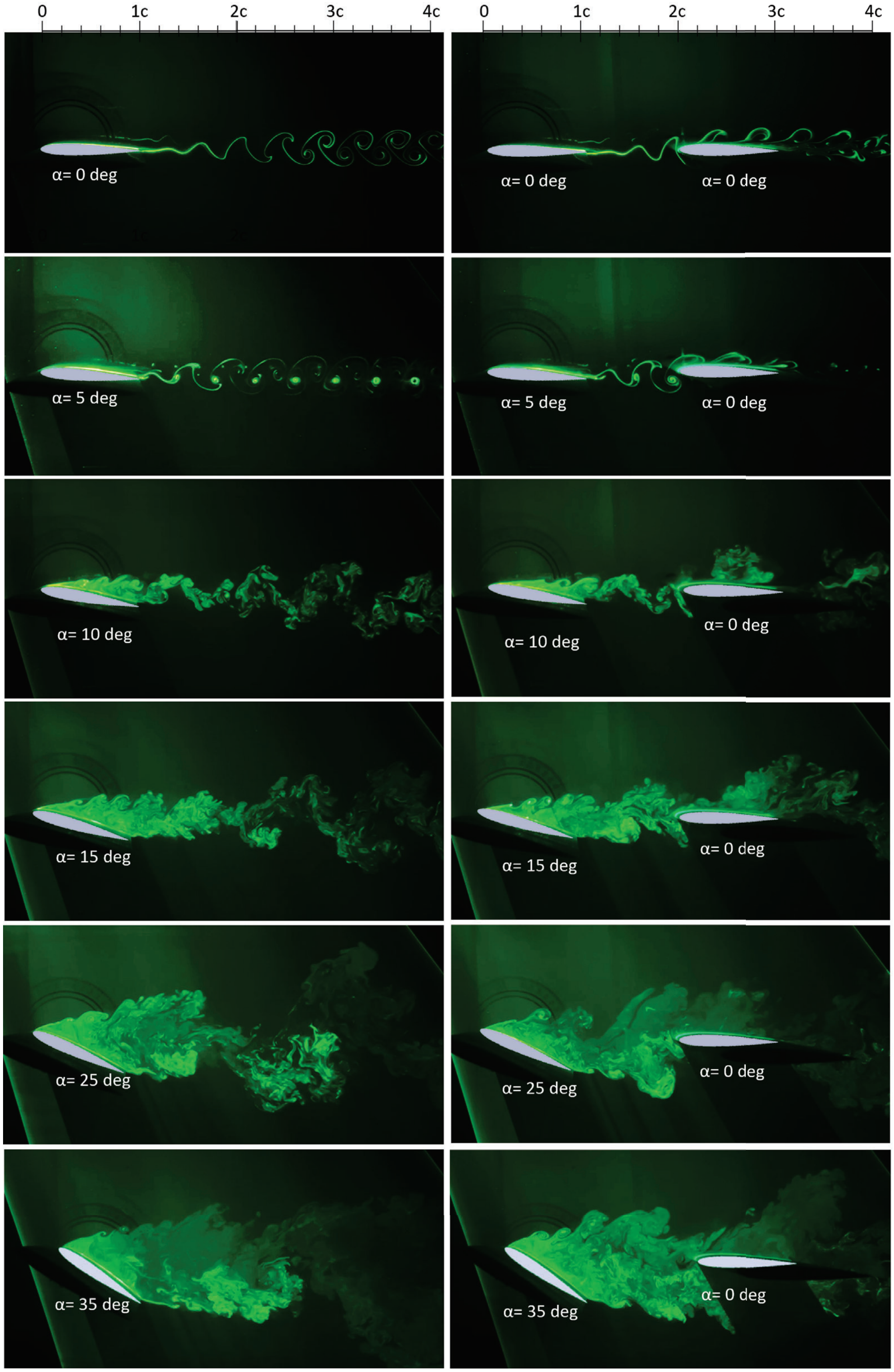

Figure 4.10: Dye flow visualization of the wing in isolation and tandem configuration at different angles of attack, Re = 20,000.

4.2 Case-2: α_2 sweep ± 90 degrees and α_1 fixed at 0, 4, 8, 11, 20, and 40 degrees

Wing-1 was fixed at different angles of attack corresponding to the regions identified by using lift curve of isolated Wing (Figure 3.14). Meanwhile, Wing 2 was swept through ± 90 degrees to characterize the coupled aerodynamic response.

4.2.1 Re = 100,000

Figures 4.12 and 4.13 show the lift and drag of Wing-1 fixed at constant angles of attack vs α_2. The presence of Wing-2 influenced the aerodynamics of Wing-1. Wing-1 held at pre-stall angles of attack (α_1 = 4, 8, and 11 degrees) produced less lift for α_2 = 0 degrees compared to the isolated case. The decrease in lift is likely due to the wake trajectory of Wing-1 which passes under Wing-2 hence it changed the separation behavior over Wing-1. The surface flow visualization results are shown in Figure 4.11. The results show that the size of the separation bubble at α_1 = 0 degrees in tandem configuration was much smaller as compared to the isolated wing (refer Figure 3.15) and flow reattached upstream of the trailing edge. The separation line on Wing-1 in tandem configuration at α_1 = 0 degrees also moved downstream towards the trailing edge. The size and location of the LSB change the slope of the curve and hence the lift at any given angle of attack.

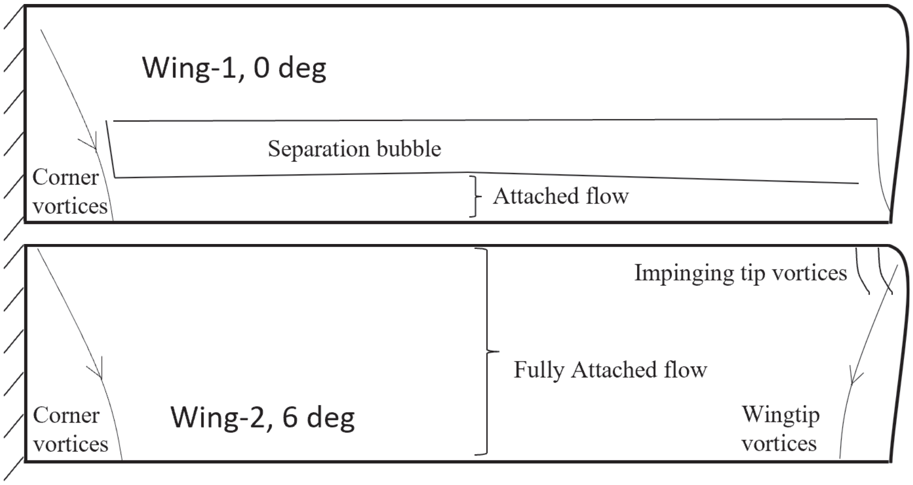

Figure 4.11: Surface flow visualization in tandem configuration α_1= 0 deg and α_2= 6 deg, Re = 100,000.

The results demonstrated that increasing the angle of attack of Wing-2 led to increased lift generation on Wing-1. This lift enhancement on Wing-1 was observed up to the stall of Wing-2. With further increases in α_2 beyond the stall angle, the lift on Wing-1 decreased and remained below that of the isolated wing, except for at $\alpha_1 = 0$ degrees where lift approached zero only when α_2 reached 90 degrees. At $\alpha_1 = 11$ degrees, Wing-1 experienced an intense stall corresponding to Wing-2 stall at positive α_2. In contrast, for increasing negative α_2, the lift of Wing-1 continued to decrease monotonically. At $\alpha_1 = 40$ degrees, the lift remained less than the isolated wing for all angles of attack of Wing-2 and C_{L1} remained unchanged at small angles of attack of Wing-2. The decreased lift at this angle of attack of Wing-1 is due to the occurrence of the secondary stall.

Hence, Wing-2 facilitated increased lift on Wing-1, for some combination of angles of attack up to Wing-2 stall. This highlights an aerodynamic interaction where Wing-2 improves the lift generation of Wing-1. However, once Wing-2 stalls, it no longer augments lift on Wing-1 likely due to the increased base pressure in the wake of Wing-1. The lift enhancement mechanism is sensitive to asymmetry in the angle of attack of the two wings, where the stall of the downstream wing can trigger adverse effects on the upstream wing.

The drag of Wing-1 remained unaffected by Wing-2 at pre-stall angles of attack of Wing-2. However, the drag decreased after Wing-1 stalled. At $\alpha_1 = 11$ degrees, there was a sharp rise in drag for Wing-1 corresponding to the drop in lift. In contrast, at $\alpha_1 = 40$ degrees, the drag remained significantly lower than that of the isolated wing across all tested angles of attack of Wing-2. Therefore, the presence of Wing-2 did not alter the drag of Wing-1 at angles of attack lower than the stall angle of Wing-2. However, Wing-2 caused a reduction in drag of Wing-1 after post-stall angles.

Figures 4.14 and 4.15 present the lift and drag response of Wing-2 for ± 90 degrees in the wake of Wing-1 fixed at different positive angles of attack. It was observed that the wake of Wing-1 significantly affected the Wing-2 lift characteristics. For $\alpha_1 = 0, 4, 8$ degrees (pre-stall), the maximum lift coefficient (C_{L2max}) and stall angle (α_{2stall}) of Wing-2 increased. The slope of the lift curve remained linear, suggesting suppression of separation bubbles due to increased upstream turbulence in the wake of Wing-1 which was also confirmed through surface flow

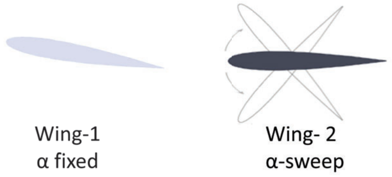

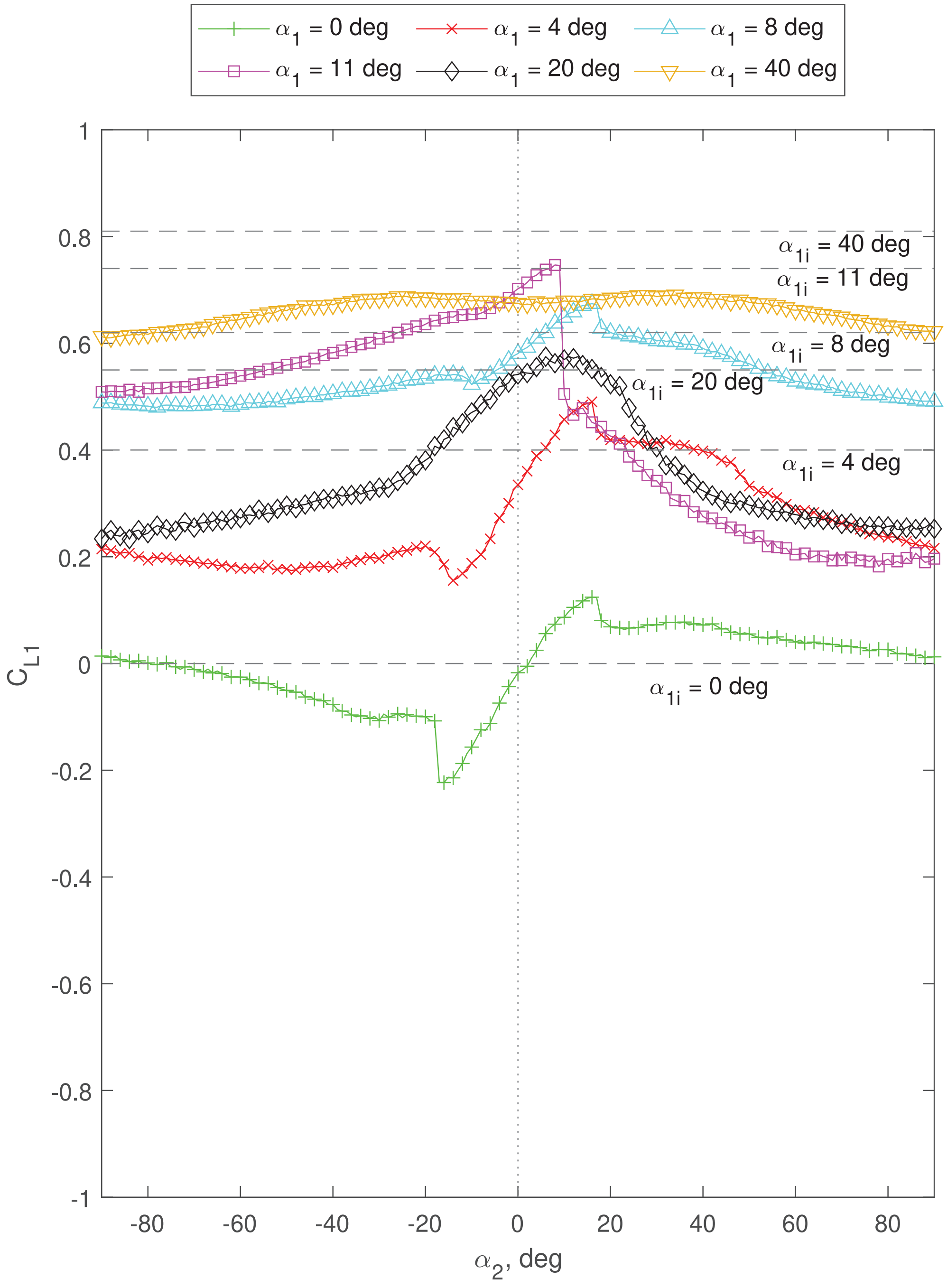

Figure 4.12: C_{L1} vs α_2, Re = 100,000.

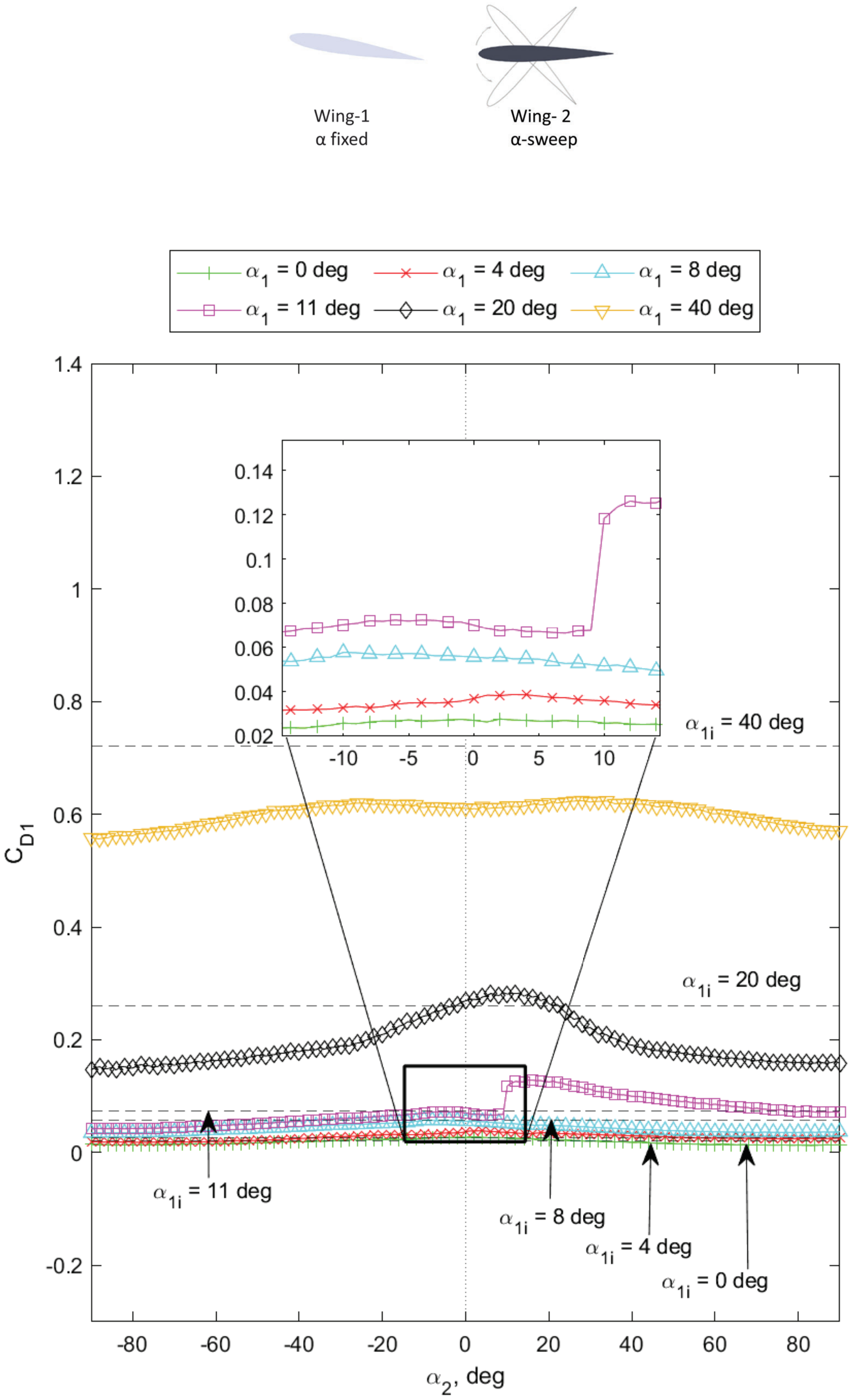

Figure 4.13: C_{D1} vs α_2, Re = 100,000.

visualization as shown in Figure 4.11. A fully attached flow was observed on Wing-2 at a positive angle of attack. C_{L2max} increased up to 12% while α_{2stall} delayed until 17 degrees. For Wing-1 held near stall (α_1 = 11 degrees), C_{L2max} was relatively unchanged but α_{2stall} was delayed to 20 degrees and with a more rounded peak, indicating a trailing edge stall of Wing-2. At α_1 = 20 degrees, C_{L2max} decreased by 12% but $\alpha_{2stall} \approx 30$ degrees and the lift curve exhibited a rounded peak. The behavior of Wing-2 resembled that at Re = 20,000, since in the wake of Wing-1 at α_1 = 20 degrees, the greater velocity deficit decreased the local velocity upstream of Wing-2, reducing the effective Reynolds number. However, the nonlinearity proximal to α_2 = 0 degrees was absent owing to the increased turbulence intensity in the wake of Wing-1. For pre-stall α_1, Wing-2 post-stall behavior resembled the isolated response. but at α_1 = 11 and 20 degrees, the behavior differed with the absence of classical leading edge stall. The lift curve had a rounded peak, suggesting a trailing edge and thin airfoil stall. For Wing-1 at 40 degrees, significantly lower lift was generated for Wing-2 due to the velocity deficit, exhibiting a nonlinear response without stall similar to very low Reynolds numbers.

At pre-stall fixed angles of attack of Wing-1, its drag remained approximately equal to the isolated wing value for low angles of attack of Wing-2. The drag decreased slightly for higher Wing-2 incidences. However, at α_1 = 11 degrees, the drag of Wing-1 rose sharply as the angle of attack of Wing-2 increased, likely because both wings stalled simultaneously. The primary stall is associated with increased drag, which explains this trend. Interestingly, the same phenomenon was not observed for negative angles. For α_1 = -40 degrees, the drag of Wing-1 remained below isolated wing values across the Wing-2 angle of attack range.

Therefore, the wake turbulence and velocity deficit generated by Wing-1 at various α_1 resulted in increased C_{L2max}, delayed stall, altered stall characteristics, and nonlinear response on Wing-2. Across all angles of attack, the drag of Wing-2 when operating downstream of Wing-1 was reduced compared to the isolated wing configuration. The drag bucket widened, likely due to delayed stall, especially when Wing-1 was fixed at 40 degrees. Under these conditions, Wing-2 generated negative drag or thrust forces from $-40 \leq \alpha_2 \leq +40$ degrees, highlighting beneficial aerodynamic interference effects. The presence of the upstream wing led to expanded ranges of low drag and thrust production for the downstream wing.

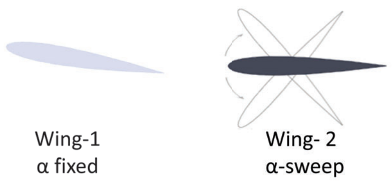

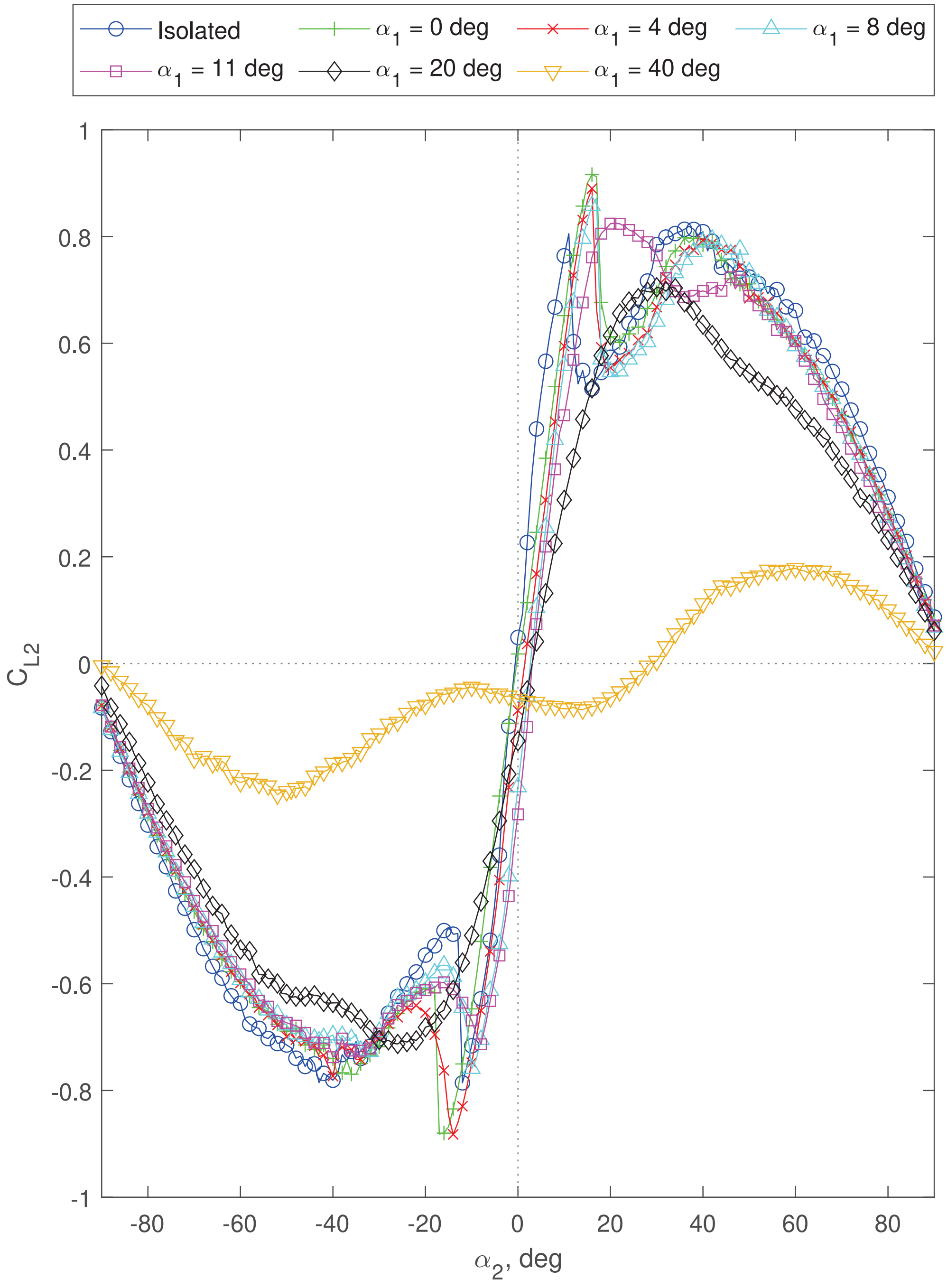

Figure 4.14: C_{L2} vs α_2 for Wing-1 held at different angles of attack, Re = 100,000.

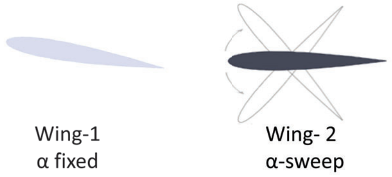

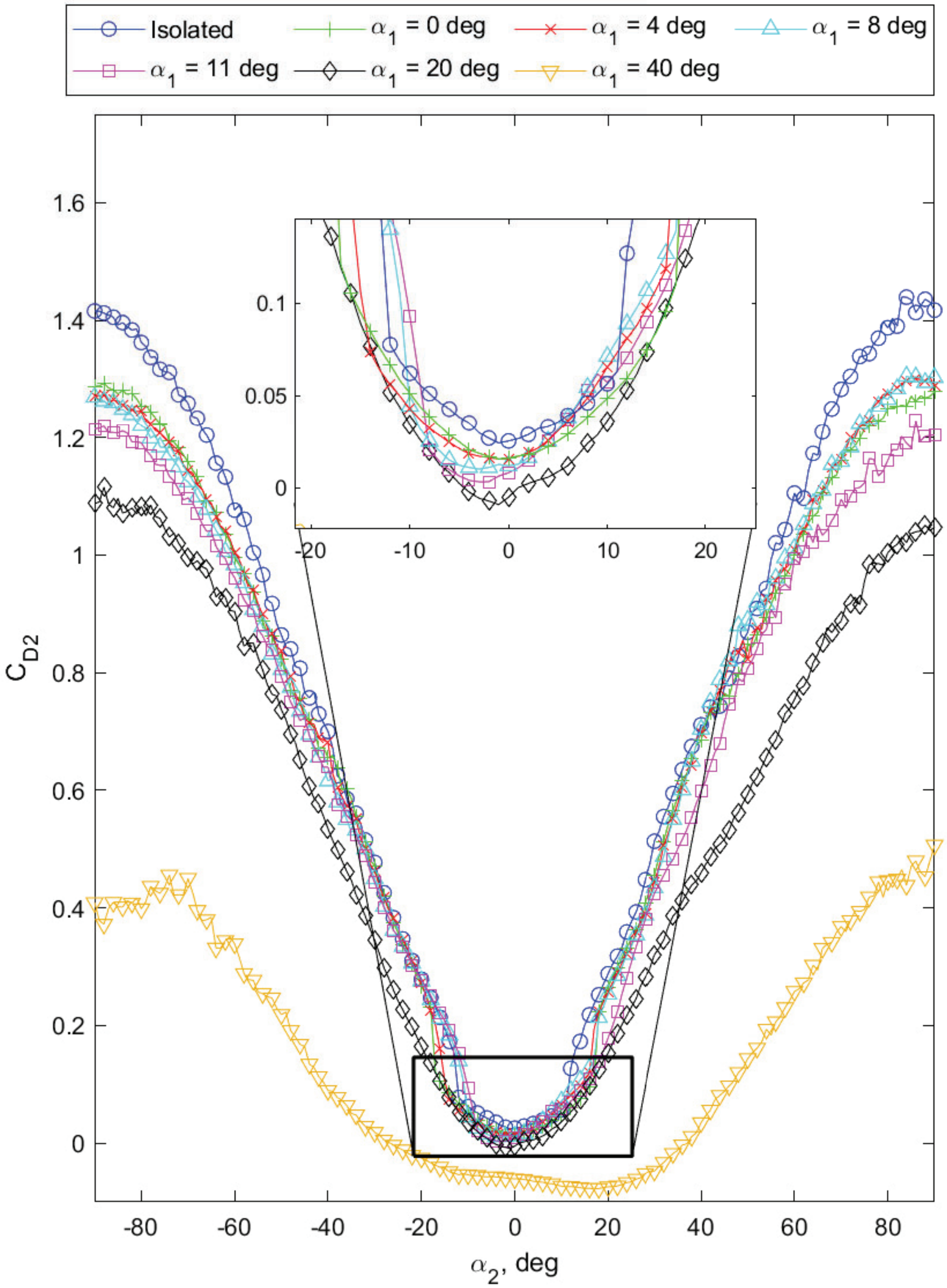

Figure 4.15: C_{D2} vs α_2 for Wing-1 held at different angles of attack, Re = 100,000.

4.2.2 Re = 20,000

Figures 4.16 and 4.17 show the lift response of Wing-1 and Wing-2 respectively at Re = 20,000. The results show that Wing-1 at various fixed angles of attack had lesser lift as compared to the isolated wing for all angles of attack of Wing-2. The response was identical to the response at Re = 100,000. For Wing-1 fixed at $\alpha_1 = 0$ degrees elicited an opposite response. Increasing the angle of attack of Wing-2 resulted in decreased lift generation of Wing-1, and vice versa although the magnitude was much smaller. This difference is ascribed to the nonlinear aerodynamic effects inherent around $\alpha = 0$, coupled with the development of flow separation bubbles on both the suction and pressure sides of the wings. The presence of Wing-1 positioned upstream of Wing-2 at zero and positive angles of attack increased the gradient of the lift curve of Wing-2 for $\alpha_1 = 0$, 4, 8, and 11 degrees as shown in Figure 4.16 and 4.17. Additionally, the nonlinear lift behavior exhibited by Wing-2 around 0 degrees in isolation was eliminated in the tandem configuration. Interestingly, for $\alpha_1 = 0$, 4, 8 degrees, the aerodynamic response of Wing-2 became analogous to that observed at Re = 100,000, with a distinct leading edge stall occurring at $\alpha_2 \approx 15$ degrees. It can be deduced that the effect of increasing Re and upstream disturbances was similar. The maximum lift coefficient (C_{L2max}) attained substantially higher values for $\alpha_1 = 4$ degrees. For $\alpha_1 = 11$ degrees, although the Wing-2 lift curve slope was linear, a behavior reminiscent of thin airfoil stall was evident, with considerably reduced maximum lift. A similar trend was observed when Wing-1 was held at 20 degrees, albeit with a further diminished lift curve gradient and maximum lift for Wing-2. Wing-1 fixed at 40 degrees resulted in significantly decreased lift generation by Wing-2, with lift coefficients remaining negative over the range $-90 \leq \alpha_2 \leq 38$ degrees. This behavior can be attributed to the wide wake, high-velocity deficit imposed on Wing-2.

From dye flow visualization results shown in Figure 6.6, the change in the angle of attack of Wing-2 deflected the wake of Wing-1 hence resulting in a change in the circulation around it. It was observed that the wake tended towards the leading edge of Wing-2, and it resulted in inducing a positive effective angle of attack to Wing-1 for positive α_2. From Figure 6.6, it is evident that the trailing edge of Wing-1 at $\alpha_1 = 0$ was in different states according to α_2.

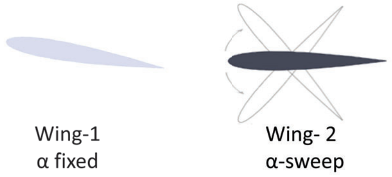

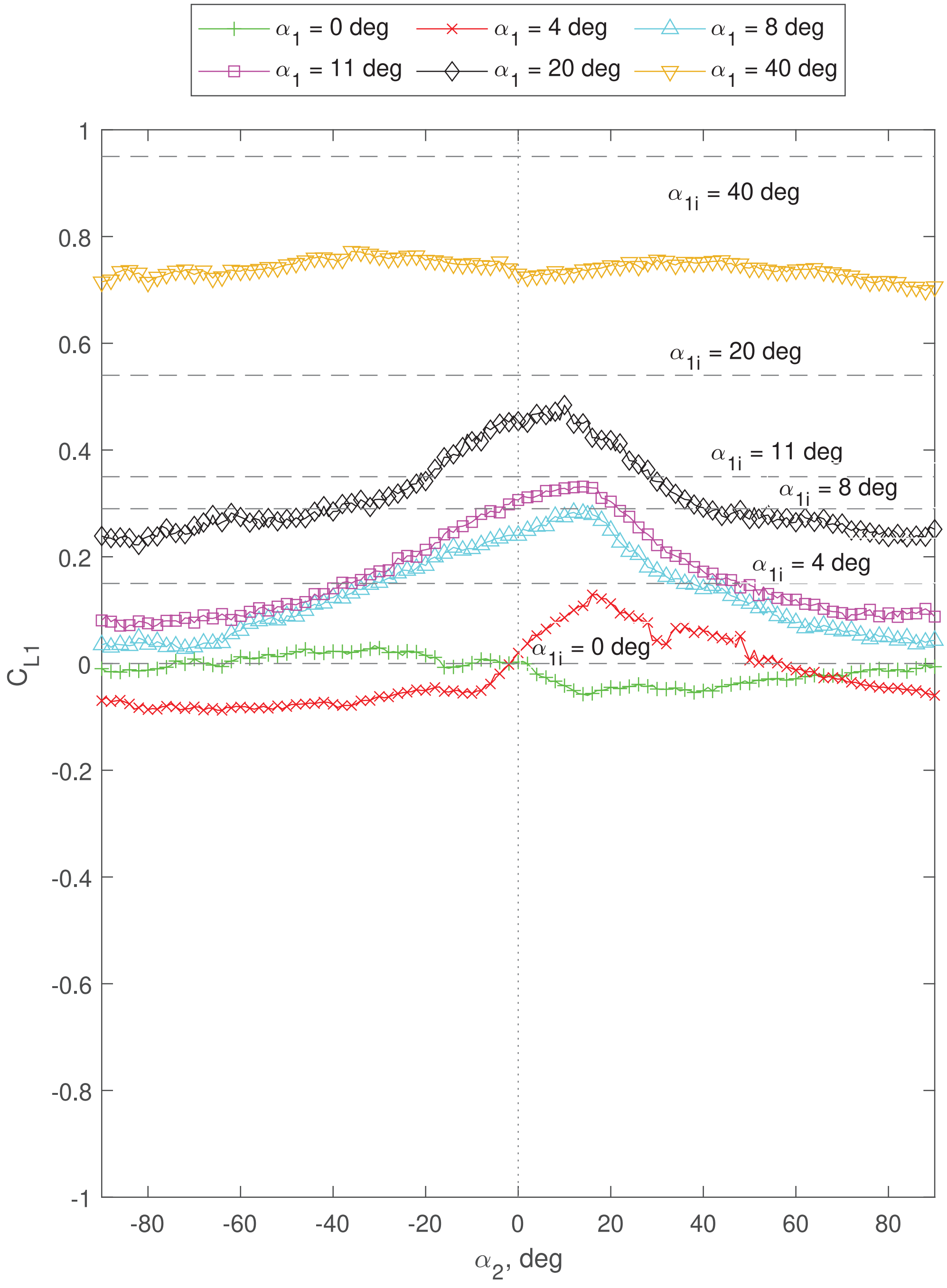

Figure 4.16: C_{L1} vs α_2, Re = 20,000.

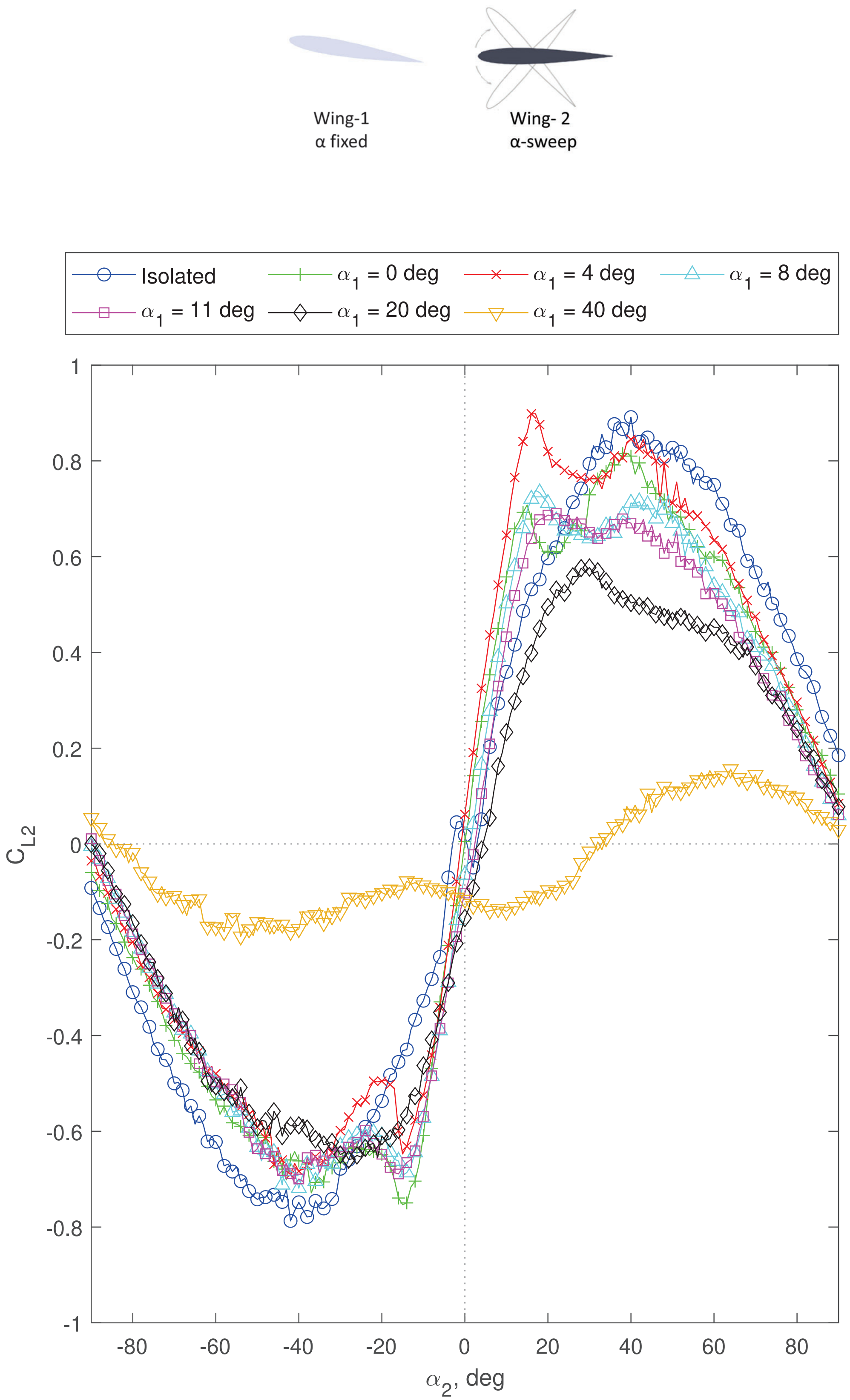

Figure 4.17: C_{L2} vs α_2 for Wing-1 held at different angles of attack, Re = 20,000.

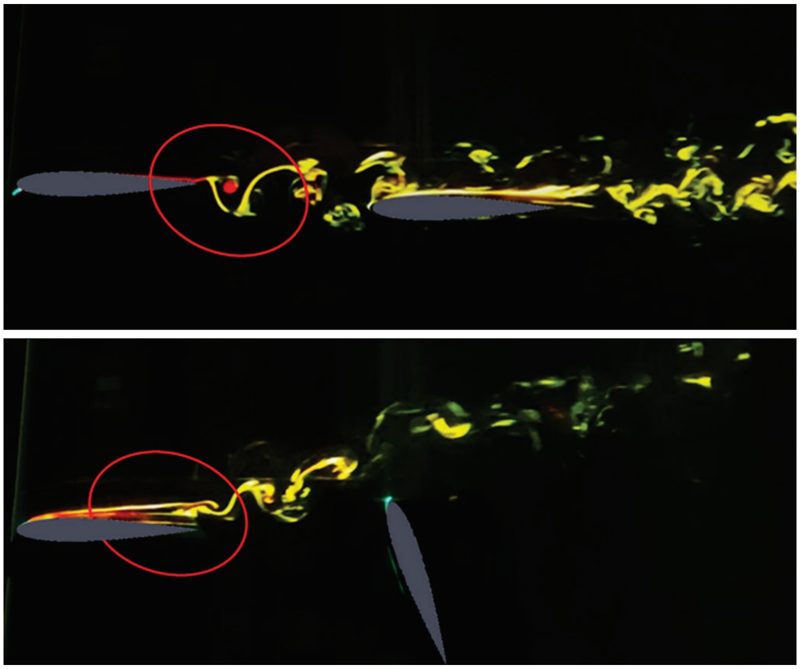

Figure 4.18: Dye flow visualization for Wing-1 at α = 0 and Wing-2 α-sweep.

4.3 Case-3: α_1 and α_2 sweep ± 90 degrees in-phase.

Both Wing-1 and Wing-2 were swept through ± 90 degrees simultaneously and their aerodynamic response is discussed below:

4.3.1 Re = 100,000

Figure 4.19 shows lift response of both Wing-1 and Wing-2 as a function of the angle of attack and data was also compared to the isolated wing. The results show that there was minimal change in lift, the slope of lift curve, maximum lift coefficient, and stall angle for Wing-1 compared to the isolated case. The stall of Wing-1 exhibited leading edge stall behavior and a distinguishable secondary stall was also observed. In contrast, the lift response of Wing-2 was significantly altered at all angles of attack. For the pre-stall angles, Wing-2 produced less lift as compared to Wing-1. The stall was delayed up to 20 degrees with a trailing edge stall characteristics. Phase reversal occurred for Wing-2 in the post-stall region. The increase in lift of Wing-1 from $\alpha = 20$ to 40 degrees led to a decrease in the lift produced by Wing-2. Subsequently, after reaching the secondary peak, as the lift of Wing-1 reduced, the lift of Wing-2 increased. The reduction in lift of Wing-2 in the wake of Wing-1 at small angles of attack can be attributed to the downwash, wake trajectory, and velocity deficit, while at higher angles of attack, it is dictated by the velocity deficit and reverse flow between the wings as discussed earlier. These effects are also coupled with an increase in turbulence intensity which changes the laminar separation, transition, and formation of separation bubble.

Figure 4.21 shows the trajectory of C_{L1} and C_{L2} with the change in the angle of attack. At low angles, simultaneously increasing the incidence of both wings resulted in increased lift for Wing-1 and Wing-2, however, the lift slope was much lower for Wing-2. Once Wing-1 reached the stall angle, the lift of Wing-2 became nearly constant. The secondary stall and two-celled separation behavior on Wing-1 (discussed in Chapter 3) correlated with the stall of Wing-2. Further increasing the angle of attack led to phase reversal in the lift response for both wings. Figure 4.20 presents the drag of Wing-1 and Wing-2 in comparison to the isolated wing. At approximately 20 degrees, when the lift of Wing-2 started to decrease, its drag also

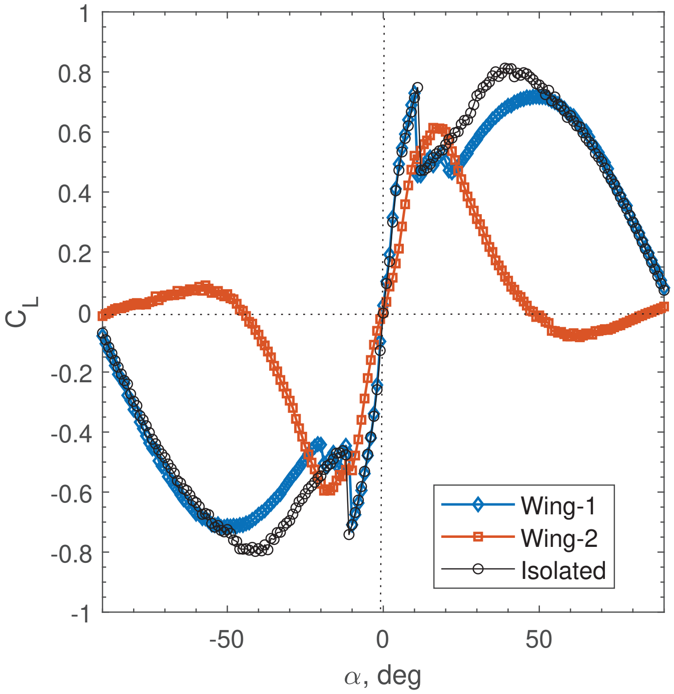

Figure 4.19: C_L vs α for Wing-1 and Wing-2 fixed at same angles of attack, Re = 100,000.

decreased and attained negative values beyond $\alpha > 40$ degrees. It should be noted that the simultaneous angle of attack sweep of Wing-1 and Wing-2 in the present configuration differs from conventional two wings mounted to a fuselage. In the latter case, at higher angles, the rear wing leaves the wake of the front wing due to positioning. In the present configuration, the suction and pressure sides of Wing-1 and Wing-2, respectively, face each other, resulting in lower pressure under Wing-2 and higher pressure over Wing-1.

4.3.2 Re = 20,000

The simultaneous angle of attack sweep of both Wing-1 and Wing-2 yielded intriguing results, as depicted in Figures 4.23 and 4.24. For Wing-2, the nonlinear behavior near zero degrees observed in the isolated wing case was eliminated in the tandem configuration. However, this nonlinearity persisted for Wing-1. A reduction in lift curve slope was evident at $\alpha = 5$ degrees for both wings, analogous to the isolated case. Notably, a second inflection point manifested around $\alpha = 20$ degrees, beyond which the response of the two wings diverged. As the angle of attack continued to increase, lift generated by Wing-1 progressed

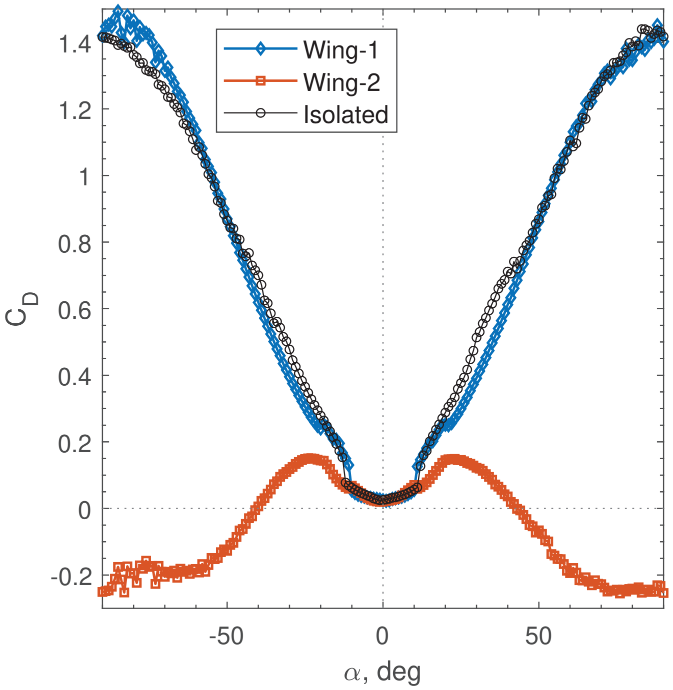

Figure 4.20: C_D vs α for Wing-1 and Wing-2 held at same angles of attack, Re = 100,000.

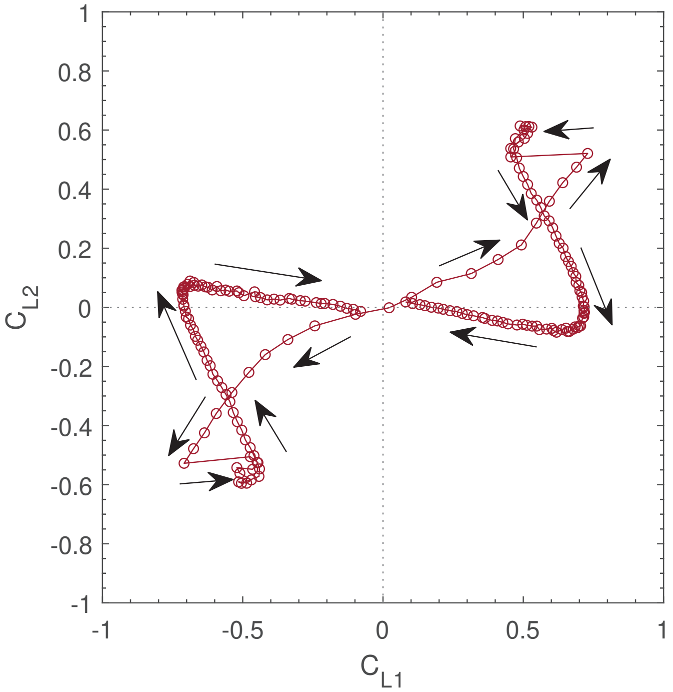

Figure 4.21: C_{L1} vs C_{L2} at same angles of attack, Re = 100,000.

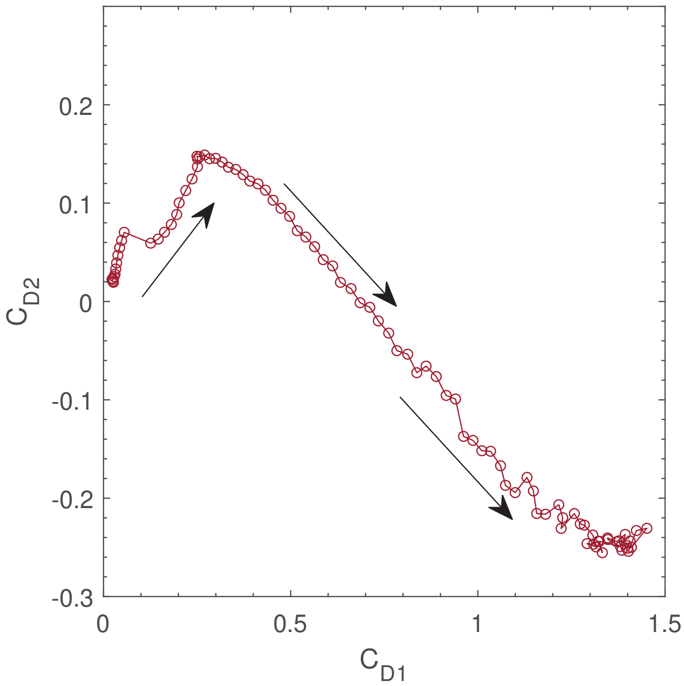

Figure 4.22: C_{D1} vs C_{D2} at same angles of attack, Re = 100,000.

further, while Wing-2 exhibited a phase reversal, with lift diminishing. Thus, at angles above α = 20 degrees, the aerodynamic response of Wing-1 and Wing-2 was inverted with respect to changes in the angle of attack. This opposed behavior was identical for both positive and negative angle sweeps. The flow visualization in Figure 4.25 demonstrates that at higher angles of attack, the pressure side of Wing-2 is subjected to the lower pressure region on the suction side of the upstream Wing-1. This pressure lowering on the pressure surface of Wing-2 results in a continued reduction in lift with an increase angle of attack for both wings. To confirm this behavior, fluorescein dye was injected near the leading edge of Wing-2, and its movement towards Wing-1 verified the adverse pressure gradient forming between the wings.

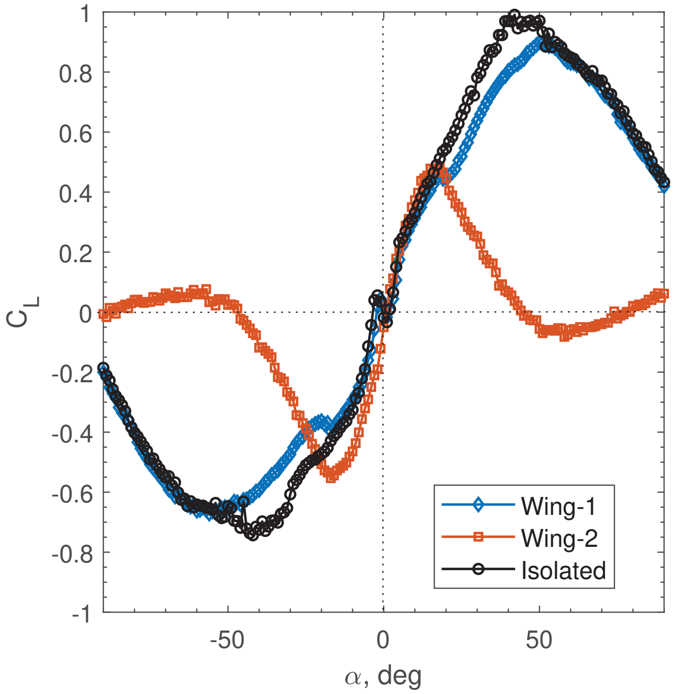

Figure 4.23: C_L vs α for Wing-1 and Wing-2 fixed at same angles of attack, Re = 20,000.

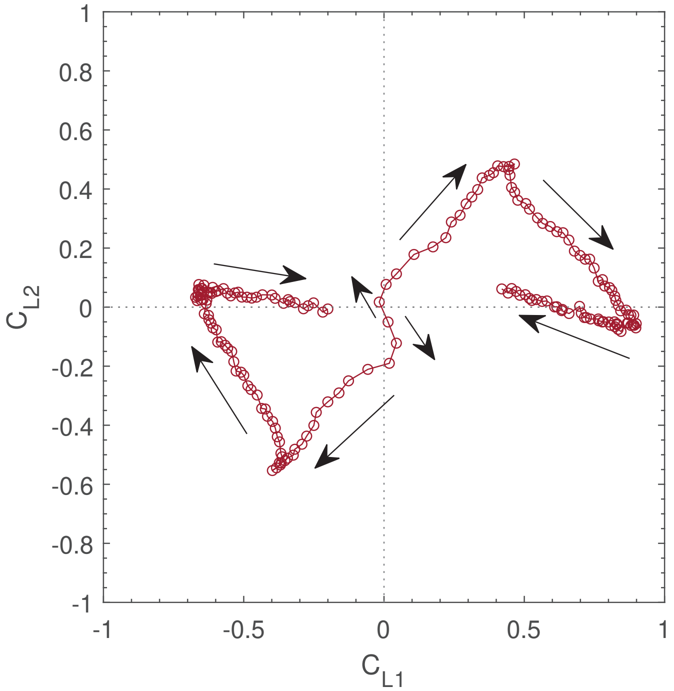

Figure 4.24: C_{L1} vs C_{L2} at same angles of attack, Re = 20,000.

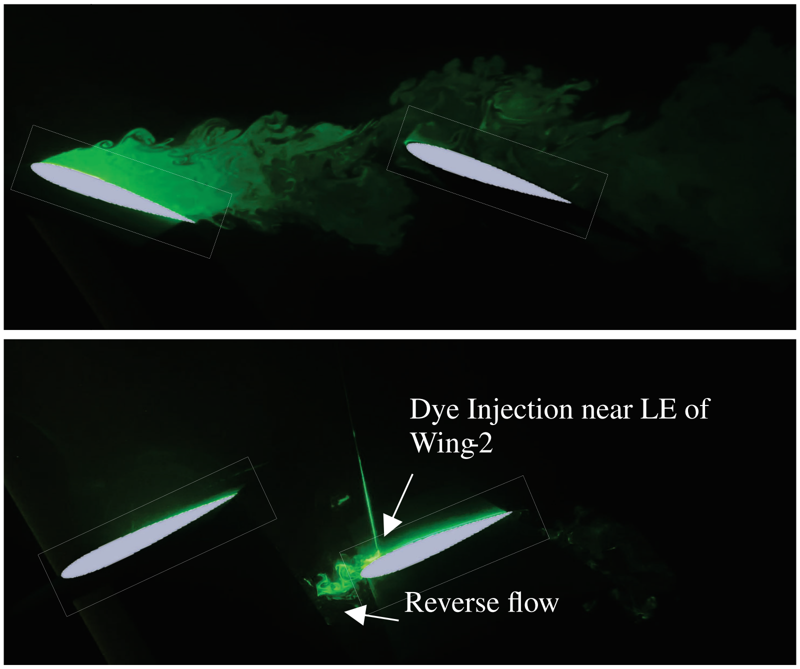

Figure 4.25: Flow visualization at post-stall angles of attack for both Wing-1 and Wing-2, Re = 20,000.

The coefficient of moment at quarter-chord pitching moment ($C_{mc/4}$) generally conformed to the changes in lift across the different tandem wing configurations and angles of attack. When operating in the wake of the upstream wing, the downstream wing exhibited reductions in C_m compared to isolated conditions, consistent with the decreased lift generation. The stall and secondary stall characteristics were reflected in the pitching moment curves. However, in the present tandem wing cases, the pitching moment data does not provide significant additional insight into the aerodynamic interactions beyond that already gleaned from the lift and drag results. For completeness, the pitching moment coefficients are included in Appendix D, but have not been incorporated into the main body of the text since they do not further elucidate the underlying physics of the tandem wing couplings. The lift and drag measurements sufficiently capture the salient features and trends of the tandem wing aerodynamics.

4.4 Aerodynamic Performance of Wings in Tandem

The lift-to-drag ratio (L/D) is an important aerodynamic metric for evaluating wing performance. As a dimensionless parameter, L/D quantifies the aerodynamic efficiency of a wing, with higher values indicating greater efficiency through producing more lift per unit drag. For tandem wing configurations, it is insightful to examine the combined L/D of the wings compared to an isolated wing case. Analyzing these impacts can provide an understanding of how the presence of a downstream wing affects the trade-off between lift generation and drag production. This section presents the L/D ratios of the tandem wings for the three test cases discussed previously. The L/D was calculated at each angle of attack for all combinations of Wing-1 and Wing-2 angles of attack. For comparison, the isolated wing L/D was also determined at each angle of attack. This allows an assessment of whether the tandem configuration improves or degrades the overall aerodynamic efficiency relative to the L/D of the single wing. L/D for the tandem wing was calculated by using the following relation:

$$\frac{L_{total}}{D_{total}} = \frac{C_{L1} + C_{L2}}{C_{D1} + C_{D2}} \tag{4.4}$$

Figures 4.26, 4.27, and 4.28 present the lift-to-drag ratios for case 1, 2 and 3, respectively. The results demonstrate that at low and pre-stall angles of attack, the overall L/D of the tandem wings was lower than that of the isolated wing. However, an aerodynamic benefit of the tandem configuration was observed in the post-stall region, approximately between the stall angle and 40 degrees angle of attack. Beyond 40 degrees, the L/D matched the isolated wing value irrespective of the angle of attack combinations tested for the two wings.

These findings suggest the tandem arrangement can improve aerodynamic efficiency with optimal angle of attack configurations between Wing-1 and Wing-2. The tandem wings also appear advantageous for delaying stall and increasing L/D at post-stall conditions. The lower L/D at small angles of attack implies greater induced and/or profile drag and reduced lift due to the fact that Wing-2 lift generation is affected by the downwash from Wing-1. Further research into the balance of lift augmentation and drag reduction mechanisms could provide greater insight into maximizing the aerodynamic benefits across operating conditions. Detailed flow field and pressure data may also elucidate the physical phenomena responsible for variations in tandem performance.

Overall, the results demonstrate that the tandem configuration can improve aerodynamic efficiency beyond stall angles but leads to a penalty at low angles. This suggests potential for exploiting tandem wings at high lift coefficients for applications such as takeoff and landing. However, the cruise regime may experience a detriment in performance. Careful design of the wing shapes and positions could help mitigate these deficiencies and extend the operational envelope with aerodynamic benefits.

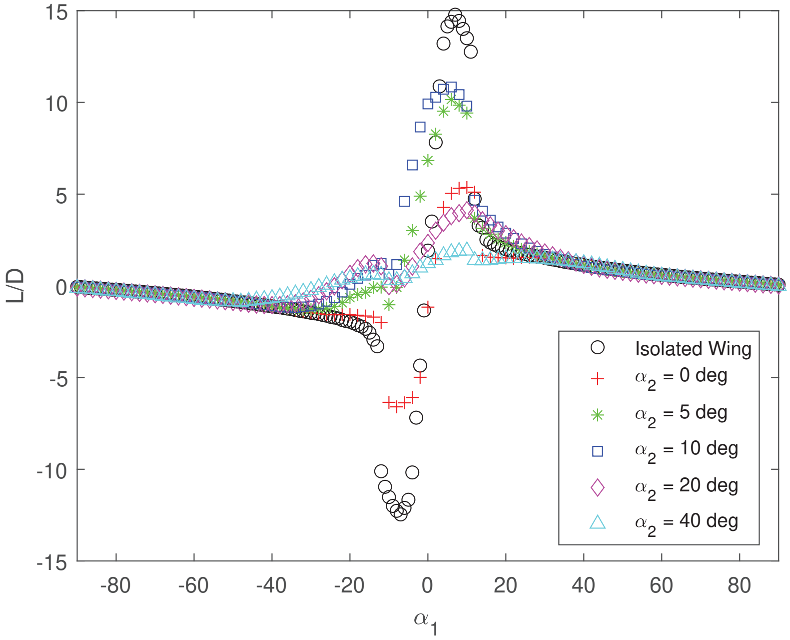

Figure 4.26: L/D vs α_1 for wings in tandem configuration at different fixed α_2, Re = 100,000.

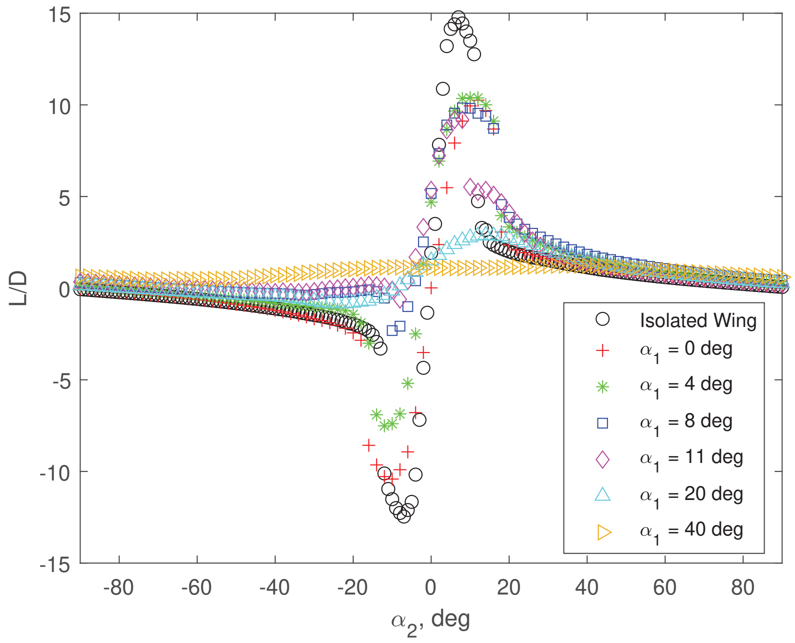

Figure 4.27: L/D vs α_2 for wings in tandem configuration at different fixed α_1, Re = 100,000.

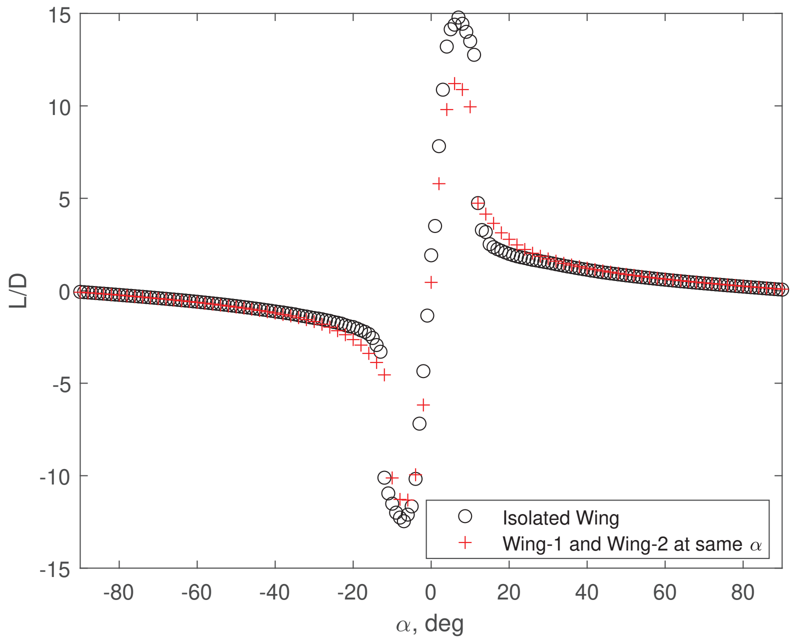

Figure 4.28: L/D vs α for wings in tandem configuration of both wings at same angles of attack, Re = 100,000.

4.5 Chapter Summary

This chapter presented an extensive experimental study on the aerodynamics of finite aspect ratio rectangular wings in close tandem configuration. The work systematically investigated three different test cases involving combinations of the upstream and downstream wing angles of attack. The comprehensive dataset provided unique insight into the complex aerodynamic interactions that manifest between wings positioned in close proximity.

In the first case, the angle of attack of the upstream wing was varied from 0 to ±90 degrees while the downstream wing was held at fixed angles. For the upstream wing, the presence of the downstream wing caused decreased maximum lift, earlier stall, and reductions in the secondary lift peak compared to isolated conditions. A distinctive secondary stall was observed around 21 degrees angle of attack. This secondary stall differed from the primary stall, exhibiting a concurrent decrease in both lift and drag. The downstream wing enabled decreased drag across angle of attack ranges. The response of the downstream wing was dictated by the wake characteristics of the upstream wing, including downwash, velocity deficit, and turbulence. Simple downwash models failed to fully predict the performance, emphasizing the interconnected roles of multiple factors.

The second case involved sweeping the downstream wing through ±90 degrees with the upstream wing fixed at various pre-stall, near stall, and post-stall angles. The downstream wing experienced altered stall behavior, delayed stall to higher angles, and nonlinear lift response depending on the upstream wing operating condition. The wake turbulence and velocity deficit generated by the upstream wing controlled the interactions. The upstream wing showed increased lift up to downstream wing stall, followed by diminished lift and sudden stall.

In the third case, both wings were swept simultaneously through the angle of attack range. The upstream wing exhibited negligible effects compared to isolated conditions. However, the downstream wing revealed reduced lift slope, delayed stall, and eventually lift reversal at higher angles. This opposed lift response was linked to the pressure coupling between the wings.

Wake surveys proved critical in elucidating the velocity deficit and turbulence generated by the upstream wing and encountered by the downstream wing. Surface oil flow visualizations illustrated modifications to the separation bubbles, transition, and stalled flow patterns on both wings due to the interactions.

Analysis of the total lift-to-drag ratio showed detriments at low angle of attack but improvements in the post-stall regime for the tandem configuration. This highlights potential aerodynamic benefits at high lift coefficients relevant to takeoff and landing.

Overall, the results demonstrated the sensitivity and complexity of tandem wing aerodynamics across operating conditions. The wings encounter coupled effects that cannot be decoupled into isolated parameters. Careful analysis of the multifaceted interactions and tradeoffs is necessary for practical implementation. The work provided extensive datasets to advance the understanding of finite aspect ratio tandem wing aerodynamics across a wide parameter space. Further research can build upon these findings to help extend the performance envelopes and capabilities of interacting lifting surfaces.

Chapter 5

Secondary Stall in Tandem Configuration

One of the most salient features of wings in tandem configuration was the occurrence of a secondary stall, a phenomenon not previously documented in the literature. This chapter elucidates this secondary stall behavior through a systematic investigation of the aerodynamic response of the front wing in the presence of the rear wing. The rear wing was positioned at varying streamwise separations within the wake and its aspect ratio was methodically varied. The focus is on the characteristics of secondary stall. The aspect ratio of the rear wing was modified utilizing a vertical traverse mechanism. The presence of the rear wing profoundly altered the post-stall performance of the front wing, engendering a secondary stall typified by precipitous declines in lift and drag under specific combinations of front wing angle of attack and wing spacing. Wind tunnel experimentation and qualitative flow visualization were employed to examine the impact of wake interactions between the tandem wings on the aerodynamic response and performance of the front wing. The results furnish enhanced fundamental comprehension of the influence of downstream bodies immersed in the wake on the global performance of tandem wing configurations. This research into secondary stalls contributes novel knowledge to the extant body of literature on tandem wing aerodynamics. The experimental setup used to investigate the secondary stall is shown in Figure 5.1.

5.1 Secondary stall in Tandem Configuration and Effect of Stagger

Figure 5.2 and Figure 5.3 show time-averaged lift and drag versus the angle of attack of Wing-1. α_1 was varied from -5 to 90 degrees, while Wing-2 was fixed at $\alpha_2 = 0$. Stagger

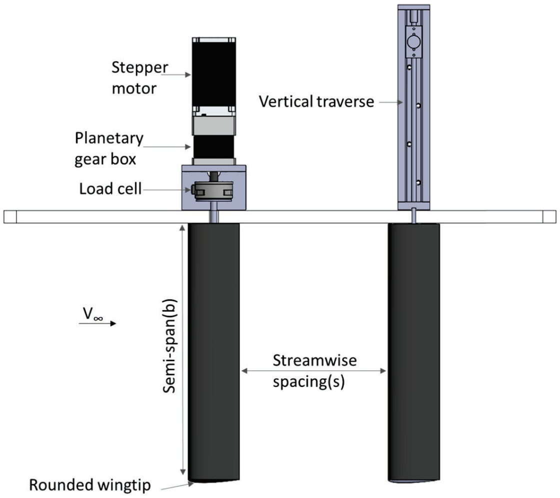

Figure 5.1: Wind tunnel setup to investigate the secondary stall.

between the wings was varied from s= 1c-4c with no vertical gap. The results are being compared with the isolated wings for reference. The findings highlight that the presence of Wing-2 had a negligible impact on the stall angle, mean lift, and drag coefficients during pre-stall angles of attack. However, a significant change in post-stall behavior was evident, as illustrated in Figure 5.2b and 5.2d. The force data shows a sudden reduction in aerodynamic forces at a critical angle of attack for each wing spacing. This abrupt decrease in both lift and drag at higher angles of attack is referred to as a "Secondary stall in tandem configuration." This distinct secondary stall contrasts with the conventional primary stall, where the decrease in lift is accompanied by an increase in drag. Notably, the secondary stall was not abrupt for spacings of 1c, 1.5c, and 4c, but it was pronounced and sudden for spacings of 2c to 3.5c. A notable drop of up to 15% in lift was recorded for a spacing of 2.5c. Du et al. [99] observed a secondary stall for a single NACA0018 airfoil tested in an open jet wind tunnel. Their analysis, employing surface flow visualization, led them to infer that the expansion of the wake in an open jet tunnel facilitated the movement of the separation point from the suction side to the pressure side of the wing. This conclusion was substantiated when the same wing was tested in a closed jet wind tunnel, where the secondary stall did not manifest. Similarly, Worasinchai et al [100] observed a secondary stall across four different airfoils (NACA0012, SG6043, SD7062, and DU06-W-200) in a partially open test section where the wake could expand. The secondary stall was not observed for isolated wings and airfoils when aerodynamic coefficients were computed at low and very low Reynolds numbers, both computationally and experimentally [24, 43], in closed test section wind tunnels and water tunnels. It is important to mention that the present investigation was conducted in a closed test section wind tunnel, and the secondary stall phenomenon was not exhibited for an isolated single wing, congruent with existing literature. The secondary stall only occurred when Wing-2 was positioned in the wake of Wing-1, i.e. in the tandem configuration. It was therefore inferred that aerodynamic interference due to Wing-2 was responsible for inducing the secondary stall.

Lift to drag ratio of Wing-1 in tandem configuration is shown in Figure 5.4 (a). The maximum L/D ratio was observed in the α range of 5 to 8 degrees, and it sharply decreased at the stall, reaching zero linearly due to a simultaneous decrease in lift and an increase in drag at higher angles of attack. A slight increase in the maximum L/D was observed for tandem configurations as compared to isolated wing. Interestingly, there was no effect of secondary stall on the lift-to-drag ratio. The variance in lift signal at each angle of attack was calculated and is shown in Figure 5.4(b). Variance represents the dispersion of the data and a smaller value of variance represents smaller fluctuations in the lift data or less unsteadiness. It was observed that for the isolated wing, the variance in the data increased at the stall angle and started to diminish gradually after approximately $\alpha = 41$ degrees. The secondary stall in tandem configurations resulted in a sudden drop of the C_L variance, however, for s = 1c the variance was less even for the pre-stall angles of attack.

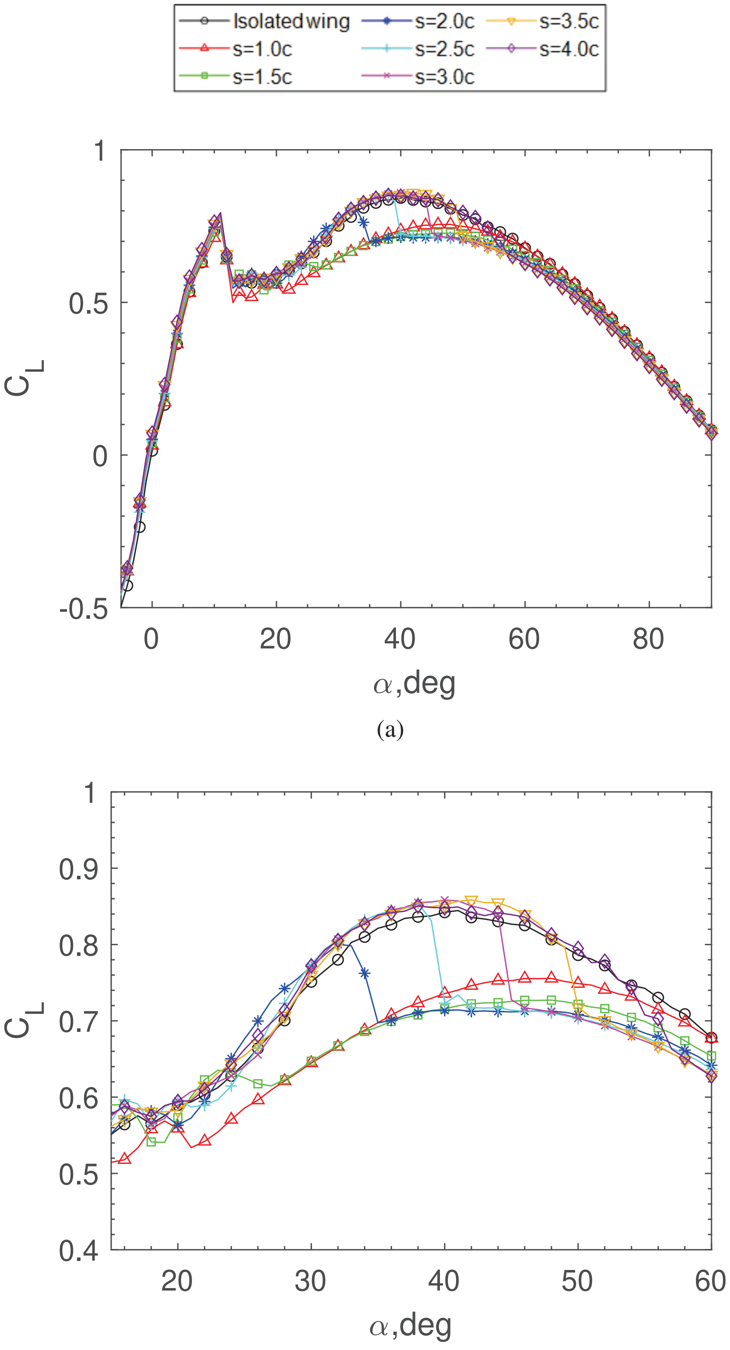

(a)

(b)

Figure 5.2: C_L vs α for Wing-1, Re = 100,000.

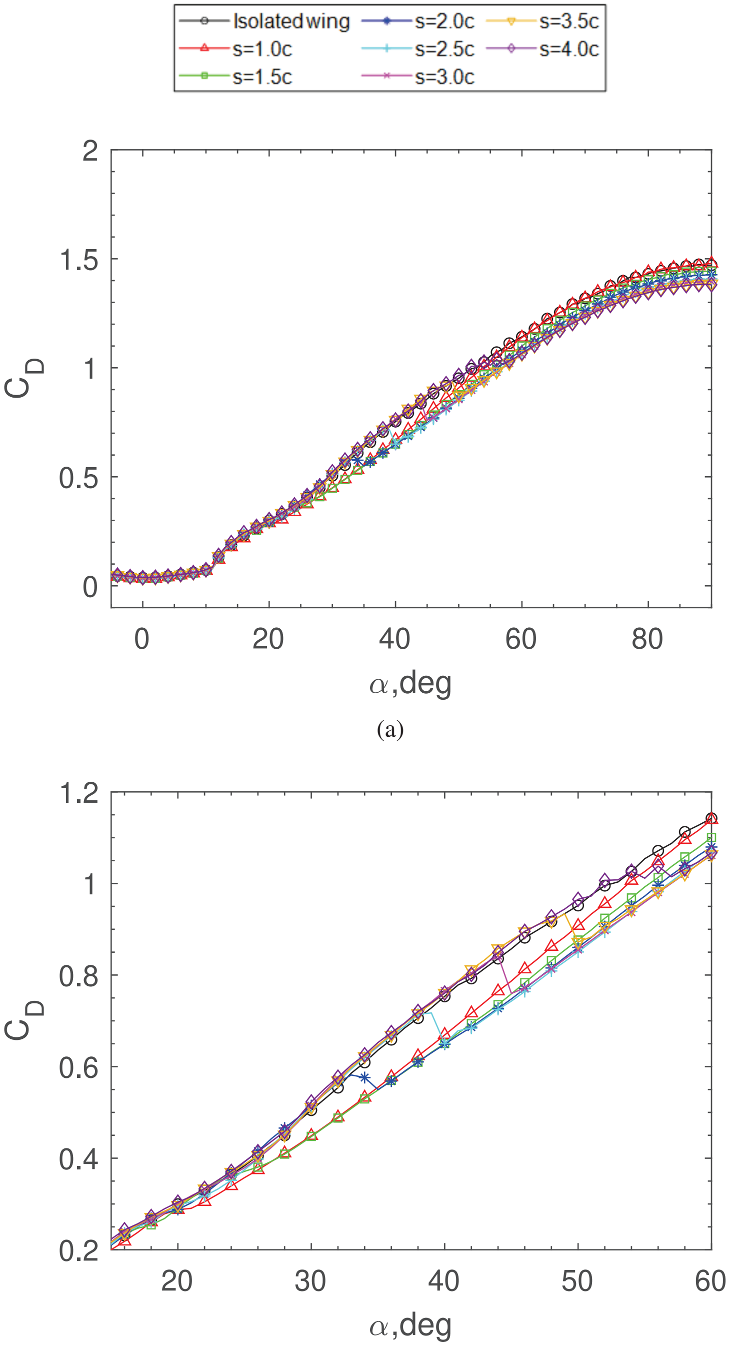

(a)

(b)

Figure 5.3: C$_D$ vs α for Wing-1, Re = 100,000.

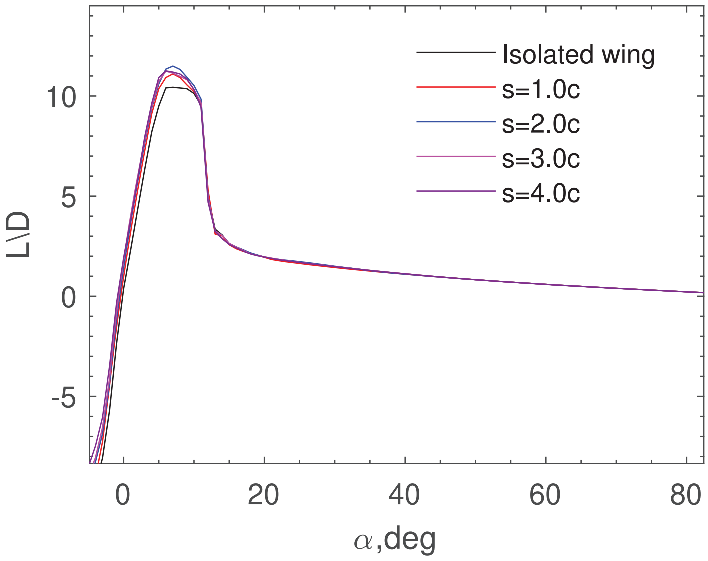

(a)

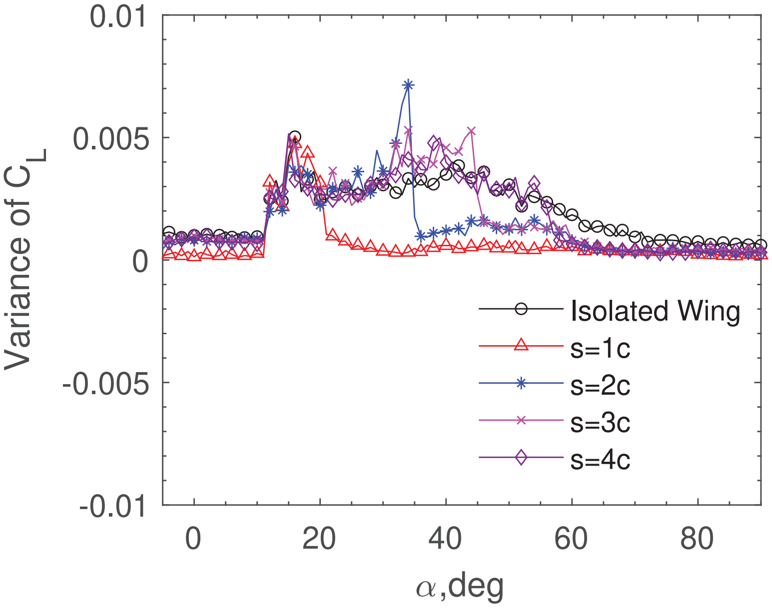

(b)

Figure 5.4: Lift-to-drag ratio Wing-1 in tandem configuration and variance in lift vs angle of attack.

To further investigate this, the power spectrum of the force signals for wings in tandem was calculated using MATLAB, and the results are shown in Figure 5.5. Results were compared with the isolated wing. The power spectrum of the isolated wing at α = 15 degrees shows a fundamental frequency of 2 Hz with a noted shift to 6 Hz for the same wing in tandem configuration when Wing-2 was placed at $\alpha = 0$ in its wake. Some low amplitude broadband spectral energy is evident from 26 Hz to 62 Hz for the wings in tandem. However, the pedestal is not measurable for the isolated wing in the same frequency range (Figure 5.5a).

Figure 5.5b shows the power spectrum of the wing at α = 32 degrees. The isolated wing at this angle of attack had the fundamental frequency at 7Hz and some subharmonic interaction, but in the tandem configuration, both subharmonic and higher harmonics appeared in the spectra. Wing-2 experienced impingement of the shear layer shed from Wing-1 that resulted in multiple high amplitude peaks ranging from 35Hz to 50Hz, which are visible in Figure 5.5b. The onset of the drop in lift at this angle of attack is associated with the higher energy of the fluid dynamic structures shedding off Wing-1. At α = 33 degrees, the decay of energy of Wing-1 became evident (Figure 5.5c), while Wing-2 spectra continued to show the effects of the impingement of the wake of Wing-1. At α = 34 degrees, no dominant frequencies in spectra of Wing-1 were observed (Figure 5.5d), and the changes in C_L became smooth (Figure 5.4).

5.2 Relationship between the angle of attack of Wing-1 at which the secondary stall occurred and streamwise spacing between the wings.

The relationship between the critical angle of attack and streamwise spacing is shown in Figure 5.6 (a). The critical angle of attack and the spacing between the wings had an almost linear relation particularly for s = 2c to 4c as highlighted by the dotted line in Figure5.6 (a). The projected distance of Wing-1 in the direction of flow was calculated using the trigonometric relationship $csin(\alpha)$ and it was found that the secondary stall occurred whenever the distance between the leading edges of the Wing-1 and Wing-2 was around 18% of the streamwise projected distance of Wing-1 as shown in Figure 5.6(b).

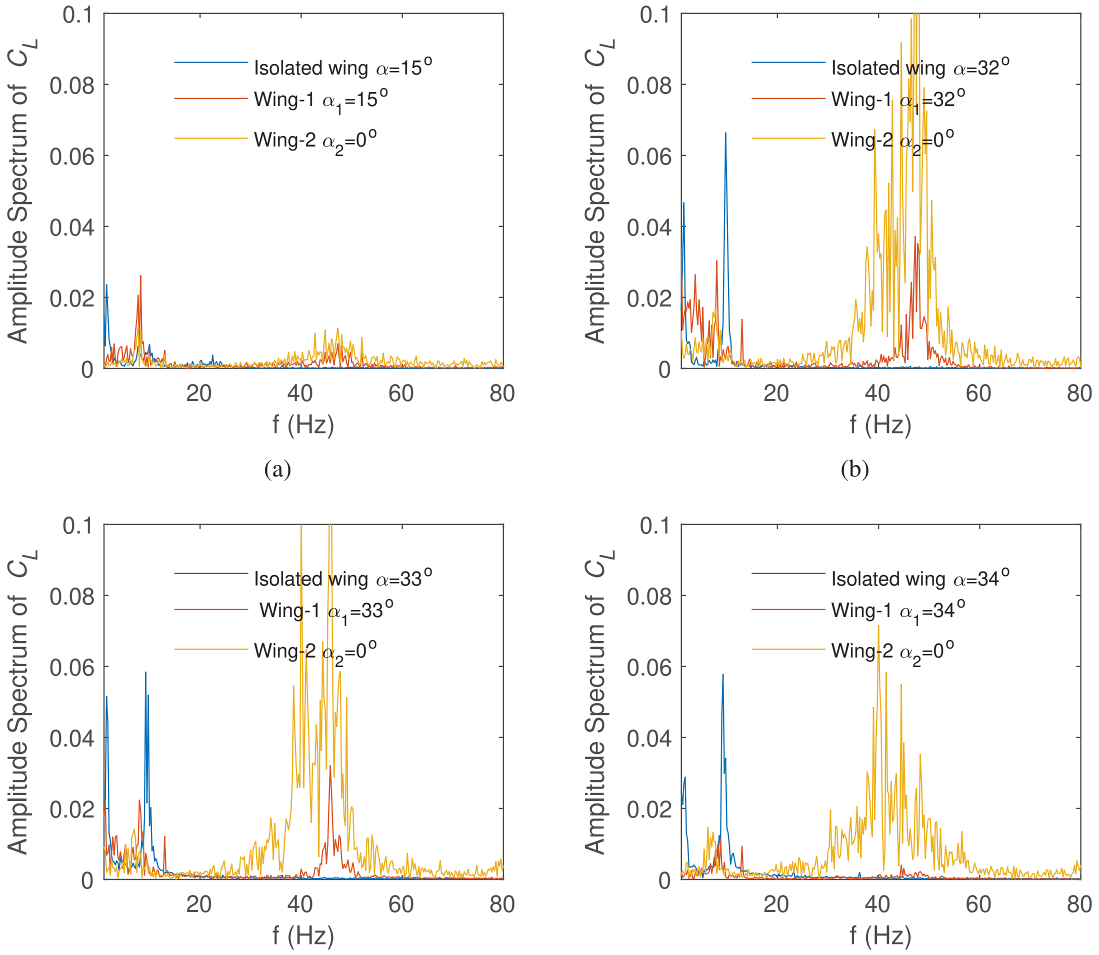

(a) (b)

(c) (d)

Figure 5.5: Amplitude spectrum of force signal for isolated wing and in tandem configuration at s = 2c.

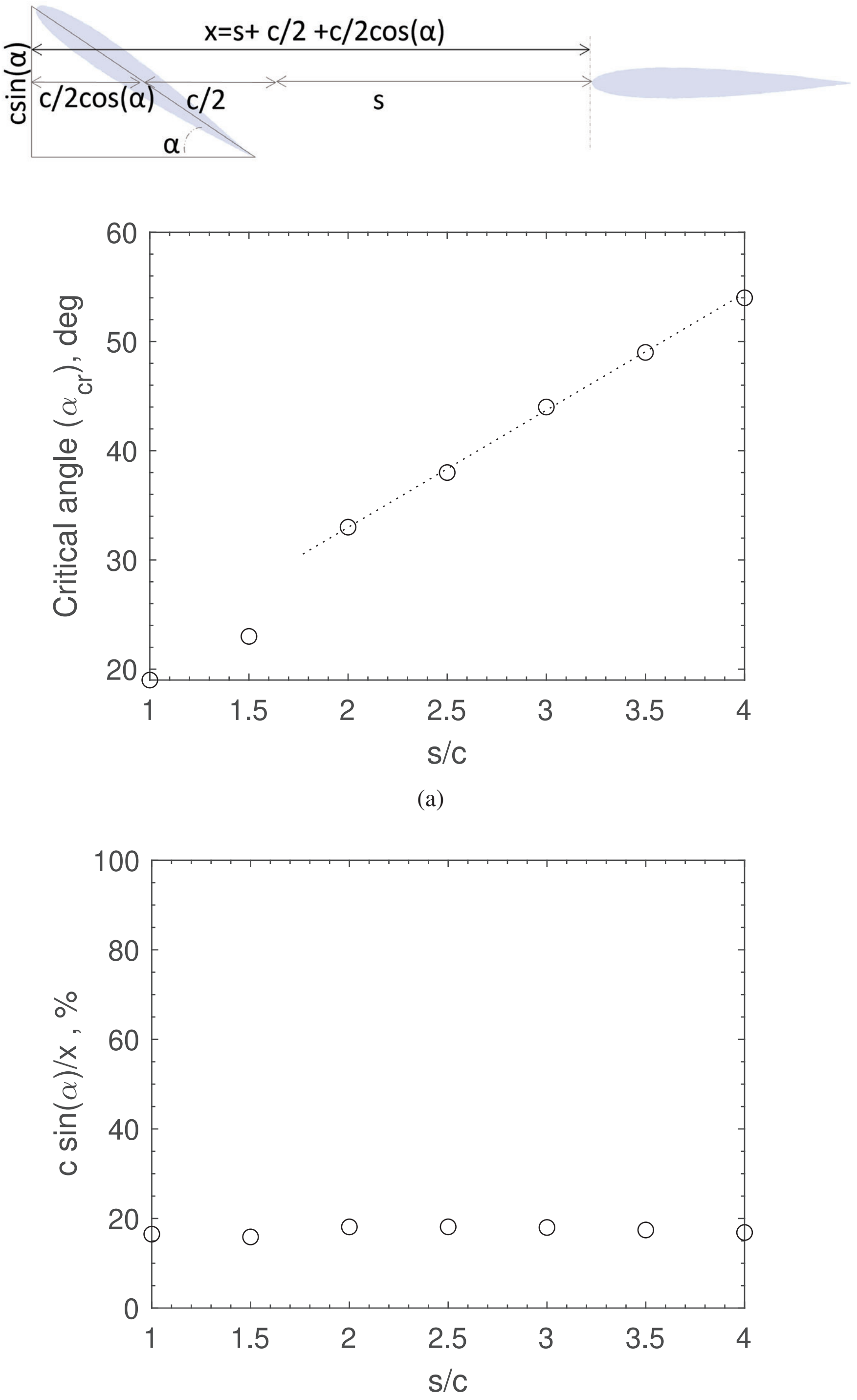

(a)

(b)

Figure 5.6: Relationship between the wing projected thickness and wing spacing when secondary stall occurred.

5.3 Secondary stall and three-dimensional behavior of Wing-1

To investigate the dependence of the secondary stall on the aspect ratio of Wing-1, two identical wings of aspect ratio 4 and chord length 7.6cm were utilized. Wings were made from PLA utilizing 3D printing technology. Tests were carried out for the aspect ratio 4 wing in isolation and in tandem configuration. To isolate the effect of wing tip vortices, a 17cm round plate was attached to the tip of Wing-1. The lift vs angle of attack for wings with and without the end plate is shown in Figure 5.7 at a streamwise spacing of s = 2c. The data is also compared with AR=6 wings in tandem for the same spacing. The results show that the secondary stall did not occur for Wing-1 having AR = 4 when in tandem configuration, however, the effects of decreasing aspect ratio were noticeable and lift values were slightly less for the angle of attack range of 35 to 60 degrees approximately. Installation of an endplate on Wing-1 produced an exaggerated secondary peak in the isolated lift curve, and the secondary stall phenomenon recurred with Wing-2 positioned in the wake. This substantiates the two-dimensional nature of the secondary stall arising from wake interactions of Wing-1, with tip vortices playing no direct role.

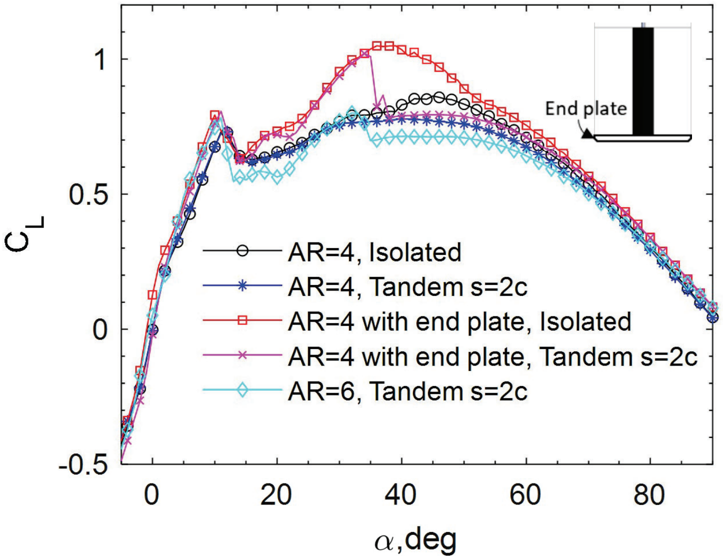

Figure 5.7: Dependence of the secondary stall on the aspect ratio of Wing-1.

5.4 Effect of Reynolds number

The dependency of secondary stall on Reynolds number was investigated by varying the wind tunnel speed to achieve lower Reynolds numbers. Experiments were conducted for tandem configuration for the streamwise spacing between the wing s = 2.0c. While the anticipated effects of decreasing Reynolds numbers, such as earlier stall onset and alterations in C_{Lmax}, were evident, the secondary stall behavior remained unaffected by these changes in Reynolds number. Notably, a discrete primary stall was not observable at the lowest Reynolds number tested (Re = 20,000) and the only stall evident corresponded to the secondary stall. This stall was not present for the isolated wing at this Reynolds number as shown in Figure 5.8(b). This observation leads to the inference that the secondary stall is primarily an inviscid phenomenon and hence independent of the Reynolds number.

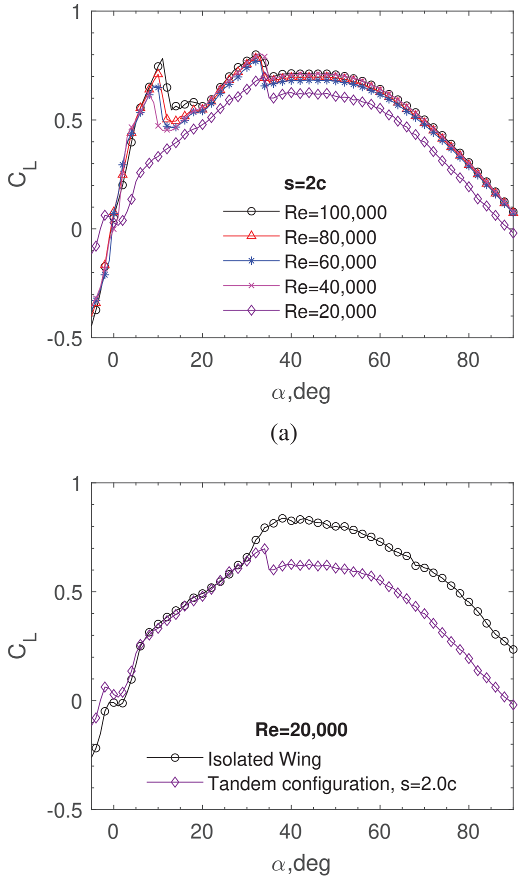

(a)

(b)

Figure 5.8: Effect of Reynolds number on the secondary stall.

5.5 Effect of the Aspect ratio of Wing-2

Wind tunnel tests were carried out by reducing the span of Wing-2 to achieve aspect ratios of 4 and 2 at different streamwise spacing. The results revealed that the behavior of Wing-1 in the tandem configuration and the secondary stall were not affected by the aspect ratio change of Wing-2.

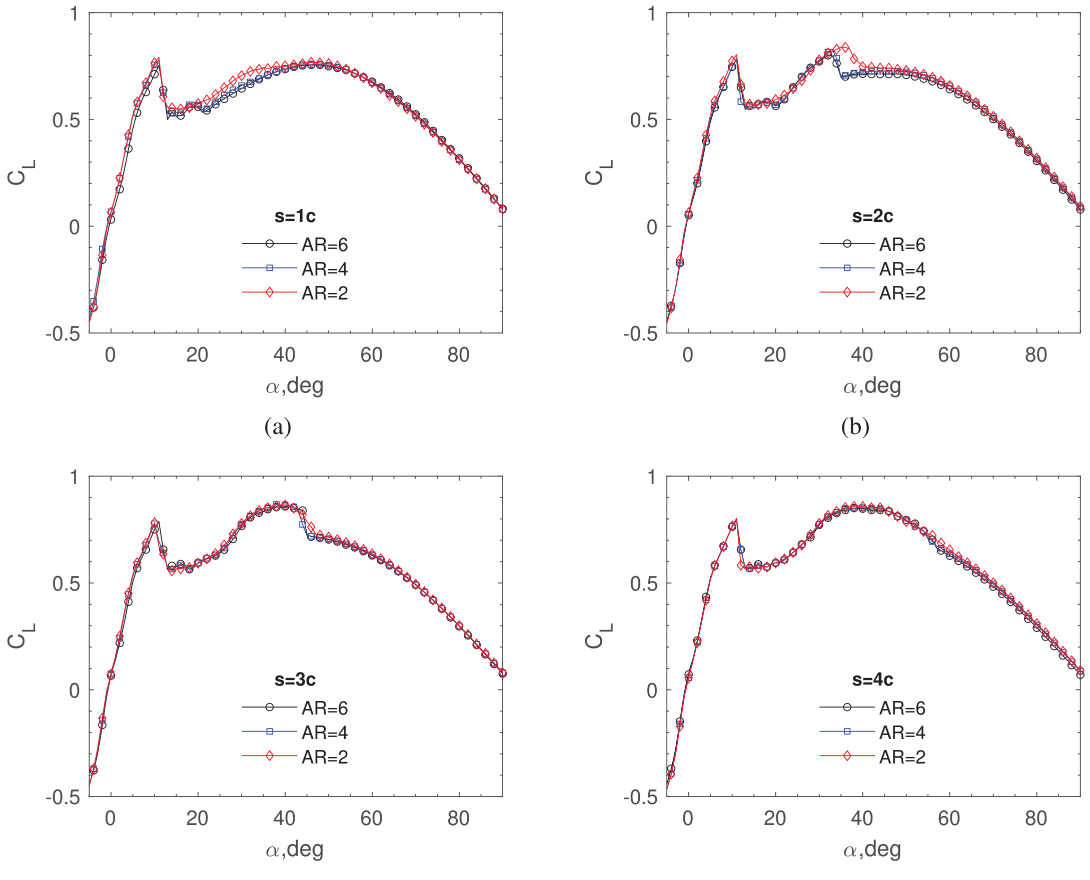

(a) (b) (c) (d)

Figure 5.9: Dependence of secondary stall on the aspect ratio of Wing-2.

5.6 Flow Visualization

Qualitative dye flow visualization was carried out at three angles of attack of 15, 25, and 35 deg, at a Reynolds number of 20,000 to understand the flow physics of the secondary stall as shown in Figure 5.10. At all three angles, there was massive separation on the suction side starting from the leading edge with clearly observable reverse flow from the trailing edge towards the leading edge. Alternate vortex shedding from the shear layer of the separated boundary layer and the shear layer from the trailing edge is visible in the wake. These vortices merge and form unstable Von Karman-type vortex streets with different vortical length scales [101]. The horizontal and vertical length scales of two connected counter-rotating vortices originating from the leading and trailing edges depend on the angle of attack as observed for the isolated wing cases. The length scales grew larger with increasing angle of attack. The initiation location of the vortex pairs in the wake moved upstream towards the trailing edge as the angle of attack increased [35]. For the tandem configurations, it was observed that the presence of Wing-2 prevented the two shear layers from interacting, depending on the angle of attack of Wing-1 and the spacing between the wings. Alternate vortex shedding was observed at $\alpha = 25$ deg for s = 2c and s = 3c, whereas at α=35 deg it was observed only for s = 3c. Therefore, the combination of the angle of attack and spacing results in two scenarios: a) Alternate and periodic vortex formation between the wings. and b) Suppression of vortex formation, with quasi-steady flow between the wings.

In the periodic vortex scenario, the ability of Wing-1 to produce vortical lift at high angles of attack and drag persisted unimpeded. However, when the interaction between the shear layers was precluded, reverse flow emanating from the leading edge of Wing-2 towards Wing-1 resulted in higher base pressure, consequently diminishing lift, drag, and fluctuations. Therefore, it was inferred that at high angles, Wing-1 behaved like a bluff body while Wing-2 acted akin to a detached splitter plate [102–104] when positioned at a critical distance, it suppressed the vortex shedding from Wing-1 that resulted in a sudden drop in aerodynamic forces.

The lift fluctuations of Wing-2 are visible in figure 5.11b when data was recorded at a higher sampling frequency and higher resolution of the angles of attack with no filter applied. Figure 5.11a shows the impingement of vortices onto the leading edge of Wing-2 and, consequently, fluctuation in C_L (Figure 5.11b). It is important to clarify that Wing-2, after a certain angle of attack of Wing-1, acted as a suppressant for the lift fluctuation of Wing-1 because the two shear layers originating from its leading and trailing edges cannot interact. Still, their impingement caused the fluctuation of aerodynamic loads on Wing-2. Fully separated flow on Wing-1 caused a local region of lower static pressure in front of Wing-2 which caused a reduction in drag, and reverse flow was also observed through flow visualization when Wing-1 approached ± 90 degrees. The amplitude of unsteady loads on Wing-2 increased with an increase in the angle of attack of Wing-1.

5.7 Chapter Summary

The secondary stall of an upstream wing(Wing-1) due to the presence of a downstream wing (Wing-2) in its wake was experimentally investigated using force data obtained in the wind tunnel testing and dye flow visualization in the water tunnel. The dependency of secondary stall on the angle of attack, spacing between the wings, the aspect ratio of Wing-2, and Reynolds number were also studied. The results show that the secondary stall is an inviscid phenomenon and independent of the Reynolds number and it was observed for two-dimensional and wings with higher aspect ratios (≥ 5). Wing-2 acts like a detached splitter and at the critical combination of the angle of attack and spacing between the wings, it suppresses the vortex shedding from Wing-1 when two shear layers originating from the leading and trailing edges of Wing-1 cannot interact. Consequently, a sharp and sudden decrease in aerodynamic forces and a reduction in lift fluctuation take place.

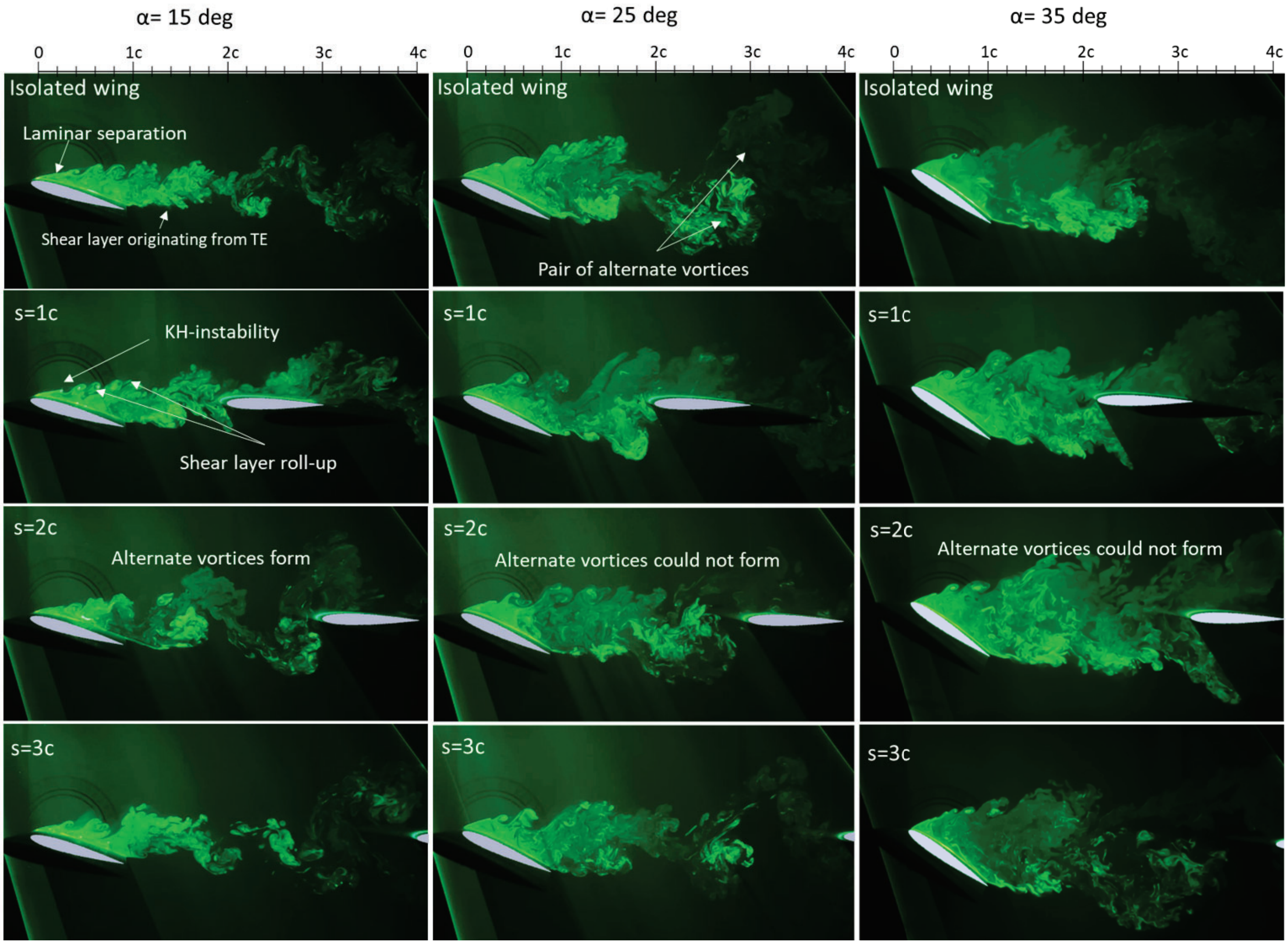

Figure 5.10: Dye flow visualization in isolation and tandem configuration.

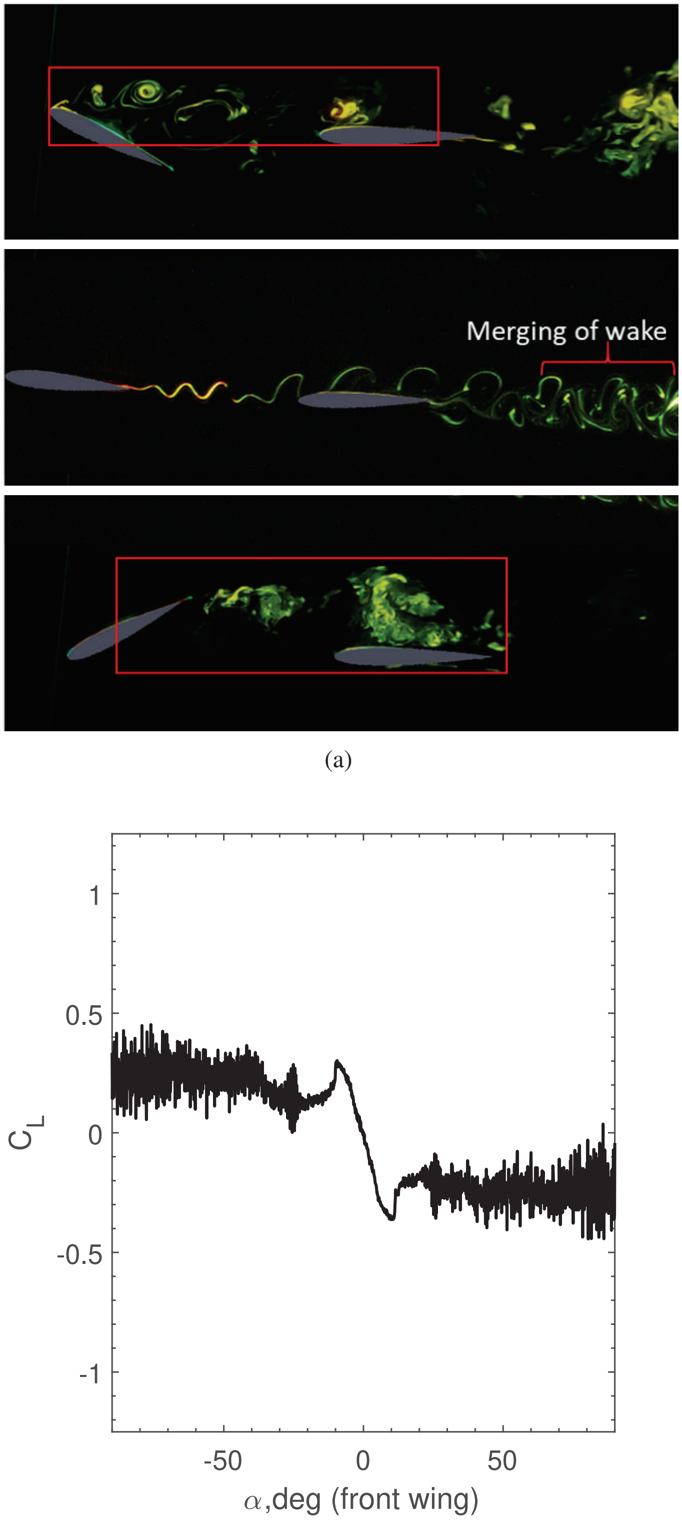

(a)

(b)

Figure 5.11: (a) Wing-2 at α = 0 and Wing-1 α-sweep of ± 90 degrees (b) Lift coefficient of Wing-2 fixed at α = 0 for Wing-1 α-sweep of ± 90 degrees at high sampling frequency (no filters) and angle of attack resolution showing unsteady loads.

Chapter 6

Effect of Stagger, Gap and Aspect ratio

This chapter includes the investigation of the aerodynamics of wings in tandem configuration at a Reynolds number of 100,000 for different streamwise spacings and vertical offsets. The aspect ratio of the front wing (Wing-1) was also varied to modify the strength and spanwise location of its tip vortex on the downstream wing (Wing-2). NACA0012 section wings with 4-inch chord lengths were used. The 3D-printed wing sections were assembled to obtain the desired aspect ratios. The wings were pitched statically from -90 to 90 degrees and data was collected at every 0.1 deg at a sampling frequency of 10 kHz and was averaged over 1,000 samples at each angle of attack. Markers were placed every two degrees to avoid clutter.

Experiments were conducted at streamwise spacings or stagger(s) of 0.5c, 1c, 1.5c, 2c, and 2.5c, and vertical gaps (G) of 0c, 0.5c, and 1c. Two cases were investigated: (a) Wing-2 at $\alpha_2 = 0$, Wing-1 α_1-sweep of ± 90 degrees, and (b) Wing-1 fixed at $\alpha_1 = 0$ degrees, Wing-2 α_2-sweep of ± 90 degrees. Aspect ratios (AR) of 3, 4, and 5 for Wing-1 were tested, with AR = 5 for Wing-2, as shown in Figure 6.1

The use of wings of 4in chord increased the blockage ratio of the test section which did not alter the overall aerodynamic behavior of the wings particularly at low angles of attack, as shown in Figure 2.6.

6.1 Effect of Aspect Ratio on the Aerodynamics of Isolated wing

Wings of different aspect ratios were tested in isolation at a Reynolds number of 100,000 to characterize their aerodynamic properties. The lift and drag coefficients as a function of angle

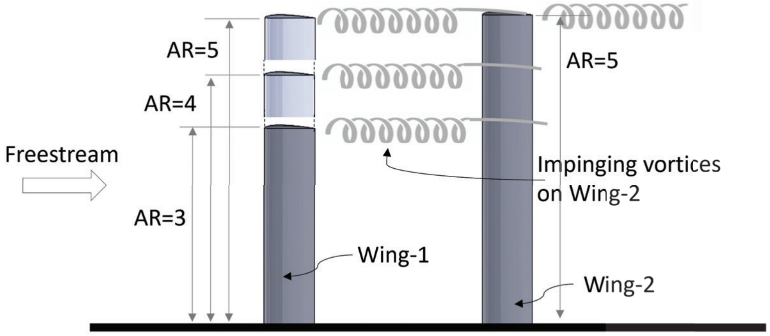

Figure 6.1: Details of Wing-1 Aspect ratios.

of attack are presented in Figure 6.2. Conventional lift curves, drag buckets, and leading-edge stall behavior were observed at all the aspect ratios investigated. A decrease in the aspect ratio resulted in a slightly decreased slope of the linear region of the lift curve and a lower maximum lift coefficient, with a small increase in the stall angle. For the AR=3 wing, the pre-stall drag was slightly higher compared to AR = 4 and 5, which was attributed to an increase in induced drag which is inversely proportional to the aspect ratio of the wing. There was a considerable difference in the aerodynamic coefficients in the post-stall angles of attack range. The reduction in aspect ratio led to decreased lift and drag coefficients after stall which was considered to be because of a lower test section blockage ratio with the lower AR wings. The increase in blockage ratio results in accelerating the flow in accordance with Bernoulli's equation to increase lift and drag.

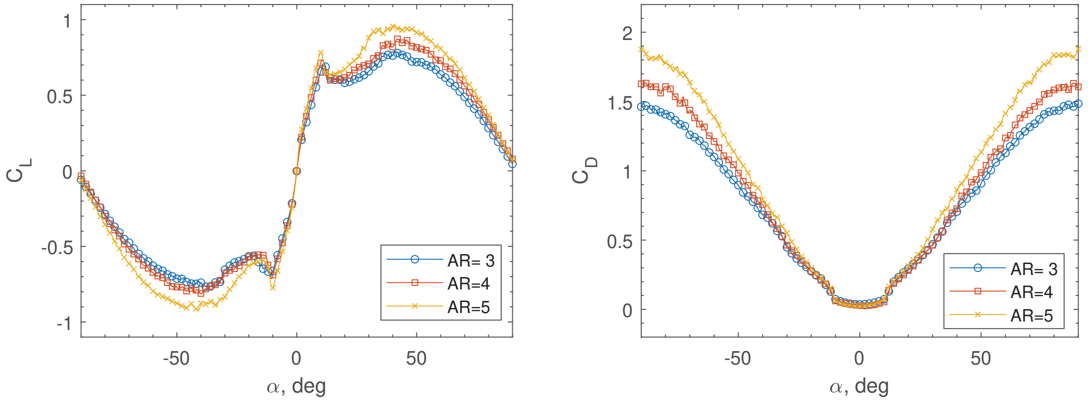

(a) (b)

Figure 6.2: Lift and drag coefficients of different aspect ratios wings in isolation.

6.2 Effect of stagger and gap

Figure 6.3 and Figure 6.4 show flow visualization of wings in tandem with Wing-1 at a positive gap. The aerodynamic interaction between wings in tandem configuration is influenced by the relative position and angle of attack of both wings. This interaction is governed by the velocity deficit in the wake, wake trajectory, increased turbulence levels, upwash/downwash effects, and pressure distribution between the wings.

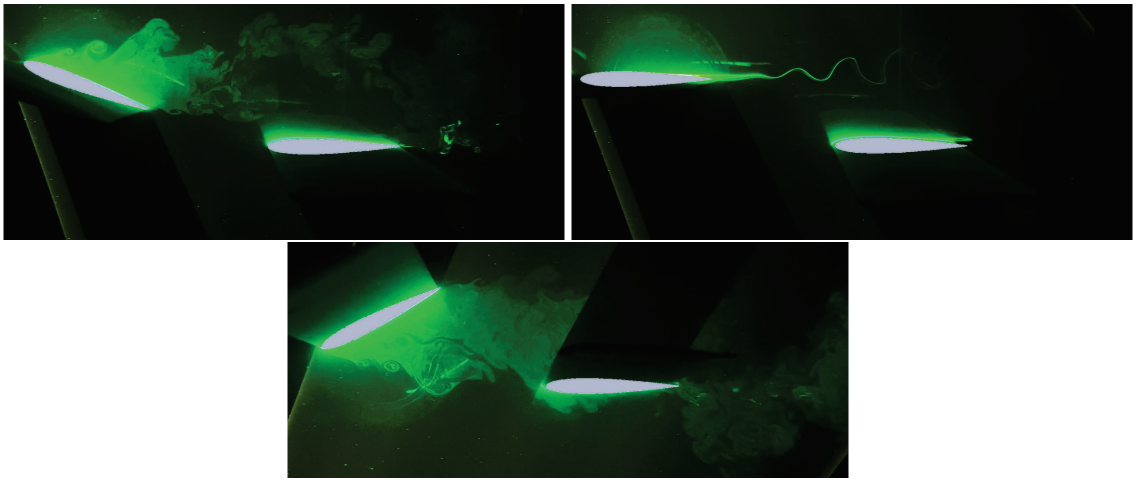

Figure 6.3: Flow visualization of wings in tandem with a positive offset, α_2 = 0 deg.

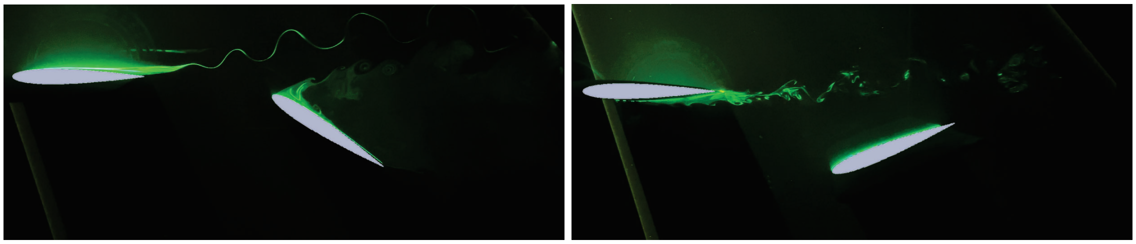

Figure 6.4: Flow visualization of wings in tandem with a positive offset, α_1 = 0 deg.

Figure 6.5 illustrates the interaction mechanism based on flow visualization results. As shown in Figure 6.5(a), when Wing-1 was at a positive angle of attack and flow had already separated on the upper surface, the location of the maximum deficit moved upward (refer to Figure 3.16), causing the wake to roll up. Consequently, Wing-2 was outside the wake of Wing-1 and an undisturbed flow. In contrast, when Wing-2 was at a positive angle of attack and α_1 = 0 deg (refer to Figure 6.5(b)), the wake of Wing-1 deflected upward, inducing a positive angle of attack on Wing-1.

The most interesting case occurred when both wings were at α = 0 deg. The wake of WIng-1 passed over the upper surface of Wing-2. It is hypothesized that the stagnation pressure at the leading edge of Wing-2 resulted in higher pressure below Wing-1. Therefore, Wing-1 and Wing-2 at α_2 = 0 in tandem configuration at a positive gap produce positive and negative lift, respectively. Furthermore, the flow was also anticipated to accelerate between the wings due to the thickness distribution of Wing-2. Figure 6.5(d) presents the case when Wing-1 was at a negative angle of attack and Wing-2 was held at α_2 = 0. This case is analogous to a positive angle of attack of Wing-1 at a negative offset due to the symmetric wings used. Wing-2 was engulfed in the wake of Wing-1. The impingement location of the separated shear layer from the leading edge of Wing 1 onto Wing-2 was crucial because it would result in the formation of LEV on upper or lower surface of Wing-2 accordingly and would produce unsteady loads. Figure 6.5(e) represents the case when Wing-1 was held at α_1 = 0 deg and Wing-2 was at a negative angle of attack. Flow was expected to accelerate on the lower side of Wing-1 because of change in area between the wings. Hence, Wing-1 effective angle of attack became negative and flow separated on the lower side. The surface vortices became unstable in the near wake region and the wake also deflected downwards.

Therefore, the intricate aerodynamic interactions between Wing-1 and Wing-2 in a tandem configuration with a positive gap depend upon the relative angle of attack between the wings. The wake generated by Wing-1 significantly influenced the pressure distribution and boundary layer behaviour of Wing-2. At certain angles of attack, the wake of Wing-1 impinged on Wing-2 resulting in flow separation or reattachment, altering lift characteristics of Wing-2. Furthermore, the pressure differential created by the accelerated flow between the wings can induce an effective change in the angle of attack for Wing-1. These complex unsteady phenomena ultimately couple the aerodynamic performance of each wing. Further wind tunnel testing and analysis of the lift and drag coefficients for the tandem wing configuration across a range of stagger and gap combinations will quantify the implications of these interactions on overall aerodynamic behavior as discussed in the next section

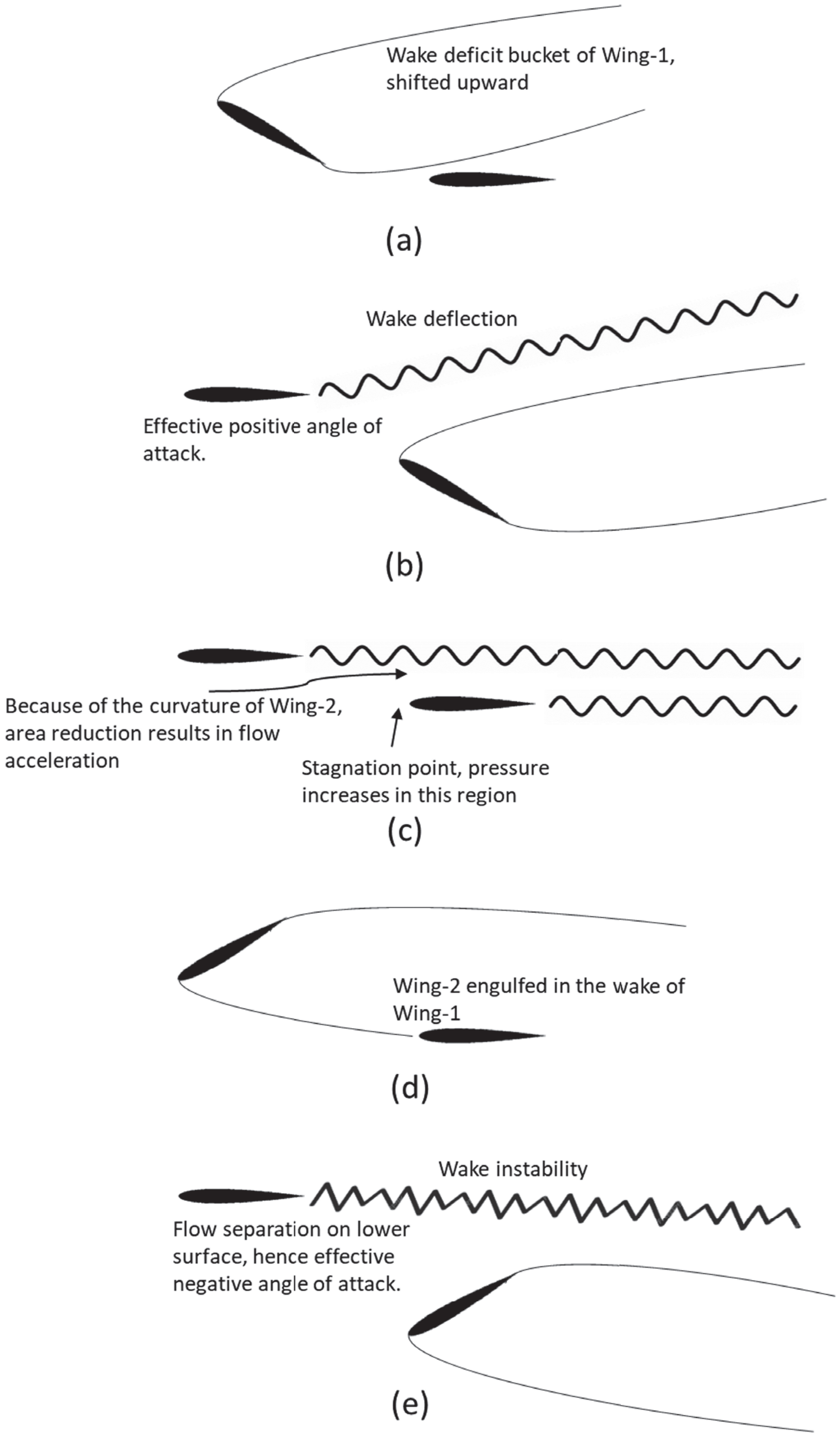

Figure 6.5: Mechanism of aerodynamic interaction of wings in tandem at a positive gap.

6.3 Case-1: α_1 sweep ± 90 degrees, and $\alpha_2 = 0$ degrees

The effect of stagger and gap on the aerodynamics of a tandem wing configuration was investigated by obtaining direct force and moment measurements. The test models consisted of two NACA0012 wings with an aspect ratio of 5. Figure 6.6 presents the lift coefficient vs angle of attack for Wing-1 and Wing-2 across a range of angles of attack of Wing-1, stagger, and gaps at Re = 100,000.

For streamwise aligned wings i.e. with no gap, the presence of Wing-2 had negligible impact on lift curve slope, maximum lift coefficient, and stall angle of Wing-1 across all tested staggers. However, differences emerged at higher post-stall angles, where Wing-1 exhibited a secondary stall at staggers ranging from s = 1.5c to 2.5c. Operating in the wake of Wing-1, Wing-2 generated lift due to the upwash and downwash induced by Wing-1 when fixed at a 0 degrees angle of attack. This aerodynamic interaction diminished as stagger distance increased, though the overall response remained consistent with prior observations discussed in Chapter 4.

For s = 0.5c and G = 0.5c, the lift curve of Wing-1 shifted left and Wing-1 produced positive lift at zero degree angle of attack, which is most likely due to the increase in pressure below Wing-1 caused by the presence of Wing-2 (refer to Figure 6.5). The wake of Wing-1 passed over the upper surface of Wing-2, which increased the pressure on the upper surface of Wing-2. Hence, Wing-2 produced a negative lift at zero degrees angle of attack, but the magnitude was small. At positive angles of attack range of Wing-1, after the stall, the lift of Wing-1 remained almost constant up to 40 deg, then decreased gradually following the isolated wing trend. The lift of Wing-2 remained approximately equal to zero, suggesting minimal interaction between the wings at $\alpha_1 > 40$ deg. The behavior was the same for the negative range beyond $\alpha_1 = -40$ deg. At negative angles of attack of Wing-1, Wing-2 produced positive lift beyond the zero lift angle of attack, due to possible flow acceleration and pressure drop over the upper surface of Wing-2. With an increased offset to G = 1c, the behavior remained similar but the increase in positive lift of Wing-2 was greater as compared to G = 0.5c. At positive α_1 beyond the stall angle, the lift of Wing-2 remained approximately zero. The increase in stagger for the gaps of G = 0.5c and 1c resulted in a decrease in the positive lift generated by Wing-2 at the negative angles of attack of Wing-1. However, at the positive range of α_1, a negative lift was produced by Wing-2 which remained unchanged until the secondary stall occurred. Beyond the secondary stall of Wing-1, Wing-2 produced positive lift which remained constant up to 90 deg. At the maximum stagger and gap tested s = 2.5c and G = 1c, for negative angles of attack of Wing-1, the coefficient of lift remained almost equal to zero. The secondary stall was observed at different stagger positions and gap locations, but it was most discrete when G = 0c.

6.4 Case-2: α_2 sweep ± 90 degrees, and $\alpha_1 = 0$ degrees

The effect of stagger and spacing on the lift coefficients of both Wing-1 and Wing-2 for case-2 are presented in Figure 6.7. The lift curve of Wing-2 in the wake of Wing-1 at $\alpha_1 =$ 0 deg became linear, with Wing-1 fixed at zero degrees producing positive and negative lift corresponding to the angle of attack of Wing-2, as discussed in Chapter 4. The maximum lift coefficient of Wing-2 was highest when the spacing between the wings was minimum, and the effect of Wing-2 on Wing-1 diminished with an increase spacings. For s = 2.5c and G = 0.5c, the effect on Wing-1 was minimal. However, introducing a gap resulted in shifting the lift curve of Wing-1, and the maximum lift coefficient of Wing-2 also decreased. Interestingly, for maximum stagger and gap, Wing-1 produced an almost constant lift for all angles of attack of Wing-2. This is likely because the flow acceleration between the wings caused the wake of Wing-1 to deflect upward, hence inducing an effective positive angle of attack. The drag response for case-1 and case-2 are shown in Figures 6.8 and 6.9. At small angles of attack, the drag of Wing-2 was higher and it decreased with an increase in the angle of attack of Wing-1, as discussed in detail in chapter 4. There was no noticeable change in the drag response of both Wing-1 and Wing-2 with variations in spacing and offset. The drag decreased for Wing-2 at post-stall angles of attack of Wing-1, even attaining negative values. This was due to a local low-pressure region upstream of Wing-2 in the wake of Wing-1 at high angles of attack, resulting in reduced drag.

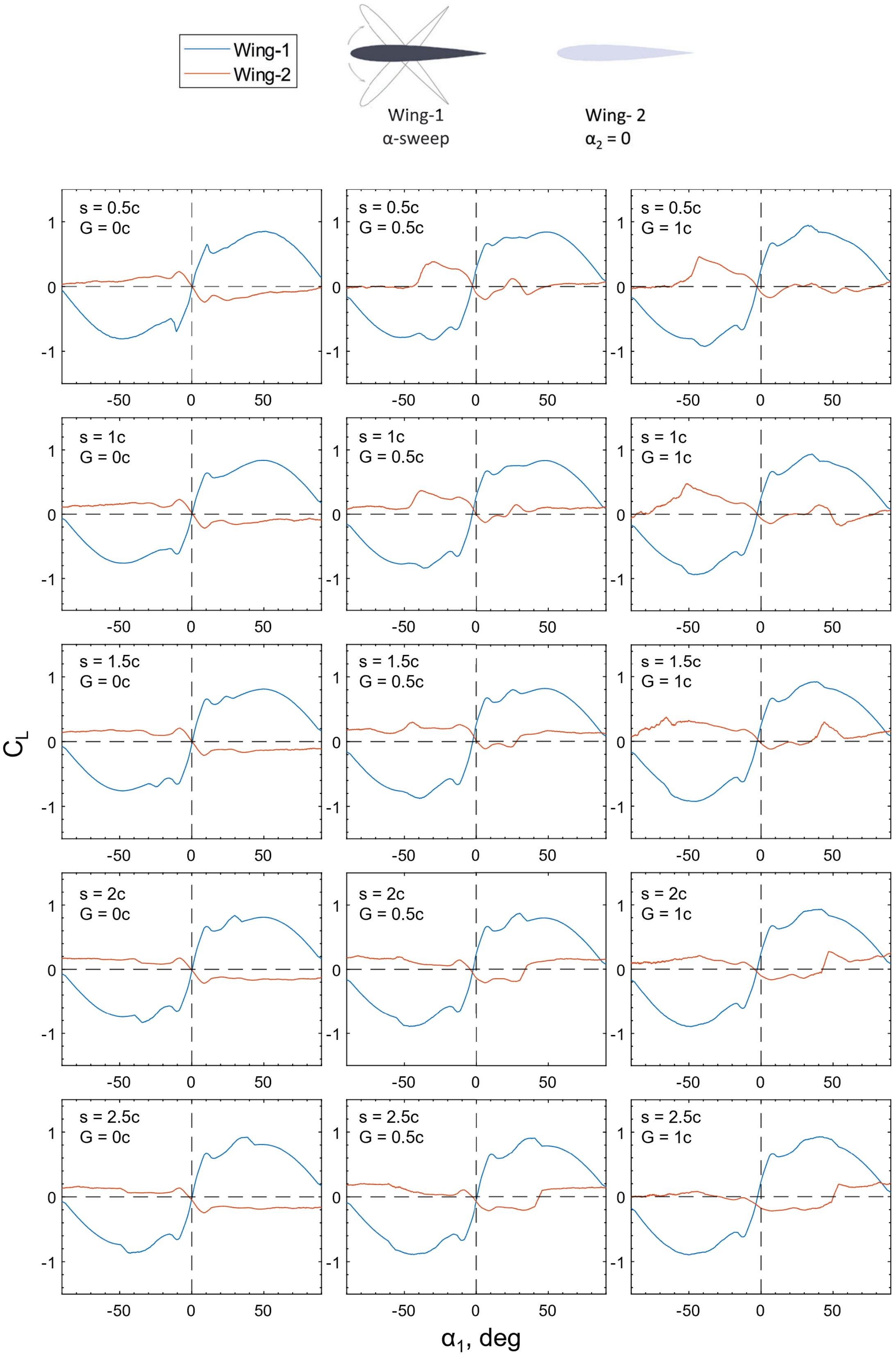

Figure 6.6: Coefficient of lift of Wing-1 and Wing-2 vs α_1, α_2 = 0 deg and Re = 100,000.

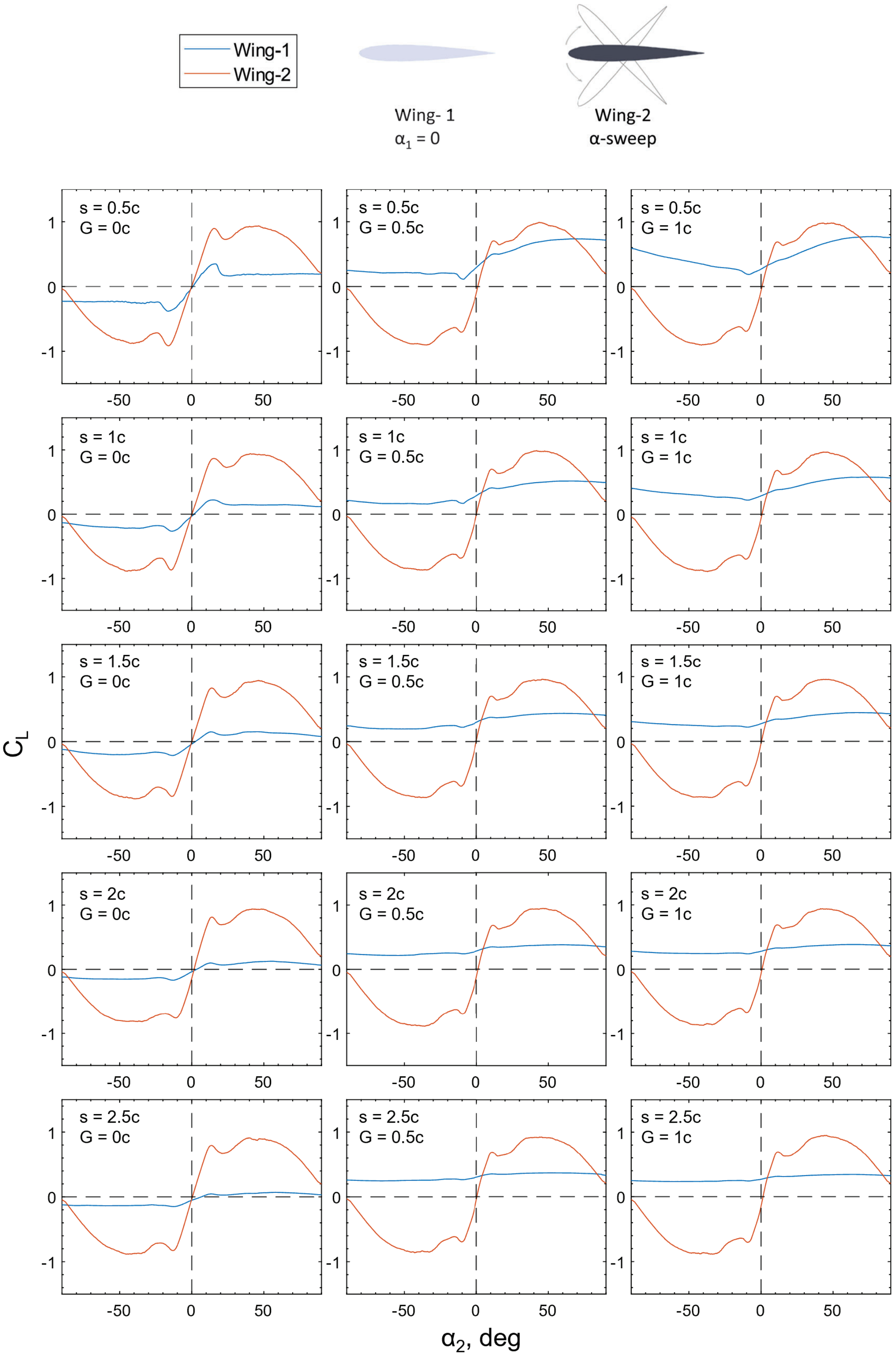

Figure 6.7: Coefficient of lift of Wing-1 and Wing-2 vs α_2, α_1 = 0 deg and Re = 100,000.

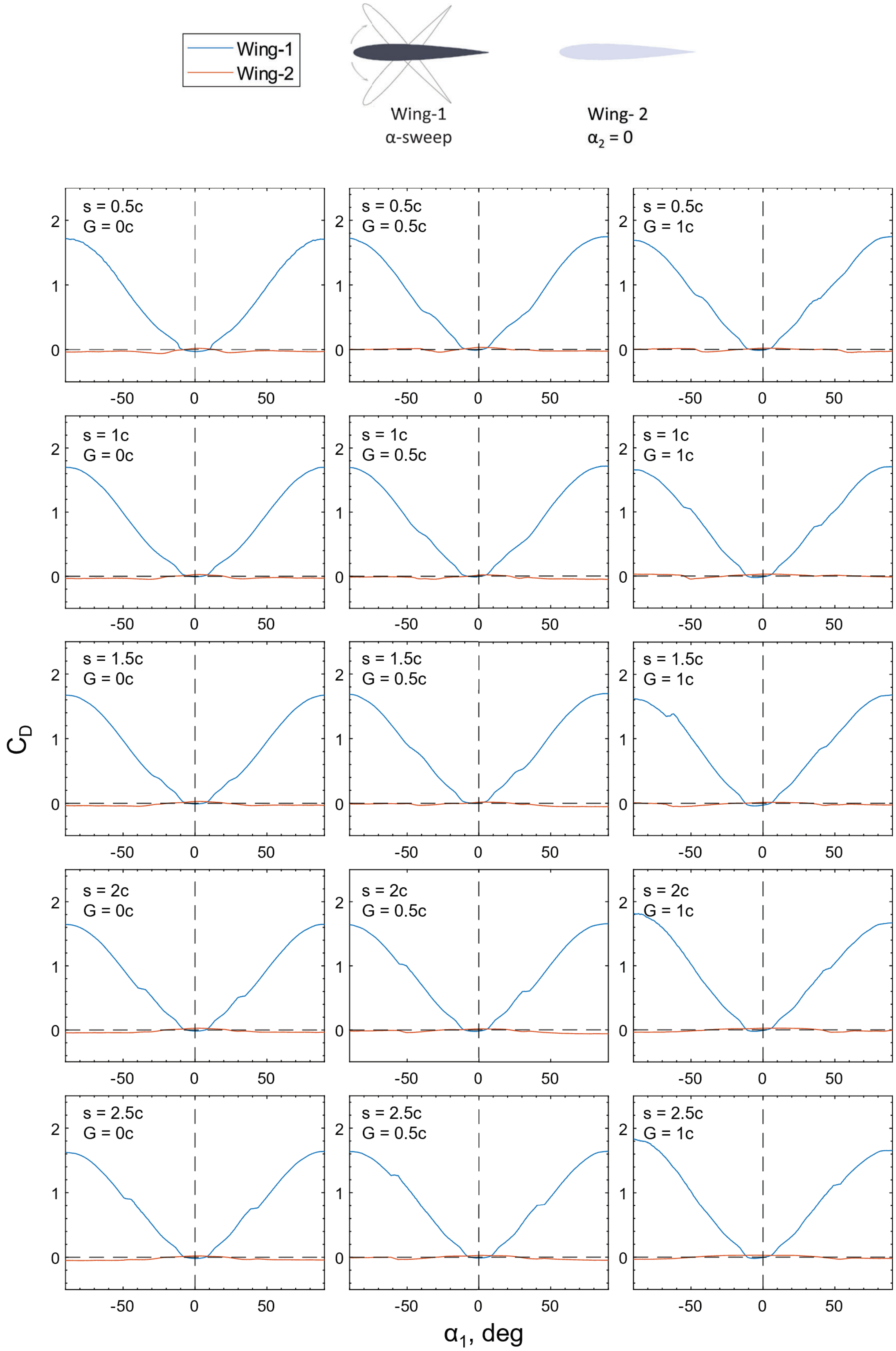

Figure 6.8: Coefficient of drag of Wing-1 and Wing-2 vs α_1, α_2 = 0 deg and Re = 100,000.

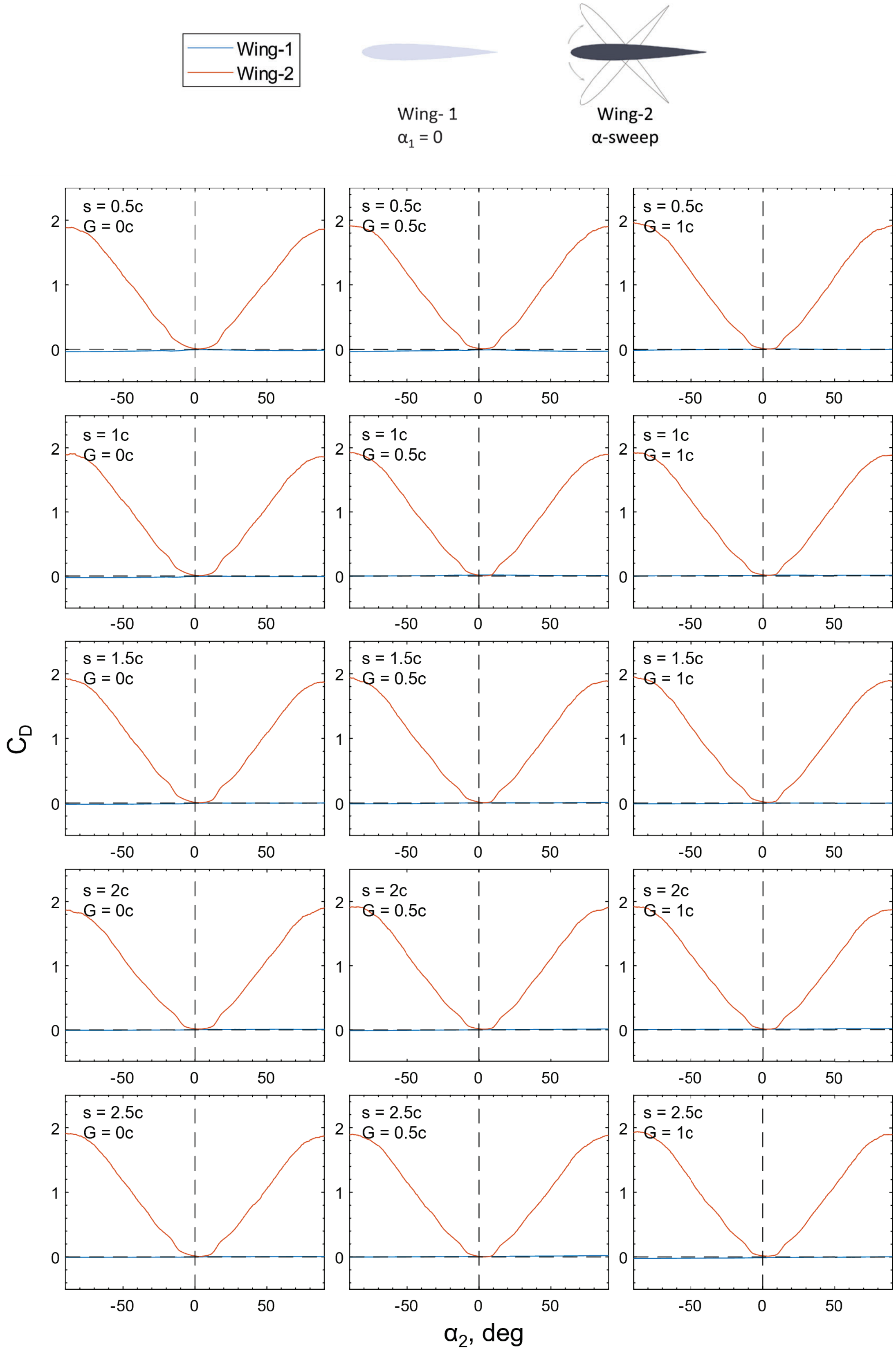

Figure 6.9: Coefficient of drag of Wing-1 and Wing-2 vs α_2, α_1 = 0 deg and Re = 100,000.

6.5 Effect of Change in Aspect ratio of Wing-1

The effect of changing the aspect ratio of Wing-1 was investigated at a streamwise spacing of 2c and gaps of G = 0, 0.5c and 1c, and the results of case-1 and case-2 are shown in Figures 6.10 and 6.11 respectively. For case-1 at G = 1c, two distinct peaks in the lift produced by Wing-2 were observed around $\alpha_1 = \pm 50$ degrees. The peak at the negative angle of attack of Wing-1 was slightly higher than at the positive angle. At very high angles of attack, Wing-1 behaved like a bluff body or flat plate facing the flow. However, unlike a flat plate, a profiled wing has a rounded leading edge and sharp trailing edge, so the vortex shedding strength from the leading and trailing edges was different. This may explain the asymmetry in the lift curve of Wing-2. Wing-1 fixed at $\alpha_1 = 0$ produced some lift due to the presence of Wing-2 at different angles of attack, with the effect consistent across vertical offsets. No significant effect of changing Wing-1 aspect ratio at zero degrees was observed on Wing-2. Importantly, there should be no or only very weak tip vortices formed when Wing-1 was at zero degrees or producing minimal lift. Changing the aspect ratio of Wing-1 did not have a significant effect on the drag response of Wing-1 and Wing-2 across the range of spacings and offsets tested. The drag of Wing-2 decreased at post-stall angles of attack of Wing-1, even becoming negative. This drag reduction was attributed to a region of locally low pressure formed upstream of Wing-2, induced by the wake of Wing-1 at high angles of attack. Surface flow visualization as shown in Figure 6.12. The change in the aspect ratio of Wing-1 impacted the flow behavior on Wing-2. At small angles of attack of Wing-1, the separation bubble of Wing-2 was bifurcated. At higher pre-stall angles, the wake of Wing-1 resulted in the portion of Wing-2 directly in the wake having fully attached flow, while the outboard section of Wing-2 experienced freestream conditions and exhibited three distinct spanwise flow regions near the tip. The intricacies of the tip vortices generated by the tandem wing configuration could be further elucidated by 3D particle image velocimetry or numerical simulations. It is hypothesized that the impingement location of the wing tip vortex core from Wing-1 determines the bifurcation of the flow and creates inboard and outboard spanwise velocity components above and below Wing-2. The presence of Wing-2 would also impact the trajectory and axial compression of the incoming vortex, becoming a case of perpendicular vortex-blade interaction.

6.6 Chapter Summary

The aerodynamics of wings in tandem at different spacing and gap was investigated. The results show that Wing-2 and Wing-1 behave in an aerodynamically coupled manner. Wing-2 operating in the wake of Wing-1 experienced a local unsteady upstream condition and reduced effective angle of attack. The downwash from Wing-1 controlled the flow over Wing-2. The flow on Wing-2 remained attached as long as the flow was attached over Wing-1. The wing induced the change in the effective angle of attack of Wing-1 by deflecting its wake and making it a situation analogous to a Fowler flap. The change in the aspect ratio of Wing-1 had a more pronounced effect at higher angles of attack. The vortex shedding from leading and trailing edges at higher angles of attack differed due to the sharpness of the trailing edge.

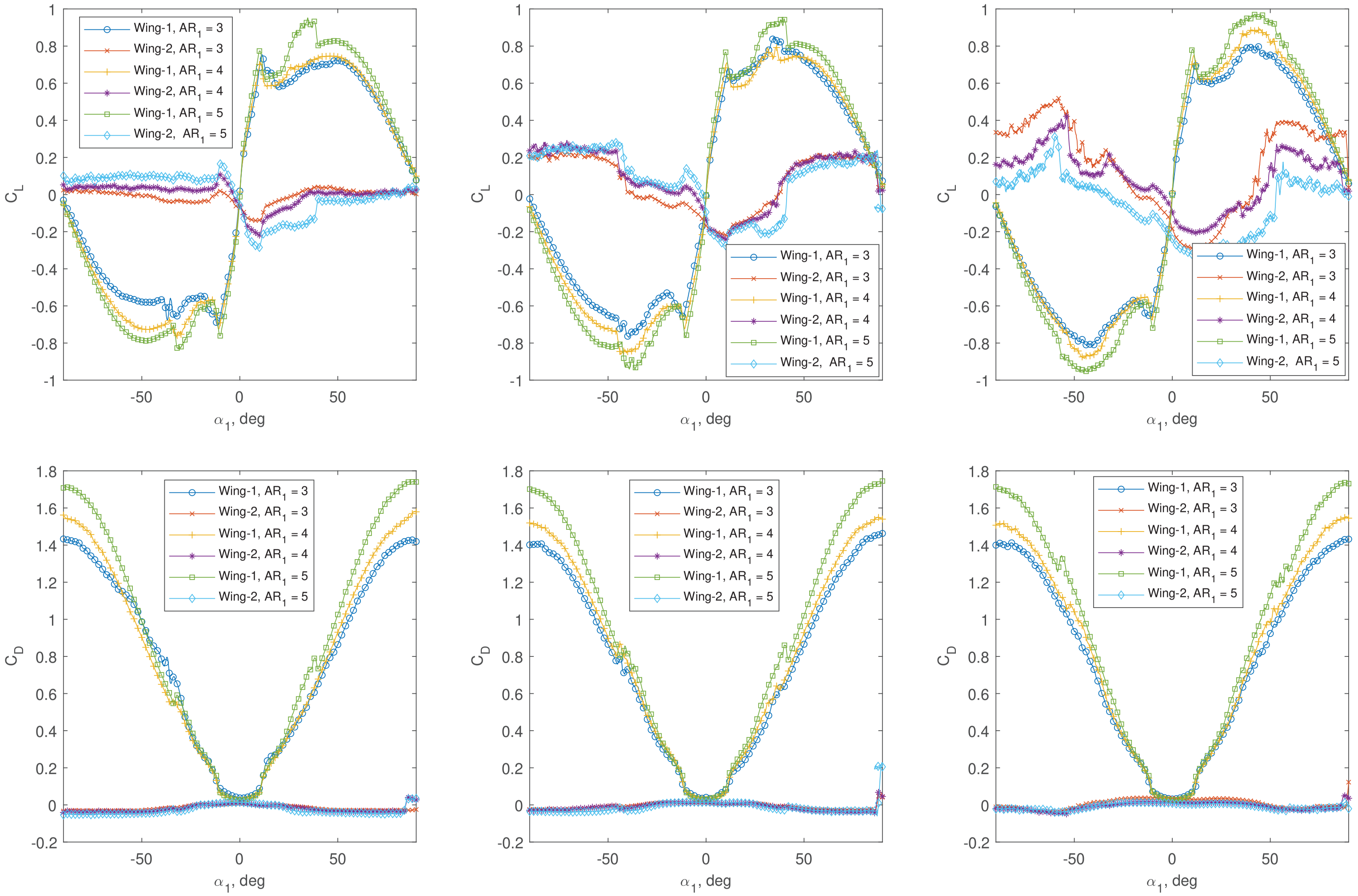

Figure 6.10: Effect of change of aspect ratio, Wing -2 at $\alpha_2 = 0$ and Re = 100,000.

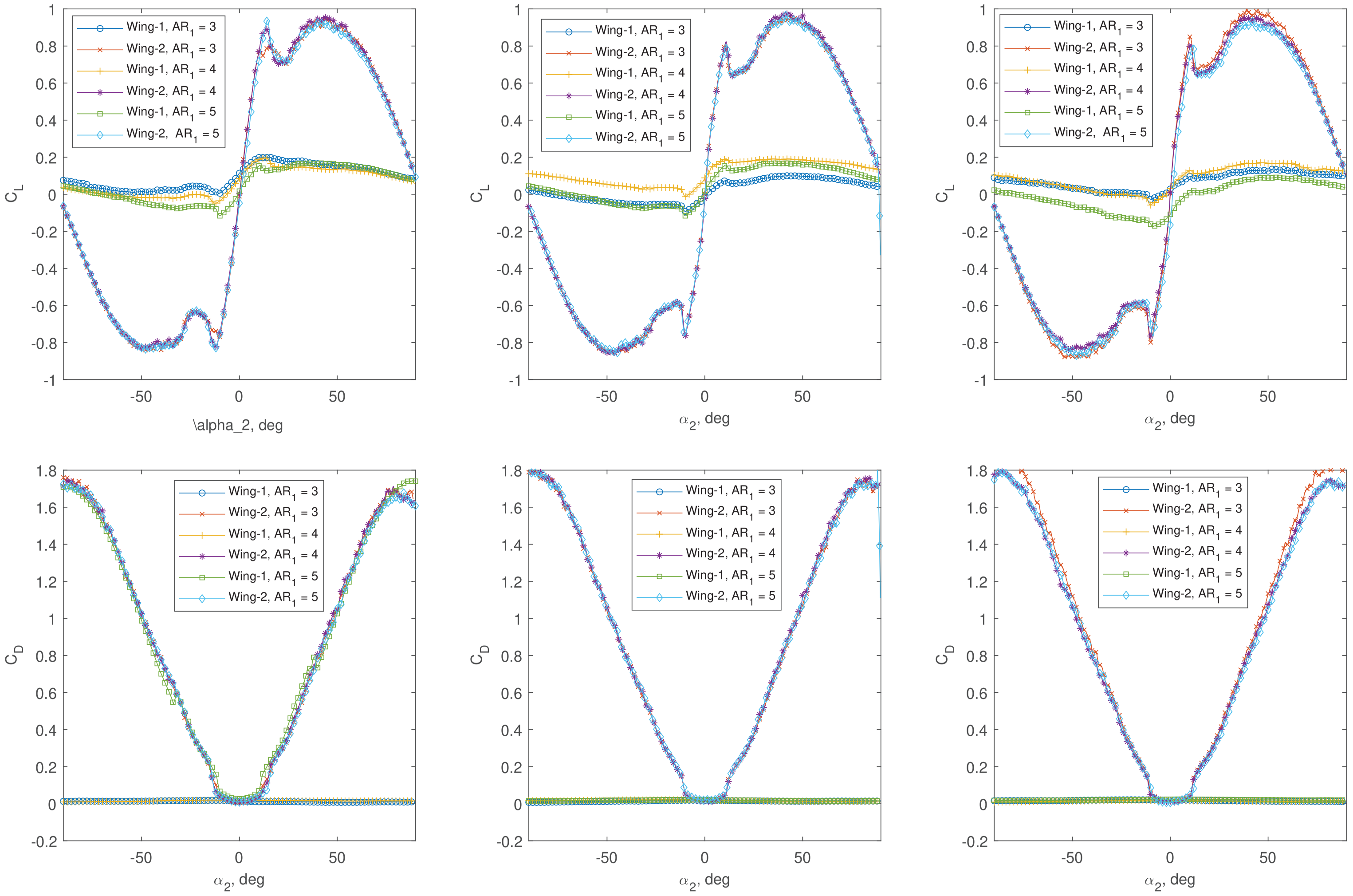

Figure 6.11: Effect of change of aspect ratio, Wing -2 at $\alpha_1 = 0$ and Re = 100,000.

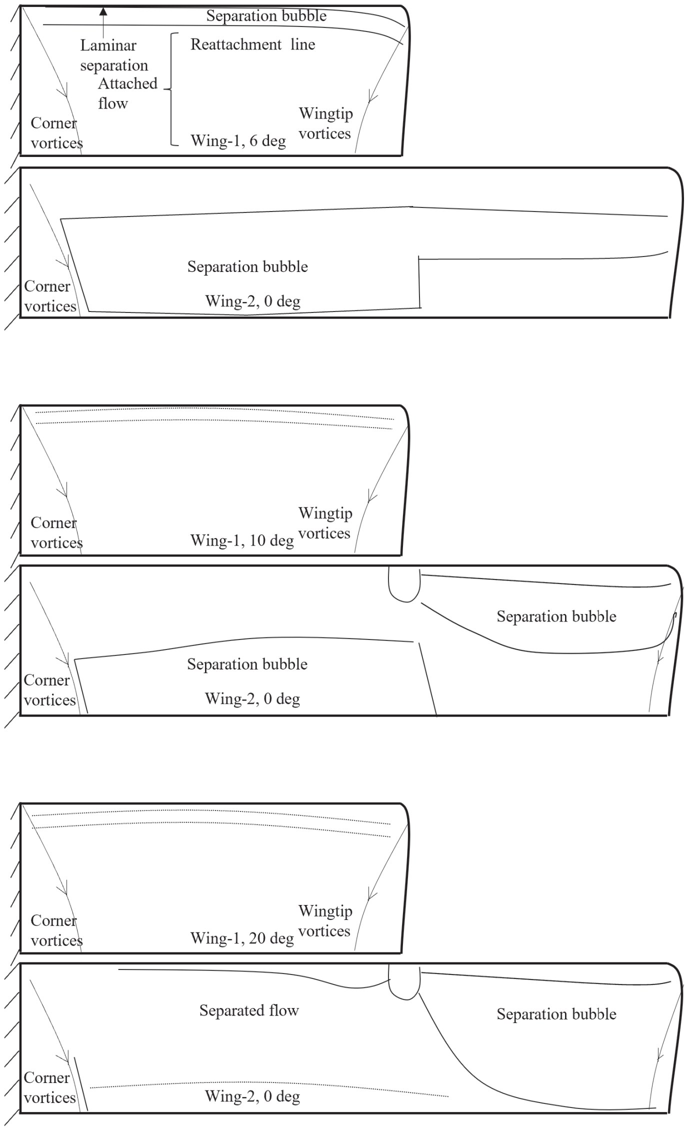

Figure 6.12: Surface flow visualization of wings in tandem.

Chapter 7

Conclusions

The aerodynamic performance of finite aspect ratio rectangular wings in tandem configuration has been systematically investigated through wind tunnel experimentation across a range of angles of attack and Reynolds numbers. The results provide new insights into the intricate couplings that manifest between upstream and downstream wings positioned in close proximity.

A detailed analysis of an isolated NACA0012 wing section established reference baselines before examining tandem arrangements. At very low Reynolds numbers, a highly nonlinear lift response was observed without a discrete classical stall. The wake was characterized by laminar instability waves and interactions between surface vortices and trailing edge vortice. At the low Reynolds number of 100,000 more conventional behavior was observed, with linear pre-stall lift at different ranges of angles of attack, an abrupt leading edge stall, and clockwise static hysteresis loop indicating formation of laminar separation bubble. The size and location of laminar separation bubble dictated the aerodynamic at low Reynolds numbers.

Introducing a second wing downstream revealed multifaceted aerodynamic interactions. A novel phenomenon termed secondary stall was observed, causing abrupt decrease in lift and drag of the upstream wing when positioned appropriately relative to the downstream wing. This secondary stall was attributed to the downstream wing suppressing vortex shedding from the upstream wing when acting akin to a bluff body with an dettached splitter plate. Secondary stall proved independent of Reynolds number and aspect ratio, representing an inviscid phenomenon linked to wake interactions.

The local onset flow for the downstream wing imposed by the upstream wake dictated boundary layer transition, separation, and reattachment characteristics. At the higher Reynolds number, increased turbulence intensity suppressed separation bubbles, delaying stall, augmenting maximum lift, and inducing trailing edge stall behavior. At very low Reynolds numbers, eliminating nonlinear response and eliciting a distinct leading edge stall for the downstream wing. Additional effects included expanded drag buckets, negative drag generation, and lift fluctuations from vortex interactions.

Simultaneous angle of attack sweeps revealed phase-reversed lift response at high angles as the pressure surface of the downstream wing experienced flow from the upstream suction surface. This coupling demonstrated the sensitivity of the aerodynamic interactions to relative wing incidence angles.

The comprehensive framework and datasets furnished fundamental perspective into low Reynolds number tandem wing aerodynamics. Key mechanisms governing performance were isolated across myriad configurations. Phenomena elucidated expand knowledge of boundary layer transition, laminar separation, secondary stalls, thrust production, lift hysteresis, and multifaceted impacts on stall characteristics. The research provides new insight to guide future small aerial vehicle development and tandem wing design optimization.

While this work systematically characterized salient features of tandem aerodynamics through direct force measurements and flow visualization, further efforts can build upon these findings along several fronts:

This research into the aerodynamics of static rectangular wings in tandem configuration provided extensive experimental datasets across a wide parameter space at low Reynolds numbers. The findings illuminated the intricacies of the coupled response and interactive effects. Ongoing work can build on these results to expand investigations into additional configurations, unsteady motions, and aeroelastic impacts. Further efforts will also benefit from validating data using high-fidelity computational techniques. Broader impacts include guiding the development of agile and efficient small aerial vehicles by exploiting aerodynamic interactions to augment capabilities across flight regimes. The fundamental knowledge furnished on boundary layer transition, vortex interactions, secondary stalls, and multifaceted performance traits establishes an empirical basis for future tandem wing research. As engineering aims to push boundaries and expand possibilities, the aerodynamic couplings revealed here showcase the complexity arising from finite wings operating in close proximity. Ongoing theoretical, computational and experimental pursuits in this rich area can uncover new phenomena while translating findings into innovative solutions that overcome challenges. The door remains open for deeper explorations into the intricacies of interacting lifting surfaces.

7.1 Future work and Recommendations

1. Additional parameters to explore include aspect ratio variations, oscillatory motions, gust encounters, and expanded wing spacing.
2. Conducting simultaneous force, surface pressure, and velocity field measurements would enable deeper analysis of the physics.
3. Validating data through high-fidelity computations using techniques like large eddy simulation.
4. Testing arrangements with three or more wings.
5. Incorporating aeroelastic effects.
6. Optimizing tandem wings for maximizing performance benefits across flight regimes.
7. Further work would be required to relate the aerodynamic interaction with the coupled pitching, rolling, and yawing moment variations to build the control models of the tandem wings.
8. Formulating reduced-order models and building tandem wing control models by relating moments to interactive effects.

References

[1] Hummel, D., "Aerodynamic aspects of formation flight in birds," *Journal of Theoretical Biology*, Vol. 104, No. 3, 1983, pp. 321–347.

[2] Bangash, Z. A., Sanchez, R. P., Ahmed, A., and Khan, M. J., "Aerodynamics of Formation Flight," *Journal of Aircraft*, Vol. 43, No. 4, 2006, pp. 907–912.

[3] Bowers P, *Unconventional aircraft*, TAB Books Inc., 1984.

[4] Jones, R., Cleaver, D. J., and Gursul, I., "Stall delay of two-wing configurations with decalage at low Reynolds numbers," *Journal of Aircraft*, Vol. 54, No. 2, 2017, pp. 847–852.

[5] Wolkovitch, J., "Subsonic VSTOL Aircraft Configurations with Tandem Wings," *Journal of Aircraft*, Vol. 16, No. 9, 1979, pp. 605–611.

[6] Pines, D. J. and Bohorquez, F., "Challenges facing future micro-air-vehicle development," *Journal of Aircraft*, Vol. 43, No. 2, 2006, pp. 290–305.

[7] Coppola, M., McGuire, K. N., De Wagter, C., and de Croon, G. C., "A Survey on Swarming With Micro Air Vehicles: Fundamental Challenges and Constraints," *Frontiers in Robotics and AI*, Vol. 7, 2 2020.

[8] Gigacz, R., Mohamed, A., Poksawat, P., Panta, A., and Watkins, S., "Exploring tandem wing UAS designs for operation in turbulent urban environments," *International Journal of Micro Air Vehicles*, Vol. 10, No. 3, 9 2018, pp. 254–261.

[9] Zhang, Q., Xue, R., and Li, H., “Aerodynamic Exploration for Tandem Wings with Smooth or Corrugated Surfaces at Low Reynolds Number,” *Aerospace*, Vol. 10, No. 5, 2023.

[10] Okulski, M. and Ławryńczuk, M., “A Small UAV Optimized for Efficient Long-Range and VTOL Missions: An Experimental Tandem-Wing Quadplane Drone,” *Applied Sciences (Switzerland)*, Vol. 12, No. 14, 7 2022.

[11] Kryvokhatko, I., “Historical Review,” *Aerodynamics of Tandem Wing Aircraft: From Dinosaurs to UAVs and Supersonic Planes*, Springer Nature Switzerland, Cham, 2023, pp. 1–23.

[12] Michelsen, W. D. and Mueller, T. J., “Low Reynolds number airfoil performance subjected to wake interference from an upstream airfoil,” *5th Applied Aerodynamics Conference*, American Institute of Aeronautics and Astronautics Inc, AIAA, 1987.

[13] Winslow, J., Otsuka, H., Govindarajan, B., and Chopra, I., “Basic understanding of airfoil characteristics at low Reynolds numbers (104–105),” *Journal of Aircraft*, Vol. 55, No. 3, 2018, pp. 1050–1061.

[14] Mcmasters, J. H. and Henderson, M. L., “Low-speed single-element airfoil synthesis,” Tech. rep., 1979.

[15] Mueller, T. J. and DeLaurier, J. D., “Aerodynamics of small vehicles,” *Annual Review of Fluid Mechanics*, Vol. 35, 2003, pp. 89–111.

[16] Anderson, J. D., *Introduction to flight* , McGraw-Hill, 8th ed., 2016.

[17] Selig, M. S. and McGranahan, B. D., “Wind tunnel aerodynamic tests of six airfoils for use on small wind turbines,” *Journal of Solar Energy Engineering, Transactions of the ASME*, Vol. 126, No. 4, 11 2004, pp. 986–1001.

[18] Kachanov, Y. S., “Physical Mechanism of laminar-boundary-layer transition,” *Annual Review of Fluid Mechanics*, Vol. 26, 1994, pp. 411–482.

[19] Horton, H. P., “Laminar separation bubbles in two and three dimensional incompressible flow,” 1968.

[20] Carmichael, B., “Low Reynolds number Airfoil Survey,” Tech. rep., NASA Contractor Report I05003, 1981.

[21] Tani, I., “Low-Speed Flows Involving Bubble Separation,” *Progress in Aeronautical Sciences, 5*, 1964, pp. 79–103.

[22] Lissaman, P. B. S., “Low-Reynolds-Number Airfoils,” *Annual Review of Fluid Mechanics*, Vol. 15, No. 1, 1983, pp. 223–239.

[23] Ohtake, T., Nakae, Y., and Motohashi, T., “Nonlinearity of the Aerodynamic Characteristics of NACA0012 Aerofoil at Low Reynolds Numbers,” *Japan Society of Aeronautical Space Sciences*, Vol. 55, No. 644, 1 2007, pp. 439–445.

[24] Alam, M. M., Zhou, Y., Yang, H. X., Guo, H., and Mi, J., “The ultra-low Reynolds number airfoil wake,” *Experiments in Fluids*, Vol. 48, No. 1, 1 2010, pp. 81–103.

[25] Roberts, W. B., “Calculation of Laminar Separation Bubbles and Their Effect on Airfoil Performance,” *AIAA Journal*, Vol. 18, No. 1, 1980, pp. 25–31.

[26] Lee, D., Kawai, S., Nonomura, T., Anyoji, M., Aono, H., Oyama, A., Asai, K., and Fujii, K., “Mechanisms of surface pressure distribution within a laminar separation bubble at different Reynolds numbers,” *Physics of Fluids*, Vol. 27, No. 2, 2 2015.

[27] O’meara, M. M. and Mueller, T. J., “Laminar separation bubble characteristics on an airfoil at low Reynolds numbers,” *AIAA Journal*, Vol. 25, No. 8, 1987, pp. 1033–1041.

[28] Gaster, M., “The Structure and Behavior of Laminar Separation Bubbles,” Tech. rep., 1969.

[29] Melvill Jones, B., “Stalling,” *The Aeronautical Journal*, Vol. 38, No. 285, 1934, pp. 753–770.

[30] Mccullough, G. B. and Gault, D. E., "Examples of three representative types of airfoil-section stall at low speed," Tech. rep., 1951.

[31] Schmitz, F., "Aerodynamics of the Model Airfoil Part I," Tech. rep., NASA-TM-X-60976, 1967.

[32] Mueller, T. J. and Batill, S. M., "Experimental studies of separation on a two-dimensional airfoil at low Reynolds numbers," *AIAA Journal*, Vol. 20, No. 4, 1982, pp. 457–463.

[33] Mueller, T. J., Pohlen, L. J., Conigliaro, P. E., Jansen, B. J., and McDonnell Douglas, J., "The Influence of Free-Stream Disturbances on Low Reynolds Number Airfoil Experiments," *Experiments in Fluids*, Vol. 1, 1983, pp. 3–14.

[34] Wang, S., Zhou, Y., Alam, M. M., and Yang, H., "Turbulent intensity and Reynolds number effects on an airfoil at low Reynolds numbers," *Physics of Fluids*, Vol. 26, No. 11, 11 2014.

[35] Huang, R. F. and Lin, C. L., "Vortex shedding and shear-layer instability of a cantilever wing at low reynolds numbers," *33rd Aerospace Sciences Meeting and Exhibit*, American Institute of Aeronautics and Astronautics Inc, AIAA, 1995.

[36] Kase, M., Mizoguchi, M., and Itoh, H., "Effect of Turbulence Intensity on Time-Averaged Aerodynamics of NACA0012 Wing at Low Reynolds Numbers," *AIAA SCITECH 2023 Forum*, AIAA SciTech Forum, 2023.

[37] de Paula, A. A., Kleine, V. G., and Porto, F. D. M., "The thickness effects on symmetrical airfoil flow characteristics at low Reynolds number," *AIAA SciTech Forum - 55th AIAA Aerospace Sciences Meeting*, 2017.

[38] Yarusevych, S., Sullivan, P. E., and Kawall, J. G., "Coherent structures in an airfoil boundary layer and wake at low Reynolds numbers," *Physics of Fluids*, Vol. 18, No. 4, 2006.

[39] McAuliffe, B. R. and Yaras, M. I., “Transition mechanisms in separation bubbles under low and elevated-freestream turbulence,” *Journal of Turbomachinery*, Vol. 132, No. 1, 1 2010.

[40] Lin, J. C. and Pauley, L. L., “Low-Reynolds-number separation on an airfoil,” *AIAA Journal*, Vol. 34, No. 8, 1996, pp. 1570–1577.

[41] Yarusevych, S., Sullivan, P. E., and Kawall, J. G., “On vortex shedding from an airfoil in low-Reynolds-number flows,” *Journal of Fluid Mechanics*, Vol. 632, 2009, pp. 245–271.

[42] Jung, Y. W. and Park, S. O., “Vortex-shedding characteristics in the wake of an oscillating airfoil at low Reynolds number,” *Journal of Fluids and Structures*, Vol. 20, No. 3, 4 2005, pp. 451–464.

[43] Kurtulus, D. F., “On the Unsteady Behavior of the Flow around NACA 0012 Airfoil with Steady External Conditions at Re=1000,” *International Journal of Micro Air Vehicles*, Vol. 7, No. 3, 2015, pp. 301–326.

[44] Rockwell, D., “Vortex-Body Interactions,” *Annual Review of Fluid Mechanics*, Vol. 30, No. 1, 1998, pp. 199–229.

[45] Walker, J. and Robinson, M., “Impingement of orthogonal unsteady vortex structures on trailing aerodynamic surfaces,” *6th Applied Aerodynamics Conference*, 1988.

[46] Jones, A. R. and Cetiner, O., “Overview of Unsteady Aerodynamic Response of Rigid Wings in Gust Encounters,” *AIAA Journal*, Vol. 59, No. 2, 2021, pp. 731–736.

[47] Yarusevych, S., Kawall, J. G., and Sullivan, P. E., “Airfoil performance at low Reynolds numbers in the presence of periodic disturbances,” *Journal of Fluids Engineering, Transactions of the ASME*, Vol. 128, No. 3, 5 2006, pp. 587–595.

[48] Zhang, Z., Wang, Z., and Gursul, I., “Delay of stall for a stationary wing placed in a wake,” *AIAA Scitech 2021 Forum*, 2021, pp. 1–17.

[49] Lefebvre, J. N., Jones, A. R., Jarman, L. M., and Smith, M. J., "Experimental and numerical investigation of airfoil performance in the wake of a circular cylinder," American Institute of Aeronautics and Astronautics Inc, AIAA, 2018.

[50] Barnes, C. J., Visbal, M. R., and Huang, P. G., "On the effects of vertical offset and core structure in streamwise-oriented vortex-wing interactions," *Journal of Fluid Mechanics*, Vol. 799, 6 2016, pp. 128–158.

[51] Barnes, C. J., Visbal, M. R., and Gordnier, R. E., "Analysis of streamwise-oriented vortex interactions for two wings in close proximity," *Physics of Fluids*, Vol. 27, No. 1, 1 2015.

[52] Chen, C., Wang, Z., and Gursul, I., "Experiments on tip vortices interacting with downstream wings," *Experiments in Fluids*, Vol. 59, No. 5, 5 2018.

[53] McKenna, C., Bross, M., and Rockwell, D., "Structure of a streamwise-oriented vortex incident upon a wing," *Journal of Fluid Mechanics*, Vol. 816, 4 2017, pp. 306–330.

[54] Turhan, B., Wang, Z., and Gursul, I., "Interaction of vortex streets with a downstream wing," *Physical Review Fluids*, Vol. 7, No. 9, 9 2022.

[55] Scharpf, D. F. and Mueller, T. J., "Experimental study of a low Reynolds number tandem airfoil configuration," *Journal of Aircraft*, Vol. 29, No. 2, 1992, pp. 231–236.

[56] Fanjoy, D. W. and Dorney, D. J., "A study of tandem-airfoil interaction in different flight regim," *35th Aerospace Sciences Meeting and Exhibit*, American Institute of Aeronautics and Astronautics Inc, AIAA, 1997.

[57] Fanjoy, D. W. and Dorney, D. J., "Numerical Simulations of Tandem-Airfoil Aerodynamics," *Aerospace Atlantic Conference & Exposition*, SAE International, 5 1996.

[58] Jones, R., Cleaver, D. J., and Gursul, I., "Aerodynamics of biplane and tandem wings at low Reynolds numbers," *Experiments in Fluids*, Vol. 56, No. 6, 6 2015.

[59] Ahmed, M. R. and Kohama, Y., “Experimental Investigation on the Aerodynamic Characteristics of a Tandem Wing Configuration in Close Ground Proximity,” *JSME International Journal Series B*, Vol. 42, No. 4, 1999, pp. 612–618.

[60] Jones, R., Cleaver, D. J., and Gursul, I., “Fluid-structure Interactions for flexible and rigid Tandem-Wings at low Reynolds numbers,” American Institute of Aeronautics and Astronautics Inc, AIAA, 2015.

[61] Khan, F. A. and Mueller, T. J., “Tip Vortex/Airfoil interaction for a low Reynolds number Canard/Wing configuration,” *Journal of Aircraft*, Vol. 28, No. 3, 1991, pp. 181–186.

[62] Faure, T. M., Hétru, L., and Montagnier, O., “Aerodynamic features of a two-airfoil arrangement,” *Experiments in Fluids*, Vol. 58, No. 10, 10 2017.

[63] Chou, H. Y., Liu, Y. C., and Hsiao, F. B., “The Aerodynamic behavioral study of two wing’s wake flow in Tandem arrangement,” *Procedia Engineering*, Vol. 67, Elsevier Ltd, 2013, pp. 1–14.

[64] Cheng, H. and Wang, H., “Prediction of Lift Coefficient for Tandem Wing Configuration or Multiple-Lifting-Surface System Using Prandtl’s Lifting-Line Theory,” *International Journal of Aerospace Engineering*, Vol. 2018, 2018, pp. 3104902.

[65] Cai, Y., Liu, G., Zhu, X., Tu, Q., and Hong, G., “Aerodynamic Interference Significance Analysis of Two-Dimensional Front Wing and Rear Wing Airfoils with Stagger and Gap Variations,” *Journal of Aerospace Engineering*, Vol. 32, No. 6, 11 2019.

[66] Salami, E., Ward, T. A., Montazer, E., and Ghazali, N. N. N., “A review of Aerodynamic Studies on Dragonfly Flight,” *Proceedings of the Institution of Mechanical Engineers, Part C: Journal of Mechanical Engineering Science*, Vol. 233, No. 18, 2019, pp. 6519–6537.

[67] Lua, K. B., Lu, H., Zhang, X. H., Lim, T. T., and Yeo, K. S., “Aerodynamics of two-dimensional flapping wings in tandem configuration,” *Physics of Fluids*, Vol. 28, 12 2016, pp. 121901.

[68] Lehmann, F.-O., "Wing–wake interaction reduces power consumption in insect tandem wings," *Experiments in Fluids*, Vol. 46, No. 5, 2009, pp. 765–775.

[69] Arranz, G., Flores, O., and García-Villalba, M., "Three-dimensional effects on the aerodynamic performance of flapping wings in tandem configuration," *Journal of Fluids and Structures*, Vol. 94, 2020, pp. 102893.

[70] "Unsteady Aerodynamics of Flapping Airfoil in Hovering Flight at Low Reynolds Numbers," *43rd AIAA Aerospace Sciences Meeting and Exhibit*, 2005.

[71] Rojratsirikul, P., Wang, Z., and Gursul, I., "Unsteady fluid–structure interactions of membrane airfoils at low Reynolds numbers," *Experiments in Fluids*, Vol. 46, No. 5, 2009, pp. 859–872.

[72] Gordnier, R. E., "High fidelity computational simulation of a membrane wing airfoil," *Journal of Fluids and Structures*, Vol. 25, No. 5, 2009, pp. 897–917.

[73] B. Barlow, J., H. Rae, W., and Pope, A., *Low Speed Wind Tunnel Testing*, John Wiley & Sons, 3rd ed., 1999.

[74] Tank, J., *Aerodynamics at Low Re: Separation, Reattachment, and Control*, Ph.D. thesis, University of Southern California, 2018.

[75] West, G. and Apelt, C., " The effects of tunnel blockage and aspect ratio on the mean flow past a circular cylinder with Reynolds numbers between 10ˆ4 and 10ˆ5," *Journal of Fluid Mechanics*, , No. 114, 1982, pp. 361–377.

[76] Mizoguchi, M. and Itoh, H., "Effect of Aspect Ratio on Aerodynamic Characteristics at Low Reynolds Numbers," *AIAA Journal*, Vol. 51, No. 7, 2013, pp. 1631–1639.

[77] "Semi-span testing at low Reynolds number," *36th AIAA Aerospace Sciences Meeting and Exhibit*, 1997.

[78] Thom, A., "Blockage Corrections in a Closed High-speed Tunnel," Tech. rep., ARC/R & M-2033, 1943.

[79] Lind, A. H., Lefebvre, J. N., and Jones, A. R., "Time-Averaged Aerodynamics of Sharp and Blunt Trailing-Edge Static Airfoils in Reverse Flow," *AIAA Journal*, Vol. 52, No. 12, 2014, pp. 2751–2764.

[80] Lee, S. H. and Han, Y. O., "Experimental Investigation of High-Angle-of-Attack Aerodynamics of Low-Aspect-Ratio Rectangular Wings Configured with NACA0012 Airfoil Section," *International Journal of Aeronautical and Space Sciences*, Vol. 21, No. 2, 6 2020, pp. 303–314.

[81] Traub, L. W., "Effects of blockage on airfoils and wings at high angles of attack," *Journal of Aircraft*, Vol. 52, No. 3, 2015, pp. 990–993.

[82] R J Mcghee, B S Walker, and B F Millard, "Experimental results for the eppler 387 airfoil at low Reynolds numbers in the langley low-turbulence pressure tunnel," Tech. rep., National Aeronautics and Space Administration Scientific and Technical Information Division, Washington,DC, 1988.

[83] Kim, D.-H., Chang, J.-W., and Chung, J., "Low-Reynolds-Number Effect on Aerodynamic Characteristics of a NACA 0012 Airfoil," *Journal of Aircraft*, Vol. 48, No. 4, 2011, pp. 1212–1215.

[84] Pranesh, C., Sivapragasam, M., Deshpande, M. D., and Narahari, H. K., "Negative lift characteristics of NACA 0012 aerofoil at low Reynolds numbers," *Sādhanā*, Vol. 44, No. 1, 2019, pp. 21.

[85] Xia, T., Dong, H., Yang, L., Liu, S., and Jin, Z., "Investigation on flow structure and aerodynamic characteristics over an airfoil at low Reynolds number—A review," 5 2021.

[86] John Anderson, *Fundamentals of Aerodynamics*, McGraw Hill, 7th ed., 2010.

[87] Huang, R., Wu, J., Jeng, J., and Chen, R., "Surface flow and vortex shedding of an impulsively started wing," *Journal of Fluid Mechanics*, Vol. 441, 2001, pp. 265–292.

[88] Schafer, R. W., "What Is a Savitzky-Golay Filter? [Lecture Notes]," *IEEE Signal Processing Magazine*, Vol. 28, No. 4, 2011, pp. 111–117.

[89] Duda, D., Uruba, V., and Yanovych, V., “Wake Width: Discussion of Several Methods How to Estimate It by Using Measured Experimental Data,” *Energies*, Vol. 14, 2021.

[90] I.H. Abbott, A. E. V. D., “Theory of Wing Sections: Including a Summary of Airfoil Data,” 1959.

[91] Sadr, M. H., Badiei, D., and Shams, S., “Developments of a semiempirical dynamic stall model for unsteady airfoils,” *Journal of the Brazilian Society of Mechanical Sciences and Engineering*, Vol. 41, No. 10, 2019, pp. 454.

[92] Sahin, M., Sankar, L. N., Chandrasekhara, M. S., and Tung, C., “Dynamic Stall Alleviation Using a Deformable Leading Edge Concept-A Numerical Study,” *Journal of Aircraft*, Vol. 40, No. 1, 2003, pp. 77–85.

[93] Selig, M., Guglielmo, J., Broern, A., and Giguere, P., “Experiments on airfoils at low Reynolds numbers,” *34th Aerospace Sciences Meeting and Exhibit*, 1996.

[94] Michael Brendel, T. J. M., “Preliminary experiments in unsteady flow on airfoils at low Reynolds numbers,” *Proceedings of the Conference on low Reynolds number Airfoil Aerodynamics*, 1985.

[95] Lind, A. H., Lefebvre, J. N., and Jones, A. R., “Time-averaged aerodynamics of sharp and blunt trailing-edge static airfoils in reverse flow,” *AIAA Journal*, Vol. 52, No. 12, 12 2014, pp. 2751–2764.

[96] Yon, S. and Katz, J., “Study of the unsteady flow features on a stalled wing,” *28th Fluid Dynamics Conference*, 1997.

[97] Watkins, S., Ravi, S., and Loxton, B., “The Effect of Turbulence on the Aerodynamics of Low Reynolds Number Wings.” *Engineering Letters*, Vol. 18, No. 3, 2010.

[98] Hall, M., “A theory for the core of a leading-edge vortex,” *Journal of Fluid Mechanics*, Vol. 11, No. 2, 1961, pp. 209–228.

[99] Du, L., Berson, A., and Dominy, R. G., "Aerofoil behaviour at high angles of attack and at Reynolds numbers appropriate for small wind turbines," *Proceedings of the Institution of Mechanical Engineers, Part C: Journal of Mechanical Engineering Science*, Vol. 229, No. 11, 2015, pp. 2007–2022.

[100] Worasinchai, S., Ingram, G., and Dominy, R., "A low-Reynolds-number, high-angle-of-attack investigation of wind turbine aerofoils," *Proceedings of the Institution of Mechanical Engineers, Part A: Journal of Power and Energy*, Vol. 225, No. 6, 9 2011, pp. 748–763.

[101] Temple, G., "Collected works of Theodore von Karman." *Journal of Fluid Mechanics*, Vol. 5, No. 2, 1959, pp. 329–336.

[102] Guan, G., He, K., Wang, P., and Yang, Q., "Study on the parameters of detached splitter plate for VIV suppression," *Ocean Engineering*, Vol. 266, 2022, pp. 113092.

[103] Hwang, J. Y., Yang, K. S., and Sun, S. H., "Reduction of flow-induced forces on a circular cylinder using a detached splitter plate," *Physics of Fluids*, Vol. 15, No. 8, 2003, pp. 2433–2436.

[104] Cheng, M., "Wake Flow Behind a Cylinder With a Detached Splitter Plate," *Proceedings of the American Society of Mechanical Engineers Fluids Engineering Division Summer Conference*, Vol. 1, 01 2005.

[99] Du, L., Berson, A., and Dominy, R. G., "Aerofoil behaviour at high angles of attack and at Reynolds numbers appropriate for small wind turbines," *Proceedings of the Institution of Mechanical Engineers, Part C: Journal of Mechanical Engineering Science*, Vol. 229, No. 11, 2015, pp. 2007–2022.

[100] Worasinchai, S., Ingram, G., and Dominy, R., "A low-Reynolds-number, high-angle-of-attack investigation of wind turbine aerofoils," *Proceedings of the Institution of Mechanical Engineers, Part A: Journal of Power and Energy*, Vol. 225, No. 6, 9 2011, pp. 748–763.

[101] Temple, G., "Collected works of Theodore von Karman." *Journal of Fluid Mechanics*, Vol. 5, No. 2, 1959, pp. 329–336.

[102] Guan, G., He, K., Wang, P., and Yang, Q., "Study on the parameters of detached splitter plate for VIV suppression," *Ocean Engineering*, Vol. 266, 2022, pp. 113092.

[103] Hwang, J. Y., Yang, K. S., and Sun, S. H., "Reduction of flow-induced forces on a circular cylinder using a detached splitter plate," *Physics of Fluids*, Vol. 15, No. 8, 2003, pp. 2433–2436.

[104] Cheng, M., "Wake Flow Behind a Cylinder With a Detached Splitter Plate," *Proceedings of the American Society of Mechanical Engineers Fluids Engineering Division Summer Conference*, Vol. 1, 01 2005.

Appendix A:

Data Acquisition and Architecture

This appendix provides instructions for the operation of the LabVIEW-based automated data acquisition system for wind tunnel testing. This system allows for the acquisition of force and moment measurements from stepper motor mounted ATI six component F/T sensor in the wind tunnel test section across a range of angles of attack. For documentation on the physical installation, wiring, and configuration of the data acquisition hardware please refer to Manual, F/T Sensor, Data Acquisition (DAQ) Systems Document #9620-05-DAQ-25. The device installation and wiring diagrams are shown in Figure A.1 and Figure A.2. The LabVIEW graphical user interface (GUI) and block diagram are depicted in Figures A.3, A.4, and A.6. To interface the DAQ with the stepper motor drivers, Connect terminal 6 (PFI 4) on each DAQ device to the corresponding motor driver Pulse+ input, Terminal 5 (GND) to Pulse- and Dir-, and connect terminal 7 to Dir+. The automated data acquisition system consists of the following components:

- Data acquisition device (NI-DAQmx) with analog input channels.
- LabVIEW virtual instrument (VI) for controlling data acquisition.
- ATI six-component force/moment sensor instrumentation and calibration data.
- Stepper motors with drivers for adjusting angle of attack.
- PC workstation running LabVIEW.

A.1 Operating Procedure for force/moment Data

1. Connect the data acquisition device analog input channels to the signal conditioning units for each force/moment sensor according to the channel configuration diagram.
2. Verify that the stepper motor controller is interfaced with the PC and that it is functional.
3. Turn on the PC workstation and launch LabVIEW. Open the automated data acquisition VI. The front panel interface for controlling the data acquisition process should appear as shown in Figure A.3.

4. For each force/moment sensor, click Browse and select the appropriate calibration file containing the calibration matrix.
5. Sample Settings - Enter the number of samples per data point and desired sampling frequency in Hz for analog input acquisition.
6. Bias Value - Click the bias button to offset the sensor output to zero for the no wind-on condition. This removes zero drift errors.
7. Output File - Define the path and filename for saving acquired data. The angle of attack information will be saved in the last column of output .txt file.
8. Angle Settings - Enter the starting angle in degrees, the angle step size, and the number of iterations. This defines the range of angles of attack to acquire data.
9. Delay - Specify the delay time in milliseconds between changing the model angle and acquiring the data point.
10. Motor Settings - Select the rotation direction and enter the step rate and step size for the stepper motor in degrees.
11. With the wind tunnel off, press the "bias" button to apply the biasing vector and remove zero errors.
12. Turn on the wind tunnel to the desired speed.
13. Select the "Data Collect" and Click the "Continue" buttons to begin automated data acquisition across the defined angle range.
14. To stop early, press Stop. Once complete, the data will be saved to the specified output file.

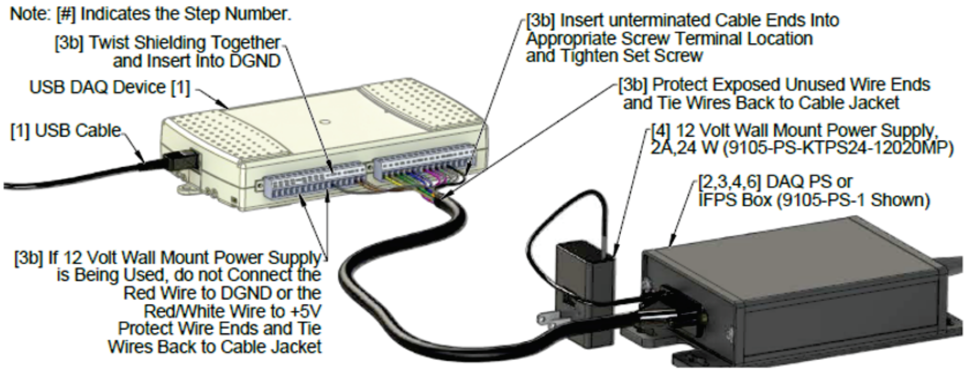

Figure A.1: Unterminated Cable Wiring (9105-C-PS-U-x) and USB DAQ Device System Installation (Manual, F/T Sensor, Data Acquisition (DAQ) Systems Document #9620-05-DAQ-25).

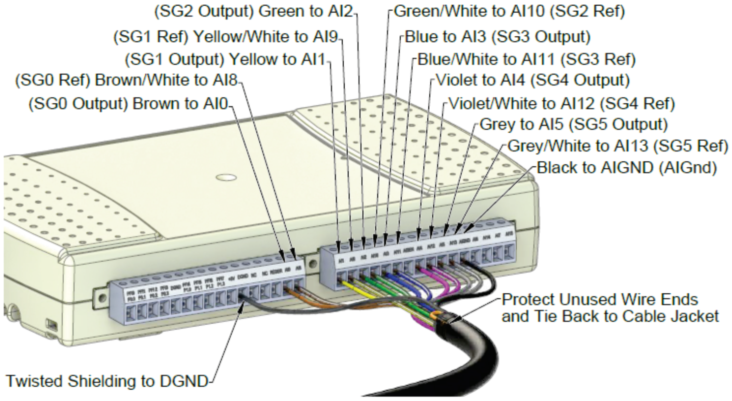

Figure A.2: Unterminated Cable Wiring (9105-C-PS-U-x) for a NI 32 Screw Terminal USB DAQ Device (Manual, F/T Sensor, Data Acquisition (DAQ) Systems Document #9620-05-DAQ-25).

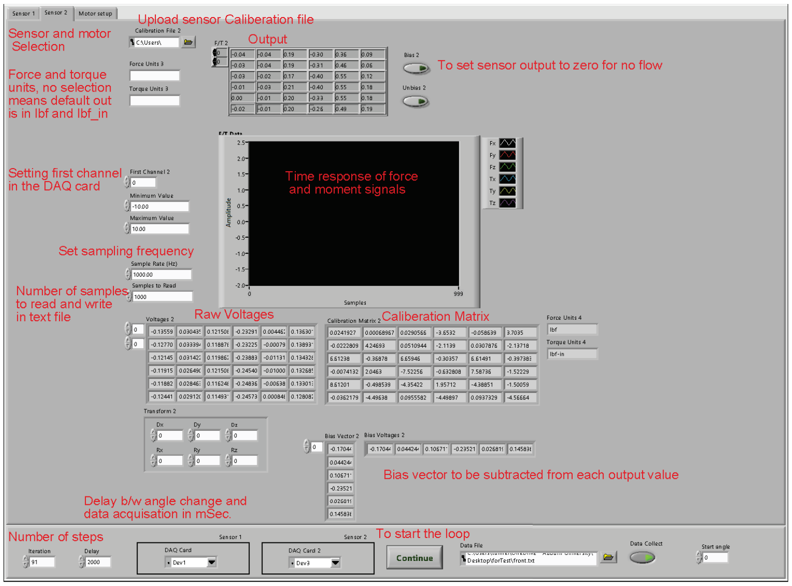

Figure A.3: Front panel of LabVIEW application

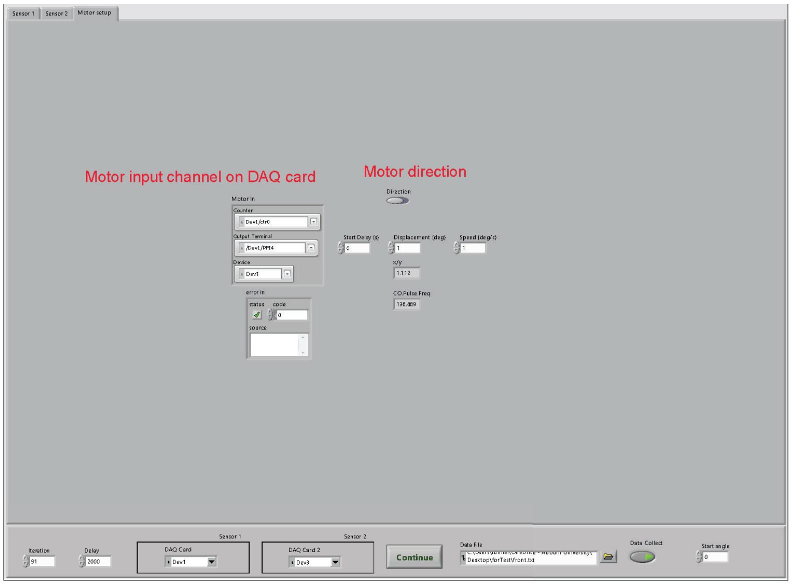

Figure A.4: Motor controls on LabVIEW application

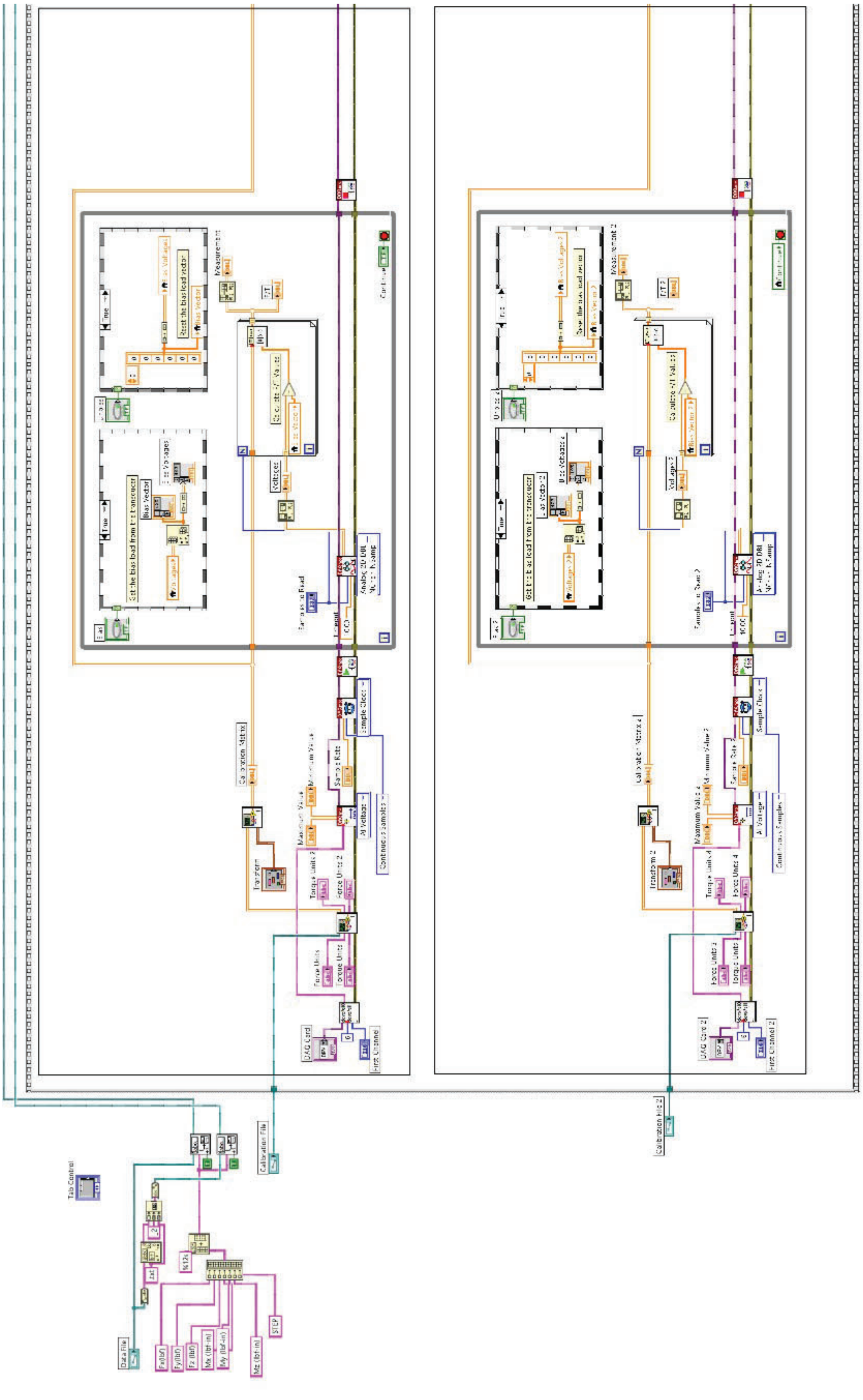

Figure A.5: LabVIEW block diagram for force/moment measurements.

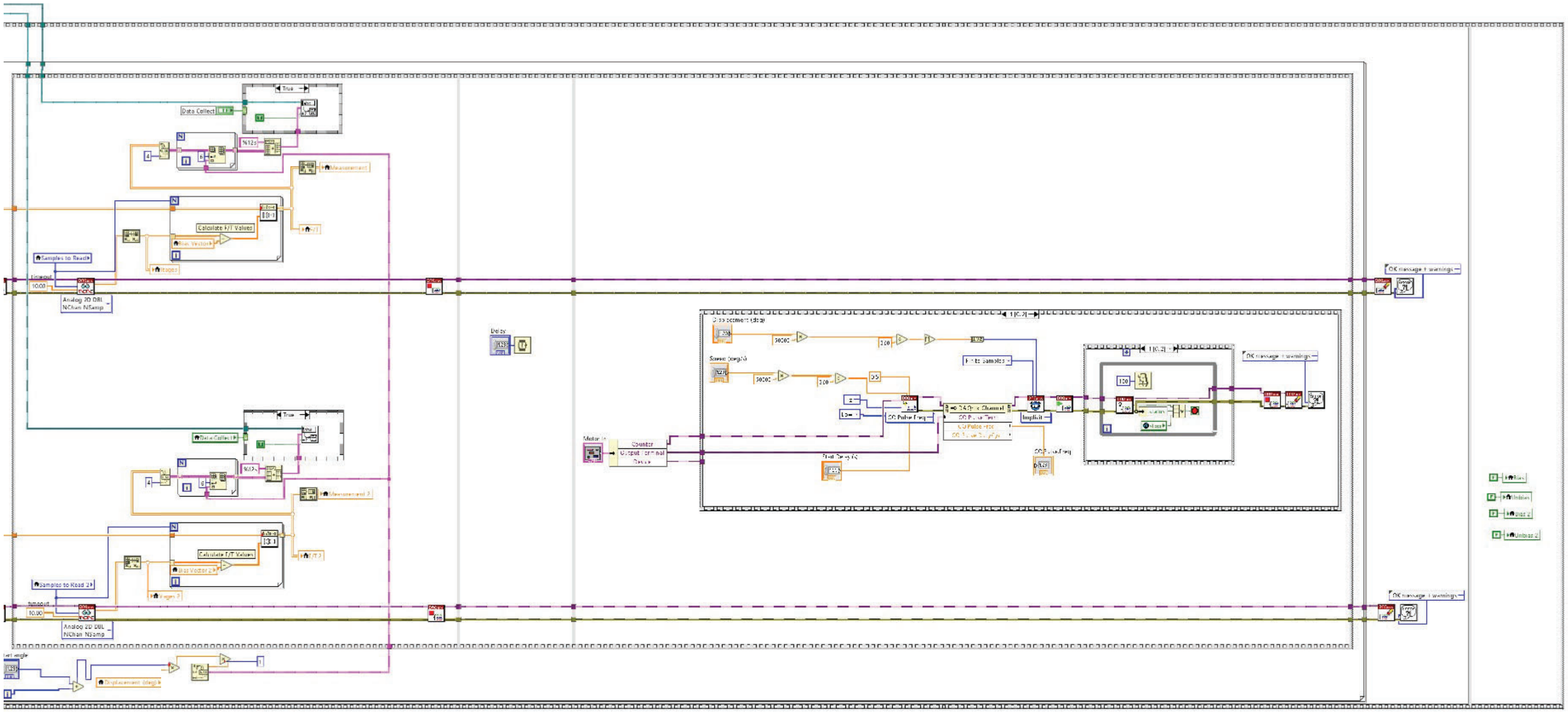

Figure A.6: LabVIEW block diagram for data writing and motor control.

A.2 Operating procedure for wake survey

To perform a wake survey using a Pitot-static tube connected to a pressure transducer and vertical traverse, integrated with a LabVIEW application:

1. Mount the Pitot-static tube securely on the vertical traverse mechanism. Connect the total and static pressure ports to the pressure transducer.
2. Position the Pitot-static tube at the starting location of the wake survey, outside of the expected wake region.
3. Open the LabVIEW VI and initialize acquisition. Input the traverse step size (e.g. 1 mm) and number of steps (e.g. 100).
4. Set a delay between traverse movement and data acquisition (e.g. 2 seconds) to allow for stabilization.
5. Start traverse motion and data acquisition. The VI will move the traverse, wait the predefined delay, then record the total and static pressure.
6. The dynamic pressure is calculated as the difference between total and static pressures. The VI converts this to velocity using Bernoulli's equation.
7. After recording the velocity, the traverse moves by the defined step size. The process repeats for the specified number of steps.
8. The VI saves the velocity deficit profile across the wake.
9. For multiple surveys, reposition the Pitot tube outside the wake and repeat the automated motion and acquisition.

Appendix B:

Surface Flow Visualization

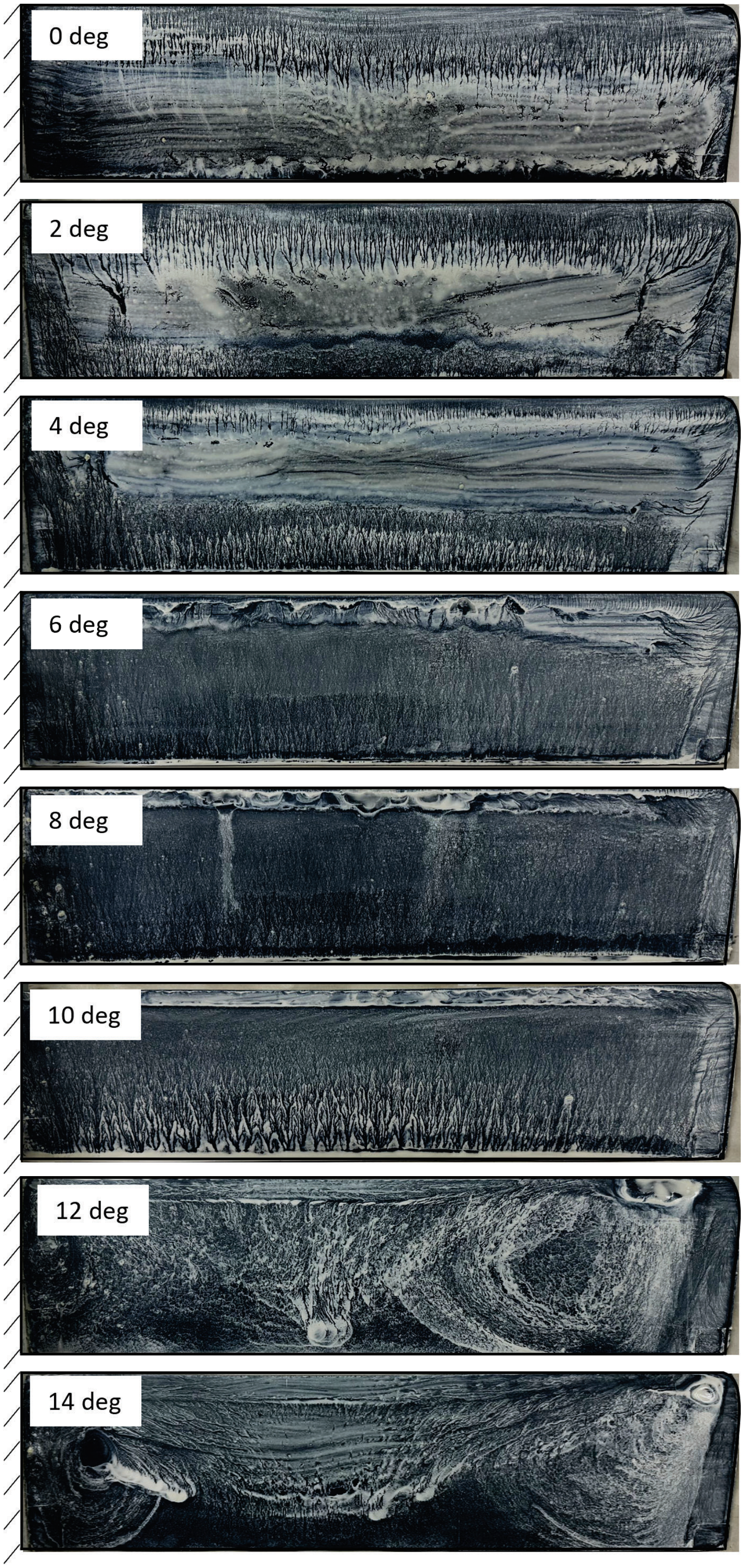

Figure B.1: Surface flow visualization for Isolated Wing at different α, Re_c = 100,000.

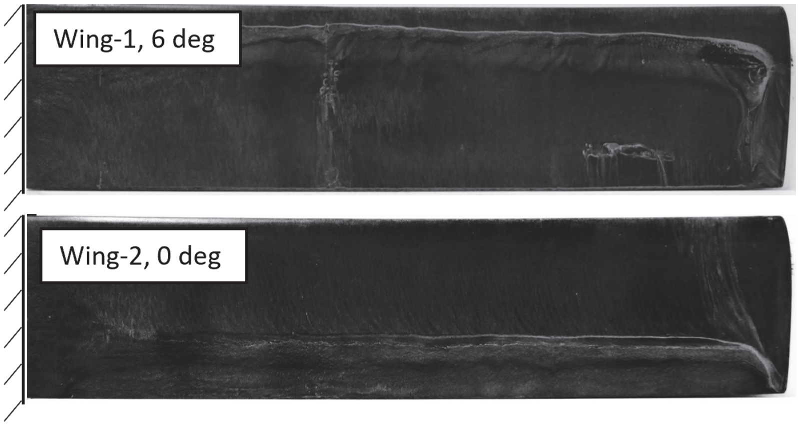

Figure B.2: Surface flow visualization tandem configuration α_1 = 6 deg and α_2 = 0 deg, Re_c = 100,000.

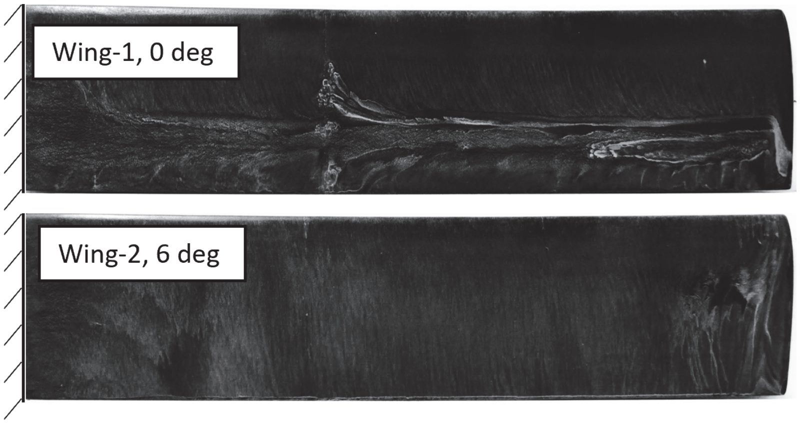

Figure B.3: Surface flow visualization tandem configuration α_1 = 0 deg and α_2 = 6 deg, Re_c = 100,000.

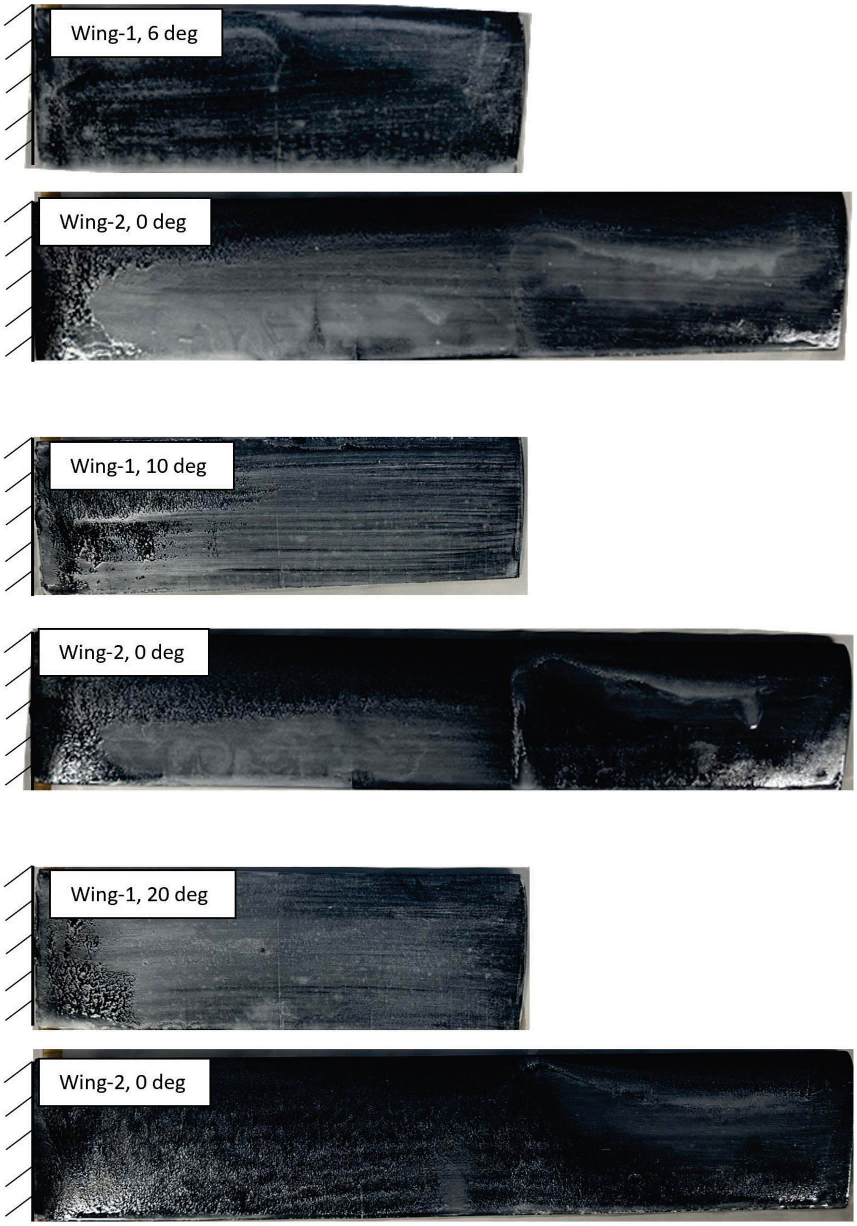

Figure B.4: Surface flow visualization tandem configuration α_2 = 0 deg and α_1 = 6,10 and 20 deg, Re_c = 100,000, AR of Wing-1 = 3 and AR of Wing-2 = 5.

Appendix C:

Unsteady response of a Finite Aspect Ratio Wing at Re = 100,000

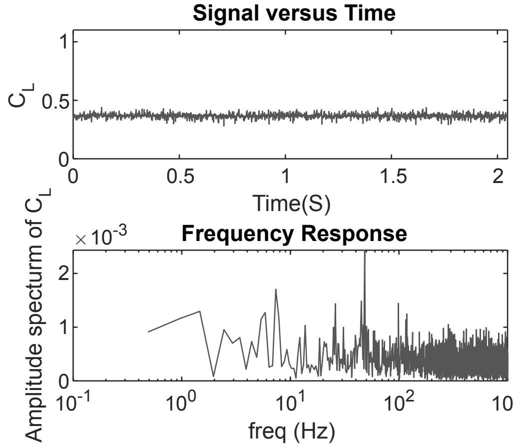

(a) $\alpha = 3$ deg

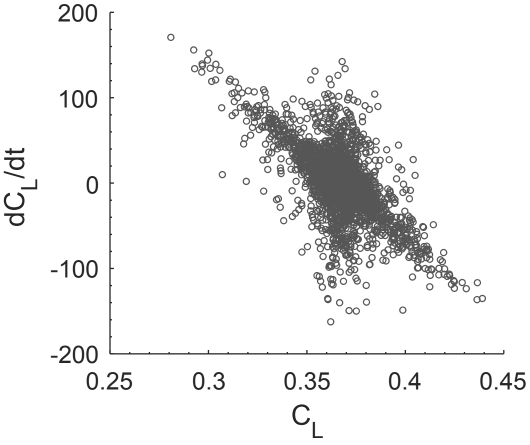

(b) $\alpha = 3$ deg

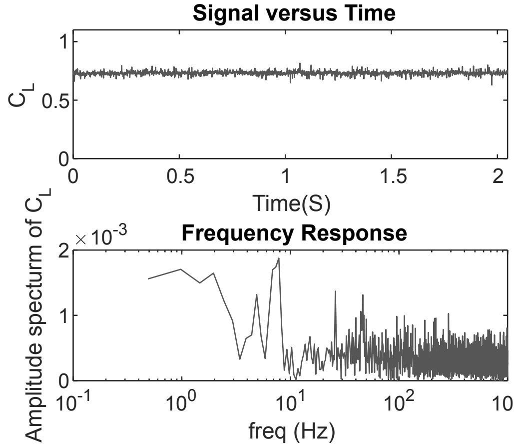

(c) $\alpha = 8$ deg

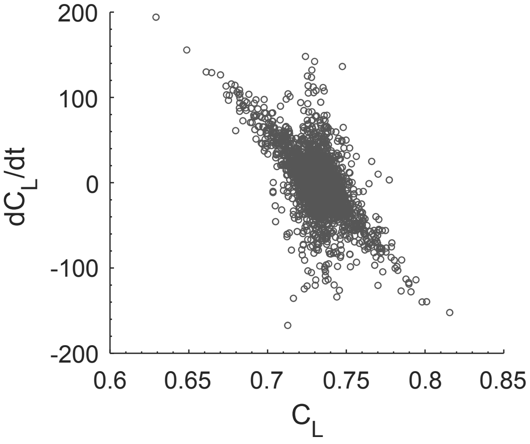

(d) $\alpha = 8$ deg

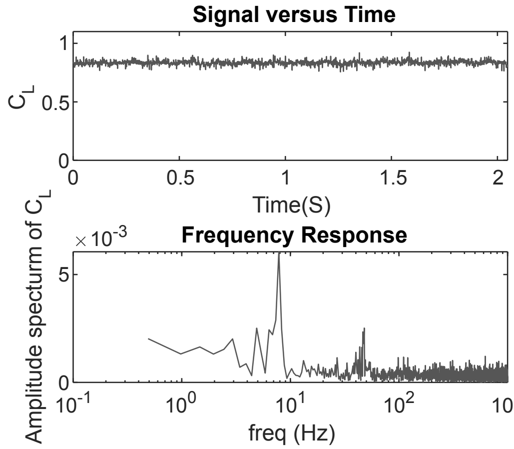

(e) $\alpha = 10$ deg

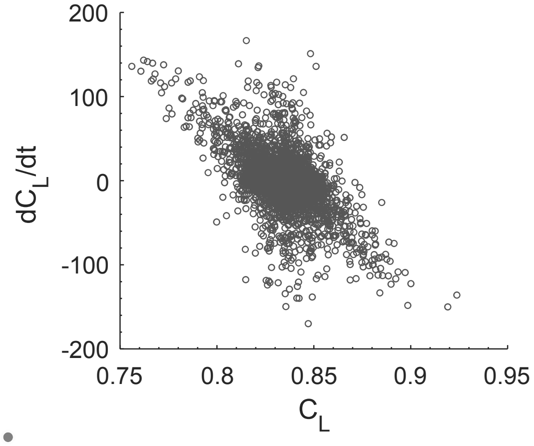

(f) $\alpha = 10$ deg

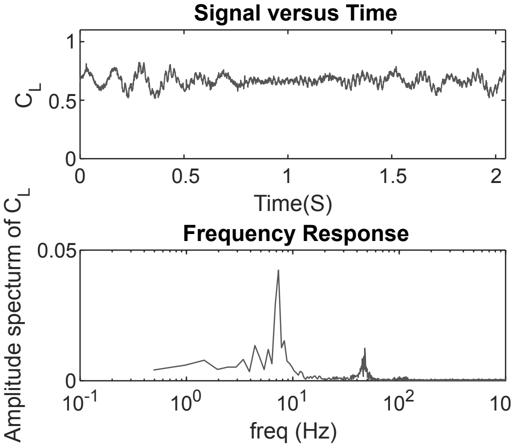

(a) α = 15 deg

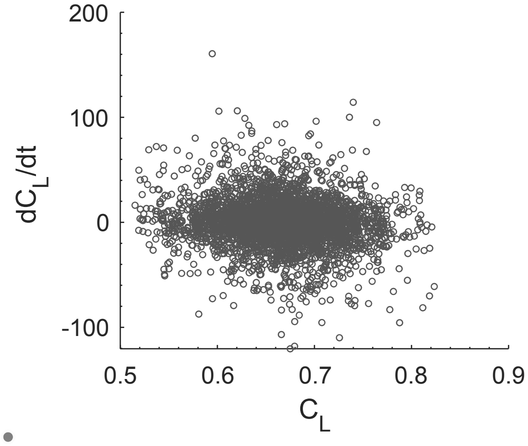

(b) α = 15 deg

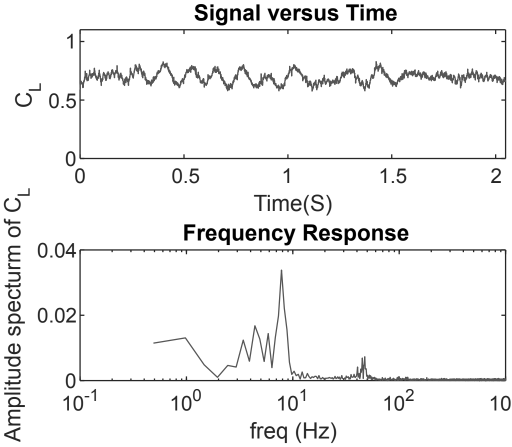

(c) α = 20 deg

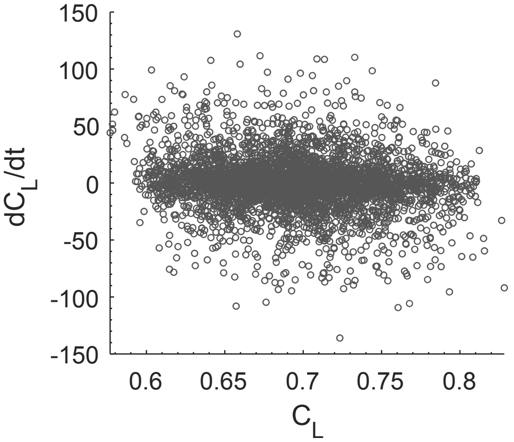

(d) α = 20 deg

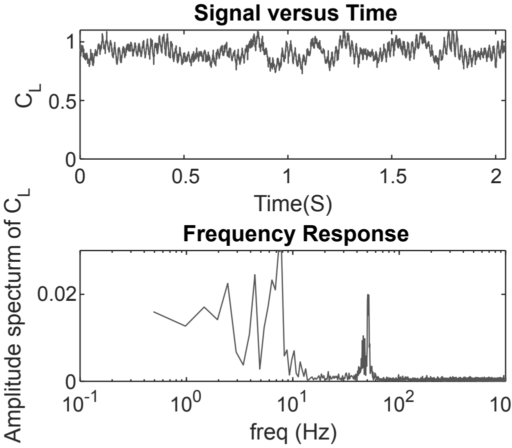

(e) α = 30 deg

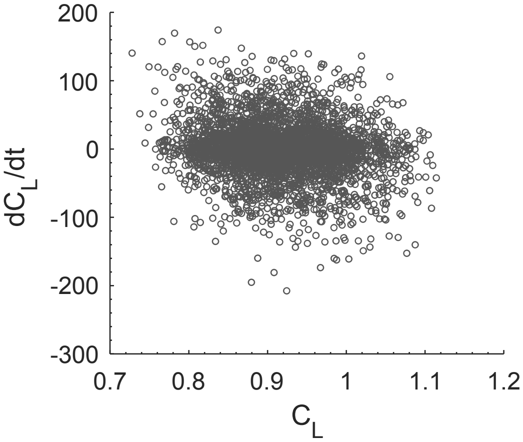

(f) α = 30 deg

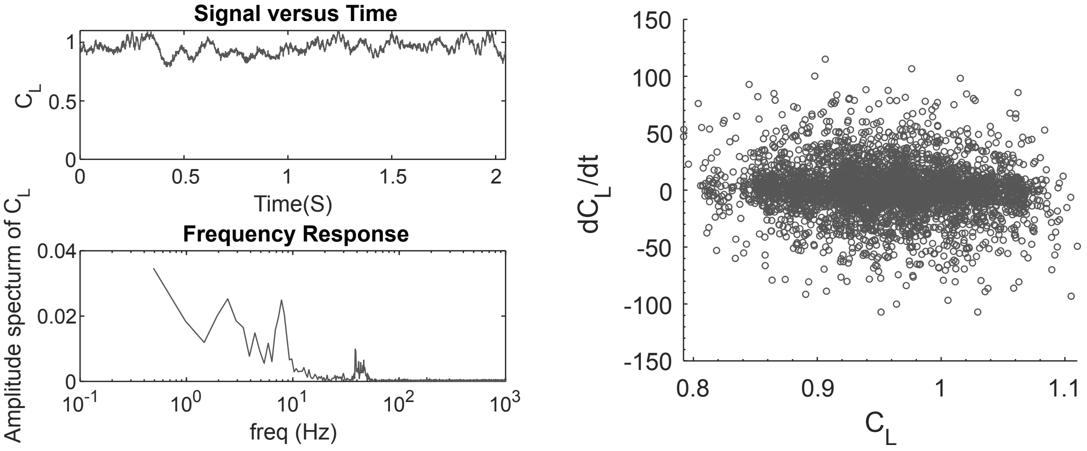

(a) α = 40 deg

(b) α = 40 deg

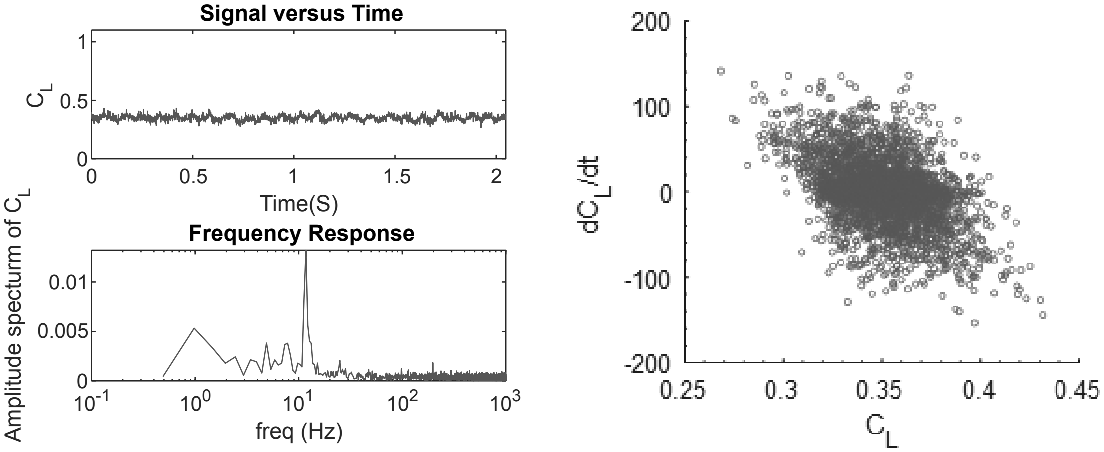

(a) α = 80 deg

(b) α = 80 deg

Figure C.2: Frequency response and Poincare’ map of isolated wing, Re = 100,000 (Raw Data).

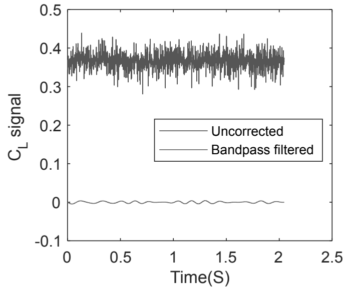

(a) $\alpha = 3$ deg

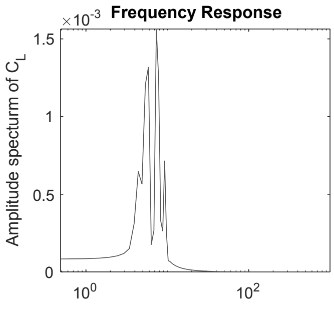

(b) $\alpha = 3$ deg

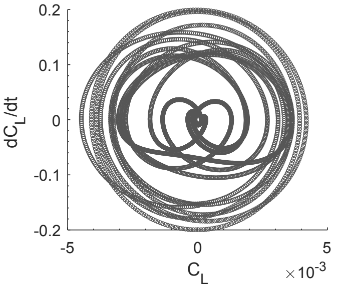

(c) $\alpha = 3$ deg

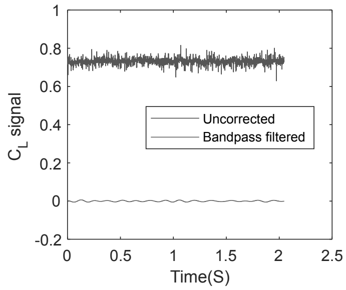

(d) $\alpha = 8$ deg

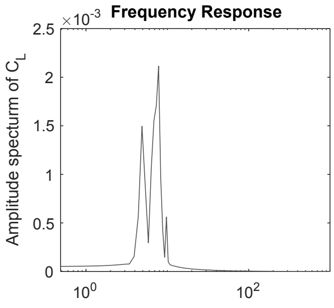

(e) $\alpha = 8$ deg

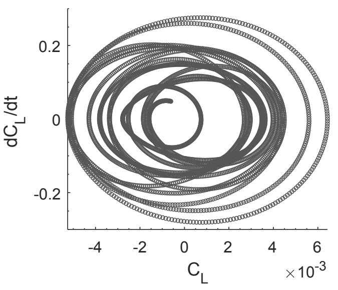

(f) $\alpha = 8$ deg

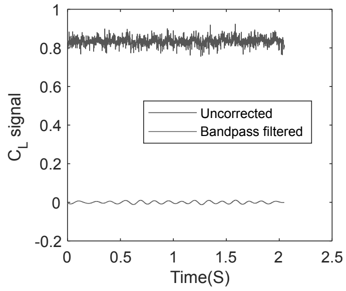

(g) $\alpha = 10$ deg

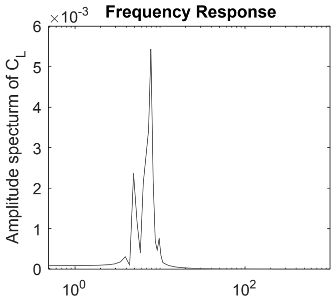

(h) $\alpha = 10$ deg

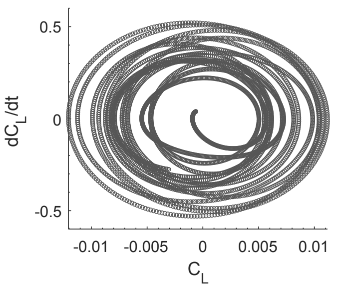

(i) $\alpha = 10$ deg

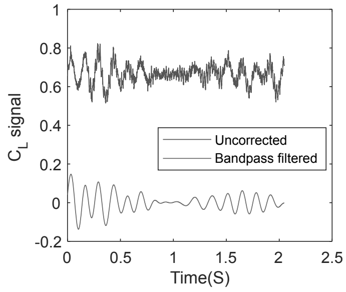

(j) $\alpha = 15$ deg

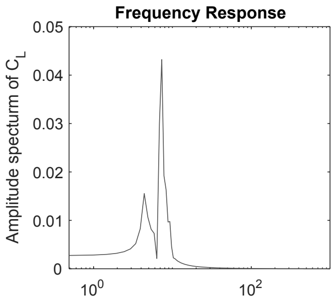

(k) $\alpha = 15$ deg

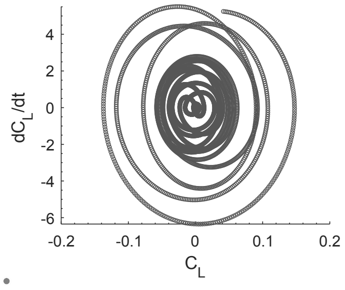

(l) $\alpha = 15$ deg

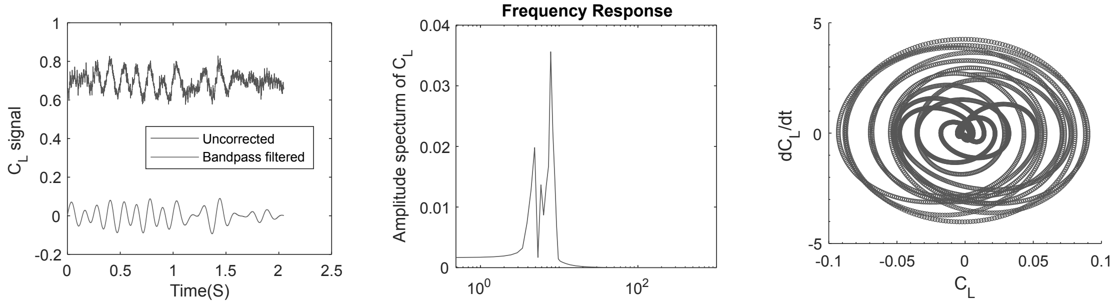

(a) α = 20 deg (b) α = 20 deg (c) α = 20 deg

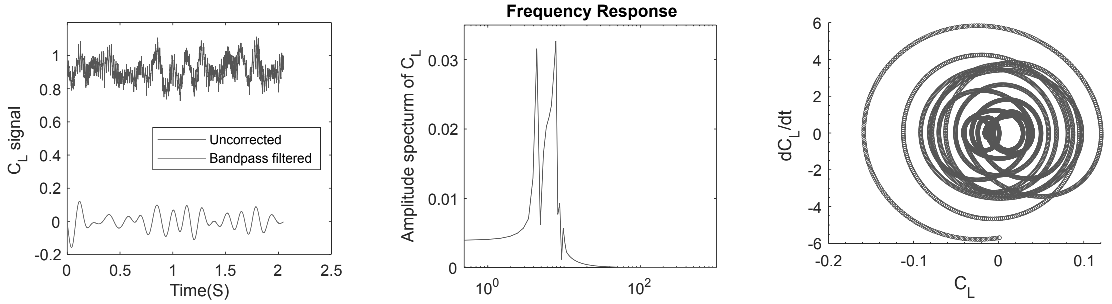

(d) α = 30 deg (e) α = 30 deg (f) α = 30 deg

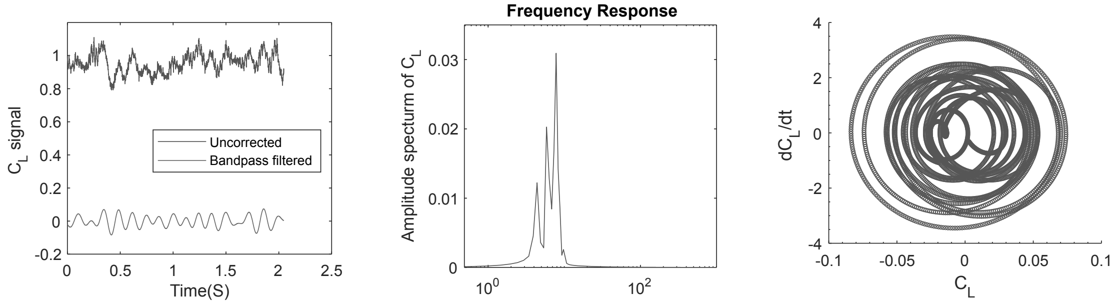

(g) α = 40 deg (h) α = 40 deg (i) α = 40 deg

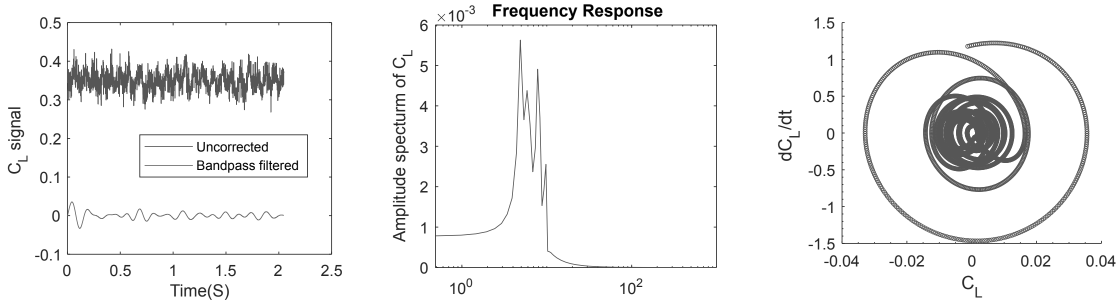

(j) α = 80 deg (k) α = 80 deg (l) α = 80 deg

Figure C.4: Time history of force signal, frequency response, and Poincare' map for isolated wing, Re = 100,000 (Bandpass filter applied).

Appendix D:

Coefficient of Pitching Moment for Wings in Tandem

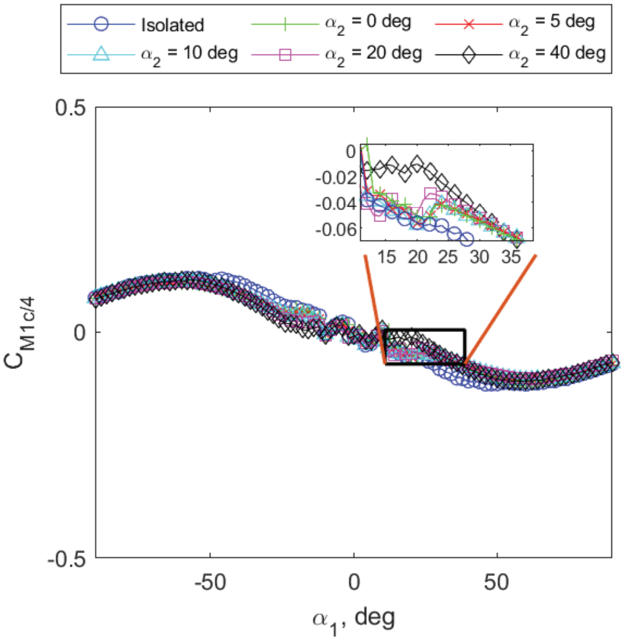

Figure D.1: $C_{M1c/4}$ vs α_1 for fixed Wing-2, Re = 100,000.

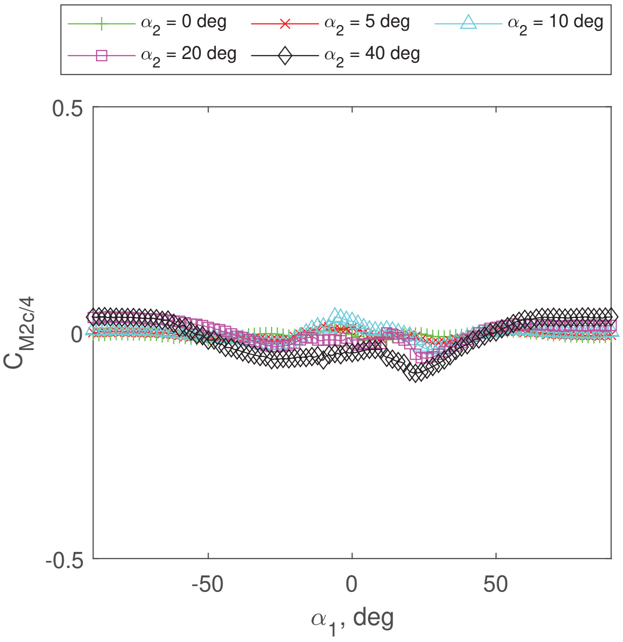

Figure D.2: $C_{M2c/4}$ vs α_1 for fixed Wing-2, Re = 100,000.

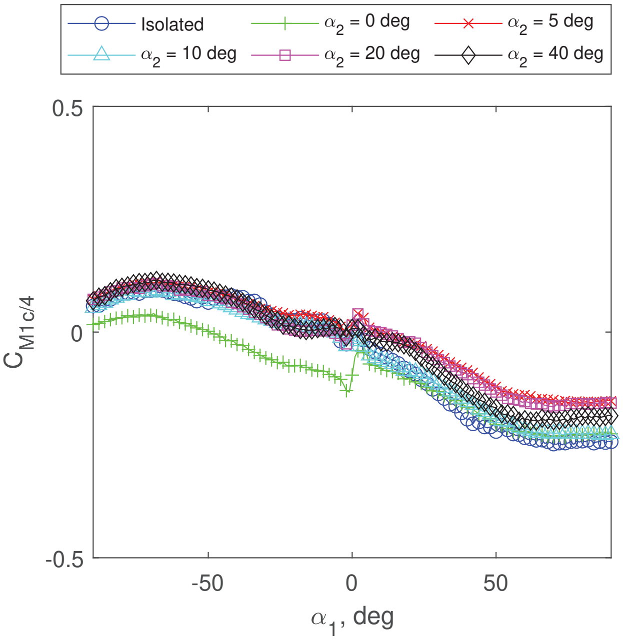

Figure D.3: $C_{M1c/4}$ vs α_1 for fixed Wing-2, Re = 20,000.

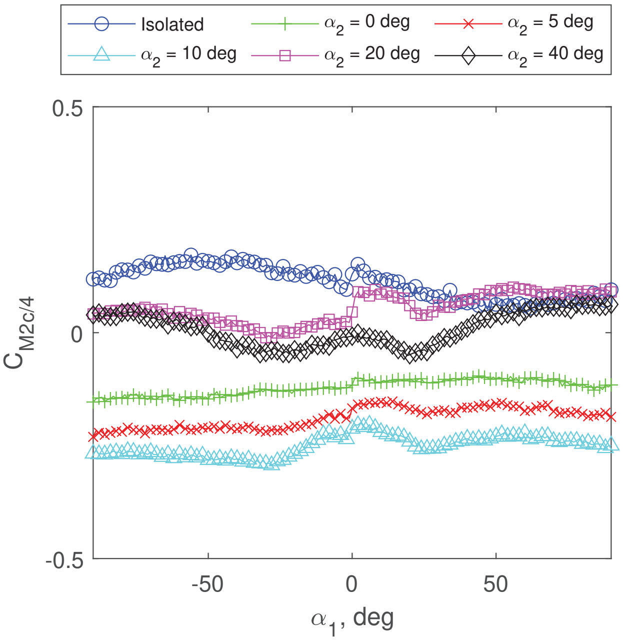

Figure D.4: $C_{M2c/4}$ vs α_1 for fixed Wing-2, Re = 20,000.

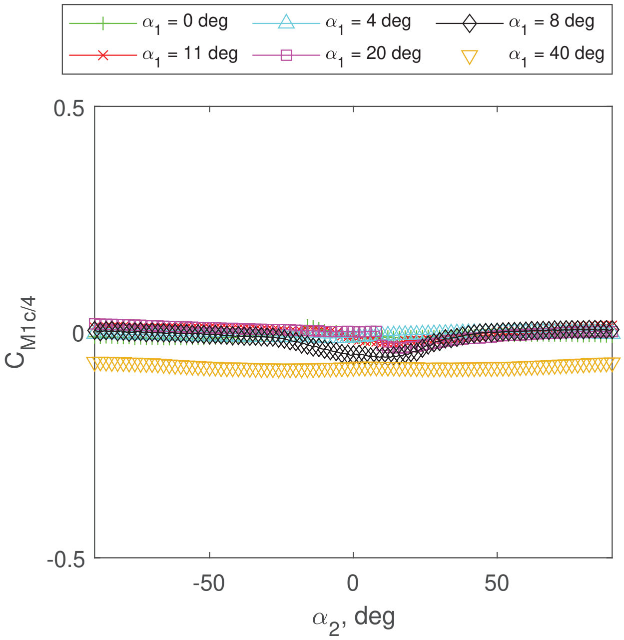

Figure D.5: $C_{M1c/4}$ vs α_2 for fixed Wing-1, Re = 100,000.

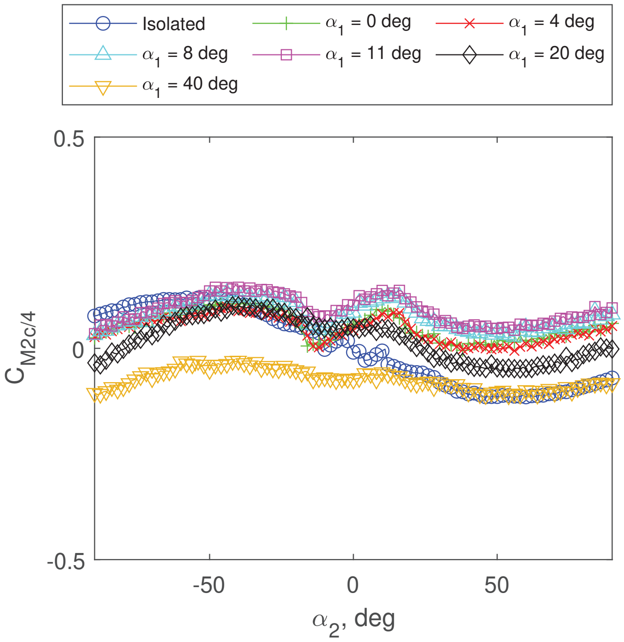

Figure D.6: $C_{M2c/4}$ vs α_2 for fixed Wing-1, Re = 100,000.

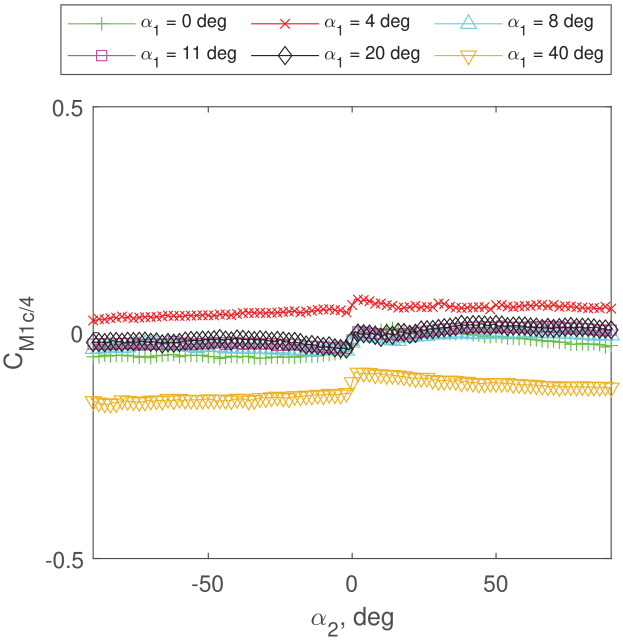

caption$C_{M1c/4}$ vs α_2 for fixed Wing-1, Re = 20,000.

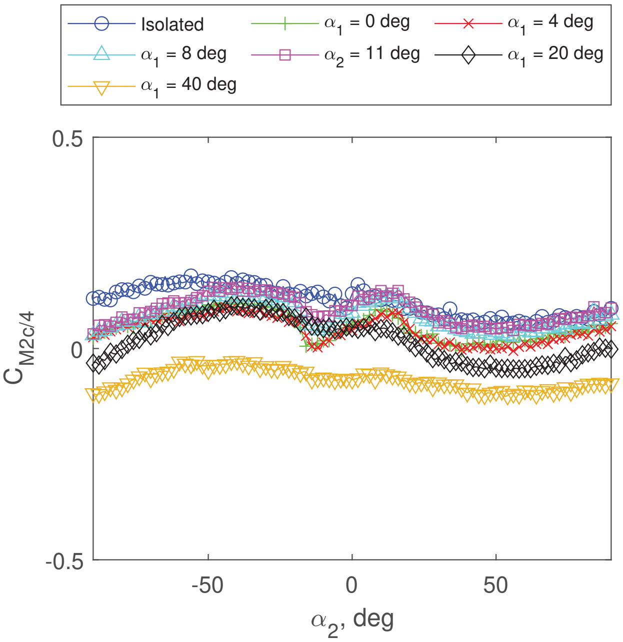

Figure D.7: $C_{M2c/4}$ vs α_2 for fixed Wing-1, Re = 20,000.

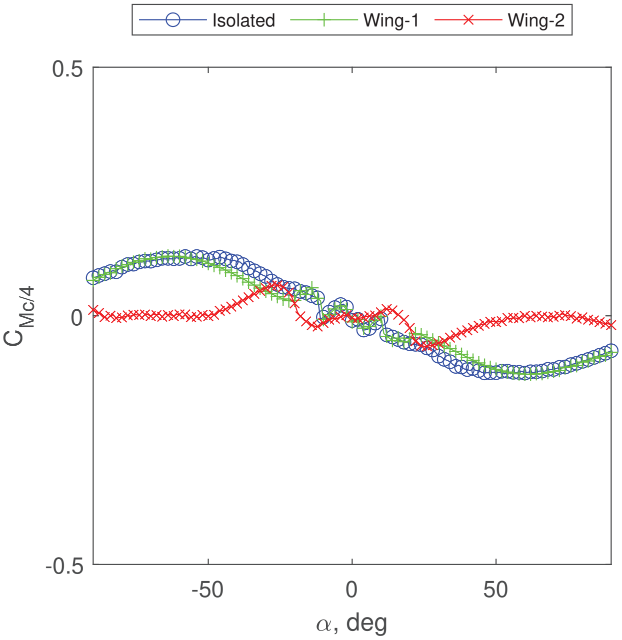

Figure D.8: $C_{Mc/4}$ vs α Wing-1 and Wing-2 at same α, Re = 100,000.

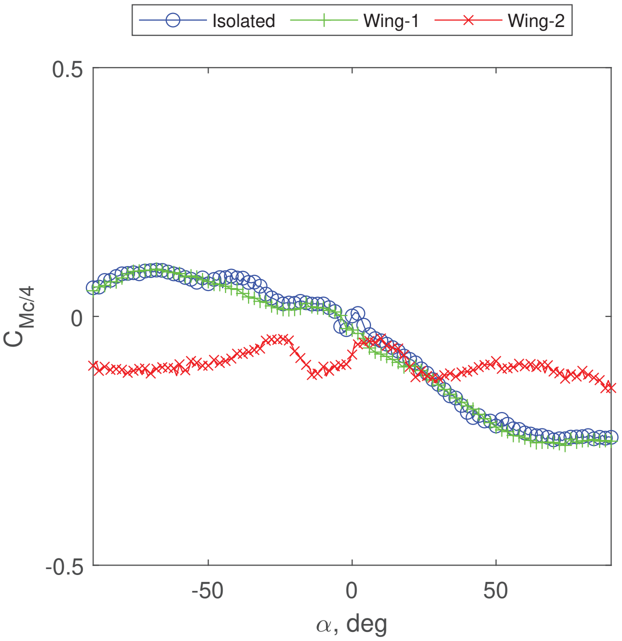

Figure D.9: $C_{Mc/4}$ vs α Wing-1 and Wing-2 at same α, Re = 20,000.